The University of Sheffield

Novel Permanent Magnet Brushless Machines Having Segmented Halbach Array

Yang Shen

A thesis submitted for the degree of Doctor of Philosophy

Department of Electronic and Electrical Engineering

The University of Sheffield

Mappin Street, Sheffield, S1 3JD, UK

15 November 2012

ABSTRACT

Permanent magnet brushless machines having Halbach array exhibit a number of attractive features. Therefore, they have been increasingly applied to different market sectors, including aerospace, industrial, domestic, renewable, and healthcare, etc. The need of fast global optimization, cost-effective design, and physical understanding of the relationship between parameters and performance requires a powerful analytical model. This thesis develops a general analytical model which is capable of predicting the electromagnetic performance of slotted/slotless permanent magnet brushless machines with both even- and odd-segment Halbach array, having different magnet remanence, magnetization angle and arc for each single magnet segment. The validity of proposed analytical model is examined by finite-element analyses.

The price of Neodymium Iron Baron magnet has been raised rapidly over the last few years, which has increased the awareness of cost-effective design and leads the magnet usage efficiency, viz. the ratio of average output torque over permanent magnet volume, to be an important design concern for industry applications. Meanwhile, the needs of high electromagnetic performance including lower torque ripple and sinusoidal air-gap flux density are also critically required. In order to meet such demands, the magnet poles having unequal-magnet height, modular high cost and low cost magnets, together with Halbach magnetization are proposed in this thesis. Based on the developed analytical models, extensive investigation has been performed. Furthermore, in order to fast optimize design parameters, e.g. optimal magnet arc ratio for 2-segment Halbach array and split ratio for external rotor PM machine, two analytical models are developed and validated by finite-element analysis and measurements.

With the aid of developed analytical models and finite element analyses, the findings provide useful guidelines for design and analysis of permanent magnet brushless machine having conventional and proposed Halbach arrays.

ACKNOWLEDGEMENTS

Many thanks are due to my supervisor, Prof. Zi-Qiang Zhu, for his continued encouragement, advice and support throughout this PhD study, which has been invaluable in the completion of this thesis.

Thanks are also due to many other current and former members of the Electrical Machines and Drives Group at the University of Sheffield, who have assisted in the research process, particularly to Dr Jintao Chen and Dr Lijian Wu for their many helpful and productive discussions.

Finally, I thank my parents for their love, encouragement and constant support for the strength to bring this task to completion.

Contents

NOMECLATURE

A_s	Stator slot area
A_{stator}, B_{stator}	Coefficient of scalar potential distribution on the stator bore
B_{ag}	Air-gap flux density
B_{ag1}	Fundamental air-gap flux density
$B_{agr}P$, $B_{agr}R$	Radial air-gap flux density with parallel and radial magnetization
$B_{agc}P$, $B_{agc}R$	Circumferential air-gap flux density with parallel and radial magnetization
B_r	Remanence of magnet
B_{rn}, $B_{\theta n}$	Radial and circumferential flux density components
B_{rm}	Remanence of mid-magnet
B_{rs}	Remanence of side-magnet
B_{rsL}	Remanence of left side-magnet
B_{rsR}	Remanence of right side-magnet
B_{rmax}	Maximum flux density in the rotor back-iron
B_{smax}	Maximum flux density in the stator tooth
b_t	Tooth body width
$C_{ei(n)}$	n^{th} order harmonic of the scalar potential distribution
D_{ri}	Rotor inner diameter
D_{ro}	Rotor outer diameter
D_{si}	Stator inner diameter
D_{so}	Stator outer diameter
D_{sf}	Shaft diameter
g_{Br}, $g_{B\theta}$	Coefficients of scalar potential distribution along the slot opening
h_{pm}	Magnet thickness
h_{pmL}	Magnet thickness of left side-magnet
h_{pmR}	Magnet thickness of right side-magnet
h_t	Tooth-tip height
k_{dn}	Winding distribution factor
k_{dsph}, k_{dcph}	Winding distribution factors of given phase for the sine and cosine flux density harmonic components
k_{pn}	Winding pitch factor
k_w	Winding factor
k_e	Coefficient of eddy current loss
k_{ex}	Coefficient of excess loss
k_h	Coefficient of hysteresis loss
i_a, i_b, i_c	Phase armature current
i_k	Amplitude of the k_{th} order phase harmonic current
l_a	Machine stack length
l_e	End-winding length
l_g	Air-gap length
l_m	Effective magnet length
m	Phase number
M_r, M_θ	Radial and circumferential components of magnetization vector
n	Harmonic order
N	Number of turns per phase
N_c	Number of turns per coil
N_s	Number of stator slots
p	Rotor pole pair number
P_{iron}	Iron loss

P_h	Hysteresis loss
P_e	Eddy current loss
P_{ex}	Excess loss
P_{cu}	Copper loss
Q	Number of slots per pole
R_m	Magnet outer radius
R_r	Rotor outer radius
R_o	Magnet inner radius
R_s	Stator inner radius
R_{mp}	Magnet arc ratio
r_{ew}	Average end-winding radius
r_{iew}	Inner end-winding radius
r_{oew}	Outer end-winding radius
T_{cog}	Cogging torque
T_{av}	Average torque
TD	Torque density
TD^*	Nominal torque density
T_{em}	Electromagnetic torque
T_{pp}	Peak-to-peak torque ripple
W_a	Pole arc of magnet pole
W_f	Pole arc of mid-magnet
W_p	Pole pitch
V_{pm}	Volume of magnet
α	Circumferential position
α_{pp}	Pole-arc to pole-pitch ratio
α_{cp}	Coil pitch angle
ε	Shaft ratio
δ	Tooth-tip ratio
η_{pm}	Magnet usage efficiency
λ	Split ratio
μ_0	Permeability of free space
μ_r	Relative permeability
Φ_{coil}	Flux through one coil
Φ_{pm}	Flux through one magnet pole
Φ_{rbi}	Flux in the rotor back-iron
ψ_{coil}	Flux-linkage per coil
ρ	Resistivity
Δh	Incremental magnet thickness
Δl_g	Incremental air-gap length
θ_k	Phase angle associated with a current harmonic
$\Delta\theta_L$, $\Delta\theta_R$	Magnetization angle of left and right side magnets
ω_r	Mechanical angular speed

CHAPTER 1 GENERAL INTRODUCTION

Since the Neodymium Iron Baron (NdFeB) magnets were developed in early 1980s [1][2], they are becoming increasingly popular across a wide range of products, such as high performance permanent magnet (PM) motors and generators for aerospace, automotive, renewable energy, and domestic applications etc. The PM can be made into many kinds of shape and magnetized [3]-[10] with certain orientation such as radial and parallel magnetization, together with a desired magnetization direction. Both the structure and magnetization of PM segments which form the rotor poles can significantly influence the air-gap flux density distribution, which in turn affects the electromagnetic performance of PM brushless machines. Therefore, in order to improve the electromagnetic performance, the magnet pole having Halbach magnetization or Halbach array was proposed in [11]. Meanwhile, the analytical models are capable and preferred to optimize the design parameters for machines and devices having Halbach array.

This thesis presents a comprehensive range of general analytical model for predicting the electromagnetic performance including flux-linkage, back-EMF, cogging torque, and electromagnetic torque waveforms of surface-mounted PM (SPM) brushless machines having either even or odd segmented conventional Halbach array. The developed analytical models are further extended to predict the electromagnetic performance of proposed SPM machines having Halbach array with mixed grade magnets and unequal height of magnet pole techniques. Moreover, the influence of design parameters, such as split ratio, on the average torque is also analytically investigated. The developed analytical models are extensively validated by finite-element analysis (FEA) and measurements on prototype machines.

1.1 Permanent Magnet Machines

This thesis is mainly confined to radial field SPM brushless machine having Halbach array, Fig.1.1, although nowadays technique offers a great variety of rotor and stator structures.

The radial field PM machines are broadly classified into three categories on the basis of the placement of PMs, i.e. the SPM machine, Fig.1.2(a), the inset PM machine, Fig.1.2(b) and the interior PM (IPM) machine, Fig.1.2(c). Normally, the SPM machine with parallel magnetized magnet exhibits quasi-sinusoidal air-gap flux density waveform, which in turn, results in low torque ripple and iron loss due to low harmonic contents. Meanwhile, the rotor weight of SPM machine could be lighter than that of IPM machine. Thus, the SPM machine is desirable for servo-motor application since high efficiency, low torque ripple and inertia

characteristics are the most concerns for such application [12]. However, the high-speed application requires the rotor having stronger structure to be able to withstand high mechanical stress [13]. With respect to this mechanical issue, the rotor sleeves made from either carbon fiber [14] or Titanium [15] are often employed for SPM rotors. On the contrary, IPM machine can exhibit more robust mechanical structure than SPM machine. Therefore, it is more suitable for high-speed applications except some extremely high speed cases. Moreover, since the fluxes through the upper rotor iron to the air-gap will be modulated and equal-potentially distributed along the outer rotor surface, thus the air-gap flux density waveform is more trapezoidal for IPM machine if the flux barrier and shaping techniques were not applied. Consequently, the amplitude of harmonic components of air-gap flux density for IPM machine are usually higher than SPM machine which causes higher fluctuated electromagnetic torque waveform and iron loss. In contrast to SPM and IPM machines, the PMs are embedded in the rotor surface for an insert PM machine. Hence, such structure can exhibit improved mechanical strength than SPM machine, while its air-gap flux density is still quasi-sinusoidally distributed if compared with IPM machine. However, the leakage flux between magnet pole and iron pole is significant. As a consequence, the output torque is reduced.

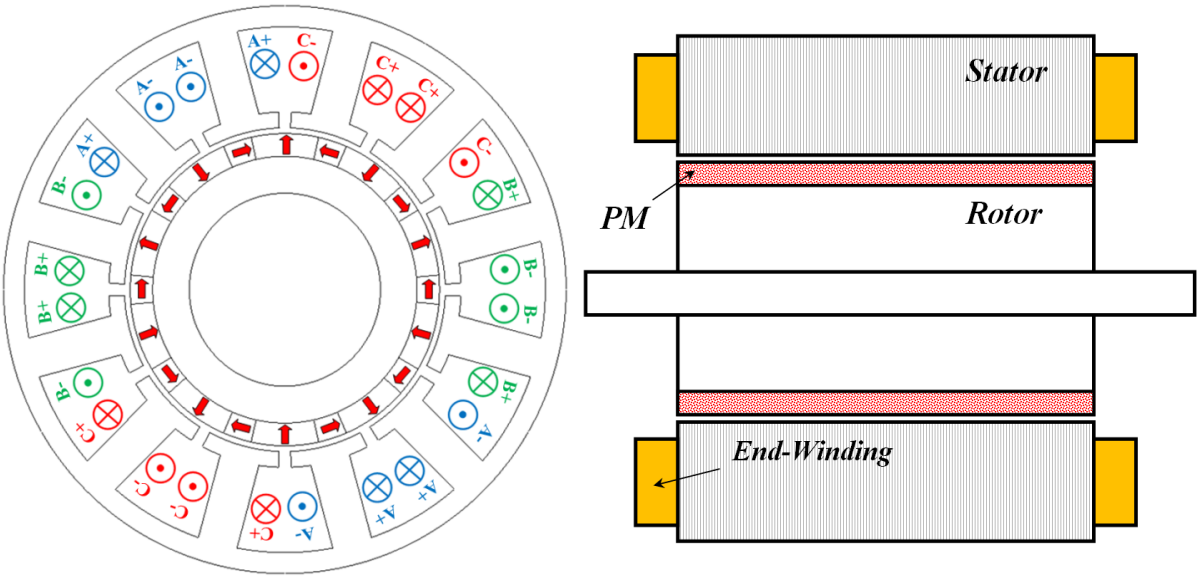

Fig.1.1. Typical radial field SPM brushless machine having 2-segment Halbach array (12-slot/10-pole)

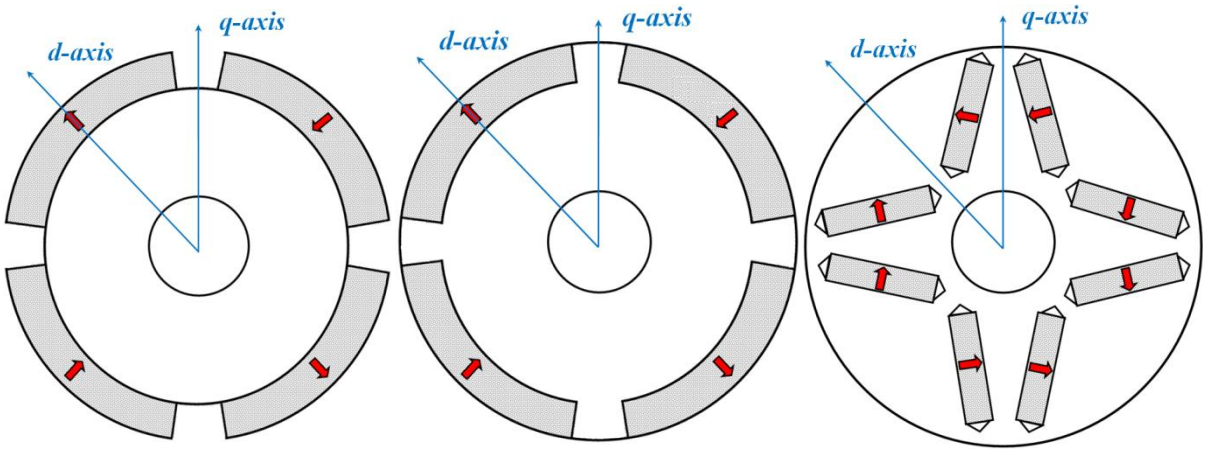

(a) SPM (b) Inset PM (c) Interior PM

Fig.1.2. Typical PM rotor configurations.

In the stator part, the winding topologies are summarized into non-overlapping and overlapping windings, in Fig.1.3, where both single and double layer windings can be applied [16]-[30]. The double layer winding could be further grouped into two-circumferential-layer winding (Fig.1.3 (b)) which is employed in non-overlapping winding machines, and two-radial-layer winding (Fig.1.3 (c)) which is employed in overlapping winding machines, respectively. The PM machine having non-overlapping double layer winding exhibits shorter end-winding length, lower mmf or spatial harmonic contents (The double layer winding exhibits lower harmonic contents than the single layer winding due to doubled coil number per phase and reduced harmonic winding factor), lower torque ripple, lower iron and magnet losses than PM machine equips single layer winding. However, PM machine having non-overlapping single layer winding exhibits higher self-inductance, higher flux weakening capability, higher fault tolerant and improved electric isolation capabilities. On the other hand, normally PM machines having non-overlapping winding can obtain higher G (least common multiple number between stator slot number N_s and rotor pole number $2p$), which leads to a higher cogging torque period and lower cogging torque amplitude than PM machine having overlapping winding, except the latest developed cases of 3-phase machine having coil pitch equal to 2 [31]. Additional advantages of PM machine having non-overlapping winding over overlapping winding includes short ending winding length, lower copper loss, limited short-circuit current and more suitable for utilizing segmented stator construction to ease the mass production, etc. Nevertheless, the richer spatial harmonic contents, especially the existing of lower and sub harmonic contents for machine having non-overlapping winding leads the rotor

and magnet loss significantly larger than PM machine having overlapping winding, and very often magnet segmentation is required in order to reduce the magnet eddy current loss.

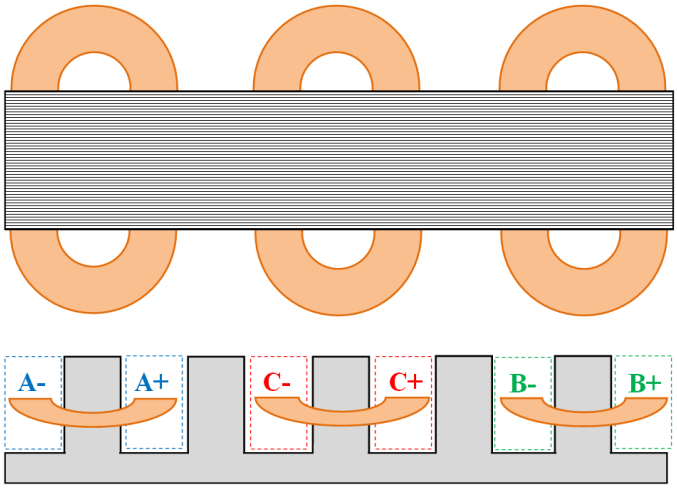

(a) Non-overlapping single layer winding

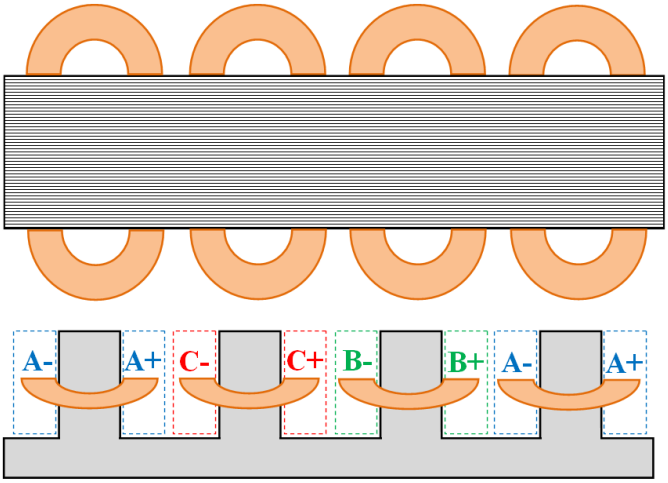

(b) Non-overlapping double layer (two-circumferential-layer) winding

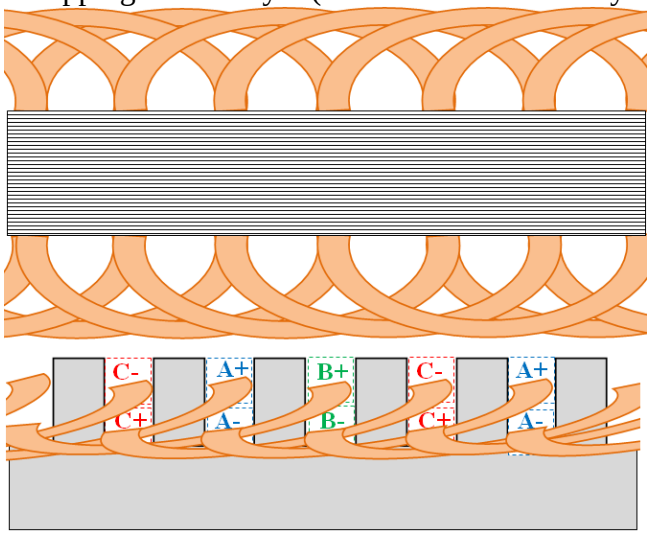

(c) Overlapping double layer (two-radial-layer) winding

Fig.1.3. Winding configurations.

It is well-known that two parasitic effects, e.g. parasitic losses and torques, existing in PM

brushless machines during their operations. There are different kinds of losses accompanying with machines when electrical and mechanical energy conversion occurs. The losses of PM machines can be mainly divided into iron loss [32]-[41], winding loss [42]-[46], magnet loss [47]-[49] and friction losses [50]. The iron loss P_{iron} contains hysteresis P_h, eddy current P_e and excess P_{ex} losses, respectively and written as:

$$P_{iron} = P_h + P_e + P_{ex} = k_h \hat{B}^{\beta} \omega_s + k_e \hat{B}^2 \omega_s^2 + k_{ex} \hat{B}^{1.5} \omega_s^{1.5} \quad (1.1)$$

where, k_h, k_e, and k_{ex} are the hysteresis, eddy current and excess loss constants, and β is the Steinmetz constant (normally β = 1.8-2.2 [34]), $\hat{B}$ is the peak flux density and ω_s is the angular frequency. The iron loss is increased significantly as speed increases. Therefore, several methods including appropriate slot/pole combination, optimal slot opening width, rotor pole shaping techniques and thin lamination, etc are used to effectively reduce the iron loss. Although the iron loss in rotor lamination is usually small since the PM field is stationary in the rotor axis, it is still observable and causing temperature rising in magnet which increases the risk of magnet to suffer irreversible demagnetization due to stator slotting and armature reaction field harmonics. Since the majority of magnets are conductive, the eddy current loss in the magnet exists. In general, the magnet loss can be classified into skin and resistance limited eddy current losses. The magnet loss can directly raise the temperature of magnet, thus it is necessarily be minimized to avoid characteristic deterioration of magnet. In order to reduce the magnet loss, the circumferential and radial magnet segmentations (to reduce resistance limited loss), plus the conductive retaining sleeve (to reduce skin limited loss) can be applied.

The parasitic torques will not produce output torque, but introduce vibration and noise. The parasitic torque contains electromagnetic torque ripples which produced by harmonic components of air-gap flux density, spatial and temporal harmonics (due to non-sinusoidal armature current), together with cogging torque. In order to minimize the electromagnetic torque ripples, optimal design should be applied for both machine and drive system [51]-[52]. Meanwhile, cogging torque is caused by interaction of PM and air-gap permeance harmonics due to slotting effect [53]. Along with the growing understanding of cogging torque has allowed a lot of methods to reduce it [54]-[56], including optimal slot/pole combination, stator/rotor skew, pole shaping, tooth notching, etc. Besides parasitic torque, the parasitic force, e.g. the unbalanced magnetic force may also exist during energy conversion if static/dynamic rotor eccentricities and diametrically asymmetrical winding distribution existing [57]-[59].

1.2 Halbach Magnetization

Nowadays, PM brushless machines are increasingly applied to the expanding industrial and commercial markets, which often critically require high electromagnetic performance. The PM brushless machines can be further separated into brushless DC (BLDC) and brushless AC (BLAC) operation modes in accordance with trapezoidal/rectangular and sinusoidal/sinusoidal back-EMF/current waveforms, respectively. In this thesis, BLAC operation mode is applied to chapter 2-5 according to the property of Halbach array as will be discussed later. Meanwhile, the BLDC operation mode is applied to chapter 6 to ease the derivation of analytical model, although BLAC is also applicable. In order to satisfy the requirement, PM brushless machines should exhibit low harmonic content in the air-gap flux density. Thus, magnets are attempted to magnetize with continuously varying direction for the purpose of obtaining sinusoidal air-gap flux density distribution. In the early 1970s, the sinusoidally distributed magnetization pattern shown in Fig.1.4(a) was firstly proposed and studied in [70], where only one-sided flux exists. Therefore, the flux is self-shielded in the magnet pole, which means the rotor back-iron can be abandoned. The idea of such self-shielding property, however, did not immediately gain widespread acceptance because of the difficulty in realization. Later, in [11], an approximated continuously varying magnetization array is achieved by using segmented magnets with varied magnetization angles, in Fig.1.4(b), and such novel magnet pole construction is named as Halbach magnetization or Halbach array hereafter.

The PM brushless machines having Halbach magnetization present some attractive features [71]-[72]. For instance, an essentially sinusoidal air-gap flux density distribution can be obtained, which in turn, results in low iron loss, sinusoidal back-EMF waveform and low electromagnetic torque ripple. Further, due to low harmonic contents of the air-gap flux density, the cogging torque is almost negligible, without resorting to skewing, shaping and adopting a fractional slot/pole combination. Since only one-sided flux exists in the Halbach array, the increased effective magnet length l_m (effective magnet length is used to represent the increased flux path due to self-shielding characteristic) leads to a higher air-gap flux density B_{ag} as interpreted in (1.2), where B_r is the remanence of magnet, l_g is the air-gap length and μ_0 is the permeability of free space. Moreover, due to self-shielding property, the usage of rotor back-iron is not essential although the back-iron is still beneficial for a very thin Halbach array.

$$B_{ag} = \frac{B_r}{1 + \mu_0 \frac{l_g}{l_m}} \tag{1.2}$$

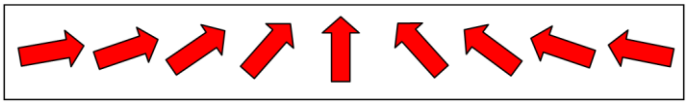

(a) Ideal Halbach magnetization

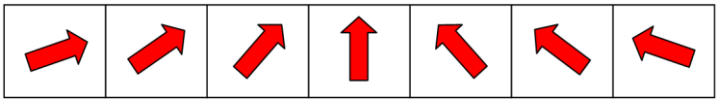

(b) Segmented Halbach array with equal pole-pitch

Fig.1.4. Two typical configurations of Halbach array.

Ultimately, with the advent of Halbach magnetization, it is extensively applied to

- axial field motor [73],
- linear machine [74]-[76],
- rotary machine [77]-[81],
- slotless machine [82]-[84],
- tubular machine [85]-[100],
- spherical motor [101][102],
- planer machine [103]-[110],
- flywheel energy storage system [111]-[117],
- magnetic bearing/coupling [118]-[128],
- magnetic gear [129]-[130],
- magnetic cylinder [131]-[141],
- magnetic refrigerator [142]-[144],
- elliptically polarizing undulator [145]-[147],
- Maglev and eddy current break systems [148]-[159], etc.

Some of the most commonly used machine types with Halbach array are discussed as follows.

1.2.1 PMLM

The PM linear machines (PMLM) are widely used for servo and high precision position control systems. Hence, the requirements of high thrust force density (defined as thrust force over rotor mass), low electromagnetic and cogging force ripples are critical. Since Halbach array exhibit self-shielding property, the rotor or mover back-iron thickness of PMLM having

Halbach array in Case A (Fig.1.5) is reduced compared to PMLM having conventional pole. Meanwhile, the increased number of magnet segment in Halbach array leads to a further improved self-shielding property. Hence, the mover back-iron can be entirely abandoned, as shown in Case B. On the other hand, the Case C exhibits slotless structure which can reduce inductance and cogging force, while Case C also further improves flux circulation path between up and lower mover than conventional poles. Therefore, it is suitable for application such as electromagnetic launch system which needs even higher control capability and dynamic performance. The inherent low air-gap flux density of slotless machine, however, still exists even though it is improved by adopting Halbach array. As a consequence, Case D is developed based on Case C. It is capable of achieving higher thrust by employing stator back-iron and toroidal winding to enhance the flux-linkage, but it has impact on the machine volume. Recently, the demand for low rare-earth magnet usage leads to a new magnet mover being developed as illustrated in Case E. However, a high strength sleeve (made by silicon carbide SiC) surround the magnet mover is needed to overcome the inherent strong internal strength between magnets. The disadvantage of sleeve is to increase the effective air-gap length which could deteriorate machine performance by reducing B_{ag}, especially when a thick sleeve is used.

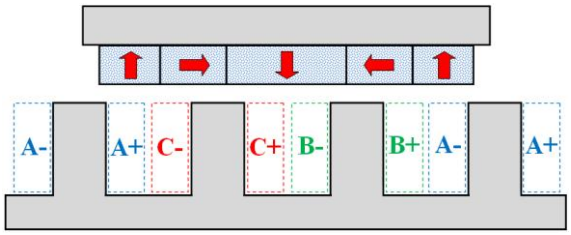

Case A. PMLM with iron-cored rotor

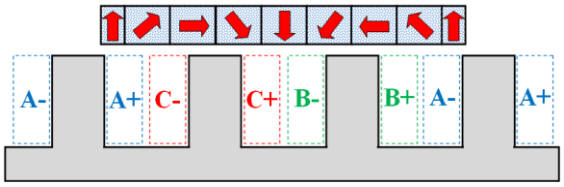

Case B. PMLM with air-cored rotor

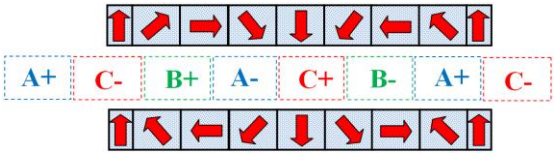

Case C. PMLM with slotless stator

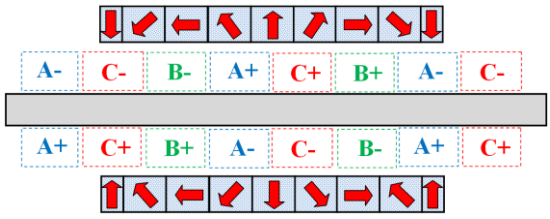

Case D. PMLM with slotless stator

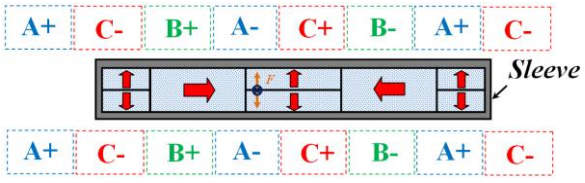

Case E. PMLM with dual slotless stator

Fig.1.5. Configuration of three typical PMLM having Halbach array.

1.2.2 PMTM

The PM tubular machine (PMTM) is a kind of PMLM. A unique feature of such linear machine is the fact that end-winding can be eliminated which leads to significant high volumetrically efficiency, whereas the end-winding in flat PMLM is evitable. Meanwhile, the mover having Halbach array without back-iron exhibits high thrust force density, which is desirable to facilitate resonate operation. Consequently, a great deal of PMTM with Halbach array has been devoted to reciprocating applications, including refrigerator compressor and wave energy generator. Both slotted and slotless structures can be adopted to PMTM, in Fig.1.6, while the cylinder magnet pole can be magnetized in radial or parallel magnetization, in Fig.1.7. Usually the cylinder magnet pole is composed by segmented magnet with parallel magnetization on the basis of low manufacture cost and high rate of finished product in contrast to magnet ring with radial magnetization. However, the cylinder magnet pole with parallel magnetized magnet segments produce non-uniformly distributed radial air-gap flux density, which may cause unbalanced radial force distribution in stator teeth.

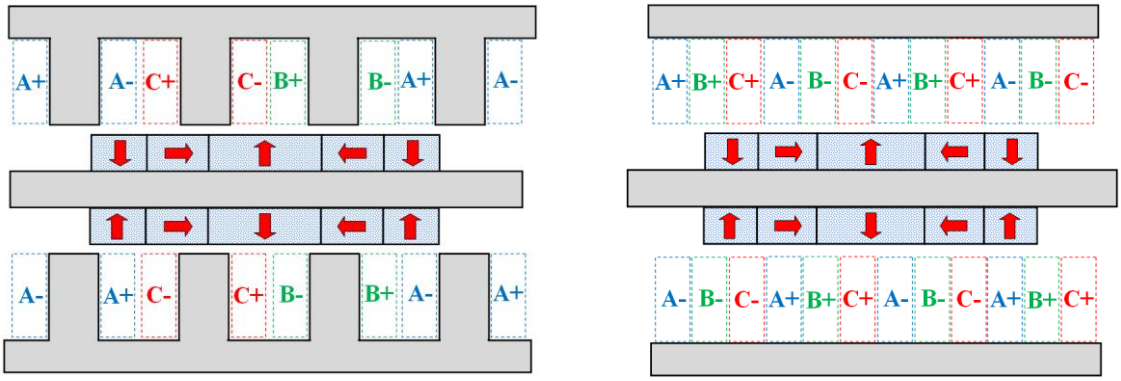

(a) Slotted PMTM (b) Slotless PMTM

Fig.1.6. Configuration of slotted and slotless PMTM

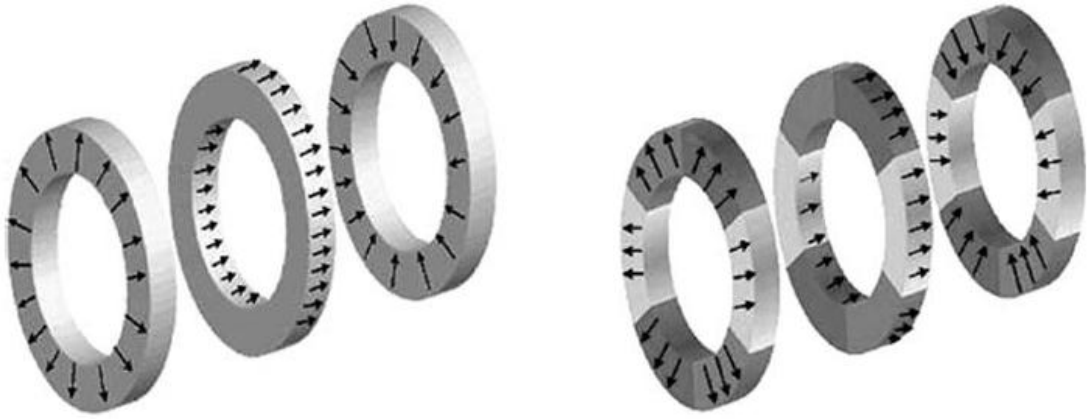

(a) Radial magnetized magnet ring (b) Parallel magnetized magnet segments

Fig.1.7. Configuration of magnet pole having two type magnetizations [86].

1.2.3 SPMRM

The SPM rotary machine (SPMRM) having Halbach array is the most attractive and widely applied configuration among other PMLM, PMTM, and axial-field PM brushless machines, etc. The Halbach array can be realized by either using discrete magnet segments (fabricated by sintered magnet segments with pre-magnetized orientation) or magnet ring (fabricated by bonded magnet ring and subsequently impulse magnetized with sinusoidal magnetization field). The Halbach array with segmented magnet exhibits high fundamental air-gap flux density and quasi-sinusoidal waveform, while the bonded magnet ring exhibits low fundamental air-gap flux density but presents sinusoidal waveform and is capable of adopting air-cored rotor. It is therefore the slotless PM brushless machine having a boned magnet ring and sinusoidal Halbach magnetization is eminently suitable for servo motor, on the basis of low torque ripples, high dynamic response and efficiency. On the other hand, the slotted PM brushless machine (Fig.1.8) is preferred to use segmented Halbach array, since the stator teeth can withstand higher saturation level. Moreover, the effective magnet length in (1.2) increases as number of magnet segment increasing, which in turn, results in higher air-gap flux density and lower harmonic contents. However, the manufacturing cost is raising proportional to the number of magnet segments. Hence, to obtain a cost-effective design, the usage of rotor back-iron becomes necessary for Halbach array with low segment number to enhance the flux path. Furthermore, both bonded magnet ring and high number of Halbach segments can achieve low parasitic torque and losses, whereas the parasitic force (UMF) can be also minimized if cooperated with slotless stator.

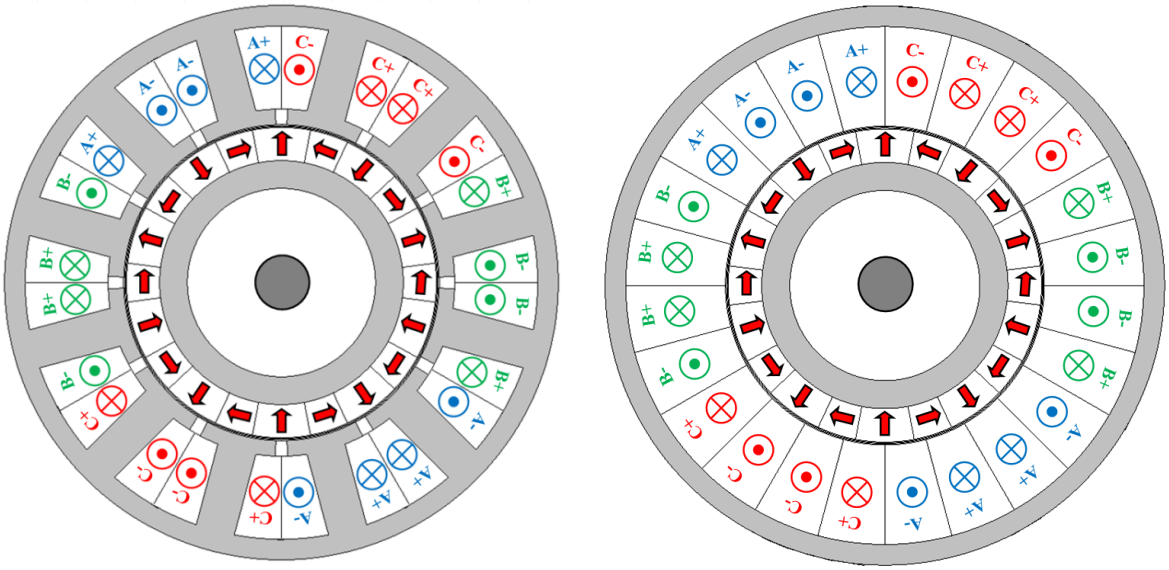

(a) Slotted PM brushless machine (b) Slotless PM brushless machine

Fig.1.8. Configuration of slotted and slotless PMRM.

Up to date, the low parasitic effects and high magnet usage efficiency η_{pm} (defined as the ratio of average torque over magnet volume) becomes increasingly important for automotive, renewable, and domestic applications. In general, such requirements are strongly depend on harmonic contents in air-gap flux density and the usage of high cost rare-earth PM. Besides Halbach array, the magnet segmentation [160]-[164], pole shaping [165]-[173], modular pole (mixed grade) [174]-[177] and stepped magnet pole [178][179] are capable of reducing harmonic contents. However, they are inevitably suffered from high magnet usage or lower output torque. Consequently, magnet poles having unequal magnet height and mixed grade magnets, together with Halbach magnetization are proposed in this thesis as investigated in Chapter 4 and 5. The proposed magnet poles are desirable to PMLM, PMTM and axial-field machine as well.

1.3 Magnetic Field Models

As regards to ever-increasing Halbach applications, the requirement of accurate prediction and optimization of electromagnetic performance for machines and devices having Halbach array becomes increasingly critical. The magnetic field model is widely used to facilitate prediction of electromagnetic performance for PM brushless machines. It can be classified into two categories: numerical and analytical models. Generally, numerical models are very accurate and capable of accounting for saturation effects, while the majority of analytical models are simple and fast, but incapable of accounting for saturation effect.

1.3.1 Numerical Models

The FEA is the most frequently used numerical method for machine design. To date, the FEA has already become very powerful with the developing of computer devices. Since the FEA is very accurate and capable of accounting saturation effect, the majority of commercial software packages for machine design are developed based on FEA, e.g. Flux, JMAG, Vector Field, Infylitica and Ansoft, etc. However, FEA is very time-consuming and complicate for modelling 3D structure, although the combined model is introduced in [180] where FEA is used to model the iron region and an analytical model is used to model air-gap region.

1.3.2 Analytical Models

The analytical models contain 1-D, 2-D slotless, 2-D slotted field models and lumped-parameter circuit model (LPC model), where the 3-D field model will be not discussed here.

A. 1-D Field Model

The 1-D field model is the most basically and widely used model to interpret physical relationship between performance and machine design parameters. It can be derived by solving Lorentz force law (electromagnetic torque) and Faraday's law (back-EMF). With the aid of 1-D field model, some of important design parameters and electromagnetic performance can be investigated and solved, such as split ratio λ for PM machine having external rotor in Chapter 6 in this thesis and cogging torque [181][182], etc. However, 1-D field model is too simple to account for the leakage fluxes and curvature effect. Thus, 2-D field model needs to be employed for accurate predictions.

B. 2-D Field Slotless Model

In a 2-D field slotless model, the assumption of infinite permeability of the iron or lamination is made. The flux density distribution is deduced by solving the governing equations, i.e. Poisson's equation in PM domain and Laplace's equation in air-gap domain, together with applied boundary conditions on the interfaces between domains. The 2-D field slotless model received most applications, since it is simpler than the slotted model. Nevertheless, it is still visibly more complicated than 1-D field model. Furthermore, unlike the 1-D field model can obtain optimal design parameter straightforward, normally the optimal result can only be scanned out in the 2-D field model. As a consequence, a simplified 2-D field model is proposed in Chapter 2, where a simple determination equation is derived based on the developed 2-D field model to directly obtain the optimal magnet ratio R_{mp} for PM slotless machine having radial magnetized 2-segment Halbach array.

C. 2-D Field Slotted Model

The stator slotting effect can distort the air-gap flux density by introducing slot harmonics. Hence, it imposes a negative impact on electromagnetic torque ripple, cogging torque, and iron loss, etc. In order to account for the slotting effect in the 2-D field model, the conformal transformation (CT) model is used with two simplified method, e.g. the relative permeance model [183] where the simplification is made by neglecting the shape deformation of magnets due to conformal mapping and the complex permeance models [184] where the simplification is made by neglecting the path deformation for the air-gap flux density calculation due to conformal mapping. It is noted that the exact CT model which considers both deformations in magnet and calculation path is extremely complicated and more like a numerical model.

On the other hand, similar to the previous 2-D field slotless motor, the air-gap domain for slotted model is separated into two sub-domains, i.e. the air-gap and the stator slot sub-domain, which is then named as the sub-domain (SD) model or method [185]. The field distribution in each sub-domain can be derived by solving the governing equations, together with the boundary conditions to the interfaces between sub-domains. The 2-D field model with the SD method exhibits higher accuracy than the simplified CT method, since the same permeance function is used in simplified CT for any rotor position while the SD model needs to evaluate the influence of the slotting effect at each rotor position.

D. LPC Model

The principle of the LPC model is based on a magnetic circuit which can be analogous to an electrical circuit. The saturation effect is accounted by calculating reluctances in iron part in which the relative permeability μ_r is varied according to the specification of BH curve. The LPC model is preferred to model complex a 3D structure, such as claw-pole machines in APPENDICES I and II, which could be very complicated in FEA. Therefore, the LPC model is treated as an alternative method to FEA. The accuracy of both the FEA and the LPC model, however, is quite sensitive to the density of FE mesh and magnetic circuit node, which in turn, could further slow the computational processing if precision calculation is required.

1.3.3 Analytical Models for Halbach Array

As discussed previously, the numerical methods, such as FEA, are very powerful, the global optimization is still very time-consuming, especially for a magnet pole having a Halbach array. Meanwhile, the numerical methods are also hard to provide insight into physical relationships between the performance and parameters. Ultimately, analytical models are preferable and capable of facilitating physical understanding, an initial design and fast global optimization, while the numerical methods are suitable for the validation and adjustment of the design.

The simple 2-D field model having perfectly sinusoidal magnetization [70][186] received its application to a rectangular pole, then, in [187], such ideally magnetized magnet pole (so called ideal Halbach array) is extended to cylindrical, planar and spherical structures as well. Furthermore, a 2-D field model for slotless PM brushless machine having ideal Halbach array with either air or iron cored rotor back-iron was developed in [188] with the consideration of both internal and external rotors. Apart from ideal Halbach array, the requirement of easy fabrication leads to an adoption by using segmented magnets to create quasi-sinusoidal

magnetization where each magnet segment exhibits the same pole-pitch [11][189]-[191]. Recently, the Halbach array which consists of two magnet segments having unequal pole-pitch is analytically investigated in [192][193], where electromagnetic performance is improved. Besides the foregoing mentioned three typical Halbach arrays, the influences of slotting effect [194], 3D effect [195], magnet shaping [196] and rotor eccentricity [197] on PM brushless machine having Halbach array are also analytically studied. With the aid of developed analytical models for Halbach arrays, a broad consensus has been reached which realizes the higher the magnet segment, the better the electromagnetic performance, but meanwhile results in difficulty in manufacturing. Thus, a compromised design is always needed since the design tradeoff between performance and manufacturing is inevitable. As a consequence, the full understanding of the influence of design parameters, such as pole-pair number, segment number, pole-pitch and magnetization angle, etc., on the electromagnetic performance has been crucial to choose a most suitable compromised design, which, in other words, means a cost-effective design. However, up to date, the lack of a general analytical model which is capable of modeling Halbach arrays having more than two magnet segments, together with variable pole-pitch and magnetization angle led the investigation and optimization very complicated.

Therefore, this thesis proposes a general analytical model based on a sub-domain (SD) method together with a novel general analytical model of magnetization vectors for Halbach arrays. The model is capable of determining the air-gap flux density waveform for slotted/slotless PM brushless machines and devices such as magnet cylinder, etc, having both even- and odd-segmented Halbach array, together with the variation freedom of magnet remanence, magnetization angle and arc for each single magnet segment. Meanwhile, the electromagnetic performance, including phase back-EMF, cogging torque and electromagnetic torque waveforms are able to be predicted.

1.4 Outline of Thesis

The focus of this thesis is to propose magnet poles with unequal magnet height and mixed grade magnets, together with optimal Halbach magnetization. The packages of general 2-D field analytical models are provided for predicting magnetic field and electromagnetic performance of proposed magnet poles and Halbach arrays. (The reference number in the bracket below shows the journal and conference papers which are resulted from this thesis and listed in APPENDIX IV)

Chapter 1 reviews the previous work, presents the main objective, outline, and main contributions of this thesis.

Chapter 2 develops a 2-D field slotless model for predicting the magnetic field of a PM brushless machine 2-segment Halbach array with both radial and parallel magnetized magnet segments, plus a simple determination equation to directly predict the optimal R_{mp} for radial magnetized 2-segment Halbach array.

Chapter 3 develops a general 2-D field model for predicting the magnetic field and electromagnetic performance of a slotted/slotless PM brushless machine having either even or odd-segment Halbach array, together with the variation freedom of magnet remanence, magnetization angle and arc for each single magnet segment.

Chapter 4 analytically investigates the electromagnetic performance for a PM brushless machine having proposed Hat- and T-type magnet poles. [J2]

Chapter 5 analytically investigates the electromagnetic performance for a PM brushless machine having proposed magnet pole with unequal magnet height and mixed grade magnets. [J3]

Chapter 6 develops 1-D analytical model for predicting the optimal split ratio for PM brushless machines having external rotor. [J4][C3][C4]

Chapter 7 makes a conclusion based on the work of this thesis.

APPENDIX I develops LPC model for optimizing the machine design parameters of claw-pole rotor brushless machine with DC excitation. [C2]

APPENDIX II develops LPC model for optimizing the machine design parameters of claw-pole stator SPM brushless machine. [C1]

1.5 Major Contributions of Thesis

The major contributions of this thesis are highlighted as follows.

(1) A simple determination equation can predict optimal magnet ratio R_{mp} for radial magnetized 2-segment Halbach array.

(2) A general analytical model is developed for PM brushless machine having segmented Halbach array.

(3) The proposed Hat- and T-type magnet poles having equal and unequal side-magnet height, mixed grade magnets and optimal Halbach magnetization are analytically investigated.

(4) Analytical model to predict optimal split ratio for PM brushless machine having external rotor.

CHAPTER 2 DETERMINATION OF THE MAXIMUM ELECTROMAGNETIC TORQUE IN PM BRUSHLESS MACHINES Having 2-SEGMENT HALBACH ARRAY

There is a need of a simple and accurate analytical model for fast and easy prediction and optimization of the electromagnetic performance, together with a clear physical understanding of the relationship between parameters and performance. In this chapter, a 2-D field slotless model is developed for predicting the electromagnetic performance for the PM brushless machine having a radial or a parallel magnetized 2-segment Halbach array. Subsequently, a simple determination equation is derived to predict the optimal magnet ratio R_{mp} for a 2-segment Halbach array.

2.1 Introduction

The PM brushless machine having Halbach array presents several attractive features. In order to achieve optimal performance, it is essential to establish accurate models for predicting the air-gap field and electromagnetic performance. Besides FEA, the 2-D field model is preferred on the basis of fast and easy for global optimization. Previously, a 2-segment Halbach array having unequal pole-arc with parallel magnetized magnet segment is analytically investigated in [192][193]. The improved magnetic performances including lower electromagnetic torque ripple, high average torque and efficiency are obtained by optimizing R_{mp} in contrast to well-known equal pole-arc case [11].

Although the aforementioned analytical models are simpler and faster than FEA, unless by scanning the design parameters, currently developed analytical models are not capable to provide straightforward optimal pole-arc or R_{mp} for for 2-segment Halbach array which is most commonly employed for the optimization of Halbach machines. Therefore, in this chapter, a 2-D field analytical model for predicting the magnetic field distribution in air- and iron-cored PM brushless machine having either radial or parallel magnetized 2-segment Halbach array with both radial and parallel magnetized magnet segment is developed. A simple determination equation (SDE) to directly predict the optimal magnet ratio for air- and iron-cored radially magnetized 2-segment Halbach array is subsequently derived, which can be also used to predict the optimal R_{mp} for parallel magnetized case. The developed 2-D field model is validated by FEA, while a comparison of the 2-D field model directly scanned and SDE predicted optimal magnet ratio is made. The investigations of the influence of the pole-pair number and magnet thickness on optimal magnet ratio are presented for both air- and

iron-cored machine having radially magnetized 2-segment Halbach array by using SDE. Meanwhile, the optimal fundamental air-gap flux density and corresponding R_{mp} for radially and parallel magnetized 2-segment Halabch arrays are also obtained. Finally, a prototype 12-slot/10-pole PM brushless machine having 2-segment Halbach array is built, and the analytical, FEA predicted and measured results are compared.

2.2 Development of Analytical Model

Fig.1.1 shows the schematic view of 12-slot/10-pole PM brushless machines having 2-segment Halbach array rotor with non-overlapping winding. In an ideal Halbach magnetized magnet cylinder, the spatial variation in the magnetization is sinusoidal and given by:

$$\vec{M} = M\,cos(p\theta)\vec{e}_r \pm M\,sin(p\theta)\,\vec{e}_\theta \tag{2.1}$$

where the sine term is negative for an internal rotor machine and is positive for an external rotor machine. $\vec{e}_r$ and $\vec{e}_\theta$ are the radial and tangential vectors in polar coordinates, p is the pole-pair number and θ is the rotor angular position. In practice, the most cost effective way of approximating/fabricating the Halbach PM rotor is to employ two pre-magnetized discrete magnet segments for a single pole where the magnetization comprises only radial and tangential directions.

The use of an analytical model to predict the field distribution within the magnet and air-gap regions of PM machine is much faster and simpler than the numerical model. Furthermore, an analytical solution can provide a useful insight into the key parameters for optimization and the trends that influence a particular design. In this section, a 2-D field slotless model is developed for a PM brushless machine having 2-segment Halbach array.

2.2.1 Magnetization Vectors

A. Radially Magnetized 2-Segment Halbach Array

The analytical model shown in Fig.2.1 is divided into 3 homogeneous regions, where region II contains radially and tangentially magnetized magnet segments, and region I and III are airspaces. The winding can be placed either in region I or region III depending on whether the motor has an internal or external rotor topology.

The magnet ratio R_{mp} is defined as the ratio of the pole-arc of mid- magnet segment W_f with radial magnetization to the pole-pitch of single pole W_p, as

$$R_{mp} = \frac{W_f}{W_p} \tag{2.2}$$

In polar coordinates, the magnetization vector $\vec{M}$ is given by:

$$\vec{M} = M_r \vec{e}_r + M_\theta \vec{e}_\theta \tag{2.3}$$

According to Fig.2.1 and Fig.2.2(a), both M_r and M_θ in one pole-pair region are given by:

$$\begin{cases} M_r = \dfrac{B_r}{\mu_0} \\ M_\theta = 0 \end{cases} \qquad -\frac{R_{mp}\pi}{2p} < \theta < \frac{R_{mp}\pi}{2p} \tag{2.4}$$

$$\begin{cases} M_r = 0 \\ M_\theta = -\dfrac{B_r}{\mu_0} \end{cases} \qquad \frac{R_{mp}\pi}{2p} < \theta < \left(1 - \frac{R_{mp}}{2}\right)\frac{\pi}{p} \tag{2.5}$$

$$\begin{cases} M_r = -\dfrac{B_r}{\mu_0} \\ M_\theta = 0 \end{cases} \qquad \left(1 - \frac{R_{mp}}{2}\right)\frac{\pi}{p} < \theta < \left(1 + \frac{R_{mp}}{2}\right)\frac{\pi}{p} \tag{2.6}$$

$$\begin{cases} M_r = 0 \\ M_\theta = \dfrac{B_r}{\mu_0} \end{cases} \qquad \left(1 + \frac{R_{mp}}{2}\right)\frac{\pi}{p} < \theta < \left(2 - \frac{R_{mp}}{2}\right)\frac{\pi}{p} \tag{2.7}$$

where B_r is the magnet remanence, and θ is the rotor angular position with reference to the centre of a magnet pole, as shown in Fig.2.1. M_r and M_θ can be expressed as Fourier series, i.e.

$$M_r = \sum_{n=1,3,5\cdots}^{\infty} M_{rn}\, cos(np\theta) \tag{2.8}$$

$$M_\theta = \sum_{n=1,3,5\cdots}^{\infty} M_{r\theta}\, sin(np\theta) \tag{2.9}$$

where

$$M_{rn} = \frac{p}{\pi} \int_{-R_{mp}\pi/(2p)}^{2\pi/p - R_{mp}\pi/(2p)} M_r\, cos(np\theta) = 2\frac{B_r}{\mu_0} R_{mp} \frac{sin\left(R_{mp}\frac{n\pi}{2}\right)}{R_{mp}\frac{n\pi}{2}} \tag{2.10}$$

$$M_{\theta n} = \frac{p}{\pi} \int_{-R_{mp}\pi/(2p)}^{2\pi/p - R_{mp}\pi/(2p)} M_\theta\, sin(np\theta) = \mp 2\frac{B_r}{\mu_0} R_{mp} \frac{cos\left(R_{mp}\frac{n\pi}{2}\right)}{R_{mp}\frac{n\pi}{2}} \tag{2.11}$$

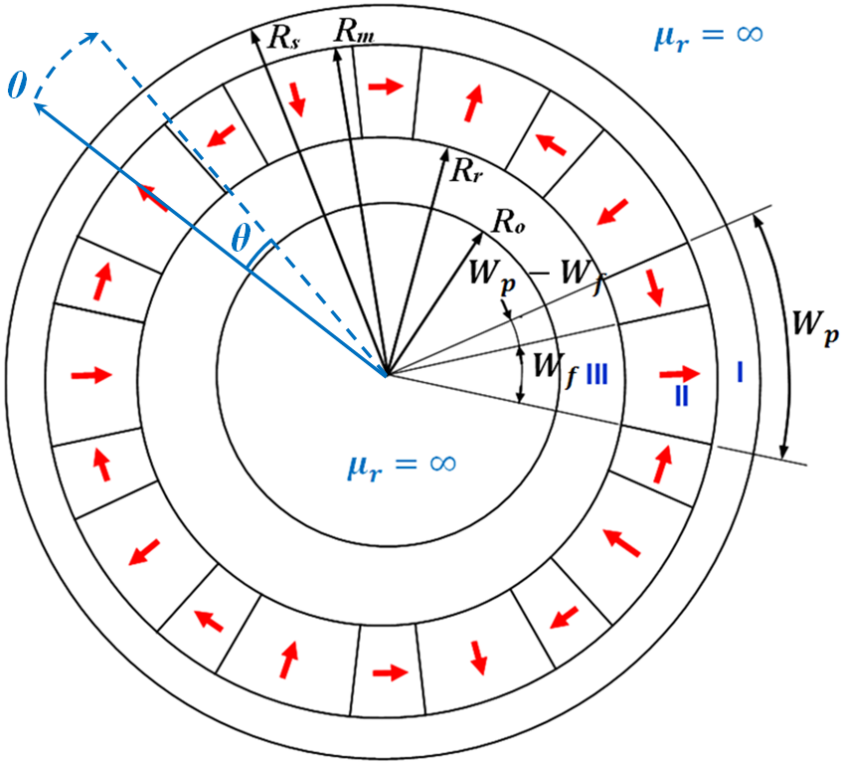

Fig.2.1. Model of two segments per pole of Halbach array PM.

B. Parallel Magnetized 2-Segment Halbach Array

Similar to radial magnetized 2-segment Halbach array, the M_r and M_θ in one pole-pair region for parallel magnetization 2-segment Halbach array (Fig.2.2(b)) are given by:

$$\begin{cases} M_r = \dfrac{B_r}{\mu_0}\cos\theta_m \\ M_\theta = -\dfrac{B_r}{\mu_0}\sin\theta_m \end{cases} \qquad -\frac{R_{mp}\pi}{2p} < \theta_m < \frac{R_{mp}\pi}{2p} \tag{2.12}$$

$$\begin{cases} M_r = -\dfrac{B_r}{\mu_0}\sin\left(\theta_m - \dfrac{\pi}{2p}\right) \\ M_\theta = \mp\dfrac{B_r}{\mu_0}\cos\left(\theta_m - \dfrac{\pi}{2p}\right) \end{cases} \qquad \frac{R_{mp}\pi}{2p} < \theta_m < \left(1 - \frac{R_{mp}}{2}\right)\frac{\pi}{p} \tag{2.13}$$

$$\begin{cases} M_r = -\dfrac{B_r}{\mu_0}\cos\left(\theta_m - \dfrac{\pi}{2p}\right) \\ M_\theta = \dfrac{B_r}{\mu_0}\sin\left(\theta_m - \dfrac{\pi}{2p}\right) \end{cases} \qquad \left(1 - \frac{R_{mp}}{2}\right)\frac{\pi}{p} < \theta_m < \left(1 + \frac{R_{mp}}{2}\right)\frac{\pi}{p} \tag{2.14}$$

$$\begin{cases} M_r = \dfrac{B_r}{\mu_0}\sin\left(\theta_m - \dfrac{3\pi}{2p}\right) \\ M_\theta = \pm\dfrac{B_r}{\mu_0}\cos\left(\theta_m - \dfrac{3\pi}{2p}\right) \end{cases} \qquad \left(1 + \frac{R_{mp}}{2}\right)\frac{\pi}{p} < \theta_m < \left(2 - \frac{R_{mp}}{2}\right)\frac{\pi}{p} \tag{2.15}$$

By solving the Fourier series, the M_{rn} and $M_{\theta n}$ for parallel magnetized 2-segments Halbach array can be obtained

$$M_{rn} = \frac{B_r}{\mu_0}\left\{\frac{\sin\left[(1+np)R_{mp}\frac{\pi}{2p}\right]}{(1+np)\frac{\pi}{2p}} + \frac{\sin\left[(1-np)R_{mp}\frac{\pi}{2p}\right]}{(1-np)\frac{\pi}{2p}}\right\}$$

$$+\frac{B_r}{\mu_0}\cdot(-1)^{\frac{1+n}{2}}\left\{\frac{\sin\left[(1+np)\left(1-R_{mp}\right)\frac{\pi}{2p}\right]}{(1+np)\frac{\pi}{2p}} - \frac{\sin\left[(1-np)\left(1-R_{mp}\right)\frac{\pi}{2p}\right]}{(1-np)\frac{\pi}{2p}}\right\} \quad (2.16)$$

$$M_{\theta n} = \frac{B_r}{\mu_0}\left\{\frac{\sin\left[(1+np)R_{mp}\frac{\pi}{2p}\right]}{(1+np)\frac{\pi}{2p}} - \frac{\sin\left[(1-np)R_{mp}\frac{\pi}{2p}\right]}{(1-np)\frac{\pi}{2p}}\right\}$$

$$+\frac{B_r}{\mu_0}\cdot(-1)^{\frac{1+n}{2}}\left\{\frac{\sin\left[(1+np)\left(1-R_{mp}\right)\frac{\pi}{2p}\right]}{(1+np)\frac{\pi}{2p}} + \frac{\sin\left[(1-np)\left(1-R_{mp}\right)\frac{\pi}{2p}\right]}{(1-np)\frac{\pi}{2p}}\right\} \quad (2.17)$$

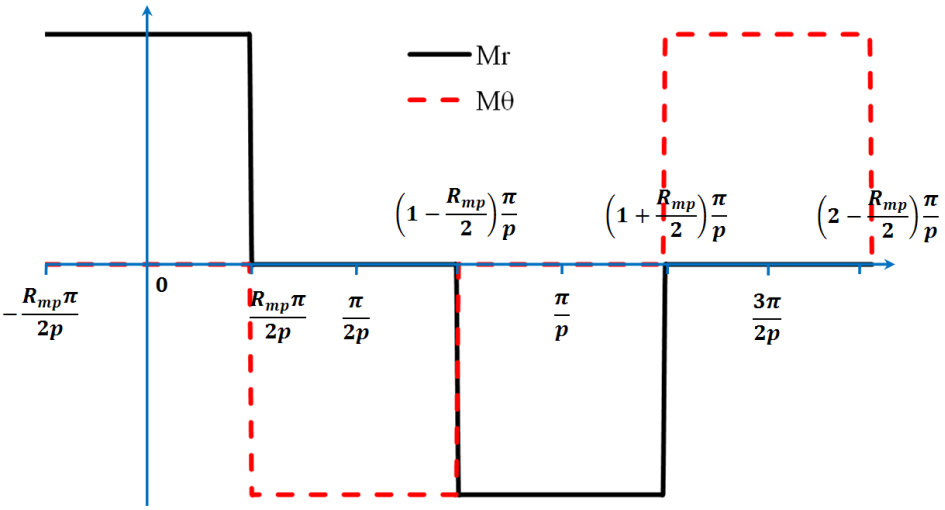

(a) Radial magnetization

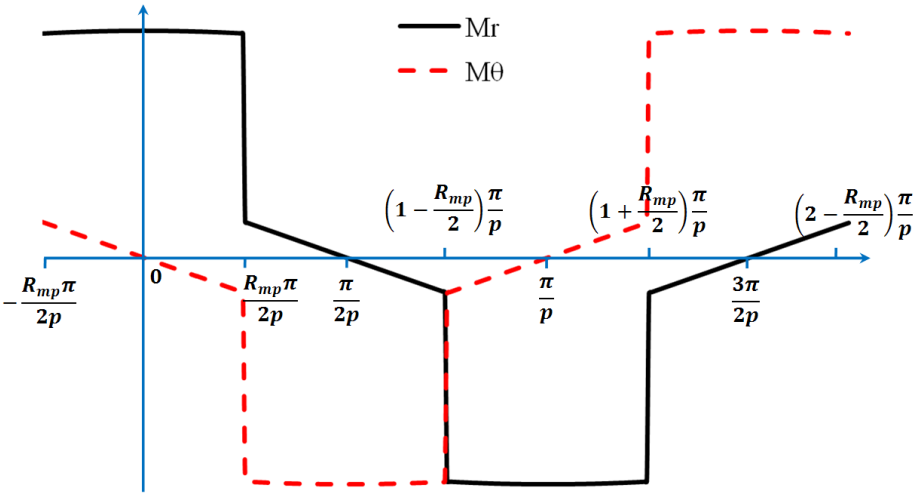

(b) Parallel magnetization

Fig.2.2. Illustration of magnetization vectors for radially and parallel magnetized 2-segment Halbach array.

2.2.2 Field Produced by Magnets

In order to obtain an analytical solution for the air-gap field distributions produced by 2-segment Halbach array, the following assumptions are made:

- The PMs have a linear demagnetization characteristic, and are fully magnetized in the direction of magnetization;
- End-effects are neglected;
- The stator and rotor back-iron is infinitely permeable.

The scalar magnetic potential distribution in airspace or air-gap is governed by Laplace'e equation, while in the permanent magnet region it is governed by a Poissonian equation, i.e.

In region I

$$\frac{\partial^2 \varphi_I}{\partial r^2} + \frac{1}{r}\frac{\partial \varphi_I}{\partial r} + \frac{1}{r^2}\frac{\partial^2 \varphi_I}{\partial \theta^2} = 0 \tag{2.18}$$

In region II

$$\frac{\partial^2 \varphi_{II}}{\partial r^2} + \frac{1}{r}\frac{\partial \varphi_{II}}{\partial r} + \frac{1}{r^2}\frac{\partial^2 \varphi_{II}}{\partial \theta^2} = \frac{div\vec{M}}{\mu_r} \tag{2.19}$$

In region III

$$\frac{\partial^2 \varphi_{III}}{\partial r^2} + \frac{1}{r}\frac{\partial \varphi_{III}}{\partial r} + \frac{1}{r^2}\frac{\partial^2 \varphi_{III}}{\partial \theta^2} = 0 \tag{2.20}$$

where the scalar potential φ is related to the components of $\vec{H}$ by:

$$\begin{cases} H_r = -\dfrac{\partial \varphi}{\partial r} \\ H_\theta = -\dfrac{1}{r}\dfrac{\partial \varphi}{\partial \theta} \end{cases} \tag{2.21}$$

And regards to (2.8),

$$div\vec{M} = \frac{M_r}{r} + \frac{\partial M_r}{\partial r} + \frac{1}{r}\frac{\partial M_\theta}{\partial \theta} = \sum_{n=1,3,5\cdots}^{\infty} \frac{M_n}{r} cos(np\theta) \tag{2.22}$$

where

$$M_n = M_{rn} + npM_{\theta n} \tag{2.23}$$

The general solutions for the scalar magnetic potential distributions in the three regions are given by:

$$\varphi_I(r,\theta) = \sum_{n=1}^{\infty} (A_{nI} r^{np} + B_{nI} r^{-np})\, cos(np\theta) \tag{2.24}$$

$$\varphi_{II}(r,\theta)=\sum_{n=1}^{\infty}(A_{nII}r^{np}+B_{nII}r^{-np})\,cos(np\theta)+\sum\frac{M_n}{1-np^2}\frac{r}{\mu_r}cos(np\theta) \quad (2.25)$$

$$\varphi_{III}(r,\theta)=\sum_{n=1}^{\infty}(A_{nIII}r^{np}+B_{nIII}r^{-np})\,cos(np\theta) \quad (2.26)$$

with the boundary conditions to be satisfied:

$$\begin{cases} H_{\theta I}(r,\theta)|_{r=R_s}=0 \\ H_{\theta III}(r,\theta)|_{r=R_0}=0 \\ B_{rI}(r,\theta)|_{r=R_m}=B_{rII}(r,\theta)|_{r=R_m} \\ H_{\theta I}(r,\theta)|_{r=R_m}=H_{\theta II}(r,\theta)|_{r=R_m} \\ B_{rI}(r,\theta)|_{r=R_r}=B_{rII}(r,\theta)|_{r=R_r} \\ H_{\theta II}(r,\theta)|_{r=R_r}=H_{\theta III}(r,\theta)|_{r=R_r} \end{cases} \quad (2.27)$$

we have,

$$B_{rI}(r,\theta)=-\mu_0\sum_{n=1,3,5\cdots}^{\infty}npA_{nI}\left(r^{np-1}+R_s^{2np}r^{-np-1}\right)cos(np\theta) \quad (2.28)$$

$$B_{\theta I}(r,\theta)=\mu_0\sum_{n=1,3,5\cdots}^{\infty}npA_{nI}(r^{np-1}-R_s r^{-np-1})\,sin(np\theta) \quad (2.29)$$

$$B_{rII}(r,\theta)=-\mu_0\sum_{n=1,3,5\cdots}^{\infty}\left[\mu_r np(A_{nII}r^{np-1}-B_{nII}r^{-np-1})+\frac{M_n}{1-(np)^2}-M_{rn}\right]cos(np\theta) \quad (2.30)$$

$$B_{\theta II}(r,\theta)=\mu_0\sum_{n=1,3,5\cdots}^{\infty}\left[\mu_r np(A_{nII}r^{np-1}+B_{nII}r^{-np-1})+\frac{npM_n}{1-(np)^2}\right]sin(np\theta) \quad (2.31)$$

$$B_{rIII}(r,\theta)=-\mu_0\sum_{n=1,3,5\cdots}^{\infty}npA_{nIII}\left(r^{np-1}+R_0^{2np}r^{-np-1}\right)cos(np\theta) \quad (2.32)$$

$$B_{\theta III}(r,\theta)=\mu_0\sum_{n=1,3,5\cdots}^{\infty}npA_{nIII}(r^{np-1}-R_0 r^{-np-1})\,sin(np\theta) \quad (2.33)$$

where

$$A_{nI}=\frac{A_{nI(a)}+A_{nI(b)}}{\left[1-\frac{\mu_r-1}{1+\mu_r}\left(\frac{R_s}{R_m}\right)^{2np}\right]\left(\frac{\mu_r-1}{1+\mu_r}R_r^{2np}-R_0^{2np}\right)-\left(\frac{\mu_r-1}{1+\mu_r}R_m^{2np}-R_s^{2np}\right)\left[1-\frac{\mu_r-1}{1+\mu_r}\left(\frac{R_0}{R_r}\right)^{2np}\right]}$$

$$A_{nI(a)} = \left[\frac{M_n}{np(1+np)} - \frac{M_{rn}}{np}\right]\left[\left(R_m^{np+1} - R_r^{np+1}\right)\left(1 - \frac{\mu_r - 1}{1+\mu_r}\left(\frac{R_0}{R_r}\right)^{2np}\right)\right]$$

$$A_{nI(b)} = \left[\frac{M_n}{np(1-np)} - \frac{M_{rn}}{np}\right]\left[\left(R_m^{-np+1} - R_r^{-np+1}\right)\left(\frac{\mu_r - 1}{1+\mu_r}R_r^{2np} - R_0^{2np}\right)\right] \quad (2.34)$$

$$B_{nI} = -R_s^{2np} A_{nI} \quad (2.35)$$

$$A_{nII} = \frac{1}{2\mu_r}\left[\left[(\mu_r + 1) - (\mu_r - 1)\left(\frac{R_s}{R_m}\right)^{2np}\right]A_{nI} - \left[\frac{M_n}{np(1-np)} - \frac{M_{rn}}{np}\right]R_m^{-np+1}\right] \quad (2.36)$$

$$B_{nII} = \frac{1}{2\mu_r}\left[\left[(\mu_r - 1)R_m^{2np} - (\mu_r + 1)R_s^{2np}\right]A_{nI} + \left[\frac{M_n}{np(1+np)} - \frac{M_{rn}}{np}\right]R_m^{np+1}\right] \quad (2.37)$$

$$A_{nIII} = \frac{(\mu_r + 1) - (\mu_r - 1)\left(\frac{R_s}{R_m}\right)^{2np}}{(\mu_r + 1) - (\mu_r - 1)\left(\frac{R_0}{R_r}\right)^{2np}} A_{nI} + \frac{\left[\frac{M_n}{np(1+np)} - \frac{M_{rn}}{np}\right]\left(R_r^{-np+1} - R_m^{-np+1}\right)}{(\mu_r + 1) - (\mu_r - 1)\left(\frac{R_0}{R_r}\right)^{2np}} \quad (2.38)$$

$$B_{nIII} = -R_0^{2np} A_{nIII} \quad (2.39)$$

It should be noted than the developed 2-D field model is not capable of analyzing the case when p =1.

For internal rotor PM machines, the particular interest is the radial component of the air-gap flux density $B_{rI}(r, \theta)$ which can be written as:

$$B_{rI}(r,\theta) = \sum_{n=1,3,5\cdots}^{\infty} K_B(n) f_{Br}(r)\, cos(np\theta) \quad (2.40)$$

Where

$$K_B(n) = \frac{-\mu_0\left[K_{B(a)} + K_{B(b)}\right]}{\left[1 - \frac{\mu_r - 1}{1+\mu_r}\left(\frac{R_s}{R_m}\right)^{2np}\right]\left[\frac{\mu_r - 1}{1+\mu_r}\left(\frac{R_r}{R_s}\right)^{2np} - \left(\frac{R_0}{R_s}\right)^{2np}\right] - \left[\frac{\mu_r - 1}{1+\mu_r}\left(\frac{R_m}{R_s}\right)^{2np} - 1\right]\left[1 - \frac{\mu_r - 1}{1+\mu_r}\left(\frac{R_0}{R_r}\right)^{2np}\right]} \quad (2.41)$$

$$K_{B(a)} = \left(\frac{M_n}{1+np} - M_{rn}\right)\left[\left[1 - \left(\frac{R_r}{R_m}\right)^{np+1}\right]\left[1 - \frac{\mu_r - 1}{\mu_r + 1}\left(\frac{R_0}{R_r}\right)^{2np}\right]\right] \quad (2.42)$$

$$K_{B(b)} = \left(\frac{M_n}{1-np} - M_{rn}\right)\left[\left[\left(\frac{R_r}{R_m}\right)^{2np} - \left(\frac{R_r}{R_m}\right)^{np+1}\right]\left[\frac{\mu_r - 1}{\mu_r + 1} - \left(\frac{R_0}{R_r}\right)^{2np}\right]\right] \quad (2.43)$$

$$f_{Br}(r) = \left(\frac{r}{R_s}\right)^{np-1}\left(\frac{R_m}{R_s}\right)^{np+1} + \left(\frac{R_m}{r}\right)^{np+1} \tag{2.44}$$

If $\mu_r = 1$, $K_B(n)$ can be simplified as:

$$K_B(n) = -\mu_0 \frac{\left(\frac{M_n}{1+np} - M_{rn}\right)\left[1 - \left(\frac{R_r}{R_m}\right)^{np+1}\right] - \left(\frac{M_n}{1-np} - M_{rn}\right)\left[\left[\left(\frac{R_r}{R_m}\right)^{2np} - \left(\frac{R_r}{R_m}\right)^{np+1}\right]\left(\frac{R_0}{R_r}\right)^{2np}\right]}{1 - \left(\frac{R_0}{R_s}\right)^{2np}} \tag{2.45}$$

2.2.3 Flux-Linkage, Back-EMF, and Electromagnetic Torque

A. Phase Flux-Linkage, Back-EMF, and Electromagnetic Torque

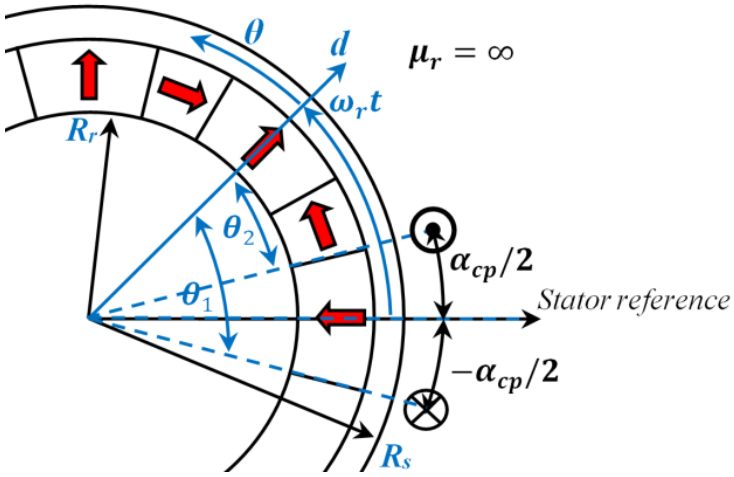

Fig.2.3. Angular displacement between rotor and the coil.

As can be seen in Fig.2.3, θ is the circumferential position in the rotor reference system. The rotor initial position is aligned with the centre of the coil for simplicity, while $\omega_r t$ represents the rotor position in accordance with stator reference at the instant t. The flux in the coil is calculated from the integral of air-gap flux density over one coil pitch ranging from θ_1=–α_{cp}/2-$\omega_r t$ to θ_2=α_{cp}/2-$\omega_r t$ in the rotor reference system:

$$\Phi_{coil-pitch} = R_s l_a \int_{\theta_1}^{\theta_2} B_{rI}(R_s, \theta) d\theta$$

where,

$$\theta_1 = -\frac{\alpha_{cp}}{2} - \omega_r t$$

$$\theta_2 = \frac{\alpha_{cp}}{2} - \omega_r t$$

then,

$$\Phi_{coil-pitch} = R_s l_a \int_{-\frac{\alpha_{cp}}{2}-\omega_r t}^{\frac{\alpha_{cp}}{2}-\omega_r t} B_{rl}(R_s,\theta)d\theta$$

$$= 2R_s l_a \sum_{n=1,3,5\cdots}^{\infty} \frac{K_B(n) f_{Br}(R_s)}{np} sin\left(np\frac{\alpha_{cp}}{2}\right) cos(n\omega_r pt)$$

$$= 2R_s l_a \sum_{n=1,3,5\cdots}^{\infty} \frac{K_B(n) f_{Br}(R_s)}{np} sin\left(\frac{np\pi}{N_s}\right) cos(n\omega_r pt) \quad (2.46)$$

where $\alpha_{cp} = 2\pi/N_s$, N_s is the stator slot number. If defining $K_{pn} = sin(np\pi/N_s)$ as the pitch factor for the 12-slot/10-pole machine, the flux-linkage with a coil having N_c turns, at any rotor position, can be expressed as:

$$\Psi_{coil} = 2R_s l_a N_c \sum_{n=1,3,5\cdots}^{\infty} \frac{K_B(n) f_{Br}(R_s)}{np} K_{pn}\, cos(n\omega_r pt) \quad (2.47)$$

where $\omega_r = 2\pi n/60$ is the rotor mechanical angular speed. Therefore, the back-EMF can be calculated according to the Faraday's law:

$$EMF_{c1}(\omega_r t) = -\frac{d\Psi_{coil}}{dt} = 2R_s l_a N_c \omega_r \sum_{n=1,3,5\cdots}^{\infty} K_B(n) f_{Br}(R_s)\, K_{pn}\, sin(n\omega_r pt) \quad (2.48)$$

For the 12-slot/10-pole SPM brushless machine, one phase winding consists of two sets of adjacent coils connected inversely. Therefore, the phase back-EMF is given by:

$$EMF_{ph} = 2[EMF_{c1}(\omega_r t) - EMF_{c1}(\omega_r t - 2\pi/N_s)] \quad (2.49)$$

The general analytical expression for phase back-EMF for any slot/pole combination can be expressed as:

$$EMF_{ph} = 2R_s l_a N_{ph} \omega_r \sum_{n=1,3,5\cdots}^{\infty} K_B(n) f_{Br}(R_s)\, K_{pn} K_{dn}\, cos[np(\omega_r t - \pi/N_s)]$$

$$= \sum_{n=1,3,5\cdots}^{\infty} E_n\, cos[np(\omega_r t - \pi/N_s)] \quad (2.50)$$

where the distributed factor $K_{dn} = sin(np\pi/N_s)$, $N_{ph} = 4N_c$ is the total number of series turns for one phase, and $E_n = 2R_s l_a N_{ph} \omega_r K_B(n) f_{Br}(R_s) K_{pn} K_{dn}$ is the amplitude of the n^{th} order phase back-EMF harmonics. It should be noted the winding distribution factors for the general slot/pole combination can be calculated as:

For q_{ph} is even $$K_{dn} = \frac{sin\left(n\frac{q_{ph}}{2}\frac{\alpha_{ph}}{2}\right)}{\frac{q_{ph}}{2} sin\left(n\frac{\alpha_{ph}}{2}\right)}$$

For q_{ph} is odd

$$K_{dn} = \frac{sin\left(nq_{ph}\frac{\alpha_{ph}}{4}\right)}{q_{ph}\,sin\left(n\frac{\alpha_{ph}}{4}\right)} \tag{2.51}$$

where the coefficients of q_{ph} (number of spoke per phase) and α_{ph} (angle between two spokes) have been elaborated discussed and can be found in [198]

B. Electromagnetic Torque

For a balanced 3-phase machine, the electromagnetic torque can generally be calculated as:

$$T_{em} = \frac{1}{\omega_r}\sum_{j=1}^{m}\sum_{n=1,3,5\cdots}^{\infty}\sum_{k=1}^{\infty} E_n\, sin\left[n\left(p\omega_r t - \frac{2\pi(j-1)}{m}\right)\right]$$

$$\times I_k\, sin\left[k\left(p\omega_r t - \frac{2\pi(j-1)}{3}\right) + \theta_k\right] \tag{2.52}$$

where I_k is the amplitude of the k_{th} order phase harmonic current, θ_k is the associated phase angle of the current harmonic and m is the number of phases. For conventional 3-phase machine operated in BLAC mode, the fundamental sinusoidal current can be expressed as:

$$\begin{cases} i_a = I\, sin(p\omega_r t) \\ i_b = I\, sin(p\omega_r t - 2\pi/3) \\ i_c = I\, sin(p\omega_r t - 4\pi/3) \end{cases} \tag{2.53}$$

Whilst for the machine operated in BLDC mode, 120^0 electrical degree square phase current waveform, the current waveform can be expressed as:

$$\begin{cases} i_a = \frac{4I}{\pi}\sum_{k=1,3,5\cdots}^{\infty}\frac{1}{k}sin\left(k\frac{\pi}{2}\right)sin\left(k\frac{\pi}{3}\right)sin(kp\omega_r t) \\ i_b = \frac{4I}{\pi}\sum_{k=1,3,5\cdots}^{\infty}\frac{1}{k}sin\left(k\frac{\pi}{2}\right)sin\left(k\frac{\pi}{3}\right)sin\left[k\left(p\omega_r t - 2\frac{\pi}{3}\right)\right] \\ i_c = \frac{4I}{\pi}\sum_{k=1,3,5\cdots}^{\infty}\frac{1}{k}sin\left(k\frac{\pi}{2}\right)sin\left(k\frac{\pi}{3}\right)sin\left[k\left(p\omega_r t - 4\frac{\pi}{3}\right)\right] \end{cases} \tag{2.54}$$

2.3 Simple Equation for determining Optimal Magnet Ratio

In this section, a SDE model is derived based on radial magnetized 2-segment Halbach array.

In order to maximize the electromagnetic torque, the integration of half cycle of flux linkage for each coil should be maximized. Thus,

$$\frac{\partial \psi_{coil}}{\partial R_{mp}} = 0 \tag{2.55}$$

where $\frac{\pi}{2} \le \theta \le \frac{3\pi}{2}$. From (2.47),

$$\partial \left\{ \sum_{n=1,3,5\cdots}^{\infty} \frac{K_B(n) f_{Br}(R_s)}{(np)^2} K_{pn} \cdot \left[sin\left(n\frac{3\pi}{2}\right) - sin\left(n\frac{\pi}{2}\right) \right] \right\} / \partial R_{mp} = 0 \tag{2.56}$$

From (2.40)-(2.45), (2.56) can be further derived as:

$$\begin{aligned} \sum_{n=1,3,5\cdots}^{\infty} \Bigg[& \cos\left(R_{mp}\frac{n\pi}{2}\right) \cdot \left(\frac{C_1(n)}{1+np} + \frac{C_2(n)}{1-np} - C_1(n) - C_2(n) \right) + np \cdot \sin\left(R_{mp}\frac{n\pi}{2}\right) \\ & \cdot \left(\frac{C_1(n)}{1+np} + \frac{C_2(n)}{1-np} \right) \Bigg] \\ & \times \frac{C_4(n)}{(np)^2 C_3(n)} K_{pn} \left[sin\left(n\frac{3\pi}{2}\right) - sin\left(n\frac{\pi}{2}\right) \right] = 0 \end{aligned} \tag{2.57}$$

then,

$$\begin{aligned} & \sum_{n=1,3,5\cdots}^{\infty} \left\{ \cos\left(R_{mp}\frac{n\pi}{2}\right) \left(\frac{C_1(n)}{1+np} + \frac{C_2(n)}{1-np} - C_1(n) - C_2(n) \right) \right. \\ & \left. \cdot \frac{C_4(n)}{(np)^2 C_3(n)} \sin\left(\frac{np\pi}{N_s}\right) \left[sin\left(n\frac{3\pi}{2}\right) - sin\left(n\frac{\pi}{2}\right) \right] \right\} = \\ & -\left[\sum_{n=1,3,5\cdots}^{\infty} \sin\left(R_{mp}\frac{n\pi}{2}\right) \cdot \left(\frac{C_1(n)}{1+np} + \frac{C_2(n)}{1-np} \right) \frac{C_4(n)}{npC_3(n)} \cdot \sin\left(\frac{np\pi}{N_s}\right) \left[sin\left(n\frac{3\pi}{2}\right) \right. \right. \\ & \left. \left. - sin\left(n\frac{\pi}{2}\right) \right] \right] \end{aligned} \tag{2.58}$$

where

$$C_1(n) = \left[1 - \left(\frac{R_r}{R_m}\right)^{np+1} \right] \left[1 - \frac{\mu_r - 1}{\mu_r + 1} \left(\frac{R_0}{R_r}\right)^{2np} \right] \tag{2.59}$$

$$C_2(n) = \left[\left(\frac{R_r}{R_m}\right)^{2np} - \left(\frac{R_r}{R_m}\right)^{np+1} \right] \left[\frac{\mu_r - 1}{\mu_r + 1} - \left(\frac{R_0}{R_r}\right)^{2np} \right] \tag{2.60}$$

$$\begin{aligned} C_3(n) = & \left[1 - \frac{\mu_r - 1}{\mu_r + 1} \left(\frac{R_s}{R_m}\right)^{2np} \right] \cdot \left[\frac{\mu_r - 1}{\mu_r + 1} \left(\frac{R_r}{R_s}\right)^{2np} - \left(\frac{R_0}{R_r}\right)^{2np} \right] \\ & - \left[\frac{\mu_r - 1}{\mu_r + 1} \left(\frac{R_m}{R_s}\right)^{2np} - 1 \right] \cdot \left[1 - \frac{\mu_r - 1}{\mu_r + 1} \left(\frac{R_0}{R_r}\right)^{2np} \right] \end{aligned} \tag{2.61}$$

$$C_4(n) = 2\left(\frac{R_m}{R_s}\right)^{np+1} \tag{2.62}$$

Finally, since the fundamental amplitude of electromagnetic torque is the most important, the optimal magnet ratio R_{mp} can be directly predicted by using the following simple determination equation as:

$$R_{mp} = \frac{2}{\pi} tan^{-1}\left[\frac{\big(C_1(1) - C_2(1)\big) - \big(C_1(1) + C_2(1)\big)p}{\big(C_1(1) + C_2(1)\big) - \big(C_1(1) - C_2(1)\big)p}\right] \tag{2.63}$$

where

$$C_1(1) = \left[1 - \left(\frac{R_r}{R_m}\right)^{p+1}\right]\left[1 - \frac{\mu_r - 1}{\mu_r + 1}\left(\frac{R_0}{R_r}\right)^{2p}\right] \tag{2.64}$$

$$C_2(1) = \left[\left(\frac{R_r}{R_m}\right)^{2p} - \left(\frac{R_r}{R_m}\right)^{p+1}\right]\left[\frac{\mu_r - 1}{\mu_r + 1} - \left(\frac{R_0}{R_r}\right)^{2p}\right] \tag{2.65}$$

For machines having iron-cored rotor, $R_0 = R_r$, thus the foregoing equations (2.64) and (2.65) can be further deduced as:

$$C_1(1) = \left[1 - \left(\frac{R_r}{R_m}\right)^{p+1}\right] \cdot \left(1 - \frac{\mu_r - 1}{\mu_r + 1}\right) \tag{2.66}$$

$$C_2(1) = \left[\left(\frac{R_r}{R_m}\right)^{2p} - \left(\frac{R_r}{R_m}\right)^{p+1}\right] \cdot \left(\frac{\mu_r - 1}{\mu_r + 1} - 1\right) \tag{2.67}$$

Moreover, for machines having air-cored rotor, $R_0/R_r = 0$ is often assumed, then, equations (2.64) and (2.65) are simplified as

$$C_1(1) = \left[1 - \left(\frac{R_r}{R_m}\right)^{p+1}\right] \tag{2.68}$$

$$C_2(1) = \left[\left(\frac{R_r}{R_m}\right)^{2p} - \left(\frac{R_r}{R_m}\right)^{p+1}\right] \cdot \frac{\mu_r - 1}{\mu_r + 1} \tag{2.69}$$

It can be seen from SDE that for maximizing the electromagnetic torque produced by the fundamental component of air-gap flux density, the optimal magnet ratio R_{mp} is only a function of the pole-pair number p, and the ratio of magnet inner radius to outer radius, R_r/R_m, or in other words, the magnet thickness, together with relative permeability of PM. It should be noticed that since SDE is derived based on electromagnetic torque maximization, the optimal R_{mp} may not exhibit smallest torque ripple. For prototype iron-cored machine with 5

rotor pole-pairs, μ_r = 1.05, and R_r/R_m = 22.275/27.5 = 0.81, the optimal magnet ratio R_{mp} can be directly predicted as 0.7 by adopting SDE.

Clearly, the above equations can be further simplified if μ_r is assumed to be 1. However, it is worth noting that in this case, for air-cored machines, $C_2(1)$ = 0, and

$$R_{mp} = \frac{2}{\pi} tan^{-1}(1) = 0.5 \tag{2.70}$$

Hence, the above optimal R_{mp} reveals that the maximum electromagnetic torque for air-cored rotor case can be obtained when the magnet segments have equal pole-arc. It is also noted that the magnet ratio is irrelevant to pole-pair number and magnet thickness for air-cored rotor if μ_r =1. Meanwhile, its optimal R_{mp} is the same as machine with p = 1 as will be shown later.

However, it is extremely difficult to derive a similar SDE for parallel magnetized 2-segment Halbach array, due to more complicated mathematic expressions in magnetization vectors than radial magnetized case. However, the developed SDE still can be adopted for parallel magnetized 2-segment Halbach array as will be discussed in the next section.

2.4 Finite-Element Validation and Investigations

The FEA has been applied to an internal rotor three-phase 12-slot/10-pole PM brushless machine having radial and parallel magnetized 2-segment Halbach arrays, and the design parameters are given in TABLE 2-I. The developed 2-D field model and linear FEA predicted air-gap flux density (where $B_{agr}P$ and $B_{agc}P$ indicate radial and circumferential air-gap flux density with parallel magnetization, while $B_{agr}R$ and $B_{agc}R$ indicate radial and circumferential B_{ag} with radial magnetization, respectively), phase back-EMF and electromagnetic waveforms are compared in Fig.2.4 when the stator slotting is neglected, i.e. equivalent slotless machine. Good agreements are achieved. The FEA predicted equal potential distribution is shown in Fig.2.5.

TABLE 2-I Machines Design Parameters (Default Unit: mm)

Rated speed, *rpm*	400	Slot opening, b_o	2.0
Pole number, $2p$	10	Air-gap length, l_g	1.0
Stator slot number, N_s	12	Active length, l_a	50
Tooth-tip height, h_t	1.5	Stator back-iron thickness, h_{sbi}	3.7
Tooth body width, b_t	-	Stator outer radius, R_{so}	50
Stator inner radius, R_s	28.5	Rotor outer radius, R_r	22.275

Magnet thickness, h_{pm}	5.225	Magnet remanence, B_r	1.2
Magnet ratio, R_{mp}	0.7		

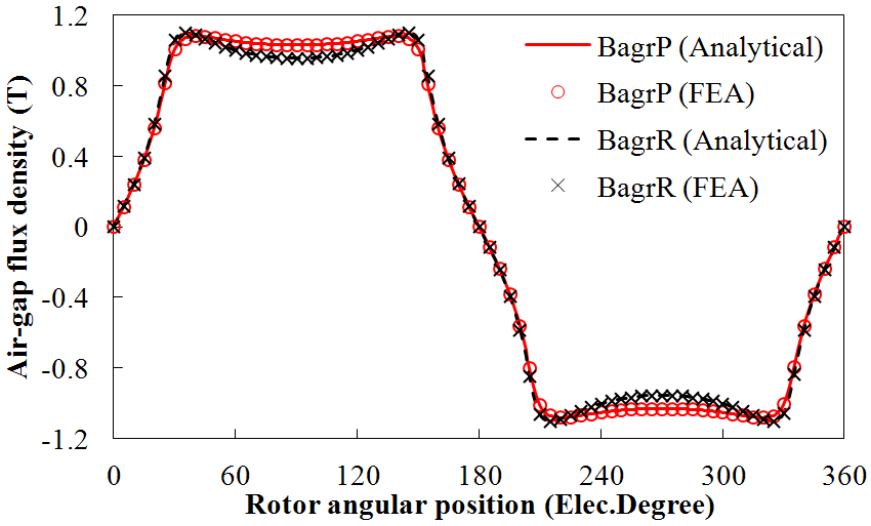

(a) Radial air-gap flux density

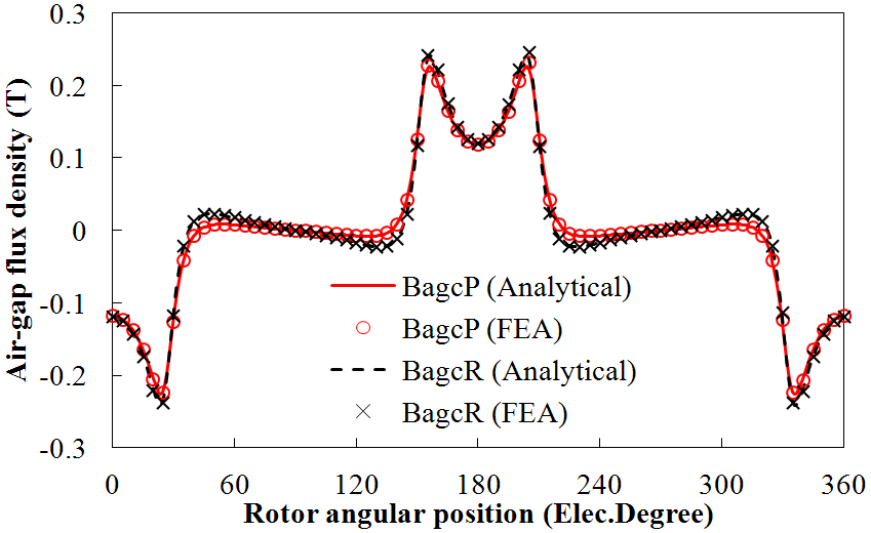

(b) Circumferential air-gap flux density

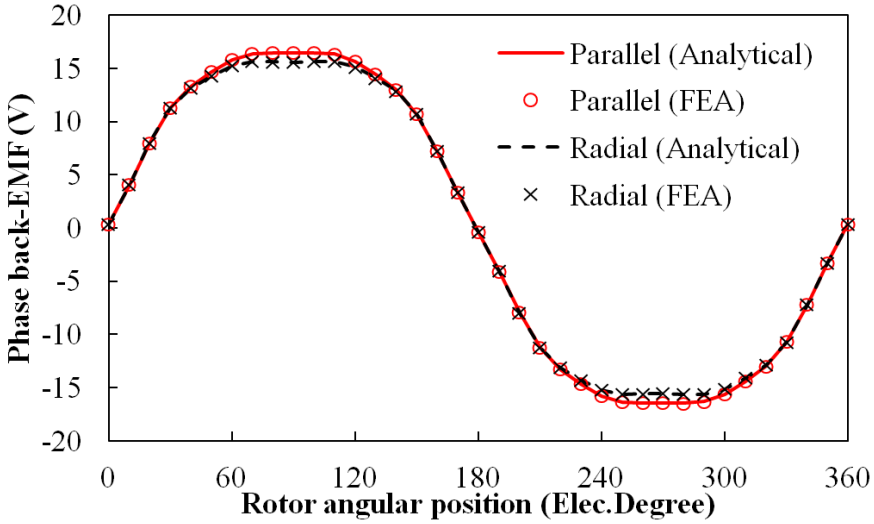

(c) Phase back-EMF, 400 rpm

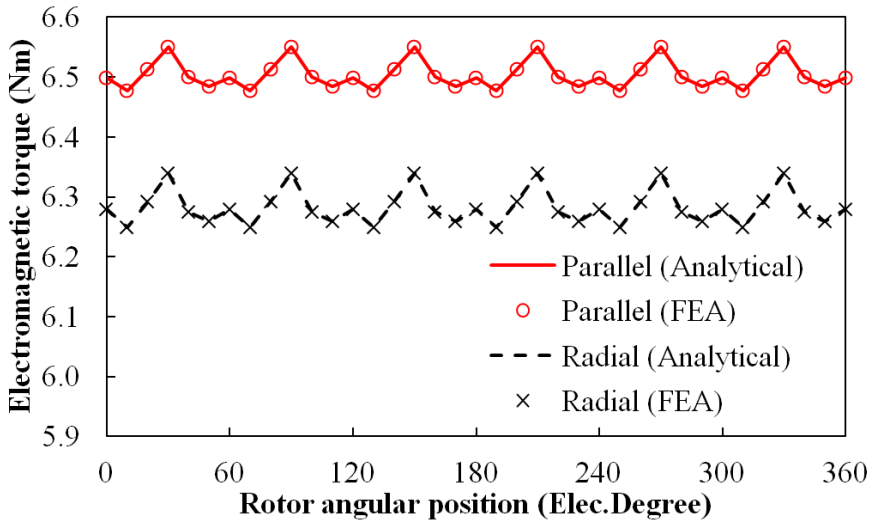

(d) Electromagnetic torque

Fig.2.4. Comparison of FEA and analytical predicted air-gap flux density, phase back-EMF and electromagnetic torque waveforms for slotless 12-slot/10-pole PM brushless machine having 2-segment Halbach array with optimal R_{mp}= 0.7.

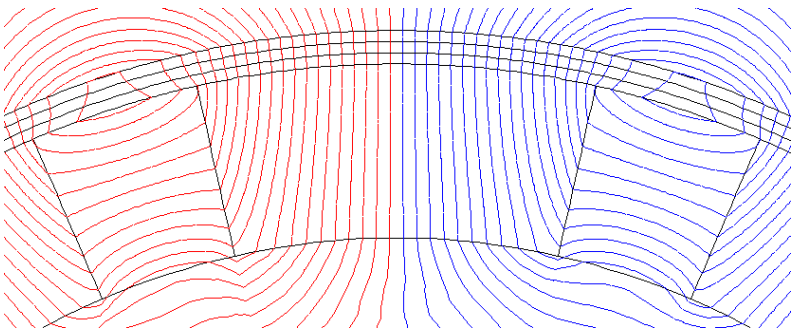

(a) Parallel magnetized 2-segment Halbach array

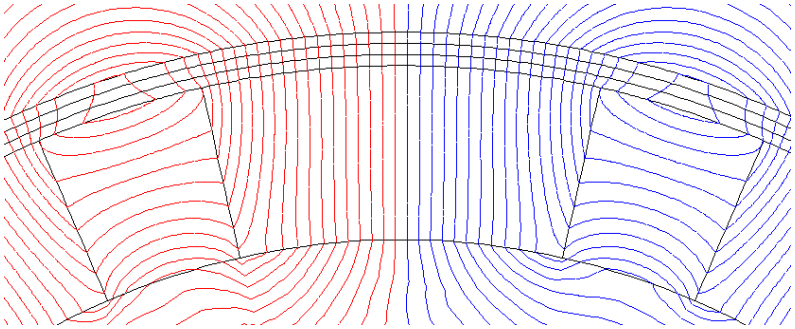

(b) Radial magnetized 2-segment Halbach array

Fig.2.5. FEA predicted equal potential distribution for slotless 12-slot/10-pole PM brushless machine having radial and parallel magnetized 2-segment Halbach arrays with optimal R_{mp}= 0.7.

The analytically scanned optimal magnet ratio R_{mp} for PM brushless machine having radial and parallel magnetized 2-segment Halbach arrays are compared as shown in Fig.2.6, where the parallel magnetized 2-segment Halbach array exhibits higher B_{ag1} than radial magnetized case. Meanwhile, the optimal magnet ratio R_{mp} which is determined by the derived SDE is also compared with analytically scanned result, where good agreement is achieved.

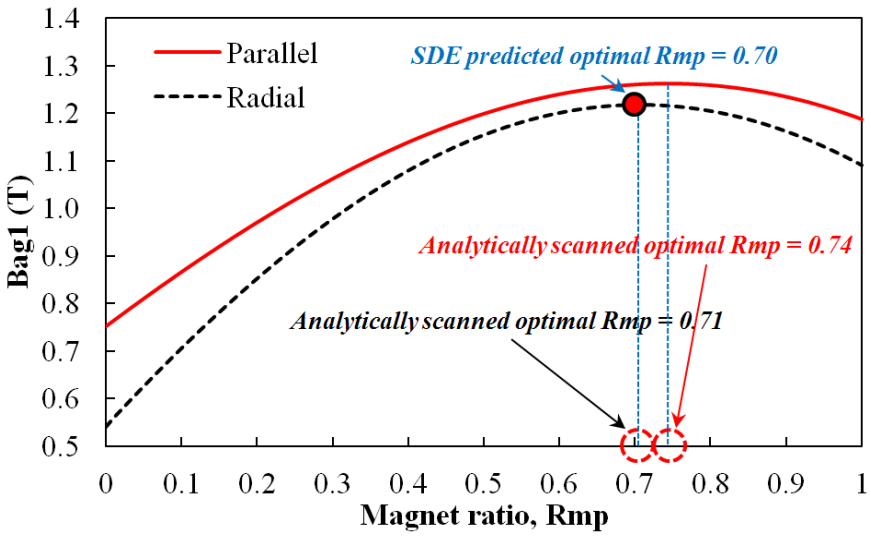

Fig.2.6. Analytically predicted variation of fundamental air-gap flux density with magnet ratio R_{mp} for 12-slot/10-pole slotless machine having radial and parallel magnetized 2-segment Halbach arrays when R_r/R_m = 0.81.

Furthermore, the variation of optimal B_{ag1} and corresponding optimal R_{mp} for both radial and parallel magnetized 2-segment Halbach arrays with rotor design parameters listed in Table I are compared as shown in Fig.2.7. It reveals that the thicker the magnet (R_r/R_m) the better the performance will be achieved for parallel magnetized Halbach array. It is noted that the optimal p exists for both radial and parallel magnetized Halbach array for given rotor

geometry, Fig.2.7. The results in Fig.2.7 and Fig.2.8 reflect that the 2-segment Halbach with parallel magnetized 2-segment Halbach array exhibits higher B_{ag1}, which in turn, leads to a higher electromagnetic torque. Nevertheless, optimal R_{mp} for both parallel and radial magnetized 2-segment Halbach arrays are similar in both amplitude and trend of variation. Consequently, the SDE can be adopted to predict the optimal R_{mp} for parallel magnetized 2-segment Halbach array as well, although small but acceptable error may exist.

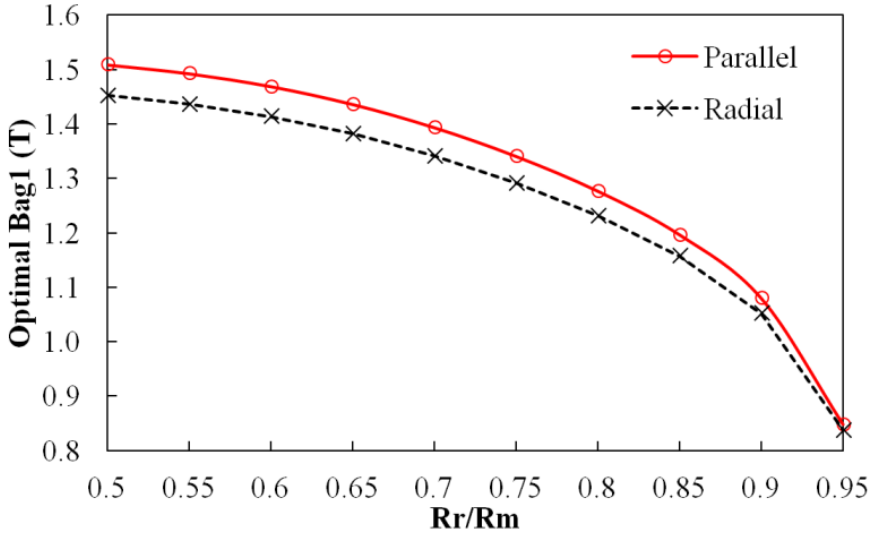

(a) Optimal B_{ag1}

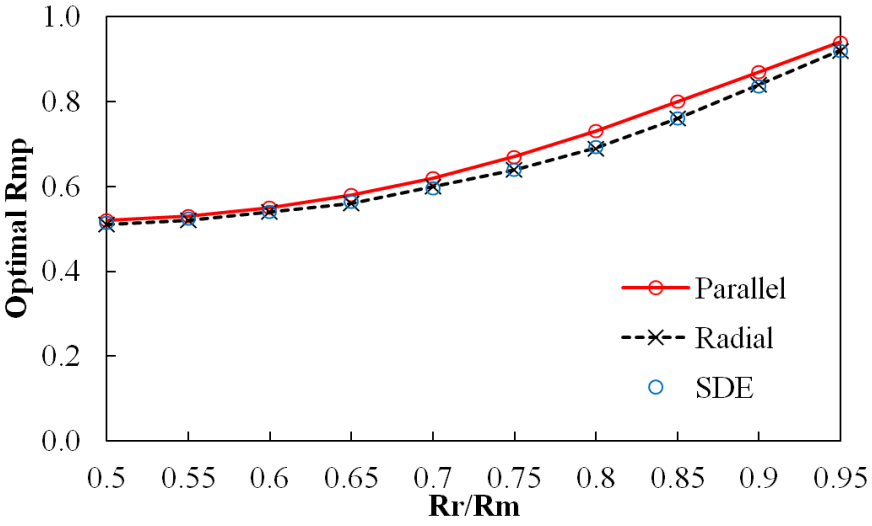

(b) Optimal R_{mp}

Fig.2.7. Variation of optimal B_{ag1} and R_{mp} with R_r/R_m for radial and parallel magnetized 2-segment Halbach arrays when p = 5.

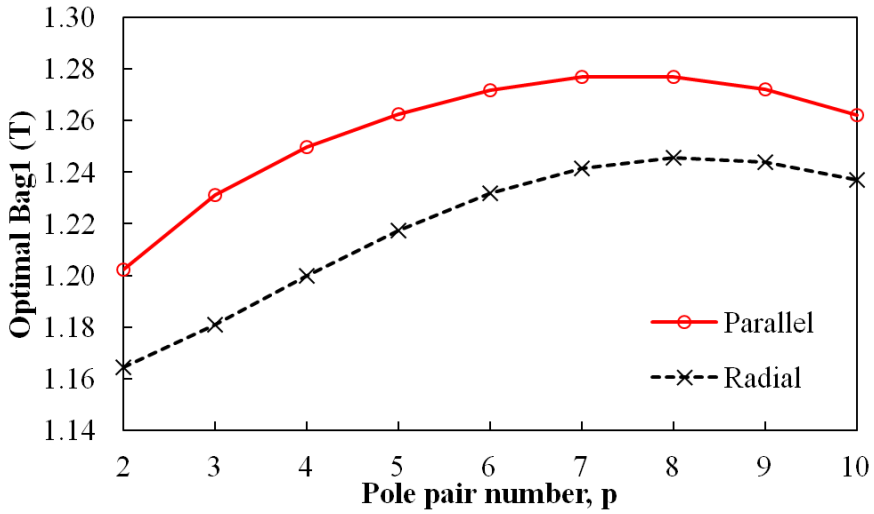

(a) Optimal B_{ag1}

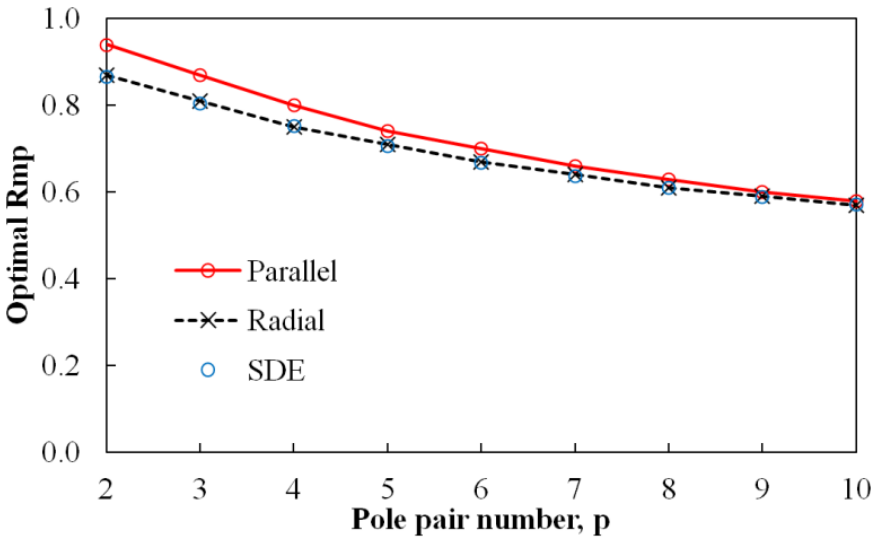

(b) Optimal R_{mp}

Fig.2.8. Variation of optimal B_{ag1} and R_{mp} with p for radial and parallel magnetized 2-segment Halbach arrays when $R_r/R_m = 0.81$.

It is necessary to study the influence of magnet thickness and pole-pair number p on optimal R_{mp} for radial and parallel magnetized 2-segment Halbach arrays. Instead of scanning the results, the proposed SDE can obtain the optimal results straightforward. Fig.2.9 shows the SDE predicted variation of optimal R_{mp} with R_r/R_m and p for iron-cored ($R_0/R_r = 1$) and air-cored ($R_0/R_r = 0$) rotor. For the iron-cored rotor topology, it can be seen that for thinner magnet thickness or the higher R_r/R_m ratio, the optimal R_{mp} tends to be high, whilst the optimal R_{mp} is lower for thicker magnet thickness. For a particular case, i.e. when $p = 1$, the optimal R_{mp} is constant and equal to 0.5. Machines having higher p exhibit lower magnet ratio R_{mp} when R_r/R_m (with reveals magnet thickness) is kept the same as for the iron-cored rotor, and higher R_{mp} for the air-cored rotor. It is also noticed that the optimal R_{mp} for the

iron-cored rotor PM brushless machine having 2-segment Halbach array is always higher than 0.5 compared with air-cored rotor cases when p is greater than 1, as shown in Fig.2.9.

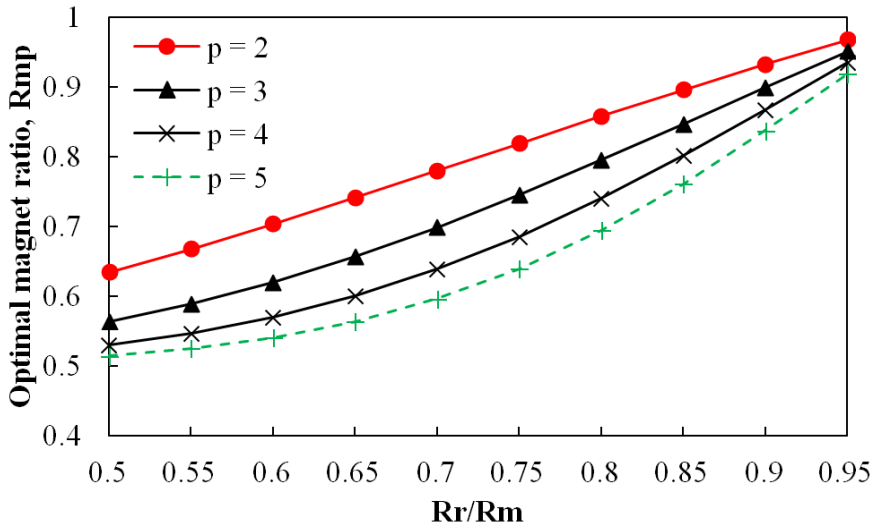

(a) Iron-cored

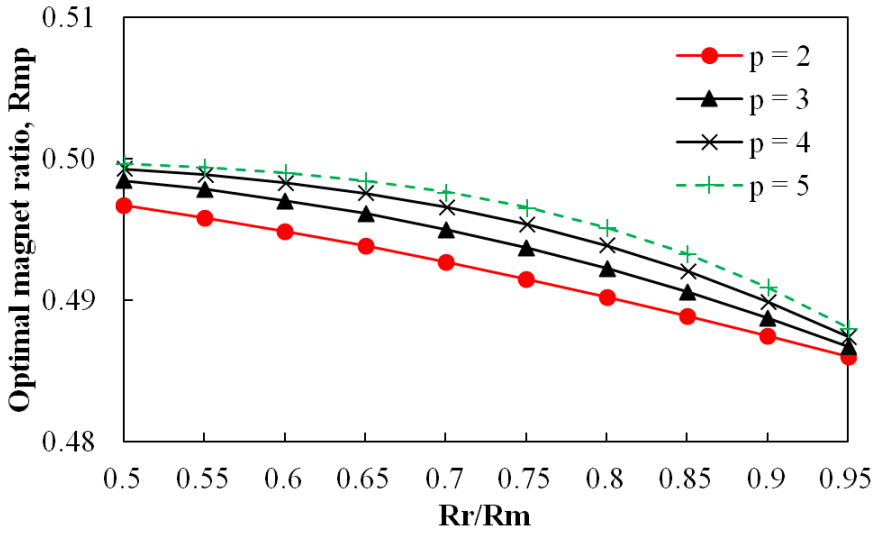

(b) Air-cored

Fig.2.9. Variation of optimal magnet ratio R_{mp} with R_r/R_m and p for iron- and air-cored rotor PM brushless machine having radial and parallel magnetized 2-segment Halbach array.

2.5 Measurements

A prototype 12-slot/10-pole PM brushless machine having 2-segment Halbach array with R_r/R_m = 0.81 and optimal R_{mp} = 0.7, together with an existing all teeth wound stator has been made as shown in Fig.2.10. It is noted that the proposed 2-D analytical model does not account for the slotting effect for the simplicity of derivation, whilst the 2-D field model with the consideration of slotting effect by adopting simplified 2-D relative permeance model [183], complex permeance model [184], and sub-domain method [185] are complicated and

difficult to derive a SDE with a clear physic insight into the relationship between the optimal R_{mp} and design parameters. On the other hand, in order to predict the cogging and output torque waveforms, the slotting effect needs to be considered by adopting sub-domain (SD) method similar to that in [185]. The detail derivations and expressions of SD method for Halbach array will be presented in Chapter 3. The 2-D field slotless model, 2-D field slotted model with SD method, FEA predicted and measured cogging torque and output torque waveforms are compared in Fig.2.11, and good agreements are achieved. It is noted that the analytically predicted output torque is higher than FEA calculated and measured results due to ignored consideration of saturation.

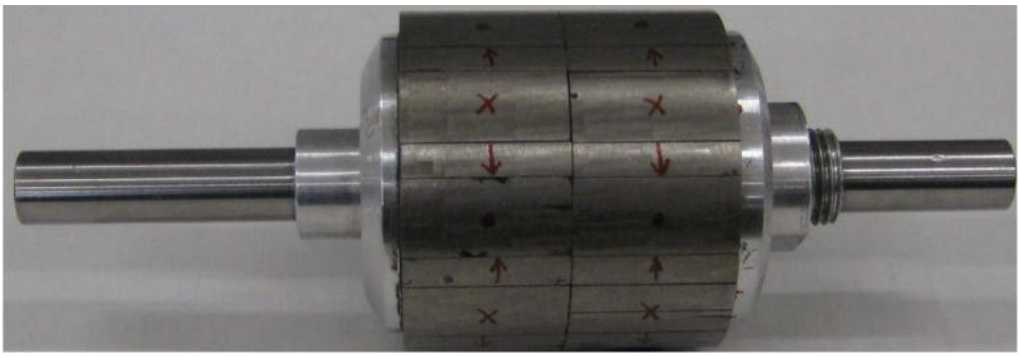

(a) Rotor with 2-segment Halbach array (R_{mp}=0.7)

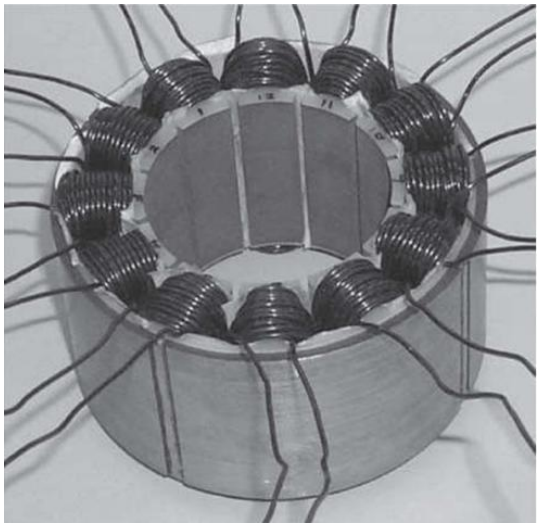

(b) 12-slot stator with non-overlapping winding

Fig.2.10. Rotor and stator for prototype 12-slot/10-pole machine.

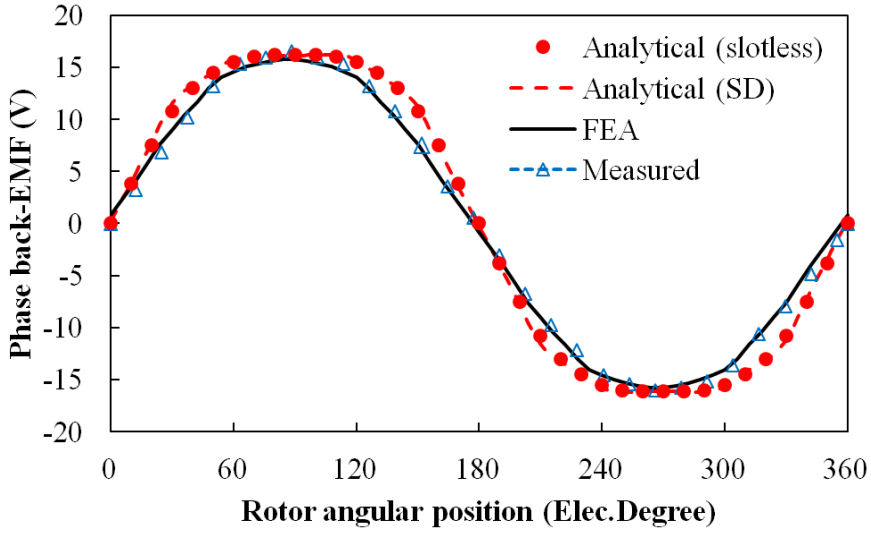

(a) Phase back-EMF at 400 rpm

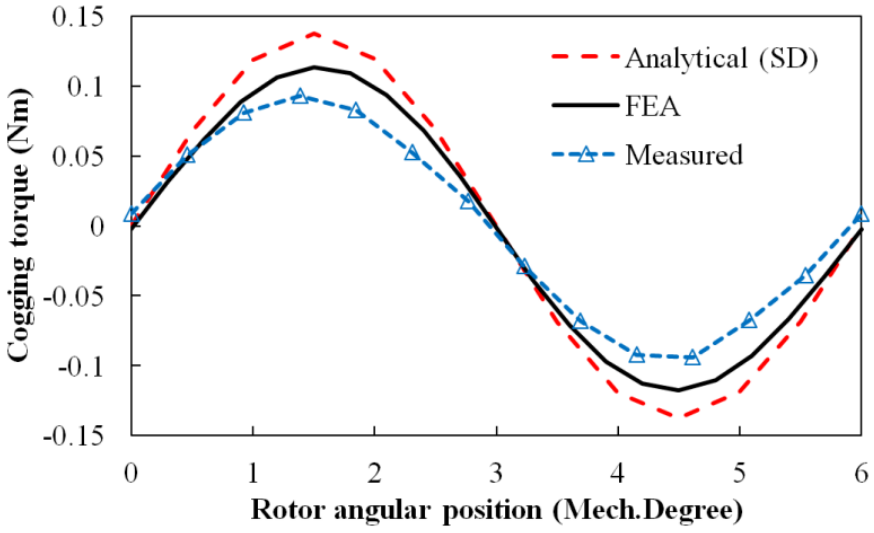

(b) Cogging torque

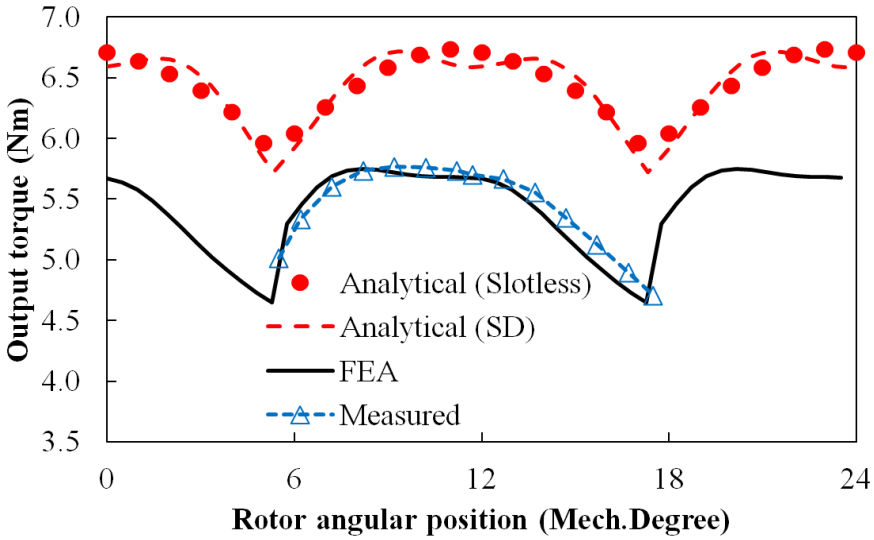

(c) Output torque at BLDC operation mode, I_{peak} = 9.07 A

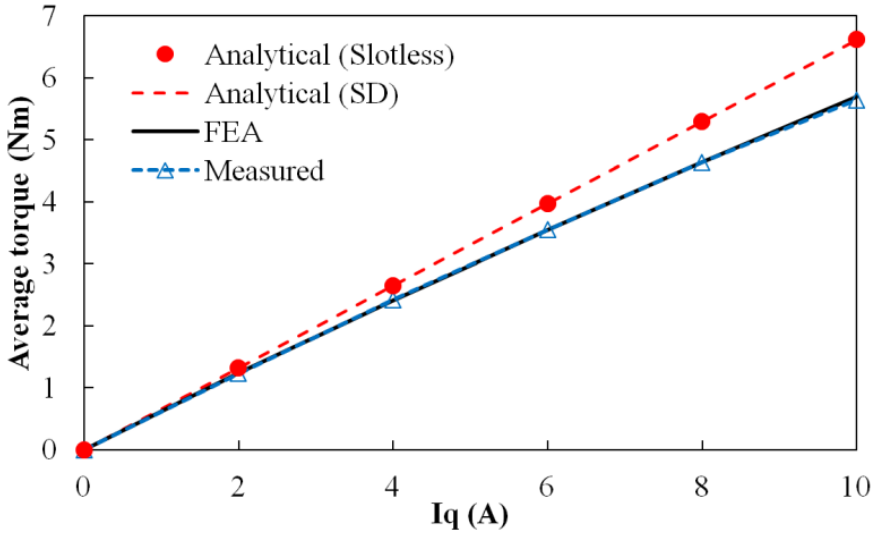

(d) Average torque against I_q

Fig.2.11. Comparison of slotless analytical model, analytical model with SD method, FEA and measured phase back-EMF, cogging torque, output torque and average torque against I_q for prototype machine.

In order to illustrate the influence of magnetic saturation, the 2-D field slotless model, 2-D field slotted model with SD method and linear FEA (μ_r is set to 40000) predicted back-EMF, cogging torque and output torque waveforms are compared in Fig.2.11 and Fig.2.13, respectively. Good agreements are achieved since the saturation effect is ignored.

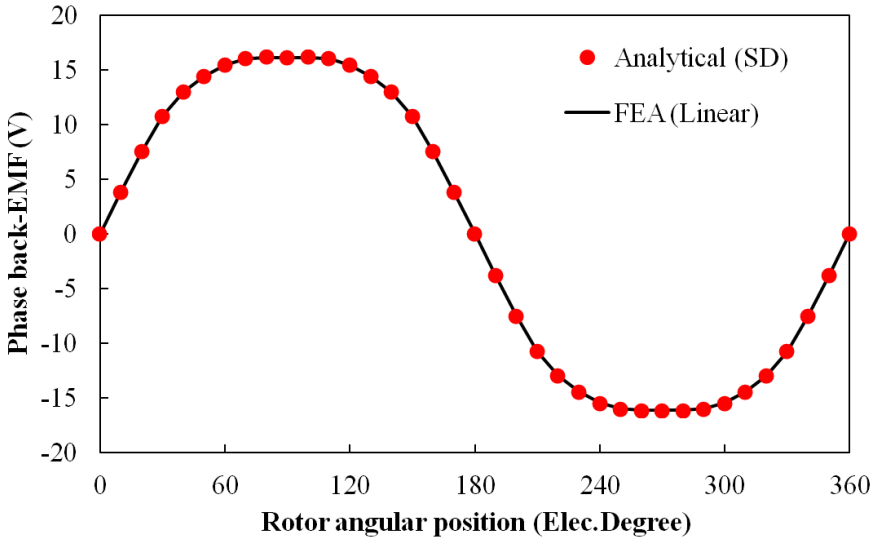

(a) Phase back-EMF at 400 rpm

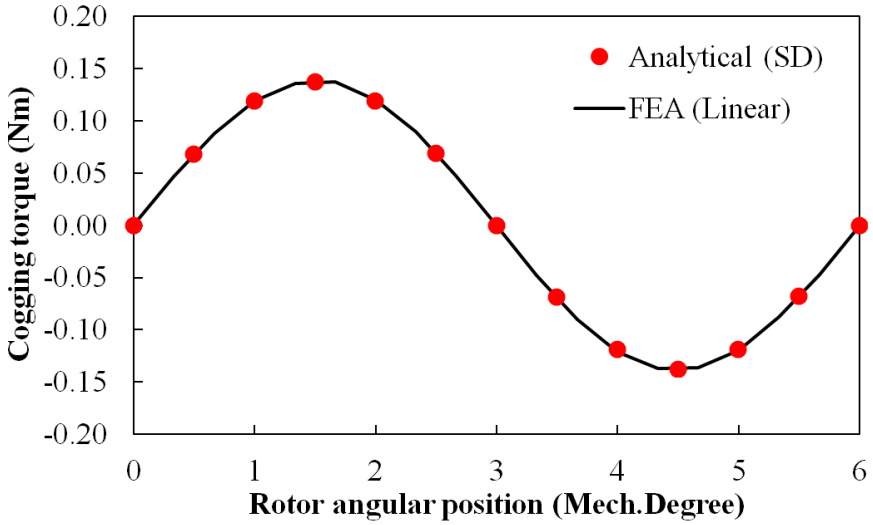

(b) Cogging torque (slotted model)

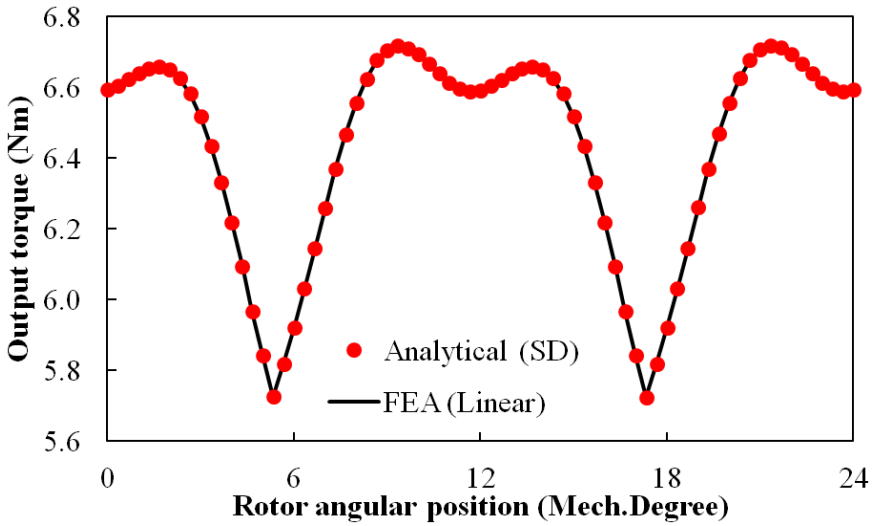

(c) Output torque at BLDC operation mode, I_{peak} = 9.07 A

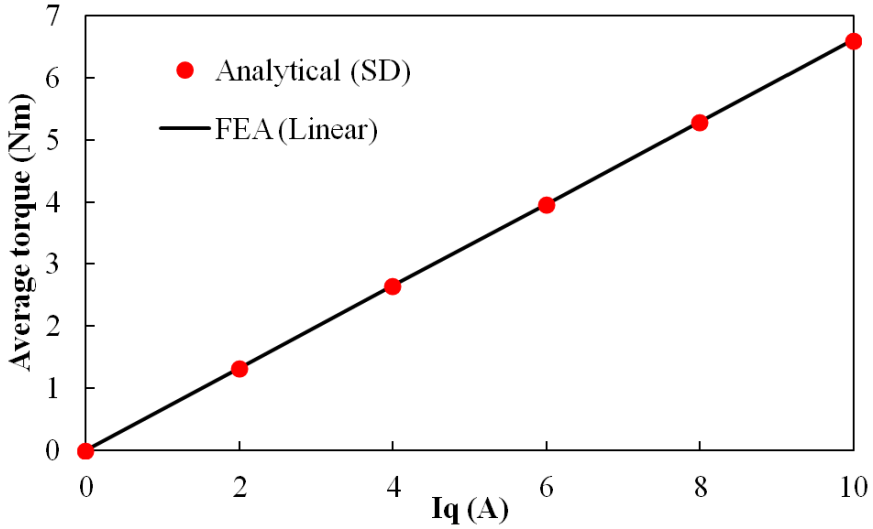

(d) Average torque against I_q

Fig.2.12. Comparison of analytical model with SD method and slotted linear FEA predicted phase back-EMF, cogging torque, output torque and average torque against I_q for prototype machine.

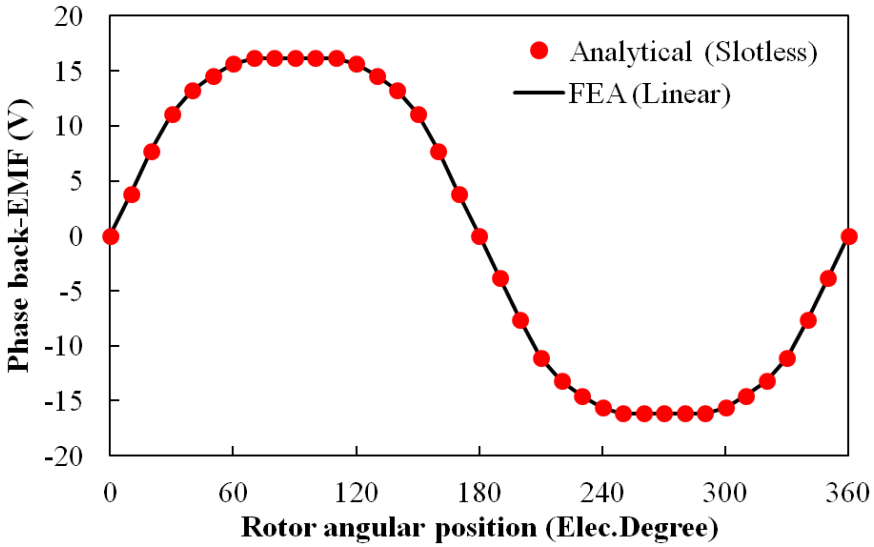

(a) Phase back-EMF at 400 rpm

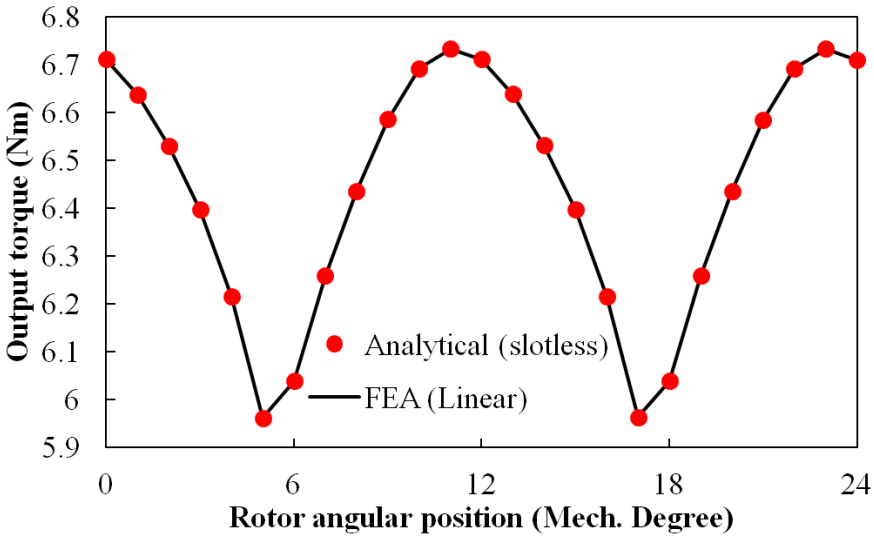

(b) Output torque at BLDC operation mode, I_{peak} = 9.07 A

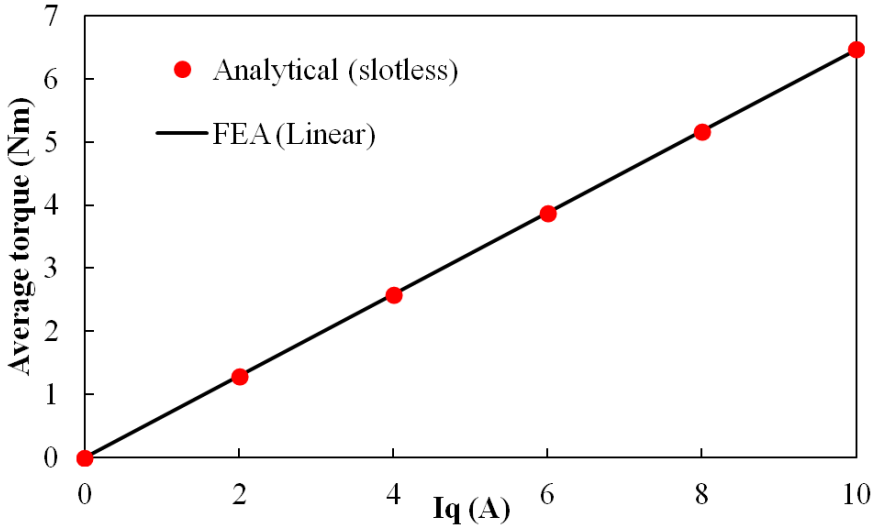

(c) Average torque against I_q

Fig.2.13. Comparison of slotless analytical model and slotless linear FEA predicted phase back-EMF, output torque and average torque against I_q for prototype machine.

2.5 Summary

This chapter presents a 2-dimentional field model and a simple equation to predict the optimal magnet ratio for air- and iron-cored, permanent magnet brushless machine having radial and parallel magnetized 2-segment Halbach arrays. The machine having parallel magnetized 2-segment Halbach array exhibits higher air-gap flux density than radial magnetized Halabch array. By using developed SDE, it is found that for maximized average torque, the optimal magnet ratio R_{mp} is only a function of pole-pair number p, magnet thickness and permeability of permanent magnet. It is found that the thicker the magnet, the lower the optimal R_{mp} for machines having iron-cored rotor. In contrast to the iron-cored rotor, the optimal magnet ratio R_{mp} increases as magnet thickness increasing for air-core rotor. Moreover, the optimal R_{mp} for the machines having iron-cored rotor is always greater than 0.5, while machines having air-cored rotor is always lower than 0.5, except the case of p =1. Further, a prototype 12-slot/10-pole machine having optimal R_{mp} = 0.7 has been made, and good agreement between analytical, FEA predicted and measured electromagnetic performances are achieved.

CHAPTER 3 GENERAL ANALYTICAL MODEL FOR CALCULATING ELECTROMAGNETIC PERFORMANCE OF PM BRUSHLESS MACHINES HAVING SEGMENTED HALBACH ARRAY

Since a Halbach array exhibits a number of attractive features, it has been increasingly applied to different market sectors, including aerospace, industrial, domestic, renewable, and healthcare, etc. The need of fast global optimization, cost-effective design, and physical understanding of the relationship between parameters and performance requires a powerful analytical model. Hence, in this chapter, a general analytical model is developed which is capable of predicting the electromagnetic performance of slotted/slotless permanent magnet brushless machines with both even- and odd-segment Halbach array, having different magnet remanence, magnetization angle and arc for each single magnet segment. The validity of proposed analytical model is examined by FEA, together with its applications for global optimization and comparative study.

3.1 Introduction

The analytical models play a very important role in the design of PM brushless machine having Halbach array. Previously developed analytical models for Halbach arrays are reviewed in Chapter 1, where a broad consensus has been reached which realizes the higher the magnet segment, the better the electromagnetic performance, but meanwhile results difficulty in manufacturing. Therefore, a compromise design is always needed since the design tradeoff between performance and manufacture is inevitable.

In this chapter, a general analytical model based on the SD method together with the developed general analytical model of magnetization vectors for segmented Halbach arrays is proposed, which is capable of modeling the air-gap flux density waveform for slotted/slotless PM brushless machines and devices such as magnet cylinder, etc, having both even- and odd-segmented Halbach array, together with the variation freedom of magnet remanence, magnetization angle and arc for each single magnet segment. Meanwhile, the electromagnetic performance, including phase back-EMF, cogging torque and electromagnetic torque waveforms are able to be predicted. The proposed general analytical model is validated by FEA. In addition, the functionality of the proposed general analytical model is presented by adopting a global optimization of the rotor pole pair number for magnet cylinder having 2-

and 3-segment Halbach array, plus a simple comparative study for a 12-slot, 2-segment Halbach machine having different pole pair number.

3.2 Development of General Analytical Model

For PM brushless machines, the field vectors $\vec{B}$ and $\vec{H}$ in both air-gap (*ag*) and PM regions are expressed as

$$\vec{B}_{ag} = \mu_0 \vec{H}_{ag} \tag{3.1}$$

$$\vec{B}_{PM} = \mu_0 \mu_r \vec{H}_{PM} + \mu_0 \vec{M} \tag{3.2}$$

where $\vec{M}$ is the residual magnetization vector, μ_0 is the permeability of air-gap, and μ_r is the relative recoil permeability of PM. By assuming the PM having linear 2nd quadrant demagnetization characteristic, the amplitude of magnetization vector $\vec{M}$ can be calculated as

$$M = \frac{B_r}{\mu_0} \tag{3.3}$$

whilst in polar coordinates $\vec{M}$ is governed by imported orientation and the magnetization of PM, which can be expressed as [64].

$$\vec{M} = M_r \vec{r} + M_\theta \vec{\theta}$$

$$= \sum_{n=1,2,3\cdots}^{\infty} M_{rn} cos(np\theta)\ \vec{r} \mp \sum_{n=1,2,3\cdots}^{\infty} M_{\theta n} sin(np\theta)\ \vec{\theta} \tag{3.4}$$

where M_r and M_θ represent the components of radial and circumferential magnetizations, '-' is for an internal rotor machine (external field), and '+' is for an external rotor machine (internal field). In order to simplify the derivation expressions, only internal rotor PM brushless machine having Halbach array is adopted in this chapter, since it is straightforward to obtain M_θ for external rotor machine by multiplying '-1'.

As can be seen in Fig.3.1 and Fig.3.2, the differences of both magnetization angle and boundary condition over one pole pitch for the end side-magnets between even- and odd-segment Halbach arrays exist when the reference axis is chosen in the middle of mid-magnet. For even-segment Halbach array, the magnetization angle θ_m of the end side-magnet is always equal to zero in contrast to odd-segment Halbach array, which could obtain an optimal θ_m in accordance with its magnet height-to-weight ratio. Further, the beginning and end boundaries over one pole pitch are placed in the middle of end side-magnet for the even-segment Halbach array, while the boundaries are placed at the end of end side-magnet for the

odd-segment Halbach array. Consequently, the analytical expressions of harmonic components for magnetization M_{rn} and $M_{\theta n}$ are separately analyzed within two groups, e.g. the even- and odd-segment Halbach arrays, respectively.

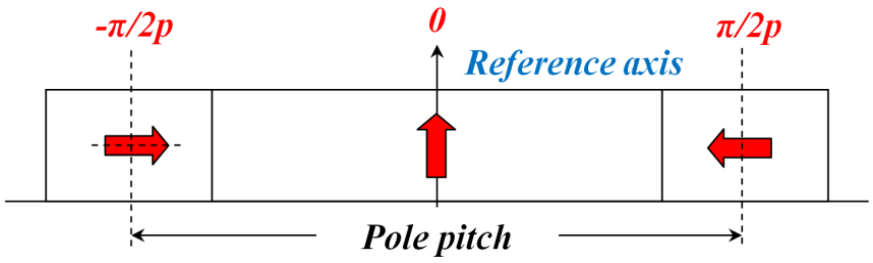

(a) 2-segment Halbach array

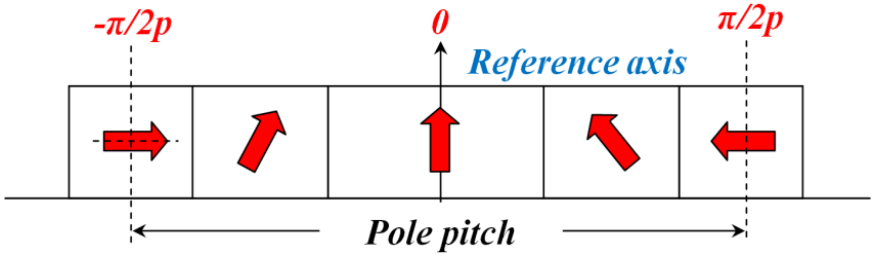

(b) 4-segment Halbach array

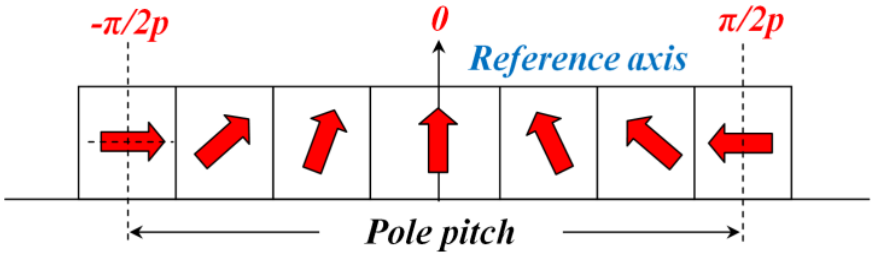

(c) 6-segment Halbach array

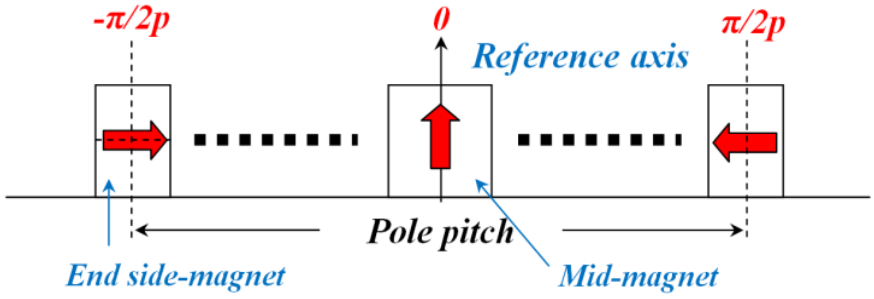

(d) 2m-segment Halbach array (m =1, 2, 3…)

Fig.3.1. Configuration of Halbach array with even-segments.

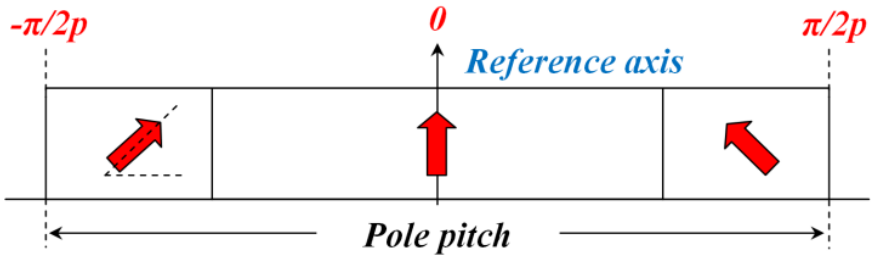

(a) 3-segment Halbach array

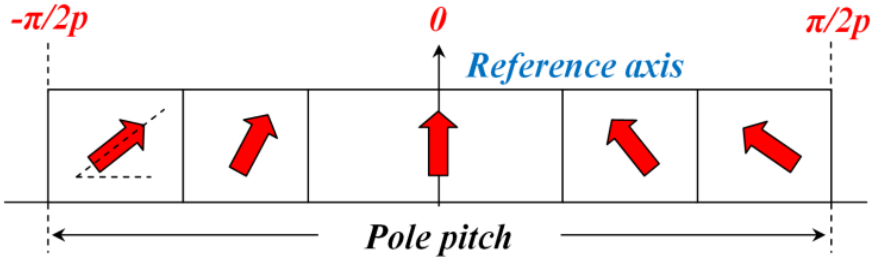

(b) 5-segment Halbach array

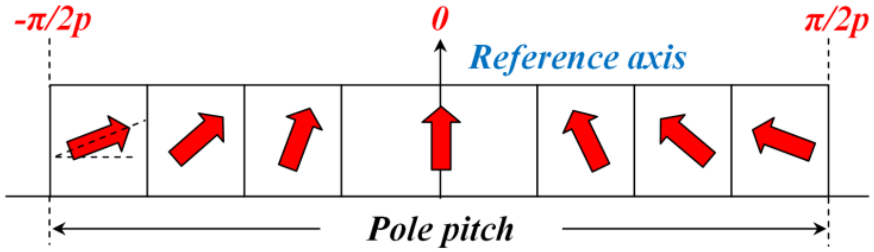

(c) 7-segment Halbach array

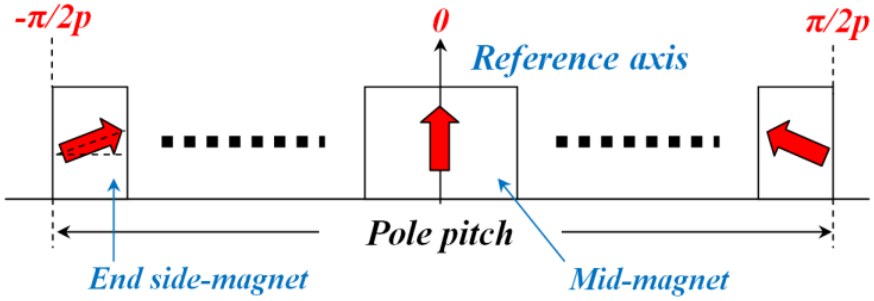

(d) (2m+1)-segment Halbach array (m =1, 2, 3…)

Fig.3.2. Configuration of Halbach array with odd-segments.

As shown in Fig.3.2, a typical segmented Halbach array consists of a mid-magnet, side-magnet and end side-magnet. Therefore, if each magnet segment is parallel magnetized, the magnetization components, with the design parameters illustrated in Fig.3.3, can be fully described in Table I over one pole-pair, where B_{rm} is the remanence of mid-magnet, B_{rs} is the remanence of both side- and end side- magnets, W_f is the pole-arc of mid-magnet, W_p is the pole-pitch, W_{ah} is the pole-arc of the h^{th} magnet pole (which includes the pole arc of mid-

magnet and the h^{th} magnet segment), the ratio of mid-magnet pole arc to pole pitch R_{mp} is defined as:

$$R_{mp} = \frac{W_f}{W_p} \tag{3.5}$$

and the ratio of the h^{th} magnet pole arc to the pole pitch R_{mph} is expressed as:

$$R_{mph} = \frac{W_{ah}}{W_p} \tag{3.6}$$

where the mid-magnet is designated as the 0^{th} magnet, hence R_{mph} for mid-magnet is described as R_{mp0}. For a 3-segment Halbach array, R_{mph} for both left and right hand side-magnets is described as R_{mp1}. Furthermore, θ_{mh} is the magnetization angle for the h^{th} magnet segment.

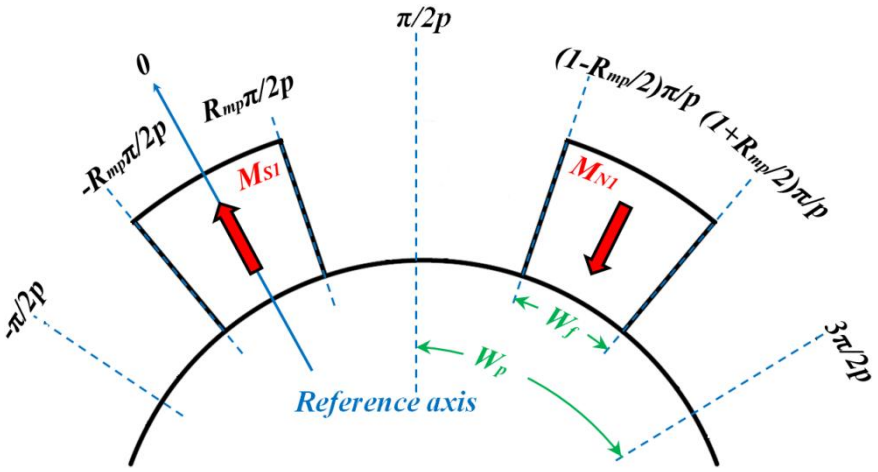

(a) Mid-magnet

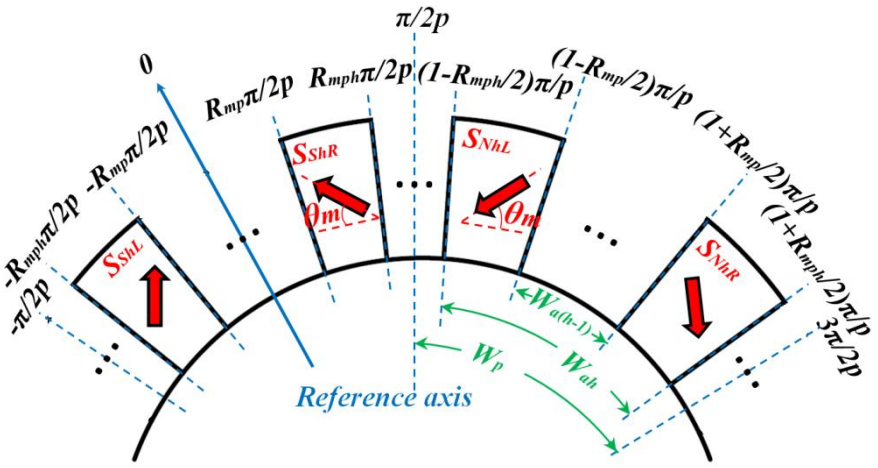

(b) Side-magnet

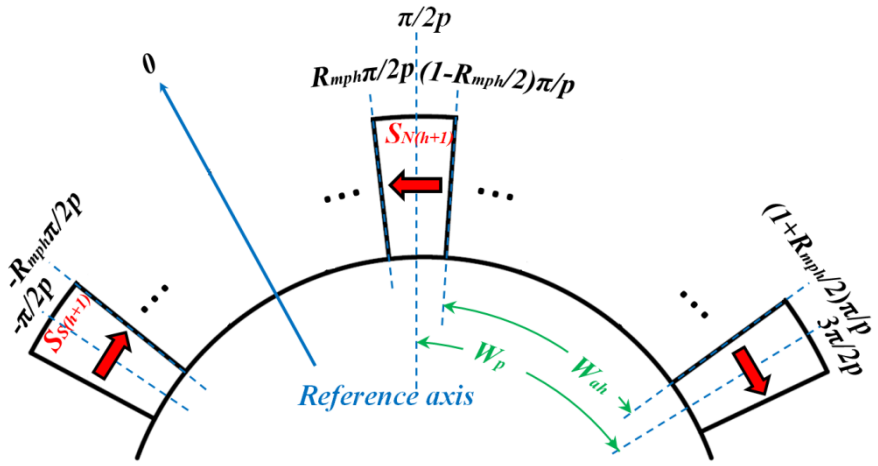

(c) End side-magnet for even-segment Halbach array

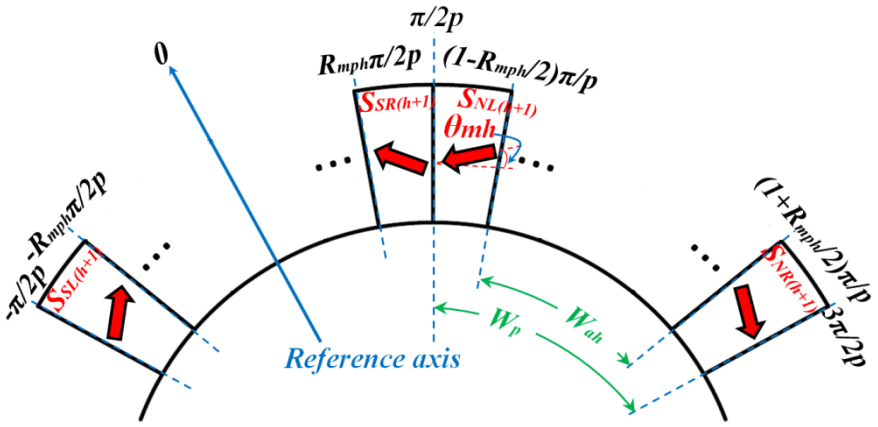

(d) End side-magnet for odd-segment Halbach array

Fig.3.3. Design parameters for mid-magnet, side-magnet, end side-magnet for even- and odd-segment Halbach arrays.

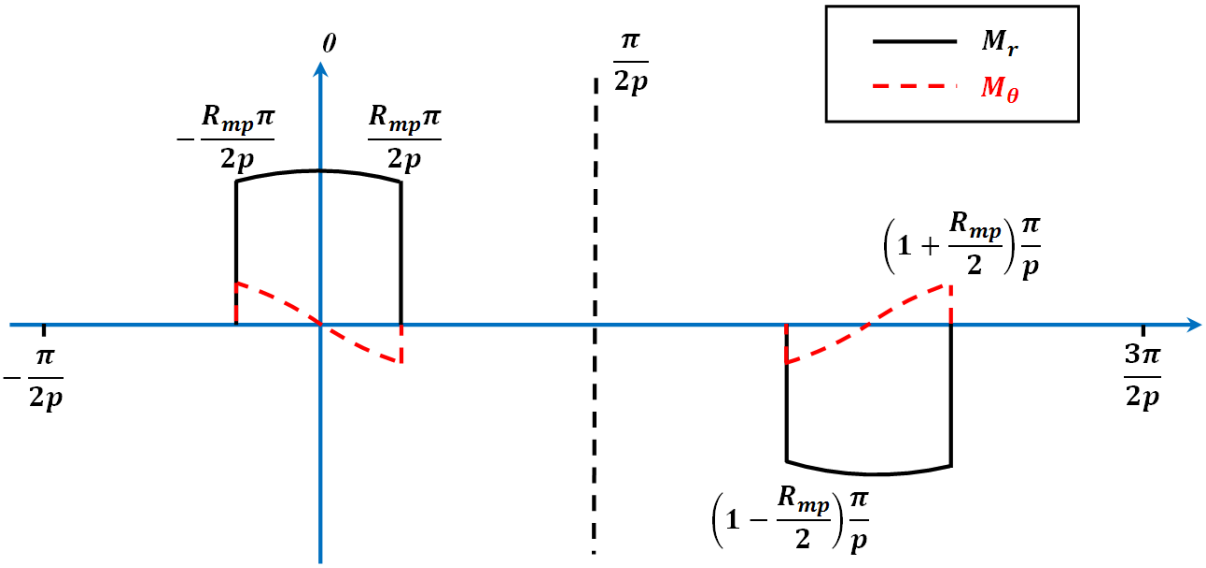

(a) Mid-magnet

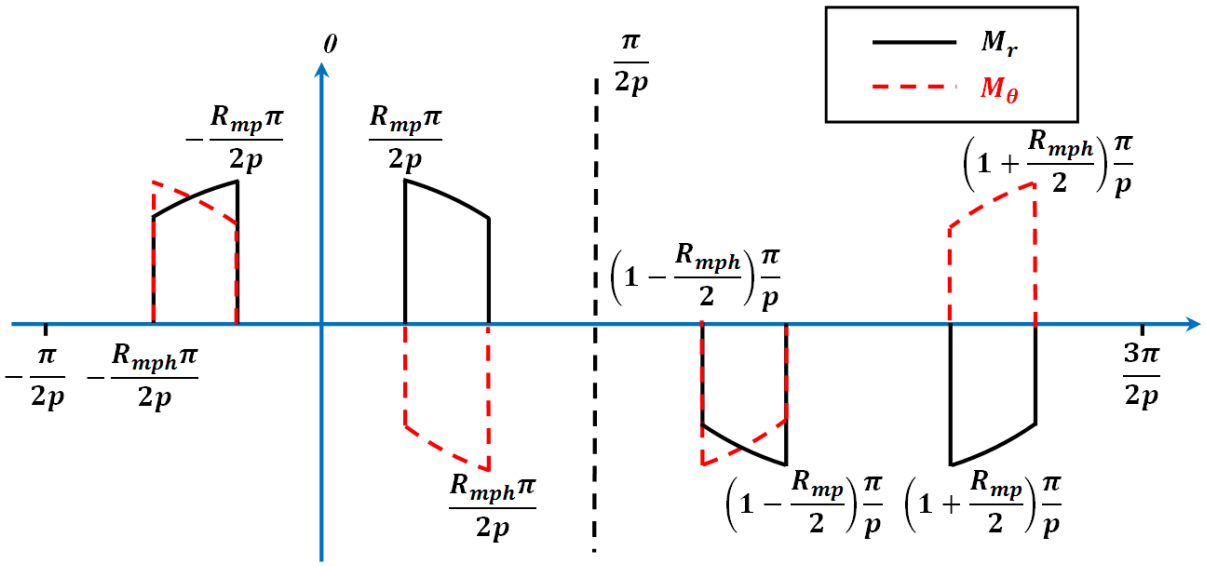

(b) Side-magnet

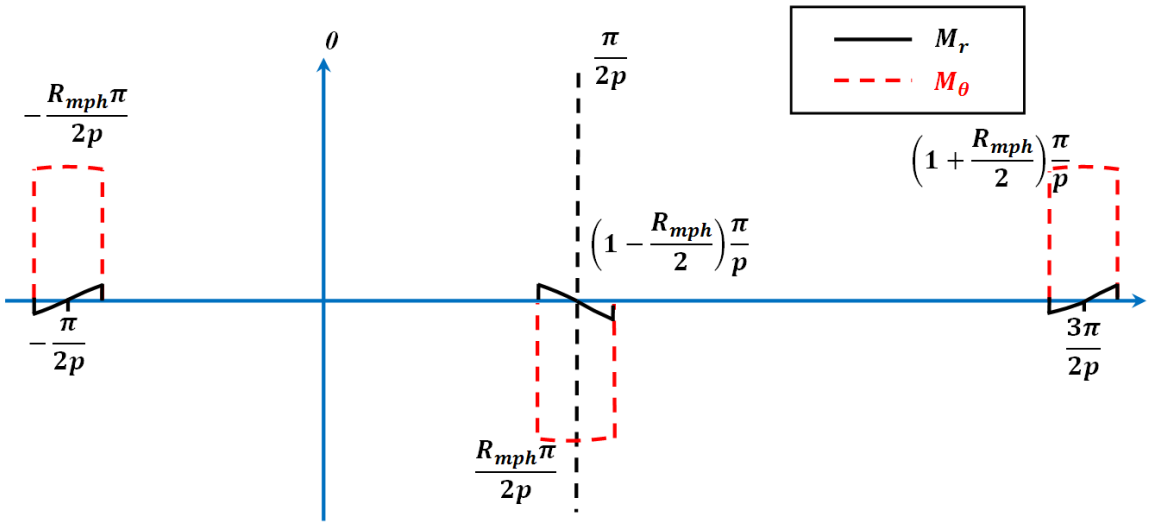

(c) End side-magnet for even-segment Halbach array

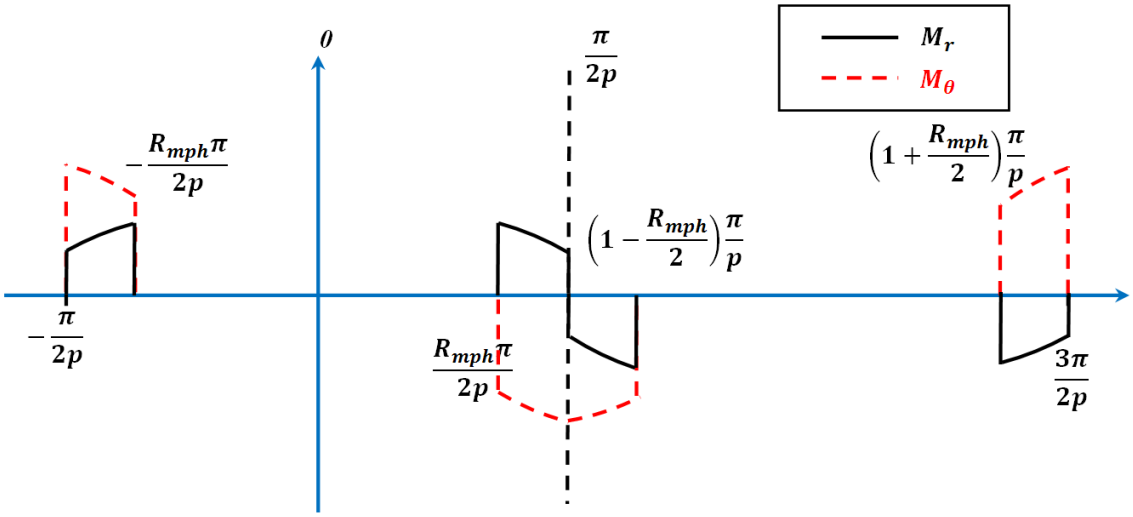

(d) End side-magnet for odd-segment Halbach array

Fig.3.4.Illustrations of magnetization vectors for different magnet segments.

TABLE 3-I MAGNETIZATION COMPONENTS FOR MAGNET SEGMENTS

Mid-magnet	***Position***
$\left.\begin{aligned} M_r &= \frac{B_{rm}}{\mu_0}\cos\theta \\ M_\theta &= -\frac{B_{rm}}{\mu_0}\sin\theta \end{aligned}\right\}$	$-\frac{R_{mp}\pi}{2p} \le \theta \le \frac{R_{mp}\pi}{2p}$
$\left.\begin{aligned} M_r &= -\frac{B_{rm}}{\mu_0}\cos\left(\theta - \frac{\pi}{p}\right) \\ M_\theta &= \frac{B_{rm}}{\mu_0}\sin\left(\theta - \frac{\pi}{p}\right) \end{aligned}\right\}$	$\left(1 - \frac{R_{mp}}{2}\right)\frac{\pi}{p} \le \theta \le \left(1 + \frac{R_{mp}}{2}\right)\frac{\pi}{p}$
Side-magnet	***Position***
$\left.\begin{aligned} M_r &= \frac{B_{rs}}{\mu_0}\sin(\theta_m + \theta + \delta) \\ M_\theta &= \frac{B_{rs}}{\mu_0}\cos(\theta_m + \theta + \delta) \end{aligned}\right\}$	$-\frac{R_{mph}\pi}{2p} \le \theta \le -\frac{R_{mp}\pi}{2p}$
$\left.\begin{aligned} M_r &= \frac{B_{rs}}{\mu_0}\sin(\theta_m - \theta + \delta) \\ M_\theta &= -\frac{B_{rs}}{\mu_0}\cos(\theta_m - \theta + \delta) \end{aligned}\right\}$	$\frac{R_{mp}\pi}{2p} \le \theta \le \frac{R_{mph}\pi}{2p}$
$\left.\begin{aligned} M_r &= -\frac{B_{rs}}{\mu_0}\sin\left(\theta_m + \theta - \frac{\pi}{p} + \delta\right) \\ M_\theta &= -\frac{B_{rs}}{\mu_0}\cos\left(\theta_m + \theta - \frac{\pi}{p} + \delta\right) \end{aligned}\right\}$	$\left(1 - \frac{R_{mph}}{2}\right)\frac{\pi}{p} \le \theta \le \left(1 - \frac{R_{mp}}{2}\right)\frac{\pi}{p}$
$\left.\begin{aligned} M_r &= -\frac{B_{rs}}{\mu_0}\sin\left(\theta_m - \theta + \frac{\pi}{p} + \delta\right) \\ M_\theta &= \frac{B_{rs}}{\mu_0}\cos\left(\theta_m - \theta + \frac{\pi}{p} + \delta\right) \end{aligned}\right\}$	$\left(1 + \frac{R_{mp}}{2}\right)\frac{\pi}{p} \le \theta \le \left(1 + \frac{R_{\mathrm{mph}}}{2}\right)\frac{\pi}{p}$
End side-magnet, even-segment Halbach array	***Position***
$\left.\begin{aligned} M_r &= \frac{B_{rs}}{\mu_0}\sin\left(\theta + \frac{\pi}{2p}\right) \\ M_\theta &= \frac{B_{rs}}{\mu_0}\cos\left(\theta + \frac{\pi}{2p}\right) \end{aligned}\right\}$	$-\frac{\pi}{2p} \le \theta \le -\frac{R_{mph}\pi}{2p}$
$\left.\begin{aligned} M_r &= -\frac{B_{rs}}{\mu_0}\sin\left(\theta - \frac{\pi}{2p}\right) \\ M_\theta &= -\frac{B_{rs}}{\mu_0}\cos\left(\theta - \frac{\pi}{2p}\right) \end{aligned}\right\}$	$\frac{R_{mph}\pi}{2p} \le \theta \le \left(1 - \frac{R_{mph}}{2}\right)\frac{\pi}{p}$
$\left.\begin{aligned} M_r &= \frac{B_{rs}}{\mu_0}\sin\left(\theta - \frac{3\pi}{2p}\right) \\ M_\theta &= \frac{B_{rs}}{\mu_0}\cos\left(\theta - \frac{3\pi}{2p}\right) \end{aligned}\right\}$	$\left(1 + \frac{R_{mph}}{2}\right)\frac{\pi}{p} \le \theta \le \frac{3\pi}{2p}$
End side-magnet, odd-segment Halbach array	***Position***

$\left.\begin{aligned} M_r &= \frac{B_{rs}}{\mu_0}\sin(\theta_{mh}+\theta+\delta_h) \\ M_\theta &= \frac{B_{rs}}{\mu_0}\cos(\theta_{mh}+\theta+\delta_h) \end{aligned}\right\}$	$-\frac{\pi}{2p} \le \theta \le -\frac{R_{mph}\pi}{2p}$
$\left.\begin{aligned} M_r &= \frac{B_{rs}}{\mu_0}\sin(\theta_{mh}-\theta+\delta_h) \\ M_\theta &= -\frac{B_{rs}}{\mu_0}\cos(\theta_{mh}-\theta+\delta_h) \end{aligned}\right\}$	$\frac{R_{mph}\pi}{2p} \le \theta \le \frac{\pi}{2p}$
$\left.\begin{aligned} M_r &= -\frac{B_{rs}}{\mu_0}\sin\left(\theta_{mh}+\theta-\frac{\pi}{p}+\delta_h\right) \\ M_\theta &= -\frac{B_{rs}}{\mu_0}\cos\left(\theta_{mh}+\theta-\frac{\pi}{p}+\delta_h\right) \end{aligned}\right\}$	$\frac{\pi}{2p} \le \theta \le \left(1-\frac{R_{mph}}{2}\right)\frac{\pi}{p}$
$\left.\begin{aligned} M_r &= -\frac{B_{rs}}{\mu_0}\sin\left(\theta_{mh}-\theta+\frac{\pi}{p}+\delta_h\right) \\ M_\theta &= \frac{B_{rs}}{\mu_0}\cos\left(\theta_{mh}-\theta+\frac{\pi}{p}+\delta_h\right) \end{aligned}\right\}$	$\left(1+\frac{R_{mph}}{2}\right)\frac{\pi}{p} \le \theta \le \frac{3\pi}{2p}$

According to Table I, the harmonic components of magnetization M_{rn} and $M_{\theta n}$ for each magnet segment can be deduced as:

(a) Mid-Magnet

$$M_{rn} = \frac{p}{\pi}\left\{\int_{-\frac{R_{mp}\pi}{2p}}^{\frac{R_{mp}\pi}{2p}}\left[\frac{B_{rm}}{\mu_0}\cos\theta\right]\cos \mathrm{n}p\theta\,\mathrm{d}\theta + \int_{\left(1-\frac{R_{mp}}{2}\right)\frac{\pi}{p}}^{\left(1+\frac{R_{mp}}{2}\right)\frac{\pi}{p}}\left[-\frac{B_{rm}}{\mu_0}\cos\left(\theta-\frac{\pi}{p}\right)\right]\cos \mathrm{n}p\theta\,\mathrm{d}\theta\right\} \tag{3.7}$$

and

$$M_{\theta n} = \frac{p}{\pi}\left\{\int_{-\frac{R_{mp}\pi}{2p}}^{\frac{R_{mp}\pi}{2p}}\left[-\frac{B_{rm}}{\mu_0}\sin\theta\right]\sin np\theta\mathrm{d}\theta + \int_{\left(1-\frac{R_{mp}}{2}\right)\frac{\pi}{p}}^{\left(1+\frac{R_{mp}}{2}\right)\frac{\pi}{p}}\left[\frac{B_{rm}}{\mu_0}\sin\left(\theta-\frac{\pi}{p}\right)\right]\sin np\theta\mathrm{d}\theta\right\} \tag{3.8}$$

(b) Side-Magnet

$$M_{rn} = \frac{p}{\pi}\left\{\int_{-\frac{R_{mph}\pi}{2p}}^{-\frac{R_{mp}\pi}{2p}}\left[\frac{B_{rs}}{\mu_0}\sin(\theta_m+\theta+\delta)\right]\cos np\theta\,d\theta\right.$$

$$+\int_{\frac{R_{mp}\pi}{2p}}^{\frac{R_{mph}\pi}{2p}}\left[\frac{B_{rs}}{\mu_0}\sin(\theta_m-\theta+\delta)\right]\cos np\theta\,d\theta$$

$$\left.+\int_{\left(1-\frac{R_{mp}}{2}\right)\frac{\pi}{p}}^{\left(1-\frac{R_{mph}}{2}\right)\frac{\pi}{p}}\left[-\frac{B_{rs}}{\mu_0}\sin\left(\theta_m+\theta-\frac{\pi}{p}+\delta\right)\right]\cos np\theta\,d\theta\right.$$

$$+\int_{\left(1+\frac{R_{mp}}{2}\right)\frac{\pi}{p}}^{\left(1+\frac{R_{\mathrm{mph}}}{2}\right)\frac{\pi}{p}}\left[-\frac{B_{rs}}{\mu_0}\sin\left(\theta_m-\theta+\frac{\pi}{p}+\delta\right)\right]\cos np\theta\,d\theta\Bigg\} \tag{3.9}$$

And

$$M_{\theta n}=\frac{p}{\pi}\Bigg\{\int_{-\frac{R_{mph}\pi}{2p}}^{-\frac{R_{mp}\pi}{2p}}\left[\frac{B_{rs}}{\mu_0}\cos(\theta_m+\theta+\delta)\right]\sin np\theta\,d\theta$$

$$+\int_{\frac{R_{mp}\pi}{2p}}^{\frac{R_{mph}\pi}{2p}}\left[-\frac{B_{rs}}{\mu_0}\cos(\theta_m-\theta+\delta)\right]\sin np\theta\,d\theta$$

$$+\int_{\left(1-\frac{R_{mp}}{2}\right)\frac{\pi}{p}}^{\left(1-\frac{R_{mph}}{2}\right)\frac{\pi}{p}}\left[-\frac{B_{rs}}{\mu_0}\cos\left(\theta_m+\theta-\frac{\pi}{p}+\delta\right)\right]\sin np\theta\,d\theta$$

$$+\int_{\left(1+\frac{R_{mp}}{2}\right)\frac{\pi}{p}}^{\left(1+\frac{R_{\mathrm{mph}}}{2}\right)\frac{\pi}{p}}\left[\frac{B_{rs}}{\mu_0}\cos\left(\theta_m-\theta+\frac{\pi}{p}+\delta\right)\right]\sin np\theta\,d\theta\Bigg\} \tag{3.10}$$

where

$$\delta=\frac{R_{mp}\pi}{2p}+\left(R_{mph}-R_{mp}\right)\frac{\pi}{4p} \tag{3.11}$$

(c) End Side-Magnet

(i). even-segment Halbach array

$$M_{rn}=\frac{p}{\pi}\Bigg\{\int_{-\frac{\pi}{2p}}^{-\frac{R_{mph}\pi}{2p}}\left[\frac{B_{rs}}{\mu_0}\sin\left(\theta+\frac{\pi}{2p}\right)\right]\cos np\theta\,d\theta$$

$$+\int_{\frac{R_{mph}\pi}{2p}}^{\left(1-\frac{R_{mph}}{2}\right)\frac{\pi}{p}}\left[-\frac{B_{rs}}{\mu_0}\sin\left(\theta-\frac{\pi}{2p}\right)\right]\cos np\theta\,d\theta$$

$$+\int_{\left(1+\frac{R_{mph}}{2}\right)\frac{\pi}{p}}^{\frac{3\pi}{2p}}\left[\frac{B_{rs}}{\mu_0}\sin\left(\theta-\frac{3\pi}{2p}\right)\right]\cos np\theta\,d\theta\Bigg\} \tag{3.12}$$

and,

$$M_{\theta n}=\frac{p}{\pi}\Bigg\{\int_{-\frac{\pi}{2p}}^{-\frac{R_{mph}\pi}{2p}}\left[\frac{B_{rs}}{\mu_0}\cos\left(\theta+\frac{\pi}{2p}\right)\right]\sin np\theta\,d\theta$$

$$+\int_{\frac{R_{mph}\pi}{2p}}^{\left(1-\frac{R_{mph}}{2}\right)\frac{\pi}{p}}\left[-\frac{B_{rs}}{\mu_0}\cos\left(\theta-\frac{\pi}{2p}\right)\right]\sin np\theta\,d\theta$$

$$+\int_{\left(1+\frac{R_{mph}}{2}\right)\frac{\pi}{p}}^{\frac{3\pi}{2p}}\left[\frac{B_{rs}}{\mu_0}\cos\left(\theta-\frac{3\pi}{2p}\right)\right]\sin np\theta\,d\theta\Bigg\} \tag{3.13}$$

(ii). odd-segment Halbach array

$$M_{rn}=\frac{p}{\pi}\Bigg\{\int_{-\frac{\pi}{2p}}^{-\frac{R_{mph}\pi}{2p}}\left[\frac{B_{rs}}{\mu_0}\sin(\theta_{mh}+\theta+\delta_h)\right]\cos np\theta\,d\theta$$

$$+\int_{\frac{R_{mph}\pi}{2p}}^{\frac{\pi}{2p}}\left[\frac{B_{rs}}{\mu_0}\sin(\theta_{mh}-\theta+\delta_h)\right]\cos np\theta\,d\theta$$

$$+\int_{\frac{\pi}{2p}}^{\left(1-\frac{R_{mph}}{2}\right)\frac{\pi}{p}}\left[-\frac{B_{rs}}{\mu_0}\sin\left(\theta_{mh}+\theta-\frac{\pi}{p}+\delta_h\right)\right]\cos np\theta\,d\theta$$

$$+\int_{\left(1+\frac{R_{mph}}{2}\right)\frac{\pi}{p}}^{\frac{3\pi}{2p}}\left[-\frac{B_{rs}}{\mu_0}\sin\left(\theta_{mh}-\theta+\frac{\pi}{p}+\delta_h\right)\right]\cos np\theta\,d\theta\Bigg\} \tag{3.14}$$

and

$$M_{\theta n}=\frac{p}{\pi}\Bigg\{\int_{-\frac{\pi}{2p}}^{-\frac{R_{mph}\pi}{2p}}\left[\frac{B_{rs}}{\mu_0}\cos(\theta_{mh}+\theta+\delta_h)\right]\sin np\theta\,d\theta$$

$$+\int_{\frac{R_{mph}\pi}{2p}}^{\frac{\pi}{2p}}\left[-\frac{B_{rs}}{\mu_0}\cos(\theta_{mh}-\theta+\delta_h)\right]\sin np\theta\,d\theta$$

$$+\int_{\frac{\pi}{2p}}^{\left(1-\frac{R_{mph}}{2}\right)\frac{\pi}{p}}\left[-\frac{B_{rs}}{\mu_0}\cos\left(\theta_{mh}+\theta-\frac{\pi}{p}+\delta_h\right)\right]\sin np\theta\,d\theta$$

$$+\int_{\left(1+\frac{R_{mph}}{2}\right)\frac{\pi}{p}}^{\frac{3\pi}{2p}}\left[\frac{B_{rs}}{\mu_0}\cos\left(\theta_{mh}-\theta+\frac{\pi}{p}+\delta_h\right)\right]\sin np\theta\,d\theta\Bigg\} \tag{3.15}$$

where, p is the number of pole pairs, n is the harmonic order,

$$\delta_h=\frac{R_{mph}\pi}{2p}+\left(1-R_{mph}\right)\frac{\pi}{4p} \tag{3.16}$$

The fully deduced general analytical models of M_{rn} and $M_{\theta n}$ for all magnet segments are given in (3.25)-(3.32) in the Appendix of this chapter. Therefore, the overall magnetization components for either even or odd-segment Halbach array can be calculated by using the foregoing derived expressions of the magnet segment. Further, in order to simplify the programming processes, the overall analytical expression for any variation of even and odd-segment Halbach array can be obtained very easily by using the superposition theory for above equations (3.7)-(3.16) with appropriate rotor position for each magnet segment.

In the SD model, the assumptions such as infinite permeable iron, linear magnet property, and negligible end-effect are usually made in order to simplify the problem. Meanwhile, the stator tooth-tip is also simplified to be straight as illustrated in Fig.3.6. The air-gap flux density distribution with the consideration of stator slotting effect is given by

$$B_{rSD} = B_{rn} - \sum_{k} g_{B_r} A_{stator} \cos k\alpha - \sum_{k} g_{B_r} B_{stator} \sin k\alpha \tag{3.17}$$

$$B_{\theta SD} = B_{\theta n} - \sum_{k} g_{B_\theta} B_{stator} \cos k\alpha + \sum_{k} g_{B_\theta} A_{stator} \sin k\alpha \tag{3.18}$$

where α is the circumferential position in stator axis (Fig. 3.5), g_{Br} and $g_{B\theta}$ are the coefficients of scalar potential distribution along the slot opening, B_{rn} and $B_{\theta n}$ are the radial and circumferential flux density components. On the other hand, A_{stator} and B_{stator} are the coefficients of the scalar potential on the surface of the stator bore which is written as:

$$A_{stator}(k) = \sum_{i=1}^{N_s} \sum_{n=1}^{n_{max}} C_{ei}(n) \eta_{si}(n.k) \tag{3.19}$$

$$B_{stator}(k) = \sum_{i=1}^{N_s} \sum_{n=1}^{n_{max}} C_{ei}(n) \xi_{si}(n.k) \tag{3.20}$$

where k is defined as harmonic order, $C_{ei}(n)$ is the n^{th} order harmonic of the scalar potential distribution which corresponds with the i^{th} slot opening. It should be noted that those two coefficients in (3.19) and (3.20) can be described as a function of the proposed general analytical model of the magnetization components of M_{rn} and $M_{\theta n}$ in (3.7)-(3.16). All the fully deduced expressions of the coefficients $C_{ei}(n)$, η_{si} and ξ_{si} can be found in APPENDIX III.

Moreover, the phase flux-linkage is calculated by assuming the armature coil to be a current sheet along the inner stator bore. Therefore, it is deduced by integrating the radial flux density distribution as:

$$\psi_{ph} = l_a(D_{ro} + 2l_g)N \sum_k \frac{1}{k} K_p K_{so}\left(b_{rs}K_{dsph} + b_{rc}K_{dcph}\right) cos(np\omega_r t) \tag{3.21}$$

where ph = A, B, C, b_{rs} and b_{rc} are the sine and cosine harmonic components of radial flux density distribution along the stator bore, K_p, K_{dsph} and K_{dcph} are the pitch and distribution factors of given phase for the sine and cosine flux density harmonic components, respectively. Consequently, the phase back-EMF is written as

$$E_{ph} = -\frac{d\psi_{ph}}{dt} \tag{3.22}$$

Meanwhile, the electromagnetic torque can be predicted by

$$T_{em} = \frac{(E_A I_A + E_B I_B + E_C I_C)}{\omega_r} \tag{3.23}$$

where ω_r is the mechanical rotational speed. In addition, by using the Maxwell stress tensor, the cogging torque can be predicted as:

$$T_{cog} = \frac{l_a r^2}{\mu_0} \int_0^{2\pi} B_{rSD} B_{\theta SD} d\alpha \tag{3.24}$$

where l_a is the axial stack length of the machine.

3.3 Finite-Element Validation

The linear FEA validation is carried out on a 12-slot/10-pole PM brushless machine having 2, 3, 4, and 5-segment Halbach arrays to testify the feasibility of proposed general analytical model for the Halbach machine. Meanwhile, the capability of the proposed general analytical model to analyse the mixed magnet grade, pole-arc to pole-pitch ratio less than one, slotless model and external rotor are also validated individually for the cases of different Halbach arrays. The design parameters for 2, 3, 4, and 5-segment Halbach arrays over one pole pair, together with the parameters for prototype machine are illustrated in Fig.3.5 and Fig.3.6, respectively, whose detailed values are given in TABLE 3-II.

It should be noted that the straight stator tooth-tips is applied to the linear FEA model which is consistent with the foregoing proposed general analytical model.

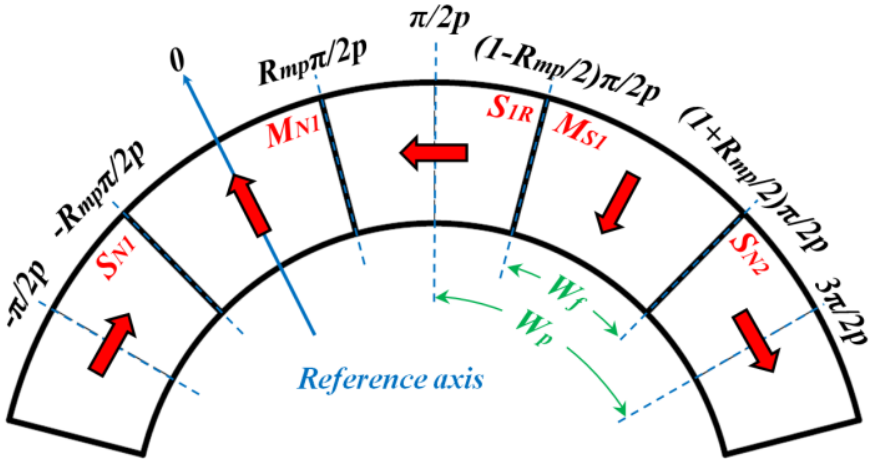

(a) 2-segment Halbach array

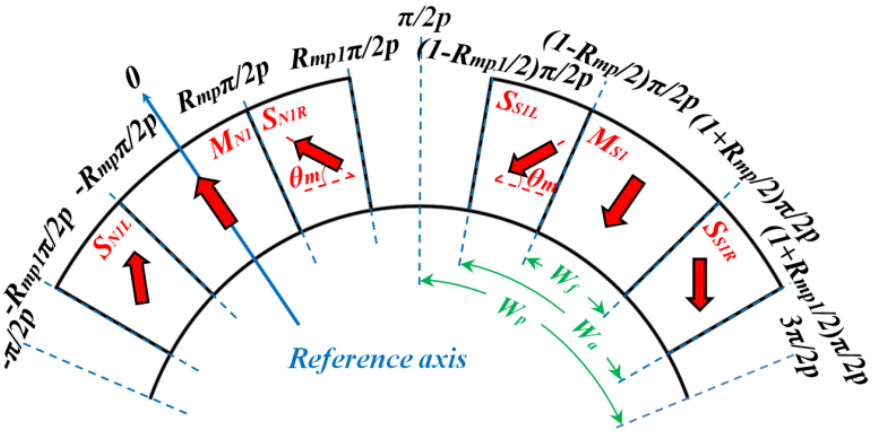

(b) 3-segment Halbach array

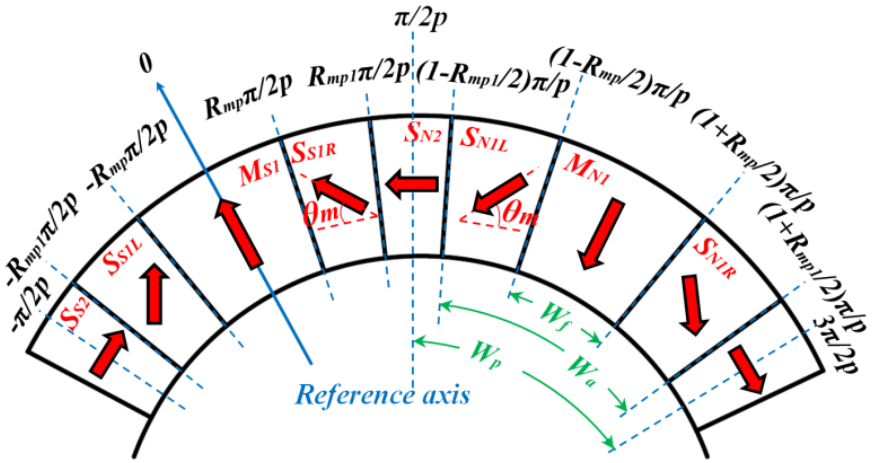

(c) 4-segment Halbach array

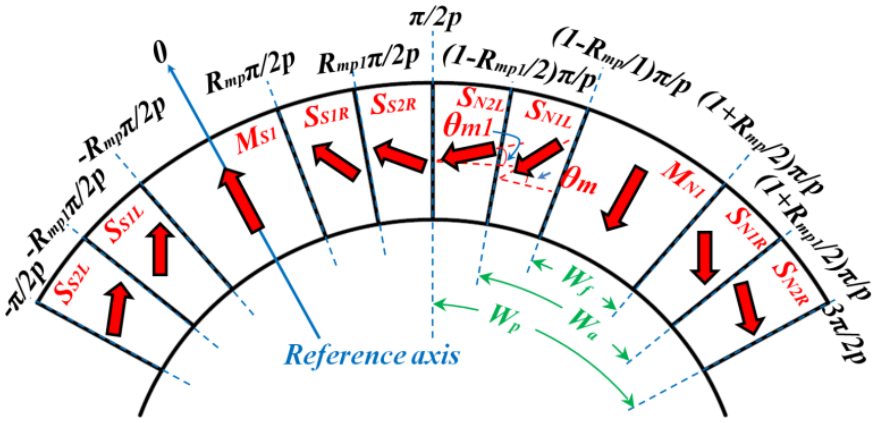

(d) 5-segment Halbach array

Fig.3.5. Design parameters for 2, 3, 4, and 5-segment Halbach array over one pole pair.

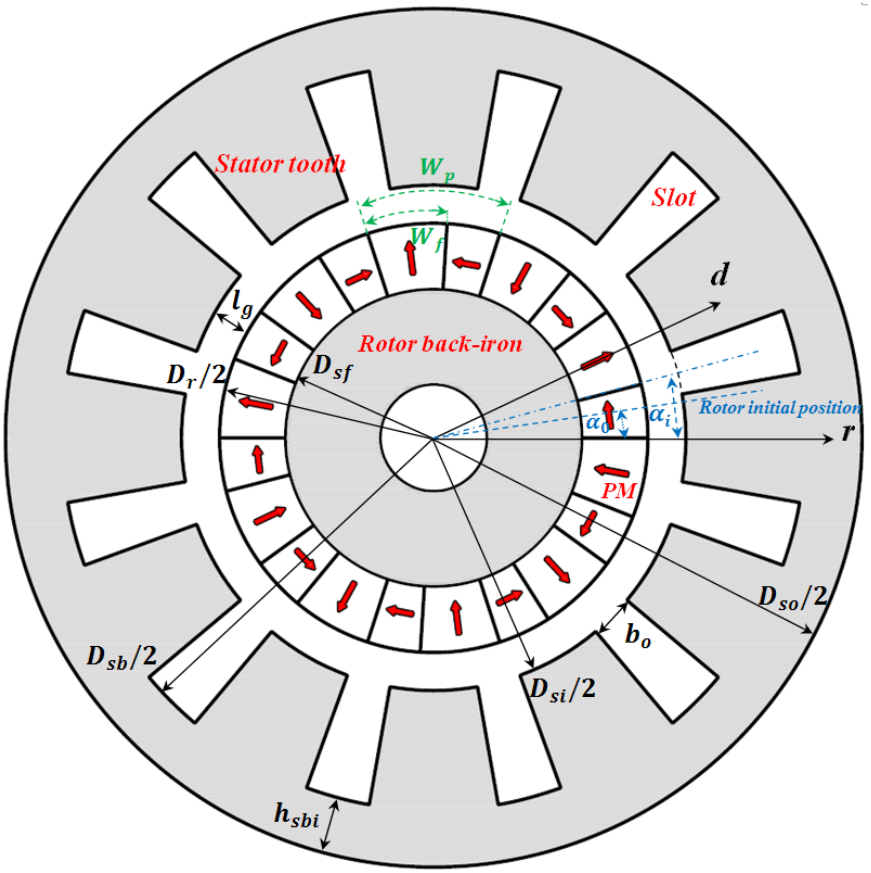

Fig.3.6. Symbols and cross-section of PM brushless machine having Halbach array.

TABLE 3-II MACHINES DESIGN PARAMETERS (DEFAULT UNIT: MM)

Rated speed, *rpm*	400	Slot opening, b_o	2.0
Pole number, $2p$	10	Air-gap length, l_g	1.0
Stator slot number, N_s	12	Active length, l_a	50
Tooth-tip height, h_t	1.5	Stator back-iron thickness, h_{sbi}	3.7
Tooth body width, b_t	-	Stator outer diameter, D_{so}	100

Stator inner diameter, D_{si}	57	Rotor outer diameter, D_{ro}	55
Rotor inner diameter, D_{ri}	49	Shaft diameter, D_{sf}	34
No. of series turns per phase, N	132	Peak phase current, I (A)	10
Relative recoil permeability, μ_r	1.05	Magnet height, h_{pm} (mm)	3
2-segment Halbach array			
Conventional		*Modular*	
Mid-magnet B_{rm} (T)	1.2	Mid-magnet B_{rm} (T)	1.2
Side-magnet B_{rs} (T)	1.2	Side-magnet B_{rs} (T)	0.4
Magnet ratio, R_{mp}	0.6	Magnet ratio, R_{mp}	0.6
Magnetization angle, θ_m	0	Magnetization angle, θ_m	0
3-segment Halbach array			
Magnet ratio, R_{mp}	0.4	Magnet ratio, R_{mp1}	0.76
Magnetization angle, θ_m	45	B_{rm} and B_{rs} (T)	1.2
4-segment Halbach array			
Magnet ratio, R_{mp}	0.4	Magnet ratio, R_{mp1}	0.76
Magnetization angle, θ_m	45	Magnetization angle, θ_m	0
B_{rm} and B_{rs} (T)	1.2		
5-segment Halbach array			
Rotor outer diameter, D_{ro}	61	Rotor back-iron thickness, h_{rbi}	3
Stator back-iron thickness, h_{sbi}	6.5	Magnet thickness, h_{pm}	3
B_{rm} and B_{rs} (T)	1.2	Air-gap length, l_g	1
Magnet ratio, R_{mp}	0.5	Magnet ratio, R_{mp1}	0.7
Magnetization angle, θ_m	60	Magnetization angle, θ_m	30

3.3.1 2-Segment Halbach Array

In contrast to the magnet pole having uniform magnet material which is named as the conventional Halbach array, the magnet pole having modular pole technique by means of mixed grade magnets becomes increasingly popular due to cost-effective design. In this section, the analytically and FEA predicted radial (B_{agr}) and circumferential (B_{agc}) air-gap flux density distributions, phase back-EMF, electromagnetic torque (it is obtained by subtracting the cogging torque from the output torque in FEA) and cogging torque waveforms are compared in Fig.3.7-Fig.3.11.

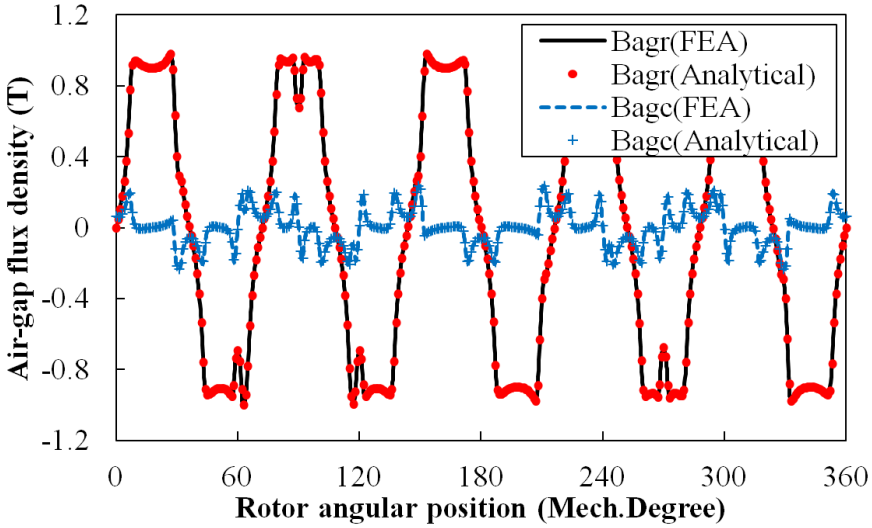

(a) Conventional

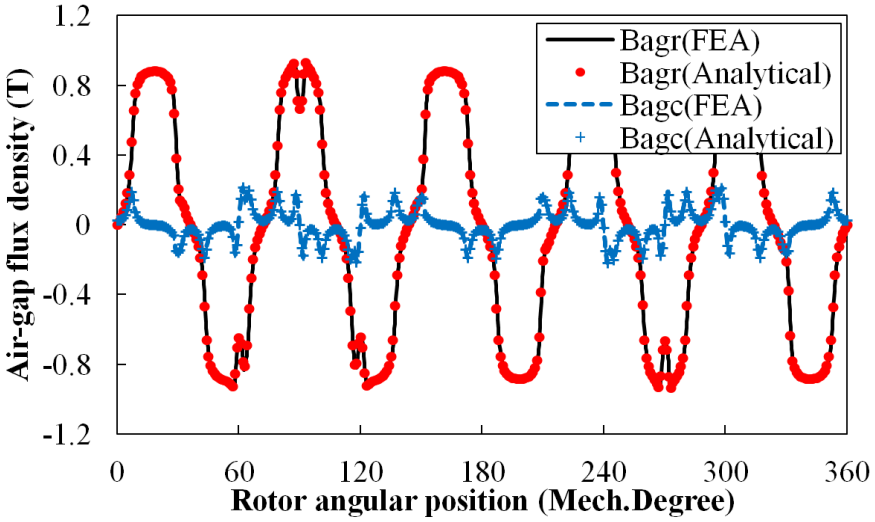

(b) Modular

Fig.3.7. Comparison of analytically and FEA predicted air-gap flux density for 12-slot/10-pole PM brushless machine having 2-segment Halbach array with both conventional and modular poles.

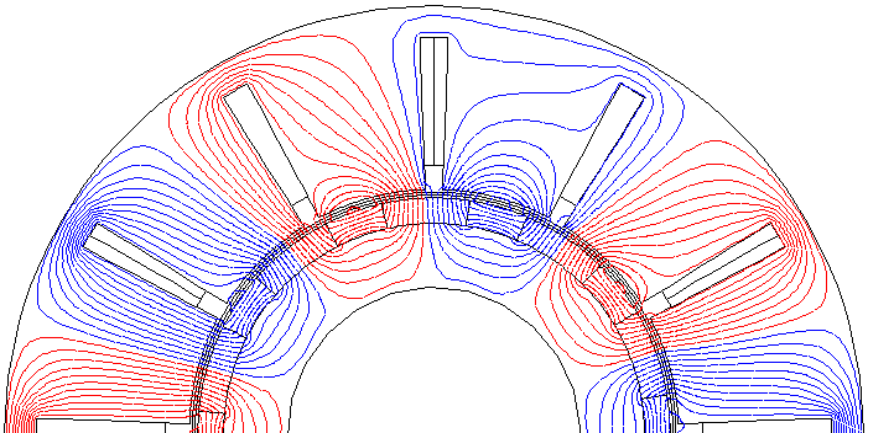

(a) Conventional

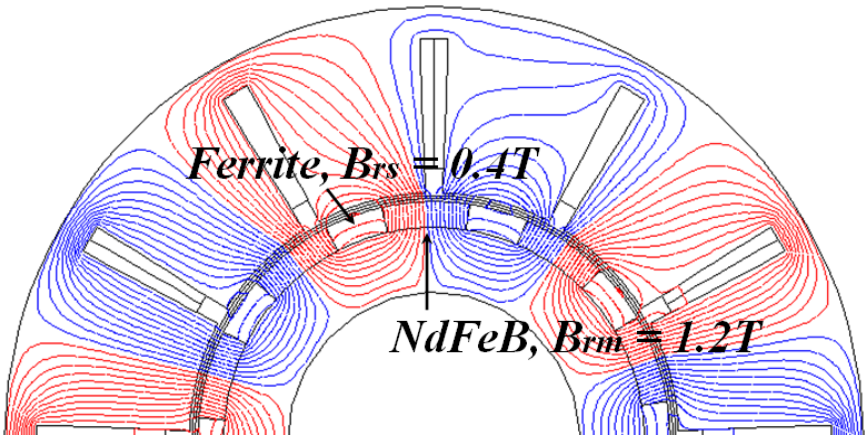

(b) Modular

Fig.3.8. FEA predicted vector potential distributions for 12-slot/10-pole PM brushless machine having 2-segment Halbach array with both conventional and modular poles.

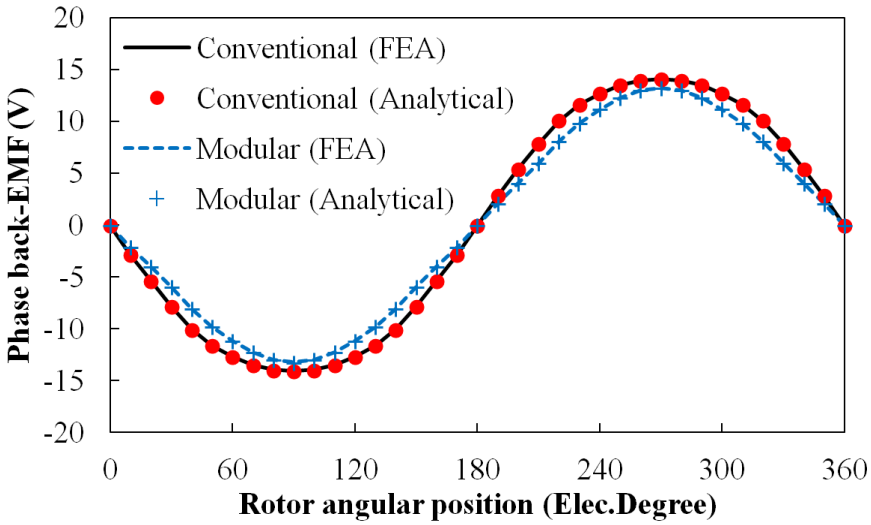

Fig.3.9. Comparison of analytically and FEA predicted phase back-EMF waveforms for 12-slot/10-pole PM brushless machine having 2-segment Halbach array with both conventional and modular poles at 400 rpm.

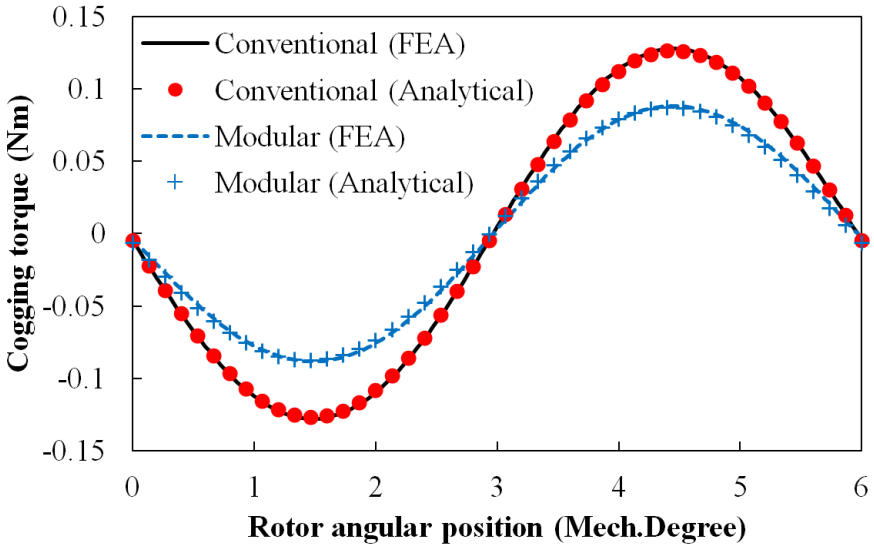

Fig.3.10. Comparison of analytically and FEA predicted cogging torque waveforms for 12-slot/10-pole PM brushless machine having 2-segment Halbach array with both conventional and modular poles.

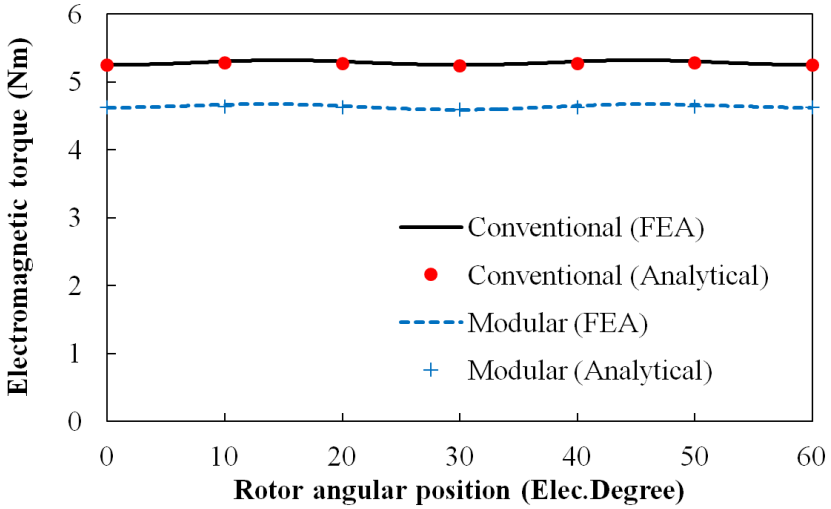

Fig.3.11. Comparison of analytically and FEA predicted electromagnetic torque waveforms for 12-slot/10-pole PM brushless machine having 2-segment Halbach with both conventional and modular poles.

3.3.2 3-Segment Halbach Array

In this section, the analytically predicted air-gap flux density distributions for the prototype machine having 3-segment Halbach array, together with pole-arc to pole-pitch ratio less than one are compared with FEA in Fig.3.12, where excellent agreement is achieved. The FEA predicted vector potential distribution is shown in Fig.3.13. In order to save the space, the validations of phase back-EMF, cogging torque and electromagnetic torque are not included here, as well as in the rest of this chapter, since their waveforms directly depend on the

accuracy of air-gap flux density predictions.

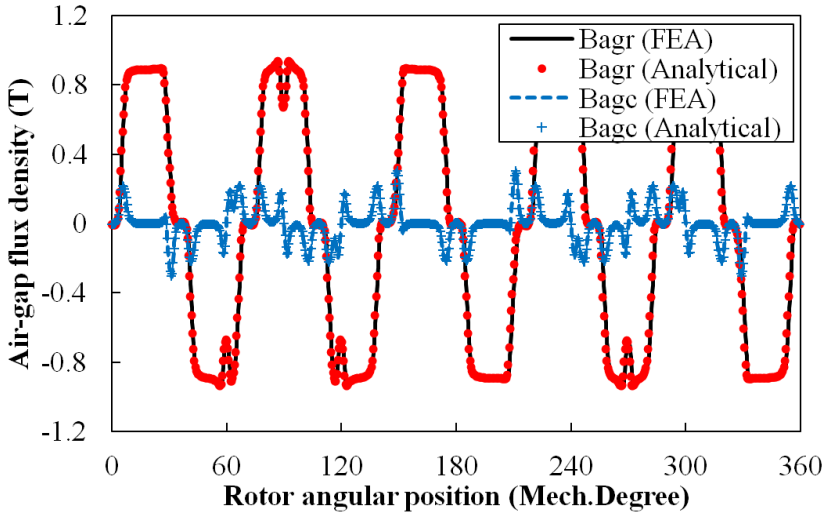

Fig.3.12.. Comparison of analytically and FEA predicted air-gap flux density for 12-slot/10-pole PM brushless machine having 3-segment Halbach array with pole-arc to pole-pitch ratio less than one.

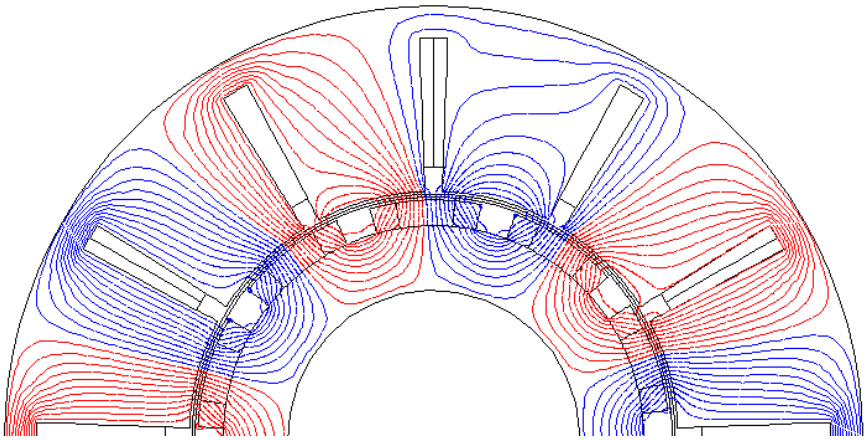

Fig.3.13. FEA predicted vector potential distribution for 12-slot/10-pole PM brushless machine having 3-segment Halbach array with pole-arc to pole-pitch ratio less than one.

3.3.3 4-Segment Halbach Array

Since Halbach array has been extensively applied for slotless machine and magnet cylinder, thus the capability of proposed general analytical model to analyze such machine is examined by simply using a Halbach cylinder, in Fig.3.14. It can be observed that the analytically deduced air-gap flux density distributions agree very well with FEA, while the FEA predicted equal-potential distribution is shown in Fig.3.15.

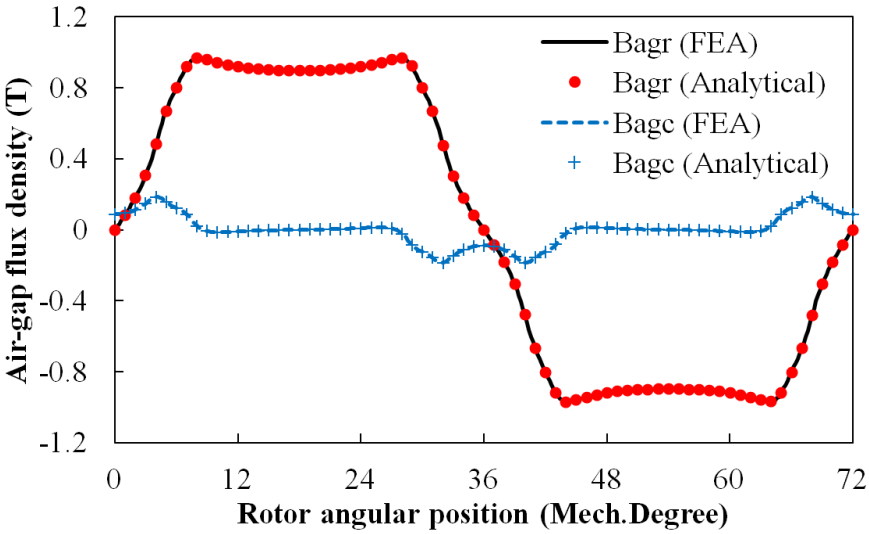

Fig.3.14. Comparison of analytically and FEA predicted air-gap flux density for 12-slot/10pole PM slotless machine having 4-segment Halbach array.

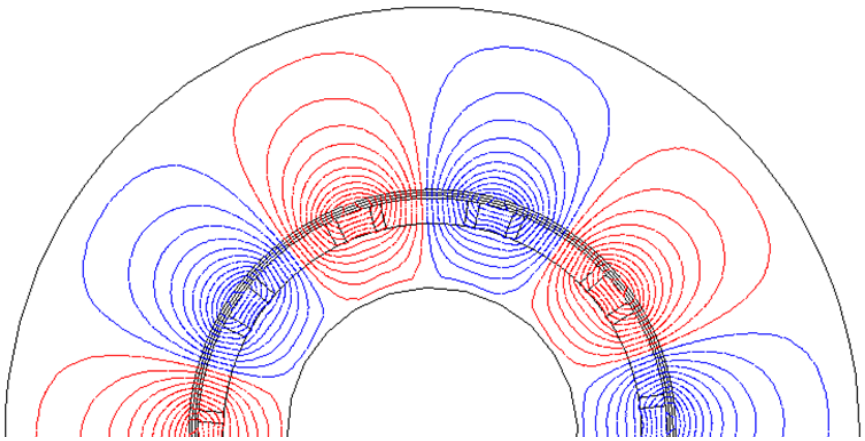

Fig.3.15. FEA predicted vector potential distribution for 12-slot/10-pole PM slotless machine having 4-segment Halbach array.

3.3.4 5-Segment Halbach Array

In this section, an external rotor magnet cylinder having 5-segment Halbach array is modeled, where excellent agreement between analytically and FEA predicted air-gap flux density waveforms is also achieved, Fig.3.16. The FEA predicted equal-potential distribution is shown in Fig.3.17.

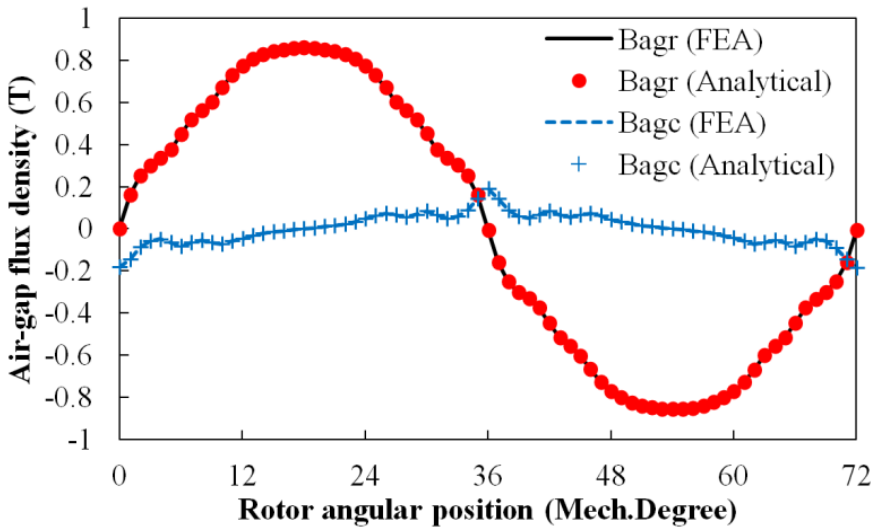

Fig.3.16. Comparison of analytically and FEA predicted air-gap flux density for external rotor magnet cylinder having 5-segment Halbach array.

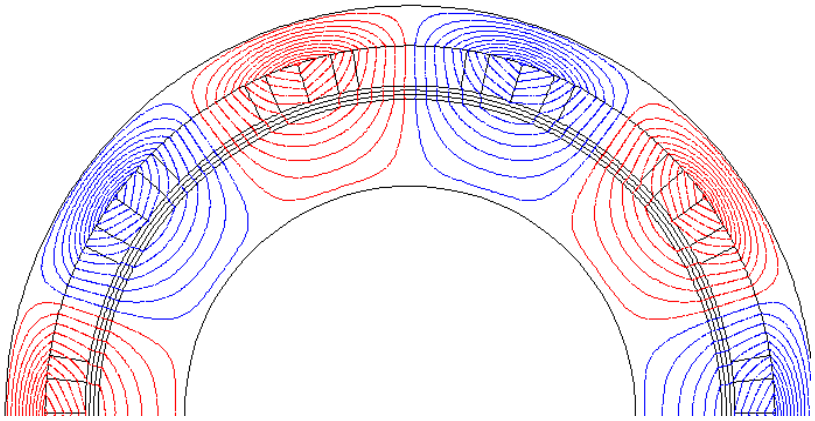

Fig.3.17. FEA predicted vector potential distribution for external rotor magnet cylinder having 5-segment Halbach array.

3.4 Investigation Based on General Analytical Model

3.4.1 Curvature Effect in 2- and 3-Segment Halbach Array

For given design parameters, e.g. D_{ro} = 55 mm and l_g = 1 mm, the optimal magnet pole pair due to curvature effect for 2- and 3-segment Halbach arrays can be obtained by globally optimizing (by scanning all target design parameters to obtain the highest electromagnetic torque) the magnet ratio R_{mp} and magnetization angle θ_m under different magnet thickness conditions with the proposed general analytical model. As can be seen in Fig.3.18(a), the 3-segment Halbach array exhibits significant higher B_{ag1} (fundamental air-gap flux density) than the magnet cylinder having conventional pole and 2-segment Halbach array. This phenomenon can be explained by adopting the well-known equation (1.2) where the incremental of effective magnet length l_m directly reflects the result of improved self-

shielding performance. Meanwhile, since the amplitude of B_{ag1} depends on flux focusing effect, the optimal pole-width to magnet thickness ratio (the relation between pole pair number and magnet thickness) is existed. Further, according to the air-gap length is fixed, the higher the rotor pole pair number, the larger the inter-pole leakage flux will be obtained. Thus, those effects results in an overall optimal pole pair number for a given Halbach segmentation numbers and magnet thickness. Further, the THD values are shown in Fig.3.18 and the corresponding optimized design parameters for the 3-segment Halbach array are highlighted as an example where their variations with magnet thickness is due to different magnet height-to-width ratios.

Since the self-shielding and flux focusing performance are directly related with the number of Halbach segmentation, hence there exists no optimal number of segmentation if only the improvement of electromagnetic performance is considered. However, there exists an optimal cost-effective design if the manufacturing cost is considered which increases proportionally to the segmentation number.

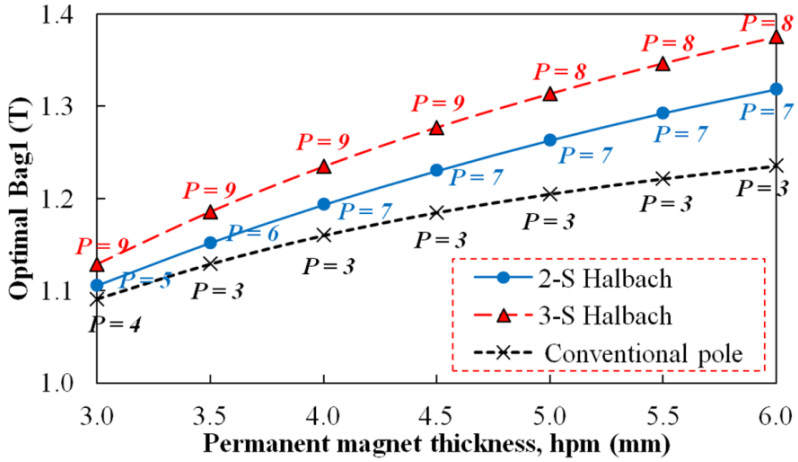

(a) Optimal B_{ag1}

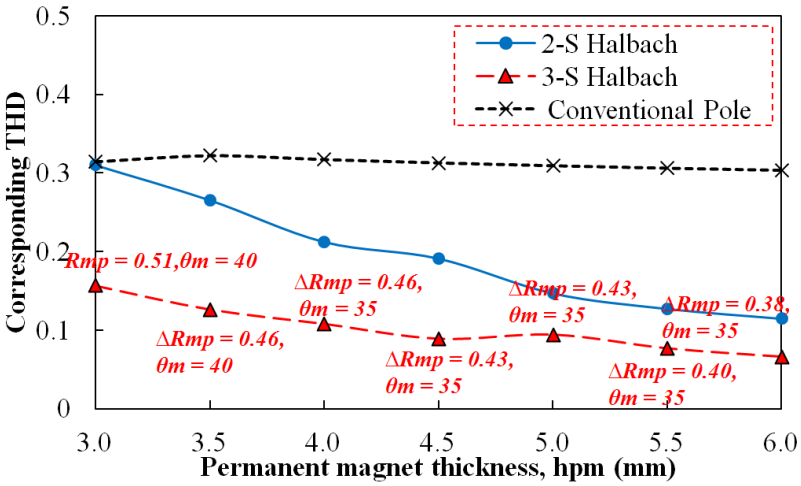

(b) Corresponding THD

Fig.3.18. Comparison of globally optimized conventional magnet cylinder, 2- and 3-segment Halbach magnet cylinders.

3.4.2 Performance Analysis for 3-Phase 12-Slot Machines Having 2-Segment Halbach Array

The proposed general analytical model can be also used for performance analysis and design parameter optimization. In this case, the performance analysis of a 3-phase 12-slot PM brushless machine having 2-segment Halbach array are compared when the number of poles is 8, 10 and 14 with the design parameters shown in Table III. The rotor design parameters are globally optimized using genetic algorithm with due account for the slotting effect in Fig.3.19, where p = 5 exhibit the largest B_{ag1}. There is an optimal pole pitch for a given rotor geometry (rotor outer diameter, magnet thickness, and air-gap length) to achieve maximum fundamental air-gap flux density due to curvature effect (for parallel magnetized magnet pole). Moreover, the phase back-EMF, cogging torque and electromagnetic torque waveforms are compared in Fig.3.20. It reveals that the 3-phase 12-slot/10-pole PM brushless machine having 2-segment Halbach array can obtain higher electromagnetic torque and lower torque ripples, while easier to be manufactured.

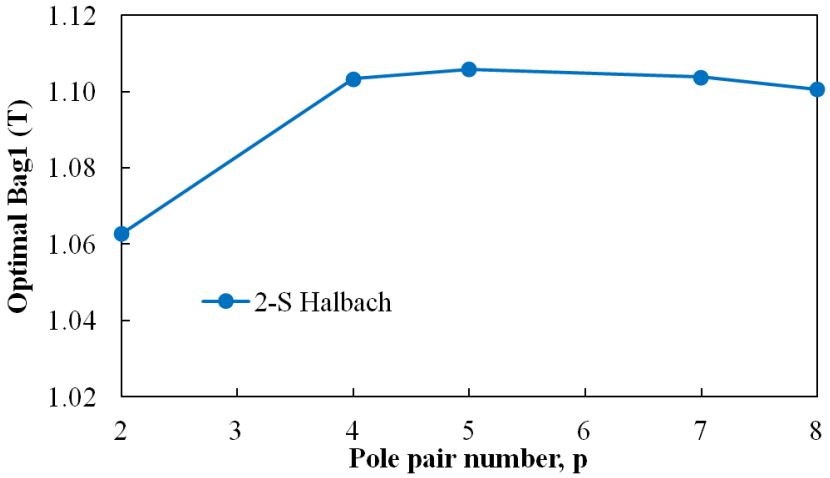

Fig.3.19. Globally optimized rotor design parameters for 3-phase 12-slot machines having 2-segment Halbach array.

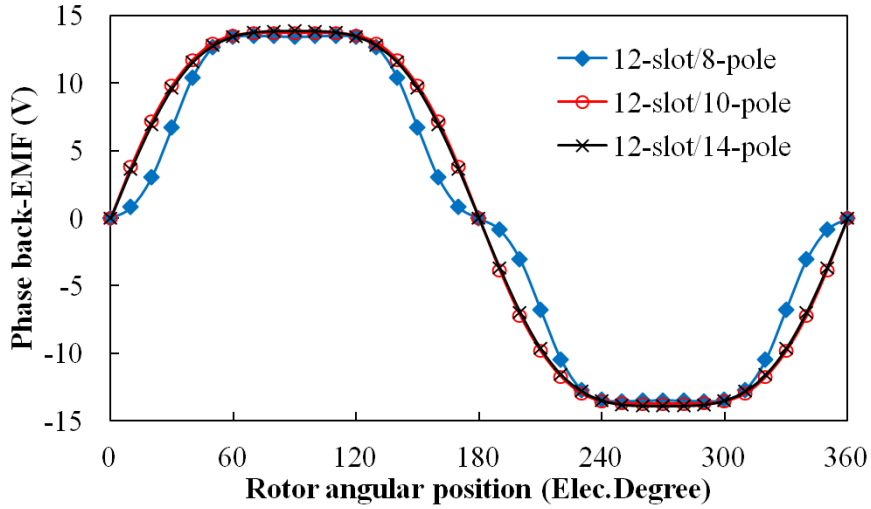

(a) Phase back-EMF, 400 rpm

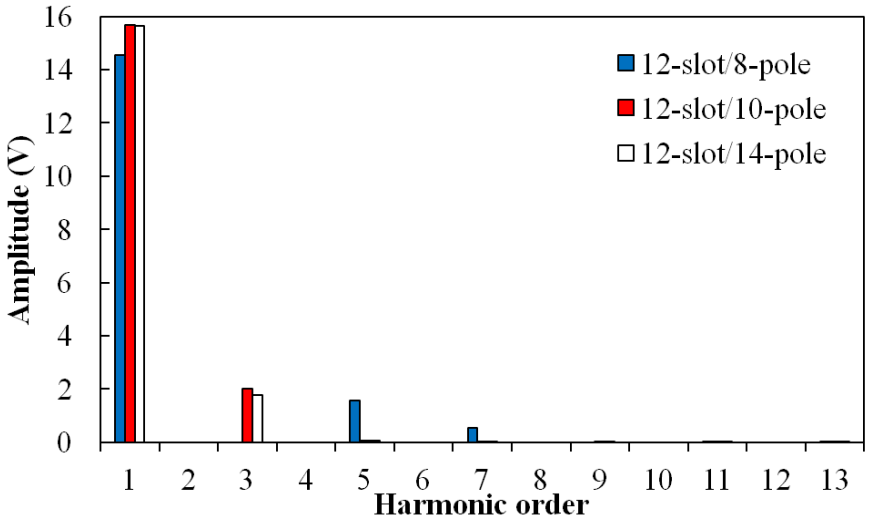

(b) Spectra of phase back-EMF

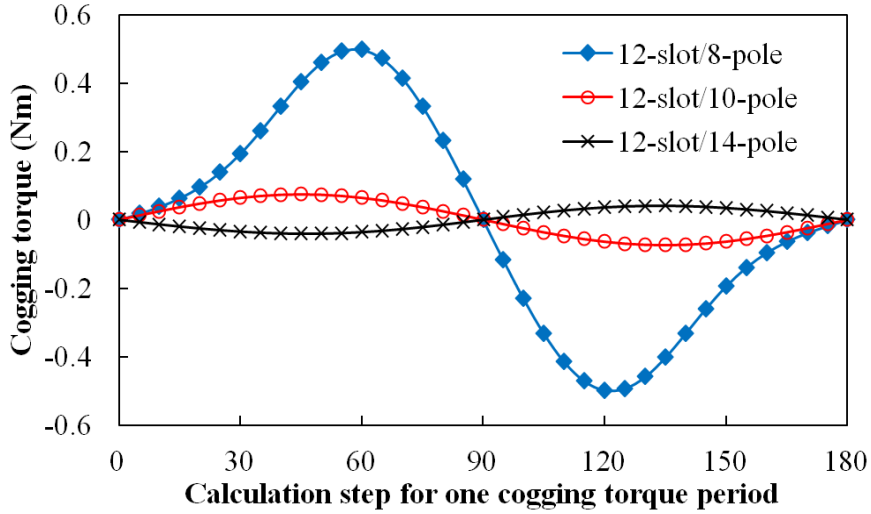

(c) Cogging torque

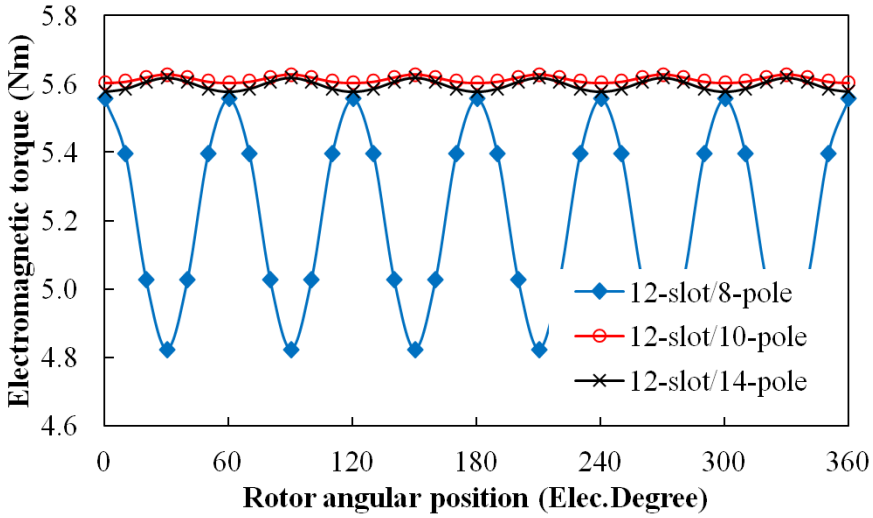

(d) Electromagnetic torque

Fig.3.20. Comparison of electromagnetic performances of 3-phase 12-slot/8-pole, 12-slot/10-pole and 12-slot/14-pole PM brushless machines having globally optimized 2-segment Halbach arrays.

3.5 Summary

This chapter has developed a general analytical model which is capable of predicting the electromagnetic performance for slotted/slotless permanent magnet brushless machines with both even- and odd-segment Halbach array, having different magnet remanence, magnetization angle and arc for each single magnet segment. The proposed general analytical model is validated by the finite-element analyses, while the accuracy of model adopting slotted/ slotless, internal/external rotor, pole-arc to pole-pitch ratio less than one and mixed magnet grade are also examined. Application examples for global optimization and comparative study by utilizing the proposed general analytical model are illustrated. The proposed analytical model is used for initial design. Then, the FEA is applied for further design adjustment if other requirements are needed, e.g. self-demagnetization withstand capability. It should be noted that the self-demagnetization is not considered in this chapter.

3.6 Appendix

The magnetization vectors in (3.7)-(3.15) are fully deduced and summarized in (3.25)-(3.32) as follows:

(a) Mid-Segment

$$M_{rn} = \frac{p}{\pi}\left\{\int_{-\frac{R_{mp}\pi}{2p}}^{\frac{R_{mp}\pi}{2p}}\left[\frac{B_{rm}}{\mu_0}\cos\theta\right]\cos np\theta\, d\theta + \int_{\left(1-\frac{R_{mp}}{2}\right)\frac{\pi}{p}}^{\left(1+\frac{R_{mp}}{2}\right)\frac{\pi}{p}}\left[-\frac{B_{rm}}{\mu_0}\cos\left(\theta-\frac{\pi}{p}\right)\right]\cos np\theta\, d\theta\right\}$$

$$= \frac{p}{\pi}\left\{\frac{B_{rm}}{2\mu_0}\left[\frac{\sin\left[(1+np)\frac{R_{mp}\pi}{2p}\right]}{1+np} - \frac{\sin\left[(1+np)\left(-\frac{R_{mp}\pi}{2p}\right)\right]}{1+np} + \right.\right.$$

$$\left.\frac{\sin\left[(1-np)\frac{R_{mp}\pi}{2p}\right]}{1-np} - \frac{\sin\left[(1-np)\left(-\frac{R_{mp}\pi}{2p}\right)\right]}{1-np}\right] -$$

$$\frac{B_{rm}}{2\mu_0}\left[\frac{\sin\left[(1+np)\left(1+\frac{R_{mp}}{2}\right)\frac{\pi}{p}-\frac{\pi}{p}\right]}{1+np} - \frac{\sin\left[(1+np)\left(1-\frac{R_{mp}}{2}\right)\frac{\pi}{p}-\frac{\pi}{p}\right]}{1+np} + \right.$$

$$\left.\left.\frac{\sin\left[(1-np)\left(1+\frac{R_{mp}}{2}\right)\frac{\pi}{p}-\frac{\pi}{p}\right]}{1-np} - \frac{\sin\left[(1-np)\left(1-\frac{R_{mp}}{2}\right)\frac{\pi}{p}-\frac{\pi}{p}\right]}{1-np}\right]\right\} \qquad (3.25)$$

and

$$M_{\theta n} = \frac{p}{\pi}\left\{\int_{-\frac{R_{mp}\pi}{2p}}^{\frac{R_{mp}\pi}{2p}}\left[-\frac{B_{rm}}{\mu_0}\sin\theta\right]\sin np\theta d\theta + \int_{\left(1-\frac{R_{mp}}{2}\right)\frac{\pi}{p}}^{\left(1+\frac{R_{mp}}{2}\right)\frac{\pi}{p}}\left[\frac{B_{rm}}{\mu_0}\sin\left(\theta-\frac{\pi}{p}\right)\right]\sin np\theta d\theta\right\}$$

$$= \frac{p}{\pi}\left\{\frac{B_{rm}}{2\mu_0}\left[\frac{\sin\left[(1+np)\frac{R_{mp}\pi}{2p}\right]}{1+np} - \frac{\sin\left[(1+np)\left(-\frac{R_{mp}\pi}{2p}\right)\right]}{1+np} - \right.\right.$$

$$\left.\frac{\sin\left[(1-np)\frac{R_{mp}\pi}{2p}\right]}{1-np} + \frac{\sin\left[(1-np)\left(-\frac{R_{mp}\pi}{2p}\right)\right]}{1-np}\right] -$$

$$\frac{B_{rm}}{2\mu_0}\left[\frac{\sin\left[(1+np)\left(1+\frac{R_{mp}}{2}\right)\frac{\pi}{p}-\frac{\pi}{p}\right]}{1+np} - \frac{\sin\left[(1+np)\left(1-\frac{R_{mp}}{2}\right)\frac{\pi}{p}-\frac{\pi}{p}\right]}{1+np} - \right.$$

$$\left.\left.\frac{\sin\left[(1-np)\left(1+\frac{R_{mp}}{2}\right)\frac{\pi}{p}-\frac{\pi}{p}\right]}{1-np} + \frac{\sin\left[(1-np)\left(1-\frac{R_{mp}}{2}\right)\frac{\pi}{p}-\frac{\pi}{p}\right]}{1-np}\right]\right\} \qquad (3.26)$$

(b) Side-Magnet

$$M_{rn} = \frac{p}{\pi}\left\{-\frac{B_{rs}}{2\mu_0}\cos\theta_m\left[\frac{\cos\left[(1+np)\left(-\frac{R_{mp}\pi}{2p}\right)+\delta\right]}{1+np} - \frac{\cos\left[(1+np)\left(-\frac{R_{mph}\pi}{2p}\right)+\delta\right]}{1+np}\right.\right.$$

$$+\frac{\cos\left[(1-np)\left(-\frac{R_{mp}\pi}{2p}\right)+\delta\right]}{1-np}-\frac{\cos\left[(1-np)\left(-\frac{R_{mph}\pi}{2p}\right)+\delta\right]}{1-np}\Bigg]+$$

$$\frac{B_{rs}}{2\mu_0}\cos\theta_m\left[\frac{\cos\left[(1+np)\frac{R_{mph}\pi}{2p}-\delta\right]}{1+np}-\frac{\cos\left[(1+np)\frac{R_{mp}\pi}{2p}-\delta\right]}{1+np}+\right.$$

$$\left.\frac{\cos\left[(1-np)\frac{R_{mph}\pi}{2p}-\delta\right]}{1-np}-\frac{\cos\left[(1-np)\frac{R_{mp}\pi}{2p}-\delta\right]}{1-np}\right]+$$

$$\frac{B_{rs}}{2\mu_0}\cos\theta_m\left[\frac{\cos\left[(1+np)\left(1-\frac{R_{mp}}{2}\right)\frac{\pi}{p}-\frac{\pi}{p}+\delta\right]}{1+np}-\frac{\cos\left[(1+np)\left(1-\frac{R_{mph}}{2}\right)\frac{\pi}{p}-\frac{\pi}{p}+\delta\right]}{1+np}+\right.$$

$$\left.\frac{\cos\left[(1-np)\left(1-\frac{R_{mp}}{2}\right)\frac{\pi}{p}-\frac{\pi}{p}+\delta\right]}{1-np}-\frac{\cos\left[(1-np)\left(1-\frac{R_{mph}}{2}\right)\frac{\pi}{p}-\frac{\pi}{p}+\delta\right]}{1-np}\right]-$$

$$\frac{B_{rs}}{2\mu_0}\cos\theta_m\left[\frac{\cos\left[(1+np)\left(1+\frac{R_{mph}}{2}\right)\frac{\pi}{p}-\frac{\pi}{p}-\delta\right]}{1+np}-\frac{\cos\left[(1+np)\left(1+\frac{R_{mp}}{2}\right)\frac{\pi}{p}-\frac{\pi}{p}-\delta\right]}{1+np}\right.$$

$$+$$

$$\left.\left.\frac{\cos\left[(1-np)\left(1+\frac{R_{mph}}{2}\right)\frac{\pi}{p}-\frac{\pi}{p}-\delta\right]}{1-np}-\frac{\cos\left[(1-np)\left(1+\frac{R_{mp}}{2}\right)\frac{\pi}{p}-\frac{\pi}{p}-\delta\right]}{1-np}\right]\right\}+$$

$$\frac{p}{\pi}\left\{\frac{B_{rs}}{2\mu_0}\sin\theta_m\left[\frac{\sin\left[(1+np)\left(-\frac{R_{mp}\pi}{2p}\right)+\delta\right]}{1+np}-\frac{\sin\left[(1+np)\left(-\frac{R_{mph}\pi}{2p}\right)+\delta\right]}{1+np}+\right.\right.$$

$$\left.\left.\frac{\sin\left[(1-np)\left(-\frac{R_{mp}\pi}{2p}\right)+\delta\right]}{1-np}-\frac{\sin\left[(1-np)\left(-\frac{R_{mph}\pi}{2p}\right)+\delta\right]}{1-np}\right]+\right.$$

$$\frac{B_{rs}}{2\mu_0}\sin\theta_m\left[\frac{\sin\left[(1+np)\frac{R_{mph}\pi}{2p}-\delta\right]}{1+np}-\frac{\sin\left[(1+np)\frac{R_{mp}\pi}{2p}-\delta\right]}{1+np}+\right.$$

$$\left.\frac{\sin\left[(1-np)\frac{R_{mph}\pi}{2p}-\delta\right]}{1-np}-\frac{\sin\left[(1-np)\frac{R_{mp}\pi}{2p}-\delta\right]}{1-np}\right]-$$

$$\frac{B_{rs}}{2\mu_0}\sin\theta_m\left[\frac{\sin\left[(1+np)\left(1-\frac{R_{mp}}{2}\right)\frac{\pi}{p}+\delta-\frac{\pi}{p}\right]}{1+np}-\frac{\sin\left[(1+np)\left(1-\frac{R_{mph}}{2}\right)\frac{\pi}{p}+\delta-\frac{\pi}{p}\right]}{1+np}+\right.$$

$$\left.\frac{\sin\left[(1-np)\left(1-\frac{R_{mp}}{2}\right)\frac{\pi}{p}+\delta-\frac{\pi}{p}\right]}{1-np}-\frac{\sin\left[(1-np)\left(1-\frac{R_{mph}}{2}\right)\frac{\pi}{p}+\delta-\frac{\pi}{p}\right]}{1-np}\right]-$$

$$\frac{B_{rs}}{2\mu_0}\sin\theta_m\left[\frac{\sin\left[(1+np)\left(1+\frac{R_{mph}}{2}\right)\frac{\pi}{p}-\delta-\frac{\pi}{p}\right]}{1+np}-\frac{\sin\left[(1+np)\left(1+\frac{R_{mp}}{2}\right)\frac{\pi}{p}-\delta-\frac{\pi}{p}\right]}{1+np}+\right.$$

$$\left.\left.\frac{\sin\left[(1-np)\left(1+\frac{R_{mph}}{2}\right)\frac{\pi}{p}-\delta-\frac{\pi}{p}\right]}{1-np}-\frac{\sin\left[(1-np)\left(1+\frac{R_{mp}}{2}\right)\frac{\pi}{p}-\delta-\frac{\pi}{p}\right]}{1-np}\right]\right\} \quad (3.27)$$

and

$$M_{\theta n} = \frac{p}{\pi}\left\{-\frac{B_{rs}}{2\mu_0}\cos\theta_m\left[\frac{\cos\left[(1+np)\left(-\frac{R_{mp}\pi}{2p}\right)+\delta\right]}{1+np}-\frac{\cos\left[(1+np)\left(-\frac{R_{mph}\pi}{2p}\right)+\delta\right]}{1+np}\right.\right.$$

$$\left.-\frac{\cos\left[(1-np)\left(-\frac{R_{mp}\pi}{2p}\right)+\delta\right]}{1-np}+\frac{\cos\left[(1-np)\left(-\frac{R_{mph}\pi}{2p}\right)+\delta\right]}{1-np}\right]+$$

$$\frac{B_{rs}}{2\mu_0}\cos\theta_m\left[\frac{\cos\left[(1+np)\frac{R_{mph}\pi}{2p}-\delta\right]}{1+np}-\frac{\cos\left[(1+np)\frac{R_{mp}\pi}{2p}-\delta\right]}{1+np}-\right.$$

$$\left.\frac{\cos\left[(1-np)\frac{R_{mph}\pi}{2p}-\delta\right]}{1-np}+\frac{\cos\left[(1-np)\frac{R_{mp}\pi}{2p}-\delta\right]}{1-np}\right]+$$

$$\frac{B_{rs}}{2\mu_0}\cos\theta_m\left[\frac{\cos\left[(1+np)\left(1-\frac{R_{mp}}{2}\right)\frac{\pi}{p}-\frac{\pi}{p}+\delta\right]}{1+np}-\frac{\cos\left[(1+np)\left(1-\frac{R_{mph}}{2}\right)\frac{\pi}{p}-\frac{\pi}{p}+\delta\right]}{1+np}-\right.$$

$$\left.\frac{\cos\left[(1-np)\left(1-\frac{R_{mp}}{2}\right)\frac{\pi}{p}-\frac{\pi}{p}+\delta\right]}{1-np}+\frac{\cos\left[(1-np)\left(1-\frac{R_{mph}}{2}\right)\frac{\pi}{p}-\frac{\pi}{p}+\delta\right]}{1-np}\right]-$$

$$\frac{B_{rs}}{2\mu_0}\cos\theta_m\left[\frac{\cos\left[(1+np)\left(1+\frac{R_{mph}}{2}\right)\frac{\pi}{p}-\frac{\pi}{p}-\delta\right]}{1+np}-\frac{\cos\left[(1+np)\left(1+\frac{R_{mp}}{2}\right)\frac{\pi}{p}-\frac{\pi}{p}-\delta\right]}{1+np}\right.$$

$$-$$

$$\left.\left.\frac{\cos\left[(1-np)\left(1+\frac{R_{mph}}{2}\right)\frac{\pi}{p}-\frac{\pi}{p}-\delta\right]}{1-np}+\frac{\cos\left[(1-np)\left(1+\frac{R_{mp}}{2}\right)\frac{\pi}{p}-\frac{\pi}{p}-\delta\right]}{1-np}\right]\right\}+$$

$$\frac{p}{\pi}\left\{\frac{B_{rs}}{2\mu_0}\sin\theta_m\left[\frac{\sin\left[(1+np)\left(-\frac{R_{mp}\pi}{2p}\right)+\delta\right]}{1+np}-\frac{\sin\left[(1+np)\left(-\frac{R_{mph}\pi}{2p}\right)+\delta\right]}{1+np}-\right.\right.$$

$$\left.\frac{\sin\left[(1-np)\left(-\frac{R_{mp}\pi}{2p}\right)+\delta\right]}{1-np}+\frac{\sin\left[(1-np)\left(-\frac{R_{mph}\pi}{2p}\right)+\delta\right]}{1-np}\right]+$$

$$\frac{B_{rs}}{2\mu_0}\sin\theta_m\left[\frac{\sin\left[(1+np)\frac{R_{mph}\pi}{2p}-\delta\right]}{1+np}-\frac{\sin\left[(1+np)\frac{R_{mp}\pi}{2p}-\delta\right]}{1+np}-\right.$$

$$\left.\left.\frac{\sin\left[(1-np)\frac{R_{mph}\pi}{2p}-\delta\right]}{1-np}+\frac{\sin\left[(1-np)\frac{R_{mp}\pi}{2p}-\delta\right]}{1-np}\right]-\right.$$

$$\frac{B_{rs}}{2\mu_0}\sin\theta_m\left[\frac{\sin\left[(1+np)\left(1-\frac{R_{mp}}{2}\right)\frac{\pi}{p}+\delta-\frac{\pi}{p}\right]}{1+np}-\frac{\sin\left[(1+np)\left(1-\frac{R_{mph}}{2}\right)\frac{\pi}{p}+\delta-\frac{\pi}{p}\right]}{1+np}-\right.$$

$$\frac{\sin\left[(1-np)\left(1-\frac{R_{mp}}{2}\right)\frac{\pi}{p}+\delta-\frac{\pi}{p}\right]}{1-np}+\frac{\sin\left[(1-np)\left(1-\frac{R_{mph}}{2}\right)\frac{\pi}{p}+\delta-\frac{\pi}{p}\right]}{1-np}\Bigg]-$$

$$\frac{B_{rs}}{2\mu_0}\sin\theta_m\left[\frac{\sin\left[(1+np)\left(1+\frac{R_{mph}}{2}\right)\frac{\pi}{p}-\delta-\frac{\pi}{p}\right]}{1+np}-\frac{\sin\left[(1+np)\left(1+\frac{R_{mp}}{2}\right)\frac{\pi}{p}-\delta-\frac{\pi}{p}\right]}{1+np}-\right.$$

$$\left.\frac{\sin\left[(1-np)\left(1+\frac{R_{mph}}{2}\right)\frac{\pi}{p}-\delta-\frac{\pi}{p}\right]}{1-np}+\frac{\sin\left[(1-np)\left(1+\frac{R_{mp}}{2}\right)\frac{\pi}{p}-\delta-\frac{\pi}{p}\right]}{1-np}\right]\Bigg\} \quad (3.28)$$

(c) End Side-Magnet

(1). even-segment Halbach array

$$M_{rn} = \frac{p}{\pi}\left\{\frac{B_{rs}}{2\mu_0}\left[-\frac{\cos\left[(1+\mathrm{np})\left(-\frac{R_{mph}\pi}{2p}\right)+\frac{\pi}{2p}\right]}{1+\mathrm{np}}+\frac{\cos\left[(1+\mathrm{np})\left(-\frac{\pi}{2p}\right)+\frac{\pi}{2p}\right]}{1+\mathrm{np}}-\right.\right.$$

$$\left.\frac{\cos\left[(1-\mathrm{np})\left(-\frac{R_{mph}\pi}{2p}\right)+\frac{\pi}{2p}\right]}{1-\mathrm{np}}+\frac{\cos\left[(1-\mathrm{np})\left(-\frac{\pi}{2p}\right)+\frac{\pi}{2p}\right]}{1-\mathrm{np}}\right]-$$

$$\frac{B_{rs}}{2\mu_0}\left[-\frac{\cos\left[(1+\mathrm{np})\left(\left(1-\frac{R_{mph}}{2}\right)\frac{\pi}{p}\right)-\frac{\pi}{2p}\right]}{1+\mathrm{np}}+\frac{\cos\left[(1+\mathrm{np})\left(\frac{R_{mph}\pi}{2p}\right)-\frac{\pi}{2p}\right]}{1+\mathrm{np}}-\right.$$

$$\left.\frac{\cos\left[(1-\mathrm{np})\left(\left(1-\frac{R_{mph}}{2}\right)\frac{\pi}{p}\right)-\frac{\pi}{2p}\right]}{1+\mathrm{np}}+\frac{\cos\left[(1-\mathrm{np})\left(\frac{R_{mph}\pi}{2p}\right)-\frac{\pi}{2p}\right]}{1+\mathrm{np}}\right]+$$

$$\frac{B_{rs}}{2\mu_0}\left[-\frac{\cos\left[(1+\mathrm{np})\left(\frac{3\pi}{2p}\right)-\frac{3\pi}{2p}\right]}{1+\mathrm{np}}+\frac{\cos\left[(1+\mathrm{np})\left(\left(1+\frac{R_{mph}}{2}\right)\frac{\pi}{p}\right)-\frac{3\pi}{2p}\right]}{1+\mathrm{np}}-\right.$$

$$\left.\left.\frac{\cos\left[(1-\mathrm{np})\left(\frac{3\pi}{2p}\right)-\frac{3\pi}{2p}\right]}{1-\mathrm{np}}+\frac{\cos\left[(1-\mathrm{np})\left(\left(1+\frac{R_{mph}}{2}\right)\frac{\pi}{p}\right)-\frac{3\pi}{2p}\right]}{1-\mathrm{np}}\right]\right\} \quad (3.29)$$

and

$$M_{\theta n} = \frac{p}{\pi}\left\{\frac{B_{rs}}{2\mu_0}\left[-\frac{\cos\left[(1+\mathrm{np})\left(-\frac{R_{mph}\pi}{2p}\right)+\frac{\pi}{2p}\right]}{1+\mathrm{np}}+\frac{\cos\left[(1+\mathrm{np})\left(-\frac{\pi}{2p}\right)+\frac{\pi}{2p}\right]}{1+\mathrm{np}}+\right.\right.$$

$$\left.\frac{\cos\left[(1-\mathrm{np})\left(-\frac{R_{mph}\pi}{2p}\right)+\frac{\pi}{2p}\right]}{1-\mathrm{np}}-\frac{\cos\left[(1-\mathrm{np})\left(-\frac{\pi}{2p}\right)+\frac{\pi}{2p}\right]}{1-\mathrm{np}}\right]-$$

$$\frac{B_{rs}}{2\mu_0}\left[-\frac{\cos\left[(1+\mathrm{np})\left(\left(1-\frac{R_{mph}}{2}\right)\frac{\pi}{p}\right)-\frac{\pi}{2p}\right]}{1+\mathrm{np}}+\frac{\cos\left[(1+\mathrm{np})\left(\frac{R_{mph}\pi}{2p}\right)-\frac{\pi}{2p}\right]}{1+\mathrm{np}}+\right.$$

$$\left.\frac{\cos\left[(1-\mathrm{np})\left(\left(1-\frac{R_{mph}}{2}\right)\frac{\pi}{p}\right)-\frac{\pi}{2p}\right]}{1+\mathrm{np}}-\frac{\cos\left[(1-\mathrm{np})\left(\frac{R_{mph}\pi}{2p}\right)-\frac{\pi}{2p}\right]}{1+\mathrm{np}}\right]+$$

$$\frac{B_{rs}}{2\mu_0}\left[-\frac{\cos\left[(1+\mathrm{np})\left(\frac{3\pi}{2p}\right)-\frac{3\pi}{2p}\right]}{1+\mathrm{np}}+\frac{\cos\left[(1+\mathrm{np})\left(\left(1+\frac{R_{mph}}{2}\right)\frac{\pi}{p}\right)-\frac{3\pi}{2p}\right]}{1+\mathrm{np}}+\right.$$

$$\left.\left.\frac{\cos\left[(1-\mathrm{np})\left(\frac{3\pi}{2p}\right)-\frac{3\pi}{2p}\right]}{1-\mathrm{np}}-\frac{\cos\left[(1-\mathrm{np})\left(\left(1+\frac{R_{mph}}{2}\right)\frac{\pi}{p}\right)-\frac{3\pi}{2p}\right]}{1-\mathrm{np}}\right]\right\} \quad (3.30)$$

(2). odd-segment Halbach array

$$M_{rn} = \frac{p}{\pi}\left\{-\frac{B_{rs}}{2\mu_0}\cos\theta_{mh}\left[\frac{\cos\left[(1+np)\left(-\frac{R_{mph}\pi}{2p}\right)+\delta_h\right]}{1+np}-\frac{\cos\left[(1+np)\left(-\frac{\pi}{2p}\right)+\delta_h\right]}{1+np}\right.\right.$$

$$\left.+\frac{\cos\left[(1-np)\left(-\frac{R_{mph}\pi}{2p}\right)+\delta_h\right]}{1-np}-\frac{\cos\left[(1-np)\left(-\frac{\pi}{2p}\right)+\delta_h\right]}{1-np}\right]+$$

$$\frac{B_{rs}}{2\mu_0}\cos\theta_{mh}\left[\frac{\cos\left[(1+np)\frac{\pi}{2p}-\delta_h\right]}{1+np}-\frac{\cos\left[(1+np)\frac{R_{mph}\pi}{2p}-\delta_h\right]}{1+np}+\right.$$

$$\frac{\cos\left[(1-np)\frac{\pi}{2p}-\delta_h\right]}{1-np}-\frac{\cos\left[(1-np)\frac{R_{mph}\pi}{2p}-\delta_h\right]}{1-np}\Bigg]+$$

$$\frac{B_{rs}}{2\mu_0}\cos\theta_{mh}\Bigg[\frac{\cos\left[(1+np)\left(1-\frac{R_{mph}}{2}\right)\frac{\pi}{p}-\frac{\pi}{p}+\delta_h\right]}{1+np}-\frac{\cos\left[(1+np)\frac{\pi}{2p}-\frac{\pi}{p}+\delta_h\right]}{1+np}+$$

$$\frac{\cos\left[(1-np)\left(1-\frac{R_{mph}}{2}\right)\frac{\pi}{p}-\frac{\pi}{p}+\delta_h\right]}{1-np}-\frac{\cos\left[(1-np)\frac{\pi}{2p}-\frac{\pi}{p}+\delta_h\right]}{1-np}\Bigg]-$$

$$\frac{B_{rs}}{2\mu_0}\cos\theta_{mh}\Bigg[\frac{\cos\left[(1+np)\frac{3\pi}{2p}-\frac{\pi}{p}-\delta_h\right]}{1+np}-\frac{\cos\left[(1+np)\left(1+\frac{R_{mph}}{2}\right)\frac{\pi}{p}-\frac{\pi}{p}-\delta_h\right]}{1+np}+$$

$$\frac{\cos\left[(1-np)\frac{3\pi}{2p}-\frac{\pi}{p}-\delta_h\right]}{1-np}-\frac{\cos\left[(1-np)\left(1+\frac{R_{mph}}{2}\right)\frac{\pi}{p}-\frac{\pi}{p}-\delta_h\right]}{1-np}\Bigg]\Bigg\}+$$

$$\frac{p}{\pi}\Bigg\{\frac{B_{rs}}{2\mu_0}\sin\theta_{mh}\Bigg[\frac{\sin\left[(1+np)\left(-\frac{R_{mph}\pi}{2p}\right)+\delta_h\right]}{1+np}-\frac{\sin\left[(1+np)\left(-\frac{\pi}{2p}\right)+\delta_h\right]}{1+np}+$$

$$\frac{\sin\left[(1-np)\left(-\frac{R_{mph}\pi}{2p}\right)+\delta_h\right]}{1-np}-\frac{\sin\left[(1-np)\left(-\frac{\pi}{2p}\right)+\delta_h\right]}{1-np}\Bigg]+$$

$$\frac{B_{rs}}{2\mu_0}\sin\theta_{mh}\Bigg[\frac{\sin\left[(1+np)\frac{\pi}{2p}-\delta_h\right]}{1+np}-\frac{\sin\left[(1+np)\frac{R_{mph}\pi}{2p}-\delta_h\right]}{1+np}+$$

$$\frac{\sin\left[(1-np)\frac{\pi}{2p}-\delta_h\right]}{1-np}-\frac{\sin\left[(1-np)\frac{R_{mph}\pi}{2p}-\delta_h\right]}{1-np}\Bigg]-$$

$$\frac{B_{rs}}{2\mu_0}\sin\theta_{mh}\Bigg[\frac{\sin\left[(1+np)\left(1-\frac{R_{mph}}{2}\right)\frac{\pi}{p}+\delta_h-\frac{\pi}{p}\right]}{1+np}-\frac{\sin\left[(1+np)\frac{3\pi}{2p}+\delta_h-\frac{\pi}{p}\right]}{1+np}+$$

$$\frac{\sin\left[(1-np)\left(1-\frac{R_{mph}}{2}\right)\frac{\pi}{p}+\delta_h-\frac{\pi}{p}\right]}{1-np}-\frac{\sin\left[(1-np)\frac{3\pi}{2p}+\delta_h-\frac{\pi}{p}\right]}{1-np}\Bigg]-$$

$$\frac{B_{rs}}{2\mu_0}\sin\theta_{mh}\left[\frac{\sin\left[(1+np)\frac{3\pi}{2p}-\delta_h-\frac{\pi}{p}\right]}{1+np}-\frac{\sin\left[(1+np)\left(1+\frac{R_{mph}}{2}\right)\frac{\pi}{p}-\delta_h-\frac{\pi}{p}\right]}{1+np}+\right.$$

$$\left.\frac{\sin\left[(1-np)\frac{3\pi}{2p}-\delta_h-\frac{\pi}{p}\right]}{1-np}-\frac{\sin\left[(1-np)\left(1+\frac{R_{mph}}{2}\right)\frac{\pi}{p}-\delta_h-\frac{\pi}{p}\right]}{1-np}\right]\Bigg\} \qquad (3.31)$$

And

$$M_{\theta n} = \frac{p}{\pi}\Bigg\{-\frac{B_{rs}}{2\mu_0}\cos\theta_{mh}\left[\frac{\cos\left[(1+np)\left(-\frac{R_{mph}\pi}{2p}\right)+\delta_h\right]}{1+np}-\frac{\cos\left[(1+np)\left(-\frac{\pi}{2p}\right)+\delta_h\right]}{1+np}\right.$$

$$\left.-\frac{\cos\left[(1-np)\left(-\frac{R_{mph}\pi}{2p}\right)+\delta_h\right]}{1-np}+\frac{\cos\left[(1-np)\left(-\frac{\pi}{2p}\right)+\delta_h\right]}{1-np}\right]+$$

$$\frac{B_{rs}}{2\mu_0}\cos\theta_{mh}\left[\frac{\cos\left[(1+np)\frac{\pi}{2p}-\delta_h\right]}{1+np}-\frac{\cos\left[(1+np)\frac{R_{mph}\pi}{2p}-\delta_h\right]}{1+np}-\right.$$

$$\left.\frac{\cos\left[(1-np)\frac{\pi}{2p}-\delta_h\right]}{1-np}+\frac{\cos\left[(1-np)\frac{R_{mph}\pi}{2p}-\delta_h\right]}{1-np}\right]+$$

$$\frac{B_{rs}}{2\mu_0}\cos\theta_{mh}\left[\frac{\cos\left[(1+np)\left(1-\frac{R_{mph}}{2}\right)\frac{\pi}{p}-\frac{\pi}{p}+\delta_h\right]}{1+np}-\frac{\cos\left[(1+np)\frac{\pi}{2p}-\frac{\pi}{p}+\delta_h\right]}{1+np}-\right.$$

$$\left.\frac{\cos\left[(1-np)\left(1-\frac{R_{mph}}{2}\right)\frac{\pi}{p}-\frac{\pi}{p}+\delta_h\right]}{1-np}+\frac{\cos\left[(1-np)\frac{\pi}{2p}-\frac{\pi}{p}+\delta_h\right]}{1-np}\right]-$$

$$\frac{B_{rs}}{2\mu_0}\cos\theta_{mh}\left[\frac{\cos\left[(1+np)\frac{3\pi}{2p}-\frac{\pi}{p}-\delta_h\right]}{1+np}-\frac{\cos\left[(1+np)\left(1+\frac{R_{mph}}{2}\right)\frac{\pi}{p}-\frac{\pi}{p}-\delta_h\right]}{1+np}-\right.$$

$$\frac{\cos\left[(1-np)\frac{3\pi}{2p}-\frac{\pi}{p}-\delta_h\right]}{1-np}+\frac{\cos\left[(1-np)\left(1+\frac{R_{mph}}{2}\right)\frac{\pi}{p}-\frac{\pi}{p}-\delta_h\right]}{1-np}\Bigg]\Bigg\}+$$

$$\frac{p}{\pi}\Bigg\{\frac{B_{rs}}{2\mu_0}\sin\theta_{mh}\Bigg[\frac{\sin\left[(1+np)\left(-\frac{R_{mph}\pi}{2p}\right)+\delta_h\right]}{1+np}-\frac{\sin\left[(1+np)\left(-\frac{\pi}{2p}\right)+\delta_h\right]}{1+np}-$$

$$\frac{\sin\left[(1-np)\left(-\frac{R_{mph}\pi}{2p}\right)+\delta_h\right]}{1-np}+\frac{\sin\left[(1-np)\left(-\frac{\pi}{2p}\right)+\delta_h\right]}{1-np}\Bigg]+$$

$$\frac{B_{rs}}{2\mu_0}\sin\theta_{mh}\Bigg[\frac{\sin\left[(1+np)\frac{\pi}{2p}-\delta_h\right]}{1+np}-\frac{\sin\left[(1+np)\frac{R_{mph}\pi}{2p}-\delta_h\right]}{1+np}-$$

$$\frac{\sin\left[(1-np)\frac{\pi}{2p}-\delta_h\right]}{1-np}+\frac{\sin\left[(1-np)\frac{R_{mph}\pi}{2p}-\delta_h\right]}{1-np}\Bigg]-$$

$$\frac{B_{rs}}{2\mu_0}\sin\theta_{mh}\Bigg[\frac{\sin\left[(1+np)\left(1-\frac{R_{mph}}{2}\right)\frac{\pi}{p}+\delta_h-\frac{\pi}{p}\right]}{1+np}-\frac{\sin\left[(1+np)\frac{3\pi}{2p}+\delta_h-\frac{\pi}{p}\right]}{1+np}-$$

$$\frac{\sin\left[(1-np)\left(1-\frac{R_{mph}}{2}\right)\frac{\pi}{p}+\delta_h-\frac{\pi}{p}\right]}{1-np}+\frac{\sin\left[(1-np)\frac{3\pi}{2p}+\delta_h-\frac{\pi}{p}\right]}{1-np}\Bigg]-$$

$$\frac{B_{rs}}{2\mu_0}\sin\theta_{mh}\Bigg[\frac{\sin\left[(1+np)\frac{3\pi}{2p}-\delta_h-\frac{\pi}{p}\right]}{1+np}-\frac{\sin\left[(1+np)\left(1+\frac{R_{mph}}{2}\right)\frac{\pi}{p}-\delta_h-\frac{\pi}{p}\right]}{1+np}-$$

$$\frac{\sin\left[(1-np)\frac{3\pi}{2p}-\delta_h-\frac{\pi}{p}\right]}{1-np}+\frac{\sin\left[(1-np)\left(1+\frac{R_{mph}}{2}\right)\frac{\pi}{p}-\delta_h-\frac{\pi}{p}\right]}{1-np}\Bigg]\Bigg\} \qquad (3.32)$$

CHAPTER 4 INVESTIGATION OF PM BRUSHLESS MACHINES HAVING UNEQUAL-MAGNET HEIGHT POLE

Since the torque ripple reduction by adopting magnet shaping methods are often associated with a negative impact on electromagnetic torque as well as increased cost, this chapter propose a magnet pole having unequal-magnet height, i.e. the Hat- and T-type magnet, together with optimized Halbach magnetization. An analytical model based on SD method is employed for investigation.

4.1 Introduction

The PM brushless machines are often a first choice for many applications as they offer high torque/power density and efficiency. Nowadays, the need of reducing torque and force fluctuation coupled with an increasing concern for PM usage efficiency (η_{pm}), i.e. the ratio of average output torque (T) over PM volume (V_{pm}), has spurred the investigation on Halbach magnetization and magnet shaping topologies. The shape of magnet pole has a significant impact on the B_{ag} distribution, which can not only vary the amplitude of B_{ag1}, but also produce torque ripples and induce vibration. Therefore, in order to optimize the machine electromagnetic performance, numerous rotor pole designs have been proposed over the past decades.

However, a design tradeoff may be required, since PM brushless machines having Halbach magnetization and magnet shaping topologies not capable of achieving low torque ripple, high B_{ag1} and η_{pm} simultaneously. For instance, the possible improvement of B_{ag1} and torque ripple by adopting Halbach magnetization depend on the number of rotor poles and magnet height-to-width ratio, which, in other words, means the thicker the magnet, the better the shelf-shielding performance. Hence, it is hardly possible to achieve higher η_{pm} for Halbach magnetization, since high magnet usage is often required. On the other hand, the magnet shaping techniques can reduce the torque ripple, but significantly increase the inter-pole leakage flux. Thus, it results in a lower B_{ag1} which in turn may reduce η_{PM}, although the magnet usage is reduced. This chapter aims to combine the merits of Halbach magnetization and magnet pole shaping to achieve low torque ripple and high η_{PM}, while avoiding the reduction of B_{ag1} and corresponding torque due to inter-pole leakage flux.

Therefore, the magnet poles having unequal-magnet height pole together with Halbach magnetization are proposed, as illustrated in Fig.4.1(a) and (b), which are designated as Hat-type and T-type magnet pole, respectively. As shown in Fig.4.1(a) and (b), each magnet pole

consists of a mid-magnet and two side-magnets which may have different magnetization angles. In each magnet, the magnetization is parallel. In order to facilitate a comparative study and design optimization, an analytical model based on SD method is developed for predicting the magnetic field distribution and electromagnetic torque, while its validity is examined by FEA The comparison study between 12-slot/10-pole PM brushless machine having Hat- and T-type magnet pole between conventional 3-segment Halbach array is taken. In addition, the influence of number of poles is also investigated. Moreover, a further comparison is made between proposed magnet pole configuration and typical magnet shaping methods [199] with same V_{pm}.

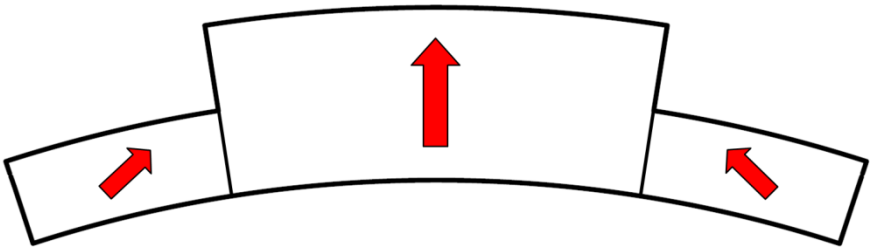

(a) Hat-type

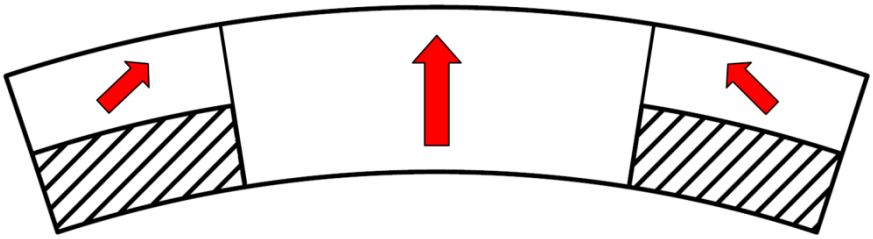

(b) T-type

Fig.4.1. Configuration of Hat- and T-type magnet poles.

4.2 Analytical Sub-Domain Models for Hat- and T-Type PM Machines

In this chapter, the foregoing developed 2-D field model with SD model in chapter 3 is utilized and further developed to analyze air-gap field distributions in the Hat-type and T-type PM machines. It is noted that the side-magnet of T-type magnet pole is supported by non-magnetic base, e.g. aluminum, Fig.4.2, which can be firmed with the rotor back-iron by either using an inserted construction or glue. However, excessive eddy current loss may be induced in the *Al* base. Therefore, other non-magnetic material with high over heat withstand capability property, e.g. ceramic, could be applied to proposed magnet pole. The later is used in order to ease the analytical model, and hence the boundary condition at the inner magnet surface is uniformly distributed.

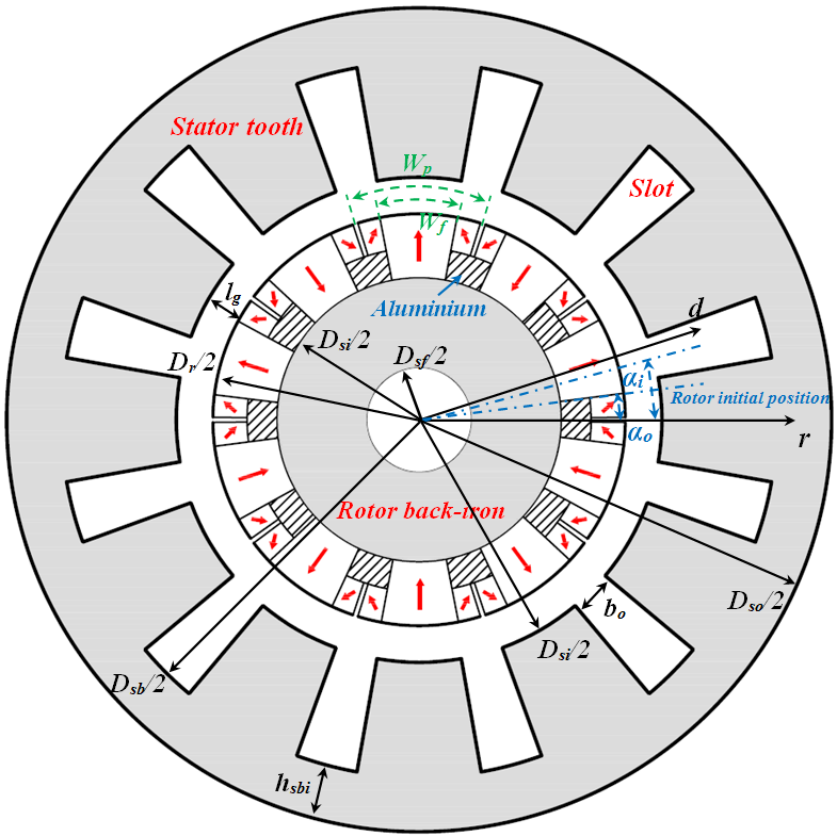

Fig.4.2. Symbols and cross-section of PM brushless machine having T-type in SD model.

In polar coordinates, the magnetization $\vec{M}$ is governed by imported orientation and magnetization of the magnets, which can be written as (3.4).

For each magnet segment, if its magnetization is parallel and the magnet height h_{pm} is equal to each other, these two magnetization components, with design parameters shown in Fig.4.3(c), can be fully described in Table I over one pole-pair, where B_{rs} is the remanence of side-magnet, and α_p is the pole-arc to pole-pitch ratio and expressed as:

$$\alpha_p = \frac{W_a}{W_p} \tag{4.1}$$

Further, $\Delta\theta$ is the magnetization angle as illustrated in Fig.4.3.

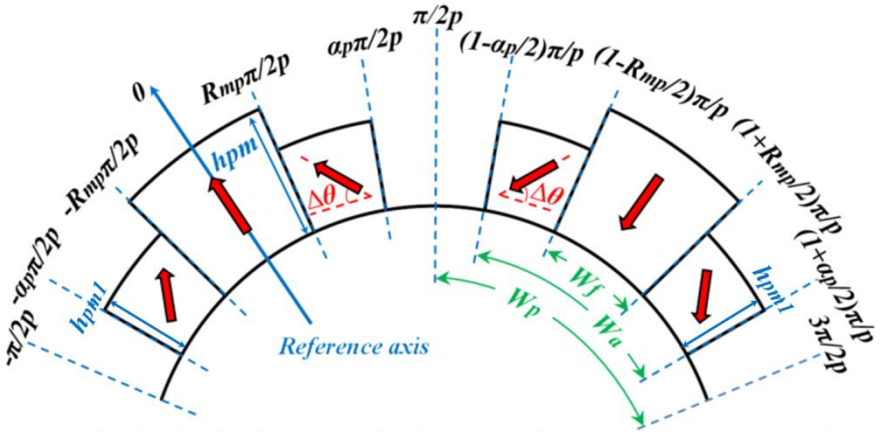

(a) Hat-type

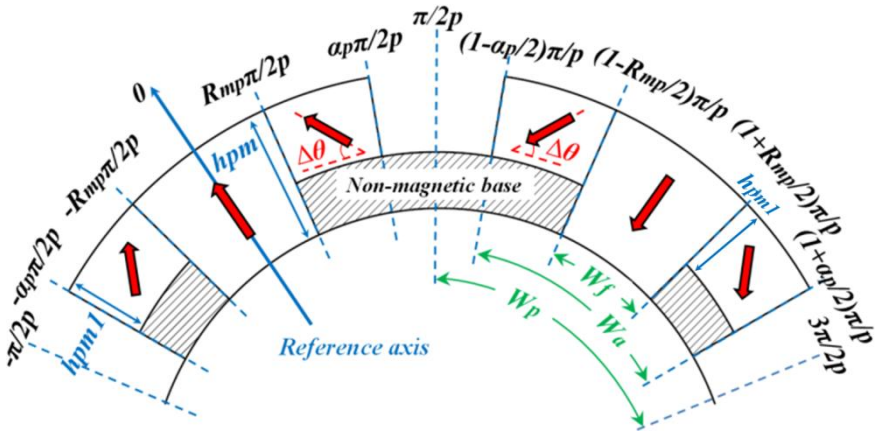

(b) T-type with non-magnetic base

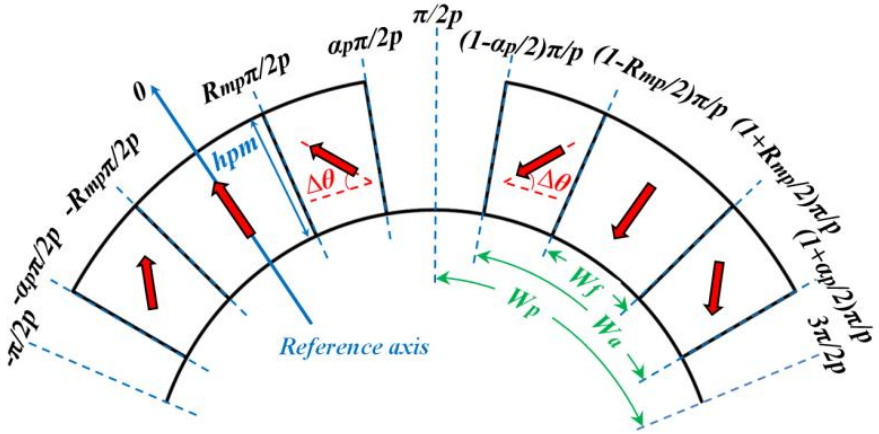

(c) General model with equal-magnet height

Fig.4.3. Design parameters for Hat- and T-type rotor magnet poles.

TABLE.4-I Magnetization Components for Hat- and T-type Over One Pole-Pair

Magnetization component	***Position***
$M_r = 0$ $M_\theta = 0$	$-\frac{\pi}{2p} \le \theta \le -\frac{\alpha_p \pi}{2p}$
$M_r = \frac{B_{rs}}{\mu_0} sin\,\Delta\theta\, cos(\theta+\delta) + \frac{B_{rs}}{\mu_0} cos\,\Delta\theta\, sin(\theta+\delta)$ $M_\theta = -\frac{B_{rs}}{\mu_0} sin\,\Delta\theta\, sin(\theta+\delta) + \frac{B_{rs}}{\mu_0} cos\,\Delta\theta\, cos(\theta+\delta)$	$-\frac{\alpha_p \pi}{2p} \le \theta \le -\frac{R_{mp}\pi}{2p}$
$M_r = \frac{B_{rm}}{\mu_0} cos\,\theta$ $M_\theta = -\frac{B_{rm}}{\mu_0} sin\,\theta$	$-\frac{R_{mp}\pi}{2p} \le \theta \le \frac{R_{mp}\pi}{2p}$
$M_r = \frac{B_{rs}}{\mu_0} sin\,\Delta\theta\, cos(\theta-\delta) - \frac{B_{rs}}{\mu_0} cos\,\Delta\theta\, sin(\theta-\delta)$ $M_\theta = -\frac{B_{rs}}{\mu_0} sin\,\Delta\theta\, sin(\theta-\delta) - \frac{B_{rs}}{\mu_0} cos\,\Delta\theta\, cos(\theta-\delta)$	$\frac{R_{mp}\pi}{2p} \le \theta \le \frac{\alpha_p \pi}{2p}$

$M_r = 0$ $M_\theta = 0$	$\frac{\alpha_p \pi}{2p} \le \theta \le \left(1 - \frac{\alpha_p}{2}\right)\frac{\pi}{p}$
$M_r = -\frac{B_{rs}}{\mu_0} sin\,\Delta\theta\, cos\left(\theta - \frac{\pi}{p} + \delta\right) - \frac{B_{rs}}{\mu_0} cos\,\Delta\theta\, sin\left(\theta - \frac{\pi}{p} + \delta\right)$ $M_\theta = \frac{B_{rs}}{\mu_0} sin\,\Delta\theta\, sin\left(\theta - \frac{\pi}{p} + \delta\right) - \frac{B_{rs}}{\mu_0} cos\,\Delta\theta\, cos\left(\theta - \frac{\pi}{p} + \delta\right)$	$\left(1 - \frac{\alpha_p}{2}\right)\frac{\pi}{p} \le \theta \le \left(1 - \frac{R_{mp}}{2}\right)\frac{\pi}{p}$
$M_r = -\frac{B_{rm}}{\mu_0} cos\left(\theta - \frac{\pi}{p}\right)$ $M_\theta = \frac{B_{rm}}{\mu_0} sin\left(\theta - \frac{\pi}{p}\right)$	$\left(1 - \frac{R_{mp}}{2}\right)\frac{\pi}{p} \le \theta \le \left(1 + \frac{R_{mp}}{2}\right)\frac{\pi}{p}$
$M_r = -\frac{B_{rs}}{\mu_0} sin\,\Delta\theta\, cos\left(\theta - \frac{\pi}{p} - \delta\right) + \frac{B_{rs}}{\mu_0} cos\,\Delta\theta\, sin\left(\theta - \frac{\pi}{p} - \delta\right)$ $M_\theta = \frac{B_{rs}}{\mu_0} sin\,\Delta\theta\, sin\left(\theta - \frac{\pi}{p} - \delta\right) + \frac{B_{rs}}{\mu_0} cos\,\Delta\theta\, cos\left(\theta - \frac{\pi}{p} - \delta\right)$	$\left(1 + \frac{R_{mp}}{2}\right)\frac{\pi}{p} \le \theta \le \left(1 + \frac{\alpha_p}{2}\right)\frac{\pi}{p}$
$M_r = 0$ $M_\theta = 0$	$\left(1 + \frac{\alpha_p}{2}\right)\frac{\pi}{p} \le \theta \le \frac{3\pi}{2p}$

Then, the harmonic components of magnetization M_{rn} and $M_{\theta n}$ for both Hat- and T-type magnets can be deduced as:

$$
\begin{aligned}
M_{rn} = \frac{p}{\pi}\Bigg\{ & \int_{-\frac{\alpha_p \pi}{2p}}^{-\frac{R_{mp}\pi}{2p}} \left[\frac{B_{rs}}{\mu_0} sin\,\Delta\theta\, cos(\theta + \delta) + \frac{B_{rs}}{\mu_0} cos\,\Delta\theta\, sin(\theta + \delta)\right] cosnp\theta\, d\theta \\
& + \int_{-\frac{R_{mp}\pi}{2p}}^{\frac{R_{mp}\pi}{2p}} \frac{B_{rm}}{\mu_0} cos\,\theta\, cosnp\theta\, d\theta \\
& + \int_{\frac{R_{mp}\pi}{2p}}^{\frac{\alpha_p \pi}{2p}} \left[\frac{B_{rs}}{\mu_0} sin\,\Delta\theta\, cos(\theta - \delta) - \frac{B_{rs}}{\mu_0} cos\,\Delta\theta\, sin(\theta - \delta)\right] cosnp\theta\, d\theta \\
& + \int_{\left(1 - \frac{\alpha_p}{2}\right)\frac{\pi}{p}}^{\left(1 - \frac{R_{mp}}{2}\right)\frac{\pi}{p}} \left[-\frac{B_{rs}}{\mu_0} sin\,\Delta\theta\, cos\left(\theta - \frac{\pi}{p} + \delta\right) - \frac{B_{rs}}{\mu_0} cos\,\Delta\theta\, sin\left(\theta - \frac{\pi}{p} + \delta\right)\right] cosnp\theta\, d\theta \\
& + \int_{\left(1 - \frac{R_{mp}}{2}\right)\frac{\pi}{p}}^{\left(1 + \frac{R_{mp}}{2}\right)\frac{\pi}{p}} \left[-\frac{B_{rm}}{\mu_0} cos\left(\theta - \frac{\pi}{p}\right)\right] cosnp\theta\, d\theta \\
& + \int_{\frac{R_{mp}}{2}\frac{\pi}{p}}^{+\frac{\alpha_p}{2}\frac{\pi}{p}} \left[-\frac{B_{rs}}{\mu_0} sin\,\Delta\theta\, cos\left(\theta - \frac{\pi}{p} - \delta\right) + \frac{B_{rs}}{\mu_0} cos\,\Delta\theta\, sin\left(\theta - \frac{\pi}{p} - \delta\right)\right] cosnp\theta\, d\theta \Bigg\}
\end{aligned}
\tag{4.2}
$$

and,

$$M_{\theta n}=\frac{p}{\pi}\left\{\int_{-\frac{\alpha_p\pi}{2p}}^{-\frac{R_{mp}\pi}{2p}}\left[-\frac{B_{rs}}{\mu_0}sin\,\Delta\theta\,sin(\theta+\delta)+\frac{B_{rs}}{\mu_0}cos\,\Delta\theta\,cos(\theta+\delta)\right]sinnp\theta\,d\theta\right.$$

$$+\int_{-\frac{R_{mp}\pi}{2p}}^{\frac{R_{mp}\pi}{2p}}\left[-\frac{B_{rm}}{\mu_0}sin\,\theta\right]sinnp\theta\,d\theta$$

$$+\int_{\frac{R_{mp}\pi}{2p}}^{\frac{\alpha_p\pi}{2p}}\left[-\frac{B_{rs}}{\mu_0}sin\,\Delta\theta\,sin(\theta-\delta)-\frac{B_{rs}}{\mu_0}cos\,\Delta\theta\,cos(\theta-\delta)\right]sinnp\theta\,d\theta$$

$$+\int_{\left(1-\frac{\alpha_p}{2}\right)\frac{\pi}{p}}^{\left(1-\frac{R_{mp}}{2}\right)\frac{\pi}{p}}\left[\frac{B_{rs}}{\mu_0}sin\,\Delta\theta\,sin\left(\theta-\frac{\pi}{p}+\delta\right)-\frac{B_{rs}}{\mu_0}cos\,\Delta\theta\,cos\left(\theta-\frac{\pi}{p}+\delta\right)\right]sinnp\theta\,d\theta$$

$$+\int_{\left(1-\frac{R_{mp}}{2}\right)\frac{\pi}{p}}^{\left(1+\frac{R_{mp}}{2}\right)\frac{\pi}{p}}\left[\frac{B_{rm}}{\mu_0}sin\left(\theta-\frac{\pi}{p}\right)\right]sinnp\theta\,d\theta$$

$$\left.+\int_{\left(1+\frac{R_{mp}}{2}\right)\frac{\pi}{p}}^{\left(1+\frac{\alpha_p}{2}\right)\frac{\pi}{p}}\left[\frac{B_{rs}}{\mu_0}sin\,\Delta\theta\,sin\left(\theta-\frac{\pi}{p}-\delta\right)+\frac{B_{rs}}{\mu_0}cos\,\Delta\theta\,cos\left(\theta-\frac{\pi}{p}-\delta\right)\right]sinnp\theta\,d\theta\right\} \tag{4.3}$$

where,

$$\delta=\frac{R_{mp}\pi}{2p}+\left(\alpha_p-R_{mp}\right)\frac{\pi}{4p} \tag{4.4}$$

The fully deduced expressions of M_{rn} and $M_{\theta n}$ are given in (4.10) and (4.11) in Appendix of this chapter.

The foregoing developed 2-D field model with SD method is used to predict air-gap flux density. Since the air-gap is non-uniformly distributed for proposed Hat- and T-type magnet poles, the superposition theory is applied as illustrated in TABLE.4-II to solve overall air-gap flux density. It is found that the overall air-gap flux density distribution for Hat-type magnet pole is calculated by initially setting B_{rm} = 0 T in (4.2)-(4.3) and change B_{rs} plus the side-magnet height h_{pm1} to the desired values (Part A) when the calculating air-gap path is fixed. Then, the air-gap flux density distribution for mid-magnet is predicted by setting B_{rs} = 0 T in (4.2)-(4.3) while B_{rm} and the mid-magnet height h_{pm} are imported with desired value (Part B). Hence, the overall air-gap flux density for H-type magnet pole is calculated by summing the foregoing predicted value of Part A and Part B. In the similar manner, the overall air-gap flux density distribution of T-type magnet pole is calculated by summing the amplitude of Part 1 and Part 3, then, minus Part 2, as illustrated in TABLE.4-II.

Furthermore, the phase back-EMF and electromagnetic torque waveforms can be predicted by using equation (3.22) and (3.23), respectively.

TABLE.4-II SUPERPOSITION FOR HAT- AND T-TYPE MAGNETS

Hat-type	***T-type***
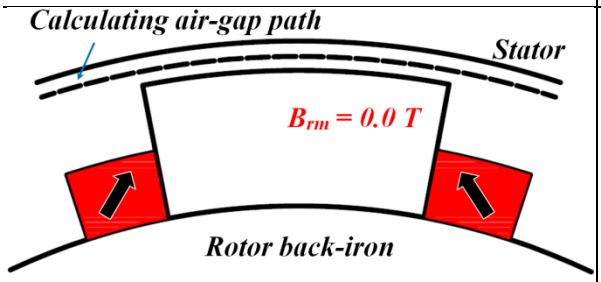	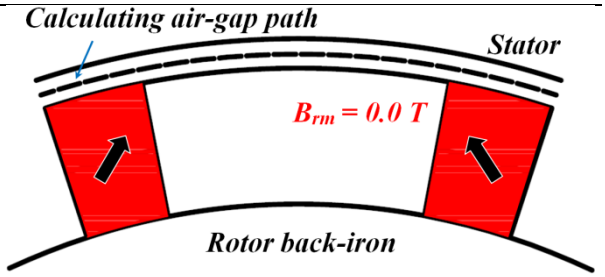
Part A	Part 1
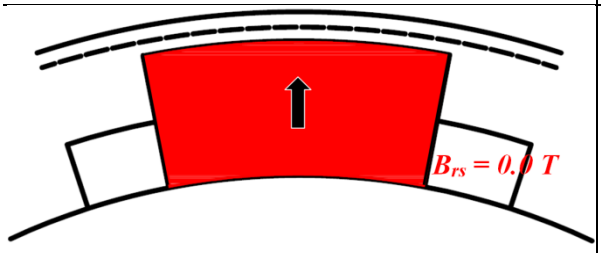	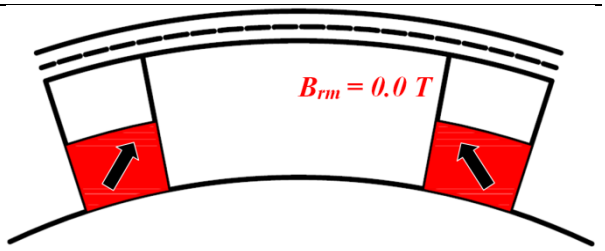
Part B	Part 2
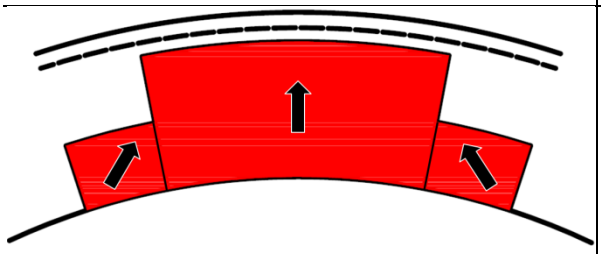	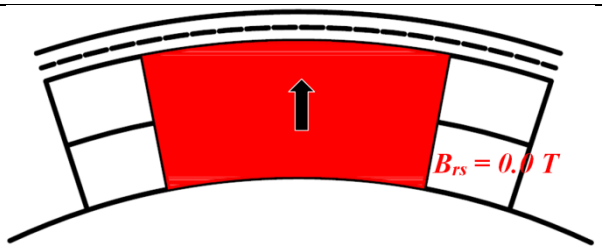
Hat-type = Part A + Part B	Part 3
	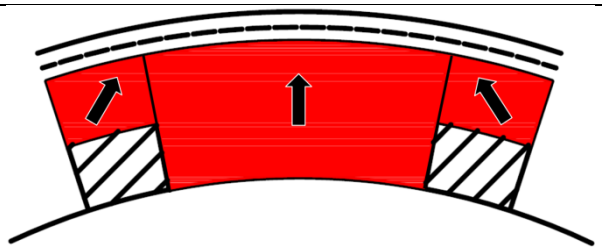
	T-type = Part 1 – Part 2 + Part 3

4.3 Finite-Element Validation

The linear FEA with μ_r = 40000 for BH curve is carried out on a 12-slot/10-pole PM brushless machine whose design parameters are shown in TABLE.4-III.

TABLE.4-III MACHINES DESIGN PARAMETERS (DEFAULT UNIT: MM)

Rated speed, rpm	400	Slot opening, b_o	2.0
Pole number, $2p$	10	Air-gap length, l_g	1.0
Stator slot number, N_s	12	Active length, l_a	50
Tooth-tip height, h_t	1.5	Stator back-iron thickness, h_{sbi}	3.7
Tooth body width, b_t	-	Stator outer diameter, D_{so}	100
Stator inner diameter, D_{si}	57	Rotor outer diameter, D_{ro}	55
Rotor inner diameter, D_{ri}	49	Shaft diameter, D_{sf}	34
No. of series turns per phase, N	132	Peak phase current, I (A)	10
NdFeB, B_r (T)	1.2	Relative recoil permeability, μ_r	1.05
Magnet ratio, R_{mp}	0.70	Pole-arc to pole-pitch ratio, α_p	0.94
Magnet height of mid-magnet, h_{pm}	3.0	Magnet height of side-magnet, h_{pm1}	1.5
Magnetization angle, $\Delta\theta$	75.24		

In order to be consistent with the foregoing developed analytical model, the stator with straight tooth-tips is also applied to the linear FEA model. The analytically and FEA predicted air-gap flux density distributions, phase back-EMF, and electromagnetic torque waveforms are compared in Fig.4.4-8 for the prototype machine having Hat- and T-type magnets, respectively, and excellent agreement is achieved.

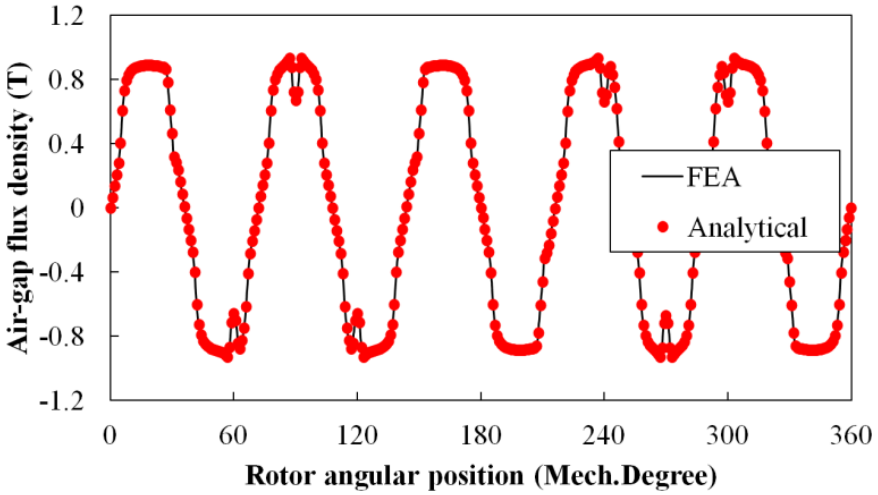

(a) Radial air-gap flux density

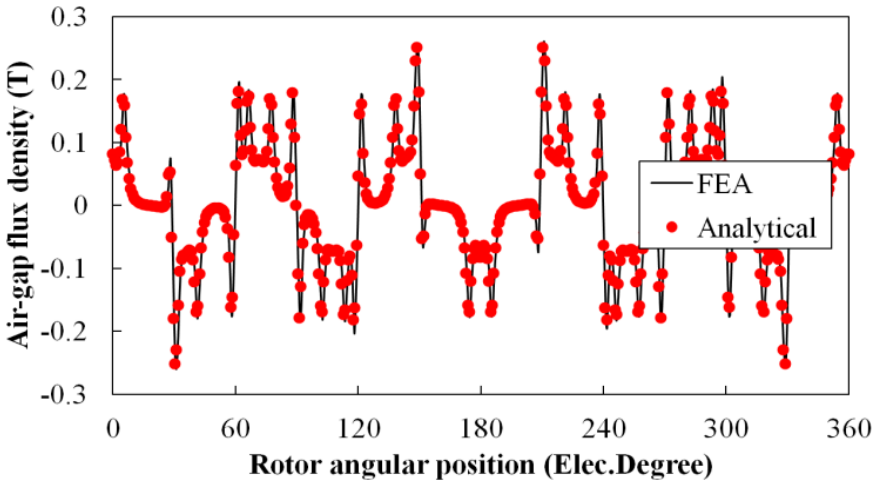

(b) Circumferential air-gap flux density

Fig.4.4. Comparison of analytical and FEA predicted air-gap flux density for 12-slot/10-pole PM brushless machine having Hat-type magnet pole.

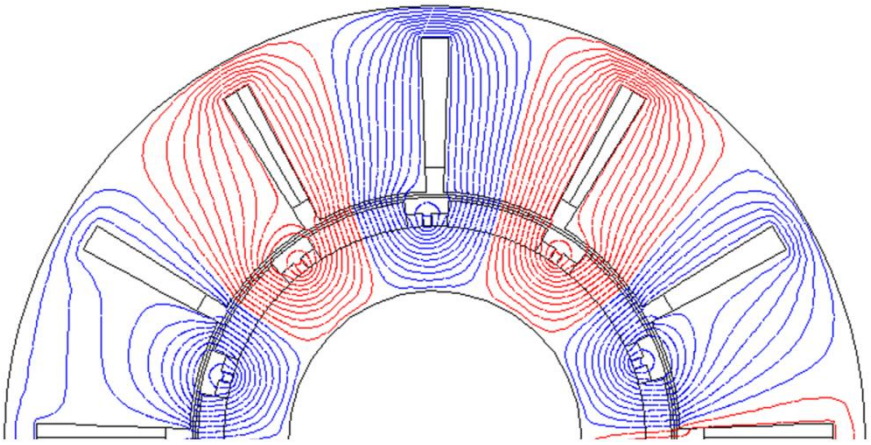

(a) Hat-type

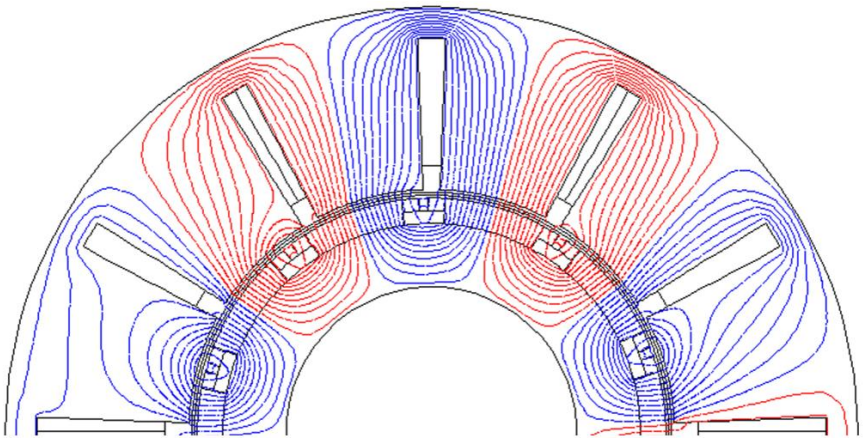

(b) T-type

Fig.4.5. FEA predicted vector potential distributions for 12-slot/10-pole PM brushless machine having Hat- and T-type magnet pole.

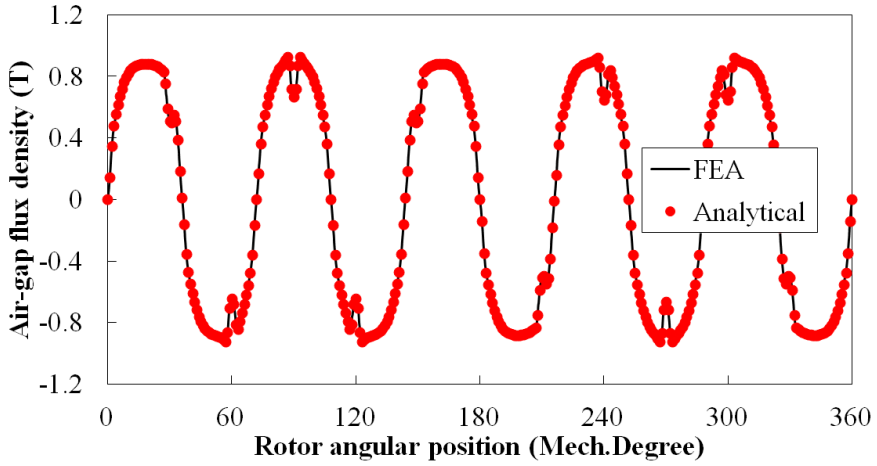

(a) Radial air-gap flux density

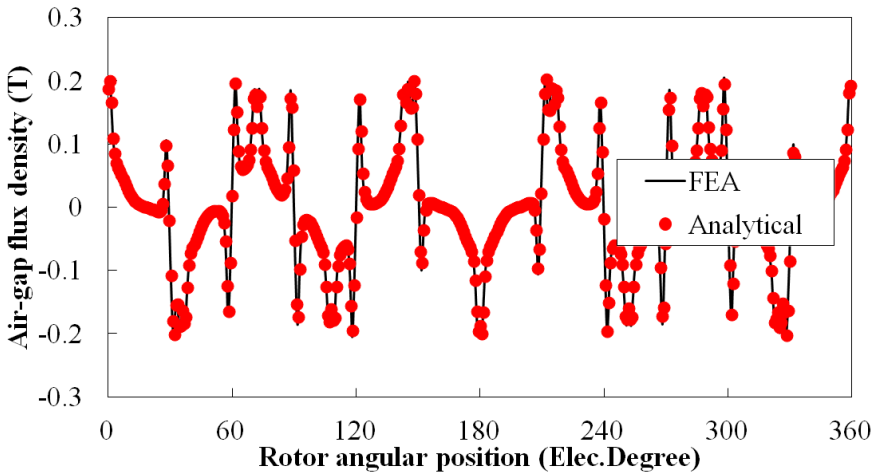

(b) Circumferential air-gap flux density

Fig.4.6. Comparison of analytical and FEA predicted air-gap flux density for 12-slot/10-pole PM brushless machine having T-type magnet pole.

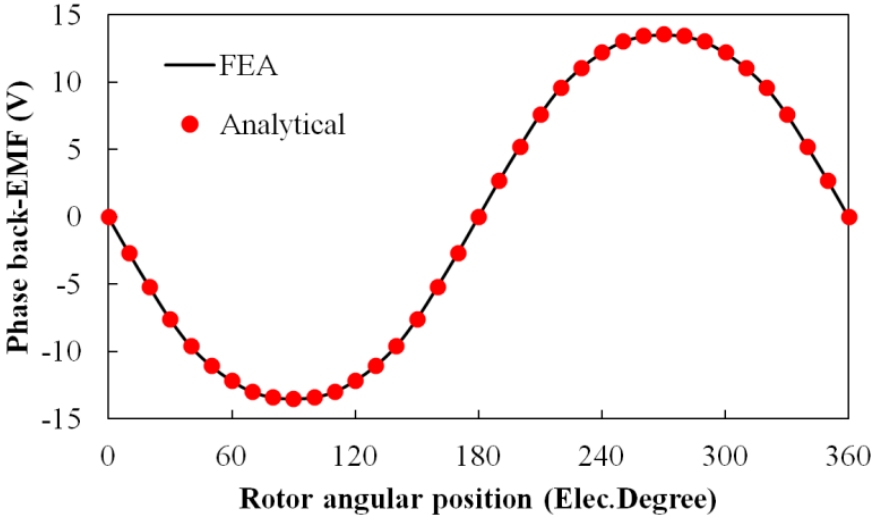

(a) Phase back-EMF, 400 rpm

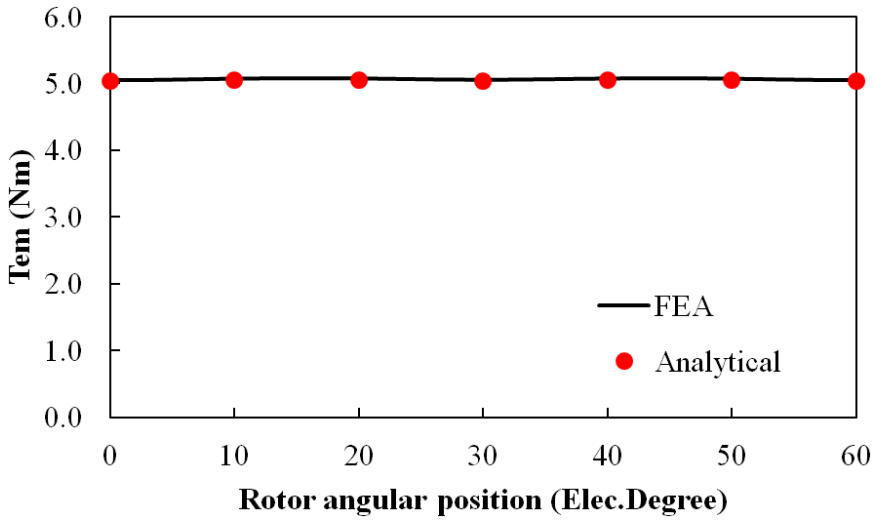

(b) Electromagnetic torque

Fig.4.7. Comparison of analytical and FEA predicted phase back-EMFs at 400 rpm and electromagnetic torque waveforms for 12-slot/10-pole PM brushless machine having Hat-type magnet pole.

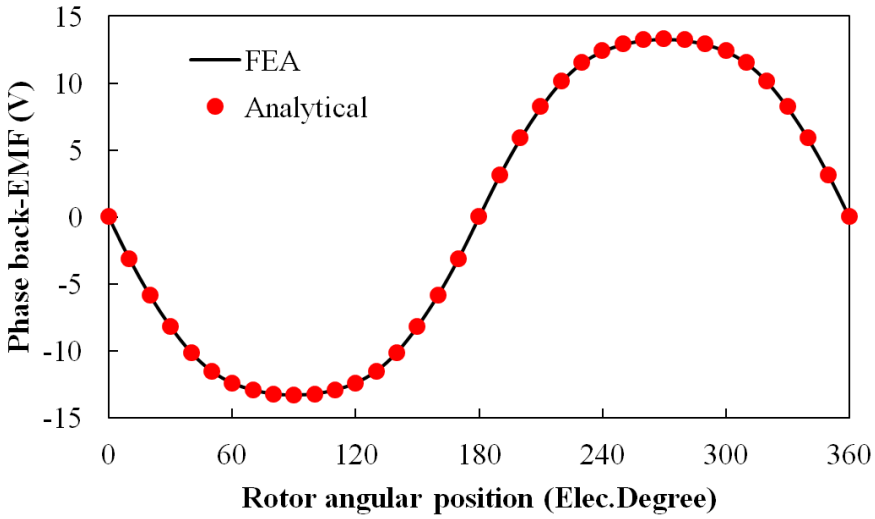

(a) Phase back-EMF, 400 rpm

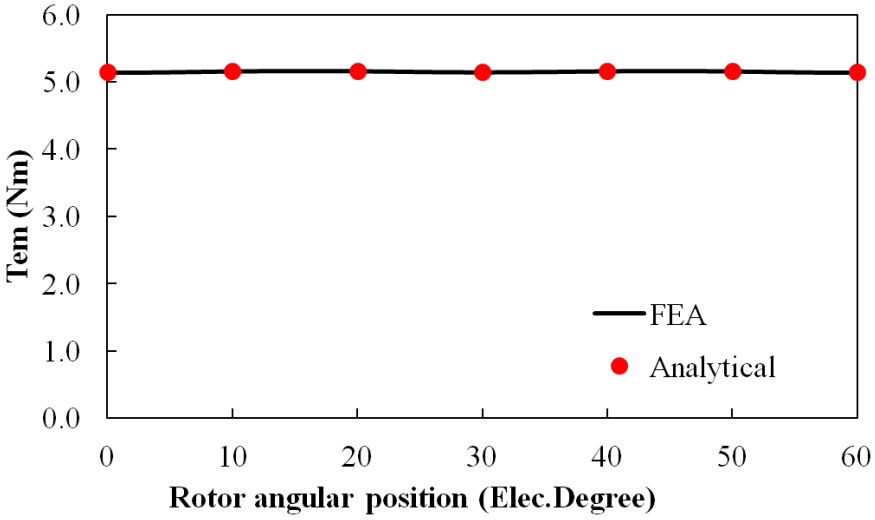

(b) Electromagnetic torque

Fig.4.8. Comparison of analytical and FEA predicted phase back-EMFs at 400 rpm and electromagnetic torque waveforms for 12-slot/10-pole PM brushless machine having T-type magnet pole.

4.4 Comparison of Machine Having Hat- and T-Type Magnet Pole with Optimized 3-Segment Halbach Array

It is noted that the amplitude of air-gap flux density in the Halbach magnetized machine can be optimized by varying both magnet ratio R_{mp} and magnetization angle $\Delta\theta$ in (4.2)-(4.3), which in turn affects T_{em}. This is reflected in Fig.4.9, which shows the variation of the optimal T_{em} with R_{mp} and $\Delta\theta$ for 12-slot/10-pole PM brushless machine having conventional (equal-magnet height) 3-segment Halbach array. The overall optimized T_{em} is obtained when α_p = 1.0, R_{mp} = 0.70 and $\Delta\theta$ = 40, respectively. It should be also noticed that since the self-shielding property of Halbach arrays strongly depends on the magnet usage and how well the two neighboring PM segments are connected to each other, thus α_p = 1 always exhibit higher B_{ag1} in contrast with α_p < 1. Therefore, α_p = 1 is treated as an optimal value in this chapter for further investigations, although the electromagnetic performance for machine having α_p < 1 can be predicted by adopting a common analytical model as illustrated in Fig.4.3. Further, the side-magnet thickness h_{pm1} of above optimized 3-segments Halbach machine is varied in order to form Hat- and T-type magnet pole. In general, however, the foregoing optimal magnetization angle needs to be re-calculated for different h_{pm1}, since the magnet height-to-width ratio for side-magnets are changed. Fig.4.10(a) compares the optimized Hat- and T-type magnet pole with the variation of $h_{pm1,}$ together with optimized $\Delta\theta$. It reveals that the T-type magnet pole exhibit significantly larger optimal T_{em} than Hat-type magnet pole if h_{pm1} is equal to half of h_{pm}. When h_{pm1} is further varied toward both two extreme regions, i.e. h_{pm1} = 0mm (conventional pole) and h_{pm1} = 3.0mm (conventional 3-segment Halbch array), then, the advantage of T-type magnet pole is diminished. In addition, the magnet usage efficiency of T-type magnet pole increases as h_{pm1} reduces, Fig.4.10(b), where η_{PM} of T-type magnet pole is the highest one compared with those of Hat-type, conventional pole and conventional 3-segment Halbach array when h_{pm1} = 1.5 is adopted. The vector potential distributions of 12-slot/10-pole PM brushless machine having forgoing optimized four kinds of magnet poles are shown in Fig.4.11. In addition, their analytically predicted T_{em} waveforms are compared in Fig.4.12.

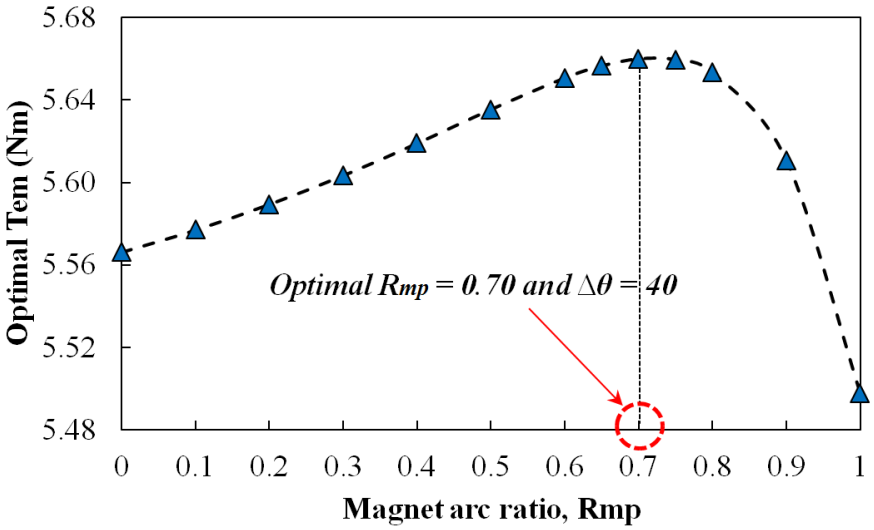

Fig.4.9. Analytically predicted variation of optimal T_{em} with both R_{mp} and $\Delta\theta$ for 12-slot/10-pole PM brushless machine having 3-segment Halbach array.

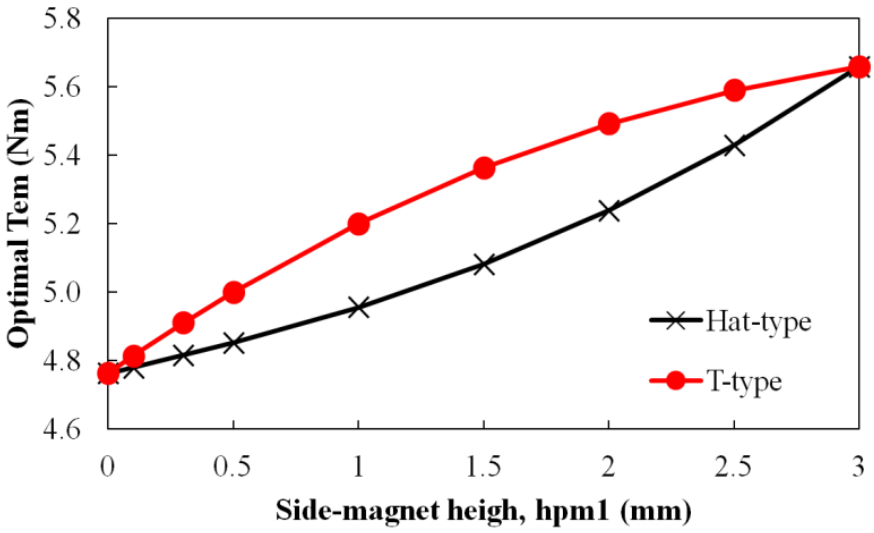

(a) Optimal T_{em}

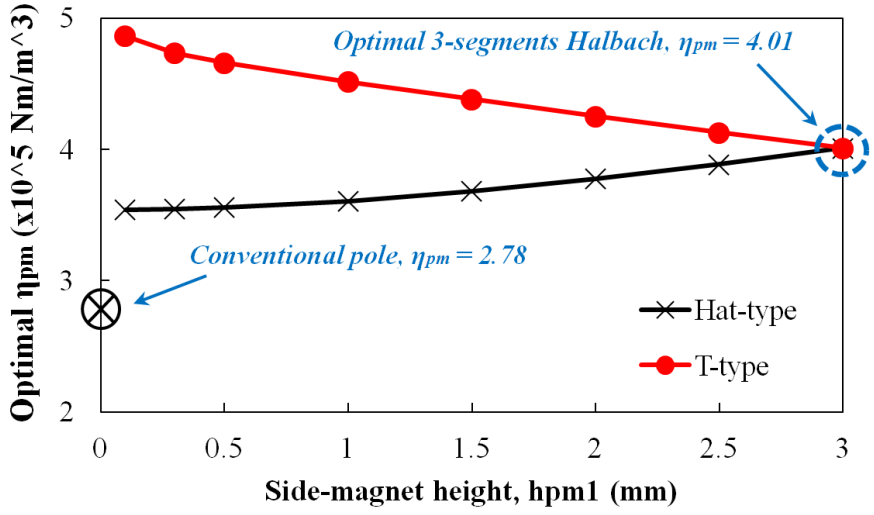

(b) Optimal η_{pm}

Fig.4.10. Analytically predicted optimal T_{em} and η_{pm} for Hat- and T-type magnet poles with the variation of h_{pm1}.

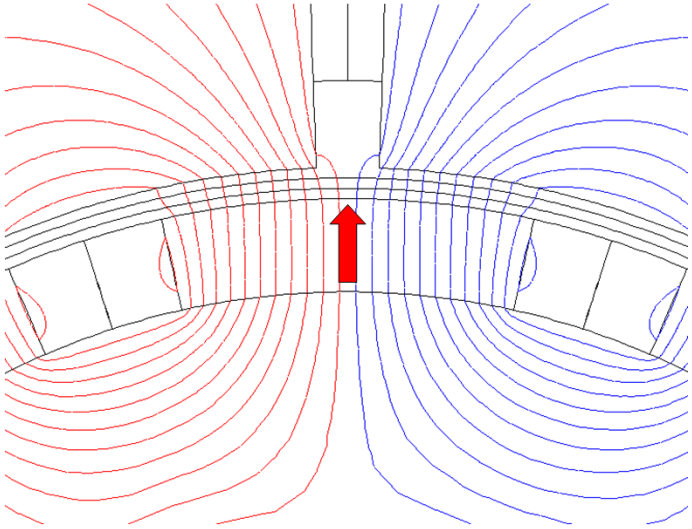

(a) Conventional pole (α_p = 0.70)

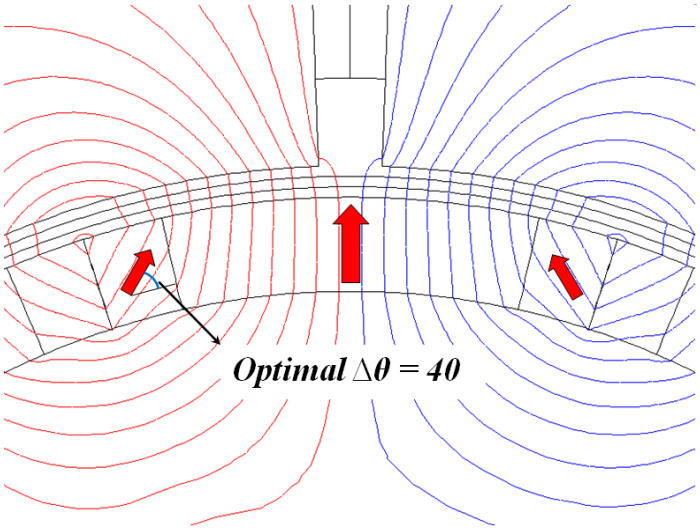

(b) Conventional 3-segment Halbach

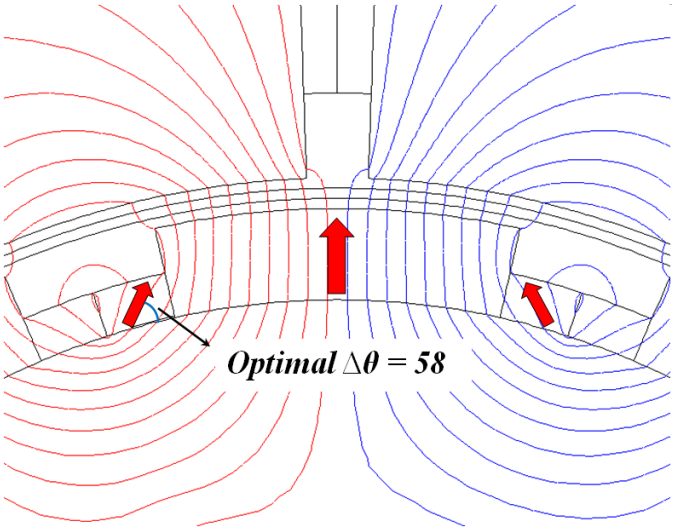

(c) Hat-type (h_{pm1} = 1.5mm)

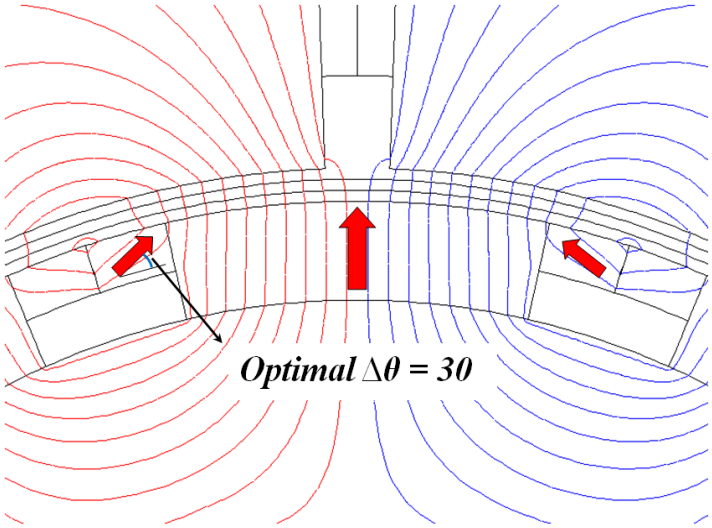

(d) T-type (h_{pm1} = 1.5mm)

Fig.4.11. Linear FEA predicted vector potential distribution of 12-slot/10-pole PM brushless machine having conventional pole, optimized conventional 3-segment Halbach array, optimized Hat- and T-type magnet poles.

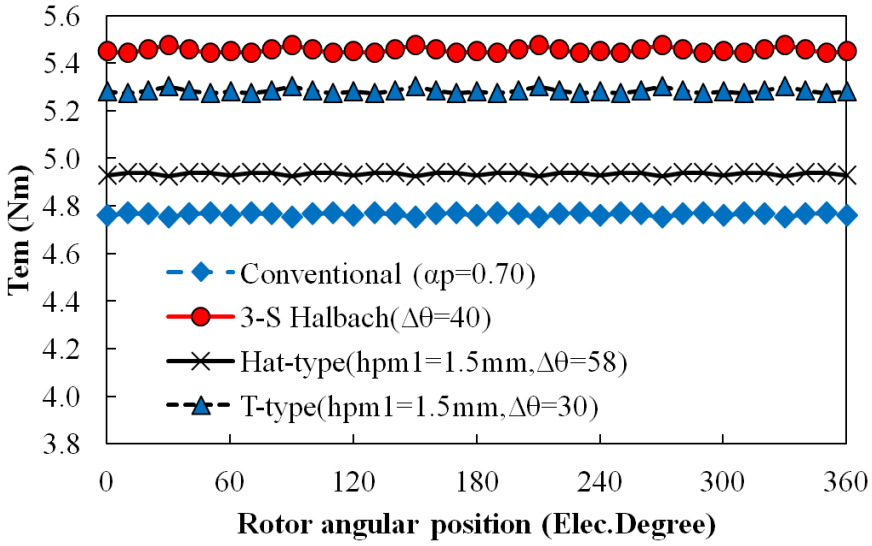

Fig.4.12. Comparison of analytically predicted T_{em} waveform between 12-slot/10-pole PM brushless machine having conventional, 3-segment Halbach, Hat- and T-type magnet pole.

4.5 Investigation on Machines Having Hat- and T-Type Magnet Pole

From the foregoing analysis, it is shown that the machine having T-type magnet pole exhibits eminently merits in contrast with H-type magnet pole which can be explained by significantly reduced inter-pole leakage flux, as highlighted in Fig.4.13. Consequently, the flux that can be effectively linked by a coil for T-type magnet pole are much higher than Hat-type magnet pole, Fig.4.14, which leads the machine a larger T_{em}. However, such merit of T-type magnet pole gradually diminishes when ΔR_{mp} (ΔR_{mp} = 1 - R_{mp}) is increased as illustrated

in Fig.4.15. It also shows that the maximum difference of T_{em} is achieved when h_{pm1} = 1.5 mm, viz. $h_{pm1} = h_{pm}/2$, a similar phenomenon can also be found in Fig.4.10(a). Moreover, it should be noted that T_{em} is very small but great than zero, although the majority of fluxes are short circuited since only tangentially magnetized magnet segments exist.

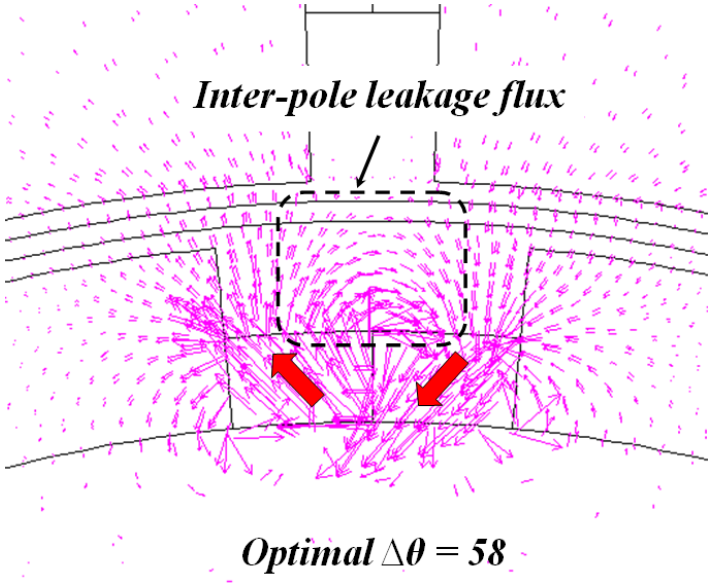

(a) Hat-type

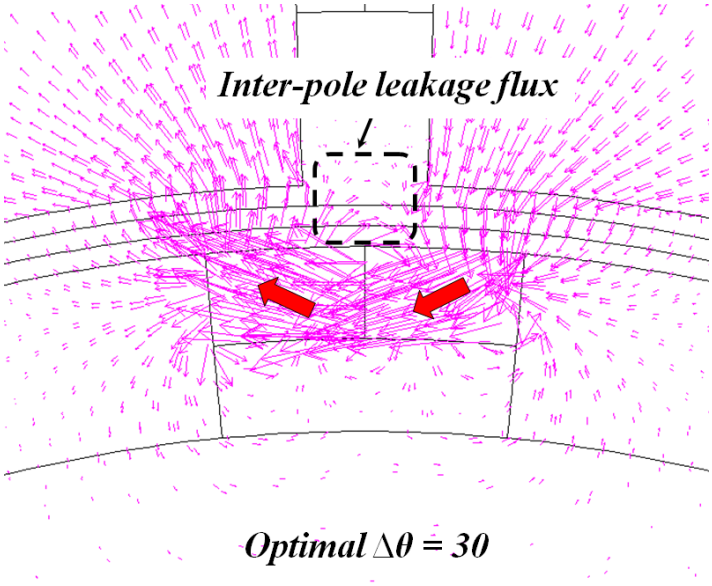

(b) T-type

Fig.4.13. Comparison of FEA predicted inter-pole leakage flux between Hat and T-type magnet pole when B_{rm} = 0 T and design parameters in Table III.

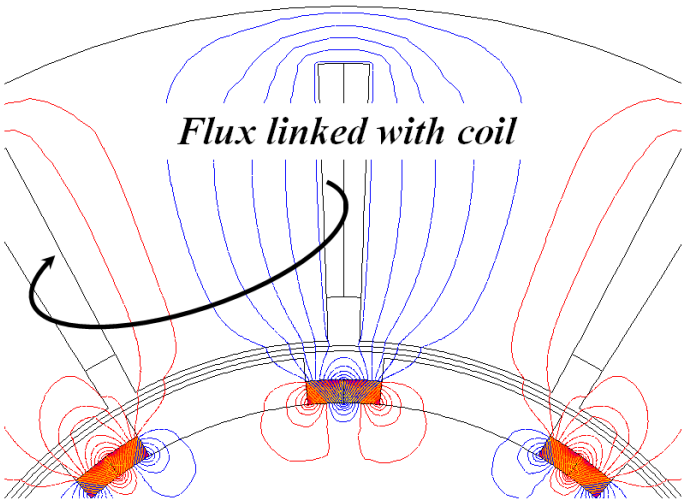

(a) Hat-type

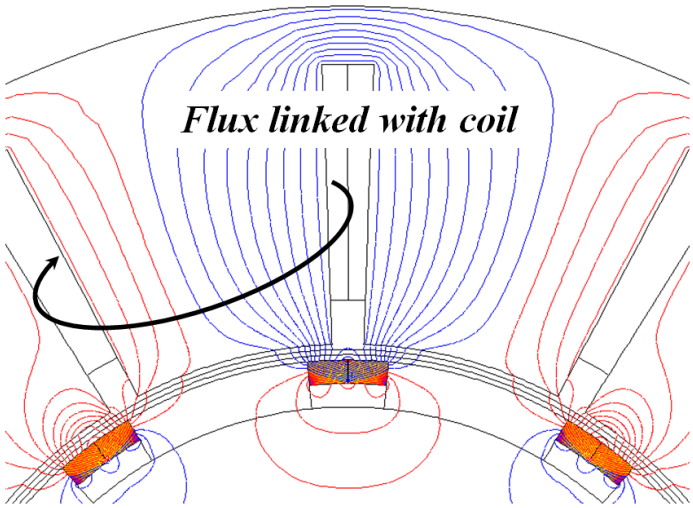

(b) T-type

Fig.4.14. Comparison of FEA predicted flux which can be linked with coil between Hat and T-type magnet pole when B_{rm} = 0 T and design parameters in Table III.

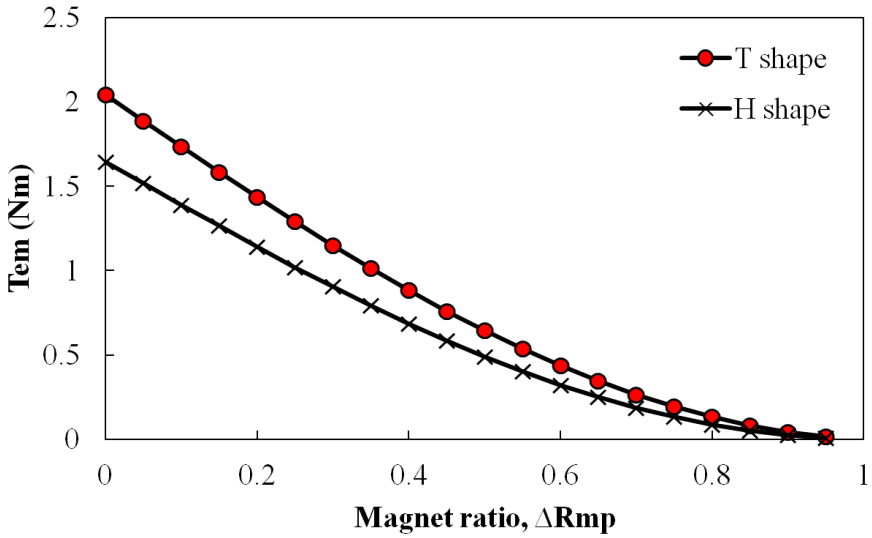

(a) h_{pm1} = 1.0 mm

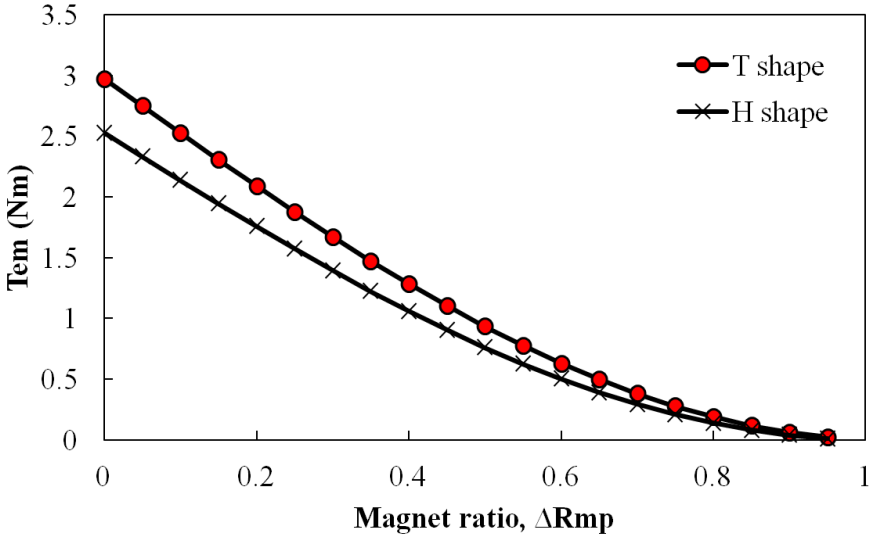

(b) h_{pm1} = 1.5 mm

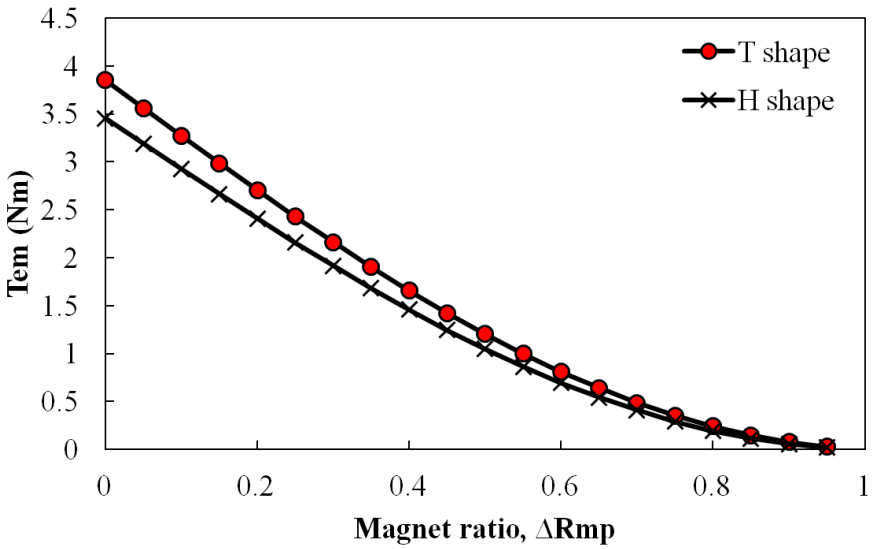

(c) h_{pm1} = 2.0 mm

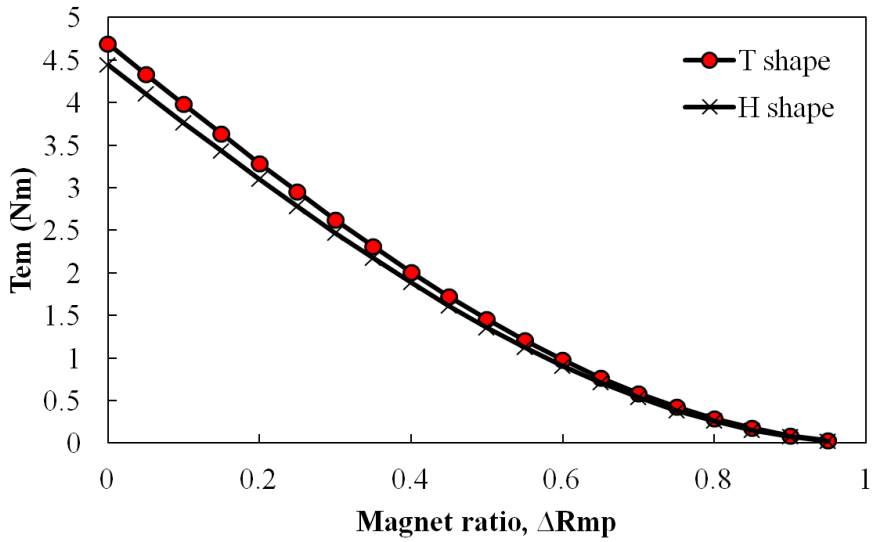

(d) h_{pm1} = 2.5 mm

Fig.4.15. Comparison of analytically predicted T_{em} for 12-slot/10-pole PM brushless machine having Hat and T-type with the variation of h_{pm1} and R_{mp} when B_{rf} = 0 T.

Furthermore, the investigation on the flux focusing effect due to rotor pole pair variation is examined by adopting a slotless model as shown in Fig.4.16. It reveals that although the amplitude of fundamental air-gap flux density for T-type magnet pole is lower in contrast with 3-segment Halbach array, the similar magnet usage efficiency which is defined as B_{ag1}/V_{pm} still demonstrates the relative merits of the machine having T-type magnet pole when p increases. It is noted that the electromagnetic torque is proportional to the amplitude of fundamental air-gap flux density. Hence, the variation of B_{ag1}/V_{pm} with the rotor pole pair number can be used to represent the variation trend of T_{em}/V_{pm}. Moreover, in case of maximum output torque is required but meanwhile high magnet usage efficiency is also needed, both Hat- and T-type magnets with p = 3 exhibit the potential to be an alternative design to the machine with the conventional 3-segment Halbach array, Fig.4.16.

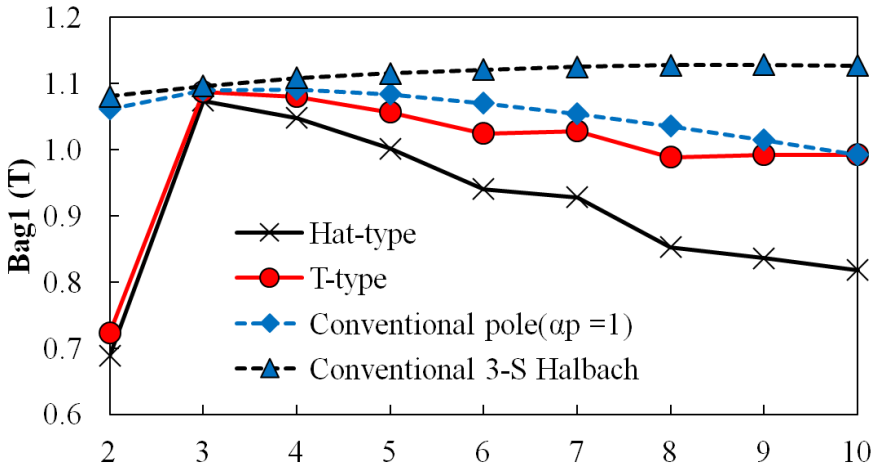

(a) B_{ag1}

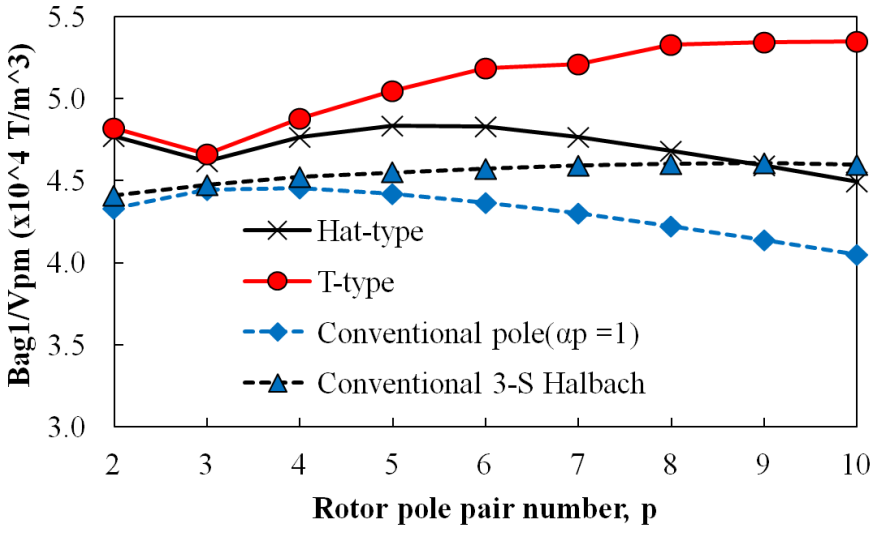

(b) B_{ag1}/V_{pm}

Fig.4.16. Comparison of analytically predicted B_{ag1} and ratio of B_{ag1}/V_{pm} for slotless machine having conventional pole, conventional 3-segment Halbach array, Hat- and T-type magnet pole with overall optimized R_{mp} and $\Delta\theta$, together with h_{pm1} = 1.5 mm.

4.6 Comparison of Hat- and T-Type Magnet Pole with Typical Magnet Shaping Techniques

Magnet shaping techniques as shown in Fig.4.17 [199] are emerging as a key technology, due to their sinusodially distributed air-gap flux density which results in low torque ripples and low magnet usage. However, the inter-pole leakage fluxes of magnet shaping are significant (Fig.4.18) which reduces the average T_{em}. On the other hand, the segmented Halbach arrays are also capable to achieve sinusoidal air-gap flux density, but increases the magnet usage. Therefore, Hat- and T-type magnet poles are introduced with the merits of both magnet shaping and Halbach array. In this section, T_{em} and η_{PM} for Hat- and T-type magnet pole are compared with optimized shaping techniques in [199].

The prototype machine in this section having same slot and pole number combination and similar geometries in contrast with the optimized magnet pole with sinusoidal arc shaping (SAS, sinusoidal arc shaping with 3rd order harmonic (SAS+3rd), inverse cosine shaping (ICS), and inverse cosine shaping with 3rd order harmonic shaping (ICS+3rd) shown in Fig.4.18 [199] by adopting the equations (4.5)-(4.8):

- For sinusoidal arc shaping (SAS):

$$\Delta h = \Delta h_{max} cos(p\theta) \tag{4.5}$$

- For sinusoidal arc shaping with 3rd order harmonic (SAS+3rd)

$$\Delta h = 1.155 \times \Delta h_{max} \left[cos(p\theta) - \frac{1}{6} cos(3p\theta) \right] \tag{4.6}$$

- For inverse cosine shaping (ICS):

$$\Delta l_g(\theta) = \frac{l_g}{cos\left(\frac{\pi}{W_p}\theta\right)} \tag{4.7}$$

- For inverse cosine shaping with 3rd order harmonic (ICS+3rd):

$$\Delta l_g(\theta) = \frac{1.155 l_g}{cos\left(\frac{\pi}{W_p}\theta\right) - \frac{1}{6} cos\left(\frac{3\pi}{W_p}\theta\right)} \tag{4.8}$$

The proposed Hat- and T-type magnet poles can be treated as a potential alternative design method instead of existing shaping techniques used in [199]. Therefore, the comparison of proposed magnet poles between foregoing mentioned magnet shaping methods are made with the constraints, i.e. the PM volume V_{pm}, the minimum air-gap length l_g = 1.0 mm, the

maximum magnet thickness h_{pm} = 3.0 mm and D_{ri} = 49 mm are fixed. Thus, V_{pm} for SAS, SAS+3rd, ICS, and ICS+3rd are fixed in this manner and their values together with T_{em} are summarized in Table IV.

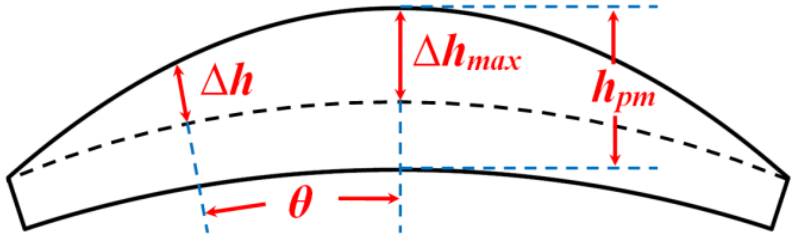

(a) Sinusoidal arc shaping (SAS)

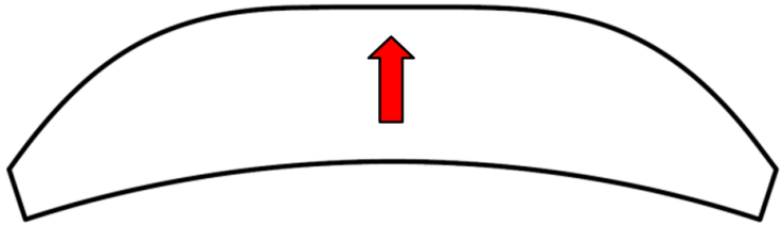

(b) Sinusoidal arc shaping with 3rd order harmonic (SAS+3rd)

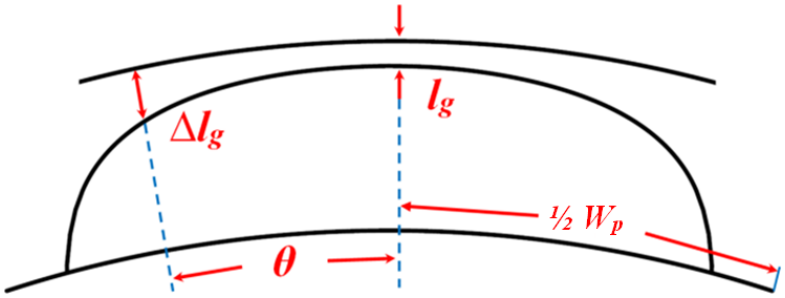

(c) Inverse cosine shaping (ICS)

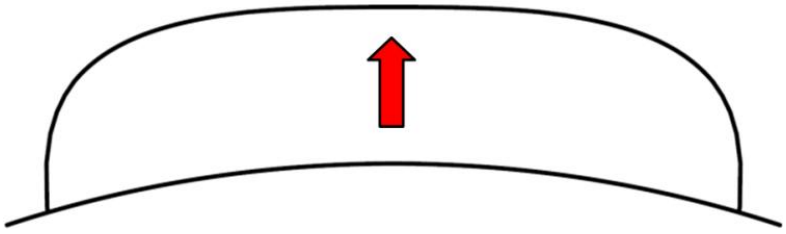

(d) Inverse cosine shaping with 3rd order harmonic (ICS+3rd)

Fig.4.17. Configurations of magnet pole having SAS, SAS+3rd, ICS and ICS+3rd shaping techniques.

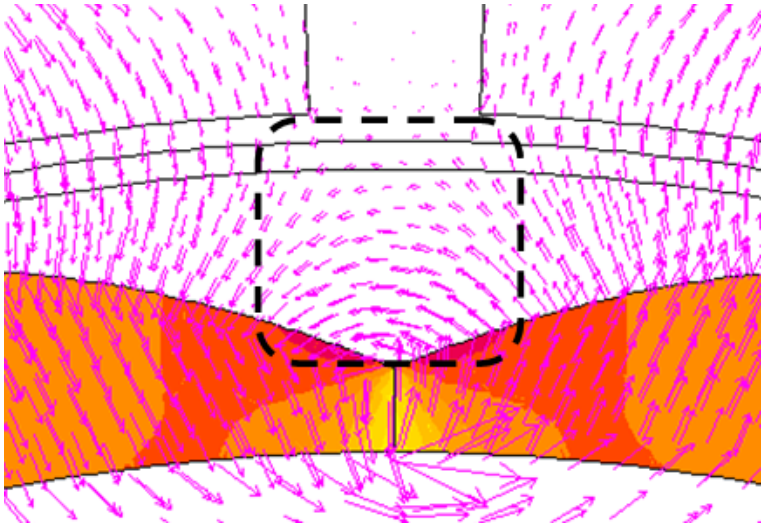

(a) SAS

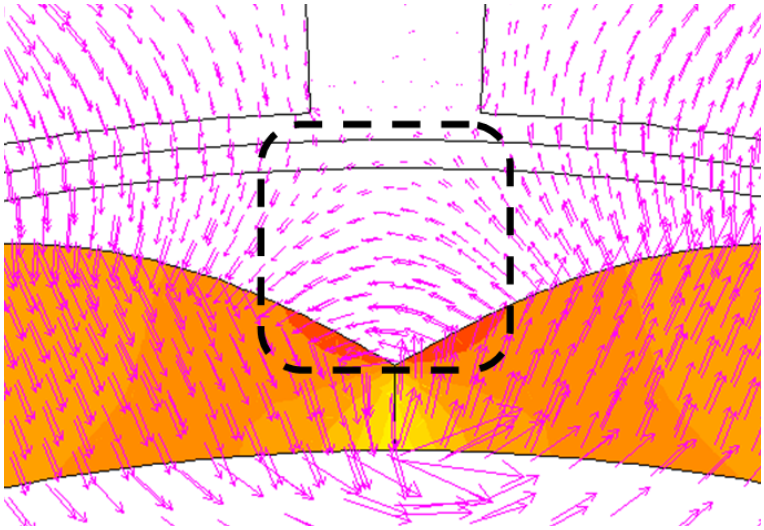

(b) SAS+3rd

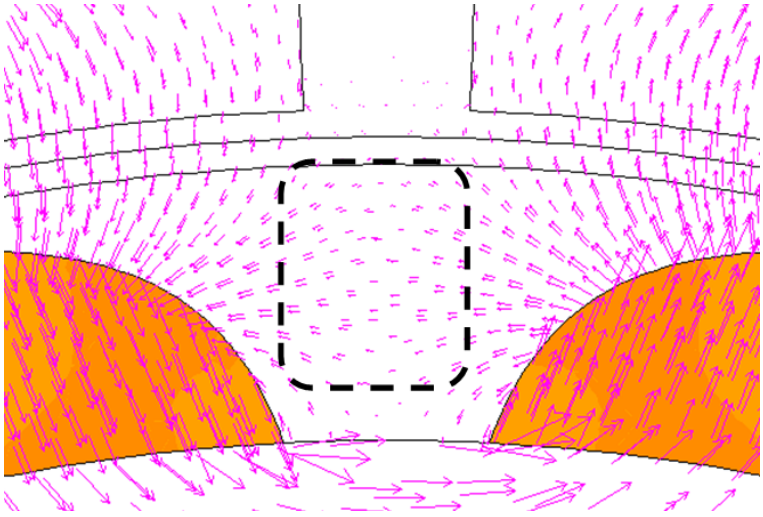

(c) ICS

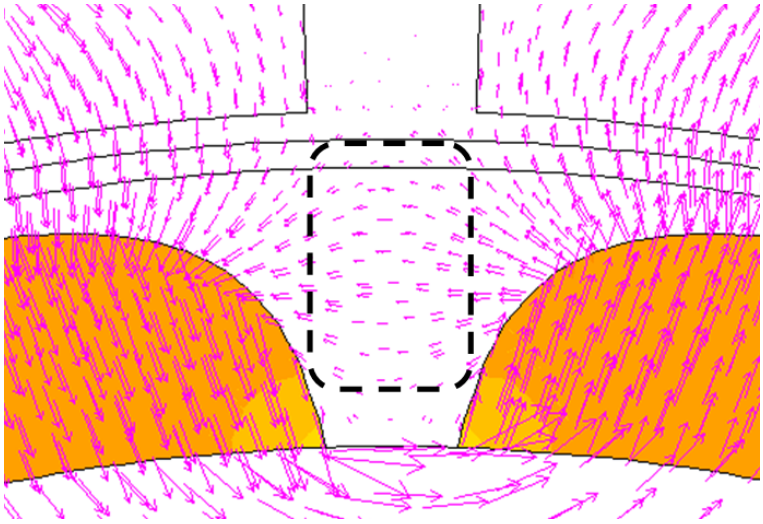

(d) ICS+3rd

Fig.4.18. Inter-pole leakage fluxes for magnet pole having SAS, SAS+3rd, ICS and ICS+3rd shaping techniques.

TABLE.4-IV LINEAR FEA PREDICTED V_{PM} AND T_{EM}

	SAS	SAS+3rd	ICS	ICS+3rd
V_{pm} (x10^{-5} m^3)	1.845	2.020	1.660	1.890
T_{em} (Nm)	4.529	4.931	4.498	4.843

Initially, the magnetization angle $\Delta\theta$ for both Hat- and T-type magnet pole are equal to 90 degree. As can be seen in Fig.4.19, the machines by adopting Hat- and T-type present higher T_{em} than other four magnet shaping methods when h_{pm1} is small which means the corresponding R_{mp} is large due to fixed V_{pm}. It is noticeable that as long as h_{pm1} = 0 mm, the magnet pole is changed into a conventional pole with α_p less than 1. Although the conventional pole with α_p less than 1 presents highest T_{em}, Hat- and T-type magnet pole having $\Delta\theta$ = 90 still exhibit potential to obtain higher T_{em} in contrast with SAS, SAS+3rd, ICS, and ICS+3rd shaping method within the same V_{pm} correspondingly.

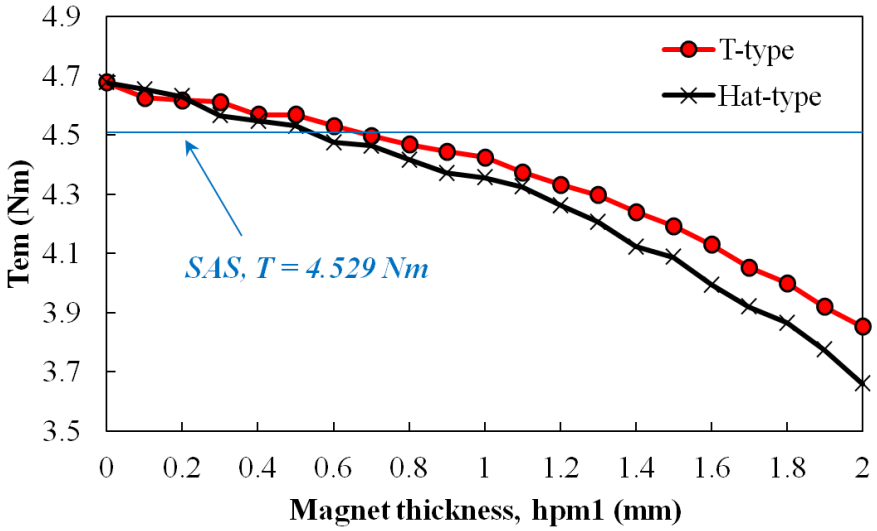

(a)Hat- and T-type versus SAS

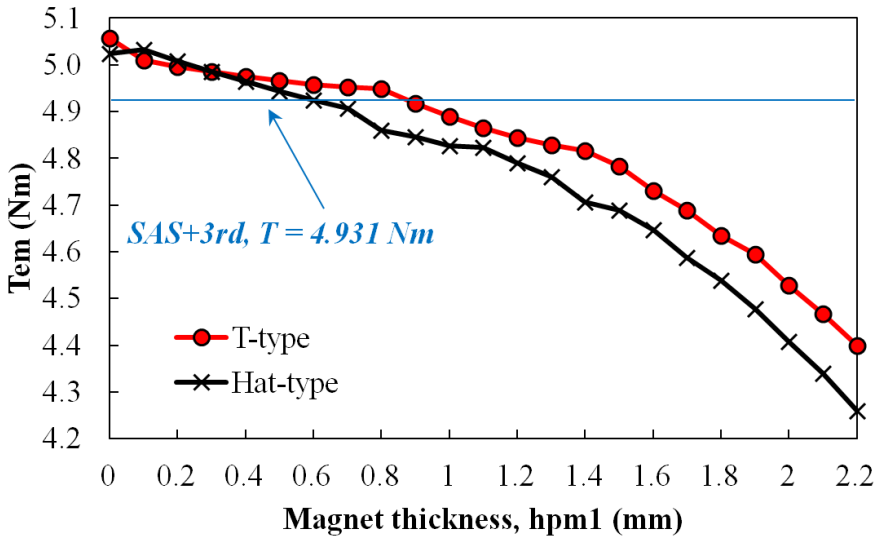

(b) Hat- and T-type versus SAS+3rd

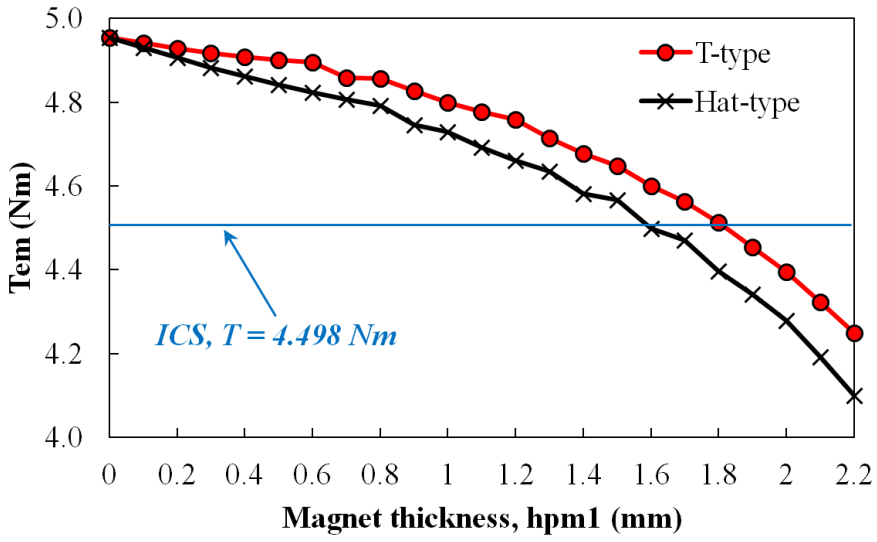

(c) Hat- and T-type versus ICS

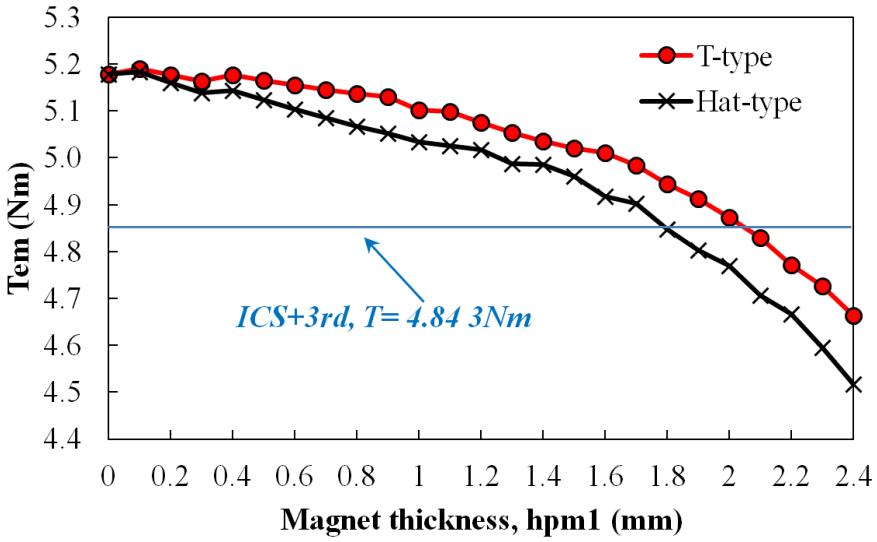

(d) Hat- and T-type versus ICS+3rd

Fig.4.19. Comparison of the analytically predicted T_{em} between 12-slot/10-pole PM brushless machines having Hat- and T-type magnet pole and linear FEA predicted T_{em} for SAS, SAS+3rd, ICS, and ICS+3rd with the same V_{pm} correspondingly.

Furthermore, with consideration of both irreversible demagnetization and manufacturing feasibility, together with maximum T_{em}, h_{pm1} is chosen to be equal to 1.0 mm (in this case, the minimum flux densities in the magnet on full load are 0.437T and 0.2879T for Hat- and T-type magnet poles, respectively) and the corresponding design parameters are listed in TABLE.4-V for further $\Delta\theta$ optimization.

TABLE.4-V INITIALLY OPTIMIZED DESIGN PARAMETERS FOR HAT AND T-TYPE, PLUS CONVENTIONAL POLE

	h_{pm1} = 1.0 mm, h_{pm} = 3.0 mm			
	SAS	SAS+3rd	ICS	ICS+3rd
Hat-type	R_{mp} = 0.63	R_{mp} = 0.74	R_{mp} = 0.53	R_{mp} = 0.66
T-type	R_{mp} = 0.62	R_{mp} = 0.73	R_{mp} = 0.51	R_{mp} = 0.65
Conventional	R_{mp} = 0.75	R_{mp} = 0.82	R_{mp} = 0.68	R_{mp} = 0.77
V_{pm} (x10^{-5} m^3)	1.845	2.020	1.660	1.890

Fig.4.20 and Fig.4.21 show the optimal T_{em} is varied as a function of $\Delta\theta$ for different V_{pm} and magnet shaping techniques. T_{em} reaches the maximum value at magnetization angle $\Delta\theta$ of 70, 64, 74, and 69 for Hat-type when V_{pm} is equal to that of SAS, SAS+3rd, ICS, and ICS+3rd shaping techniques, respectively. Meanwhile, T_{em} reaches the maximum value at $\Delta\theta$ of 34, 26, 42, and 32 for T-type magnet pole when V_{pm} is equal to that of SAS, SAS+3rd, ICS, and

ICS+3rd shaping techniques, respectively.

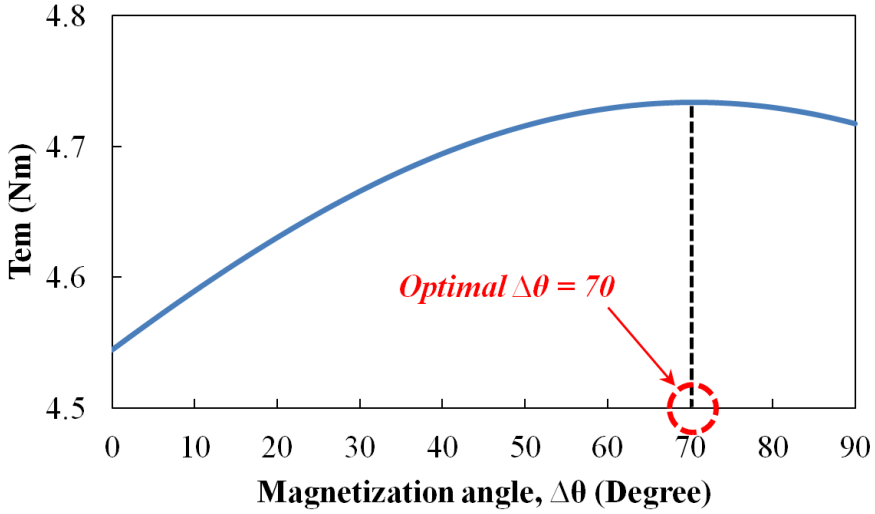

(a) V_{pm} equal to SAS

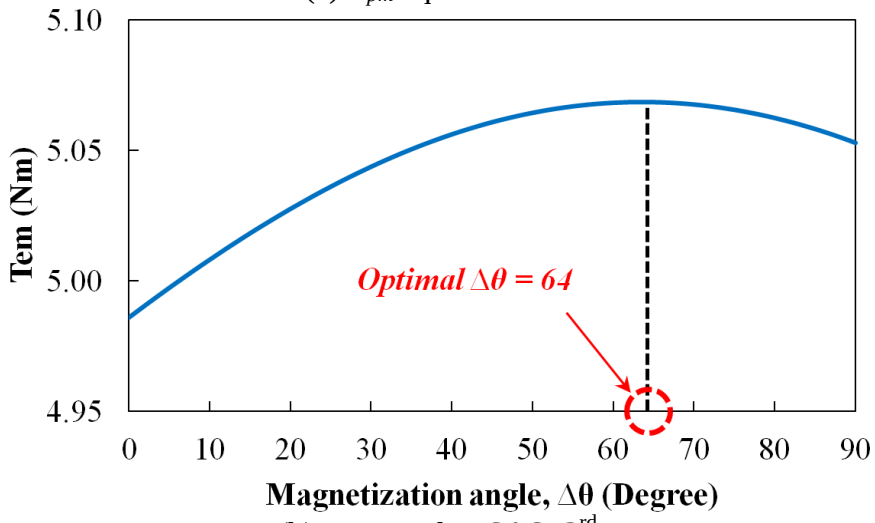

(b) V_{pm} equal to SAS+3rd

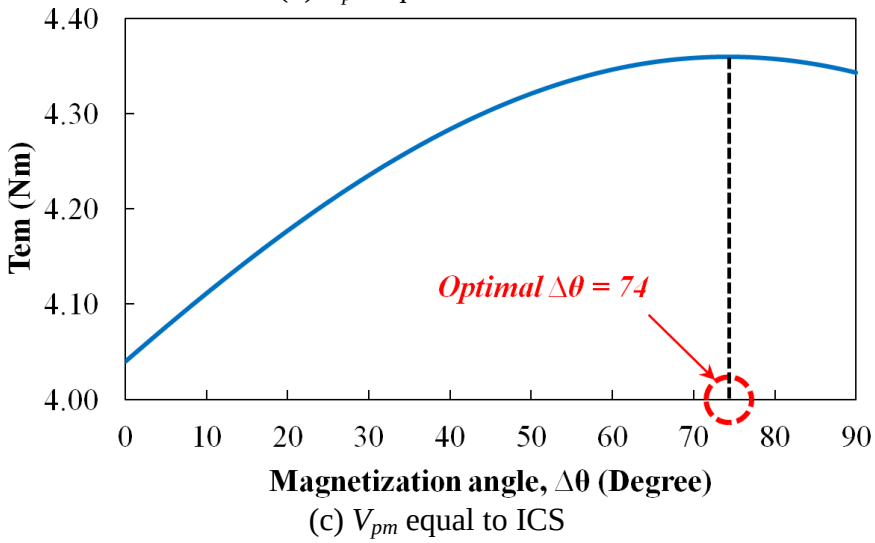

(c) V_{pm} equal to ICS

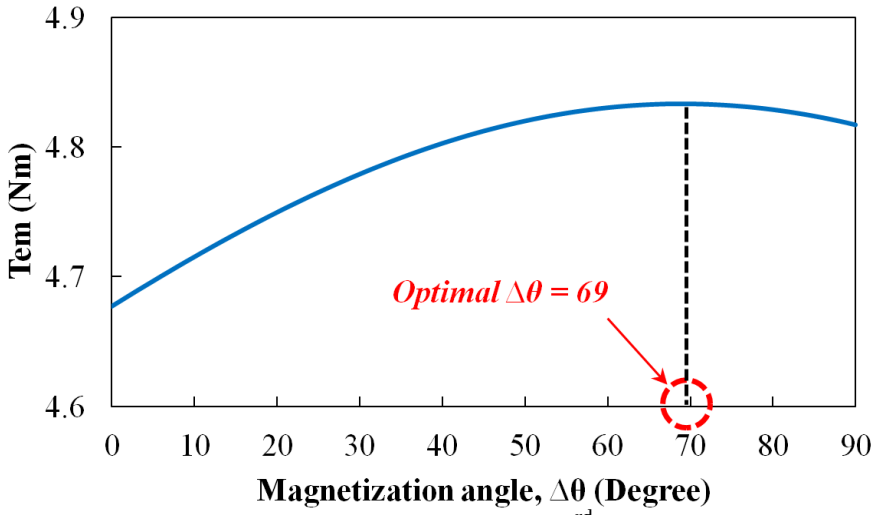

(d) V_{pm} equal to ICS+3rd

Fig.4.20. Analytically predicted variation of optimal $\Delta\theta$ for 12-slot/10-pole PM brushless machine having Hat-type magnet pole.

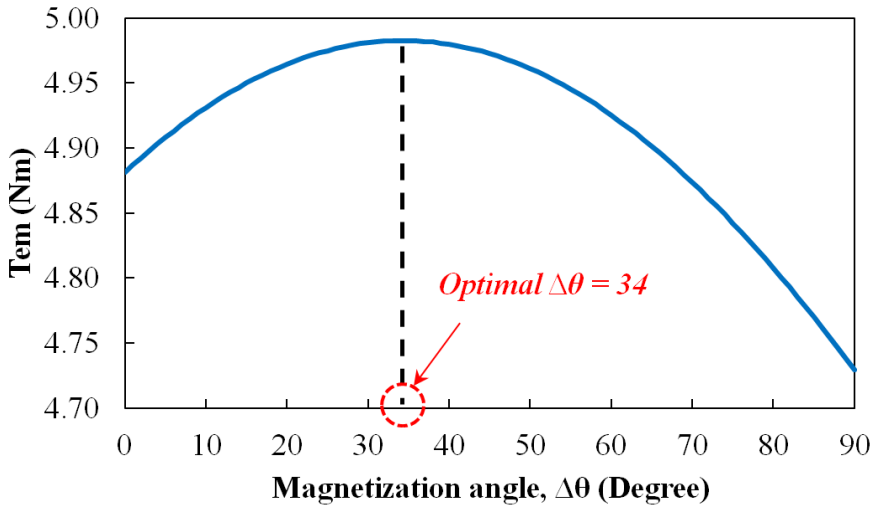

(a) V_{pm} equal to SAS

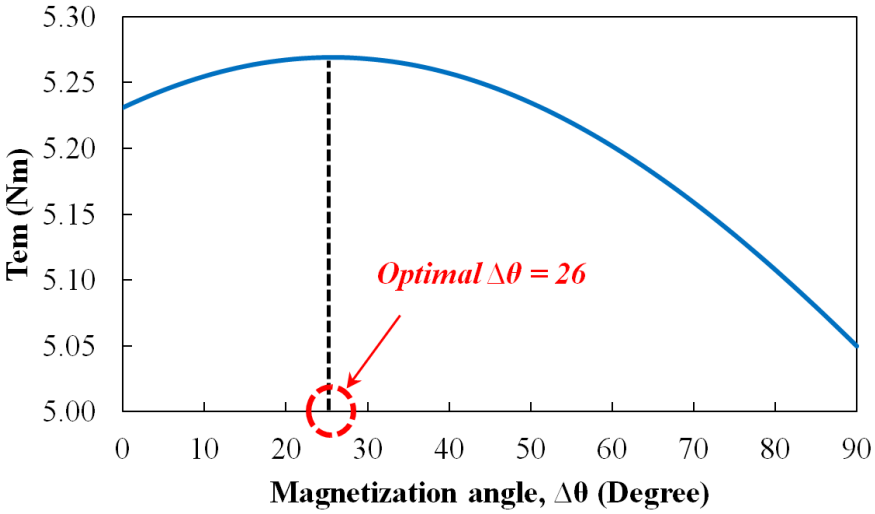

(b) V_{pm} equal to SAS+3rd

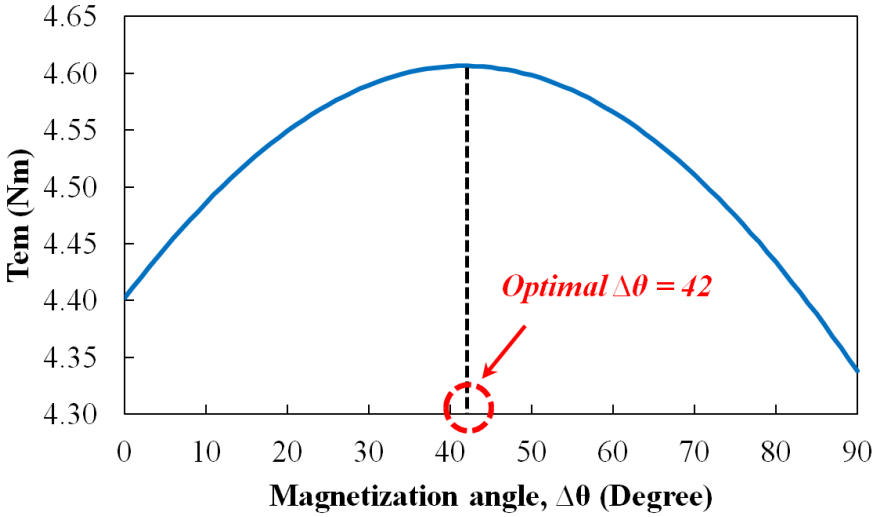

(c) V_{pm} equal to ICS

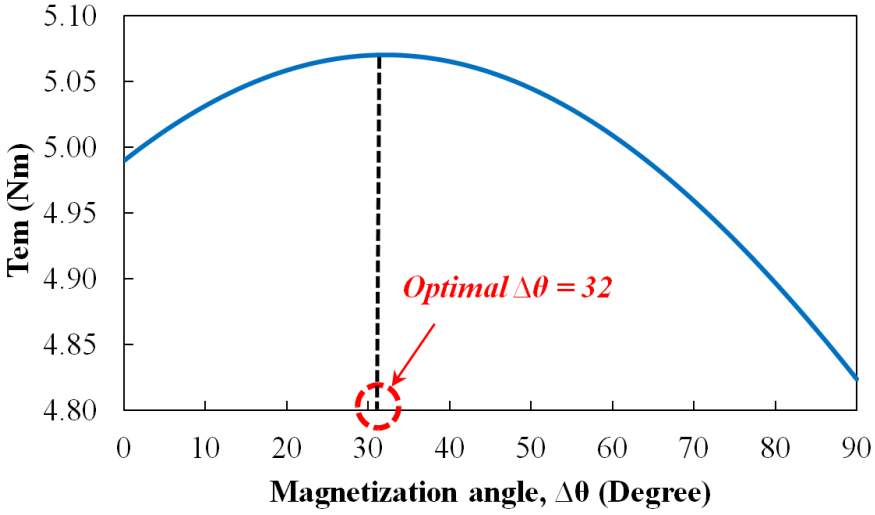

(d) V_{pm} equal to ICS+3rd

Fig.4.21. Analytically predicted variation of optimal $\Delta\theta$ for 12-slot/10-pole PM brushless machine having T-type magnet pole.

Fig.4.22 indicates that the amplitude of T_{em} is significantly boosted by using T-type magnet pole with optimal $\Delta\theta$. The comparison shows that about maximum 5% and 10% increase of torque can be achieved by adopting Hat- and T-type magnet pole in contrast with sine and cosine magnet shaping techniques, but such merit diminishes as V_{pm} reduces. Although the peak-to-peak T_{em} ripple ((4.9)) for magnet pole having both Hat and T-type magnet pole increased by 0.88% and 0.53%, respectively, if compared with both sine and cosine magnet shaping techniques, it is still relatively small and acceptable for high performance applications. Furthermore, the magnet usage for T-type magnet pole is more efficiently than magnet shaping techniques as shown in Table VI.

$$T_{pp} = \frac{T_{max} - T_{min}}{T_{av}} \tag{4.9}$$

where, T_{max} is the maximum amplitude of T_{em} waveform, T_{min} is the minimum amplitude of T_{em} waveform, and T_{av} is the average value of T_{em} waveform.

As can be seen from Fig.4.22 and TABLE.4-VI, the conventional magnet pole having α_p < 1 is main contender with T-type magnet pole when V_{pm} is equal to each other. Therefore, the influence of pole pair number needs to be investigated for understanding the best application for T-type magnet pole in contrast with conventional magnet pole having α_p < 1. For simplicity, Fig.4.24 compares the analytically predicted B_{ag1} for slotless model between conventional magnet pole, Hat- and T-type under four different V_{pm} conditions by having fixed design parameters listed in Table V, where each condition presents the same V_{pm} when p =5 in accordance with SAS, SAS+3rd, ICS and ICS+3rd shaping techniques, respectively. It is observed that the higher the pole pair number, the larger the value of B_{ag1} will be obtained for T-type in contrast with Hat-type and conventional magnet pole (α_p < 1), due to reduced curvature effect. In contrast to analytically predicted results, the amplitudes of electromagnetic torque for different magnet pole structures are decreased by nearly 5%, while the corresponding torque ripples are increased by 10% if compared with non-linear FEA predicted results in Fig 4.23 and Table 4-VII, respectively.

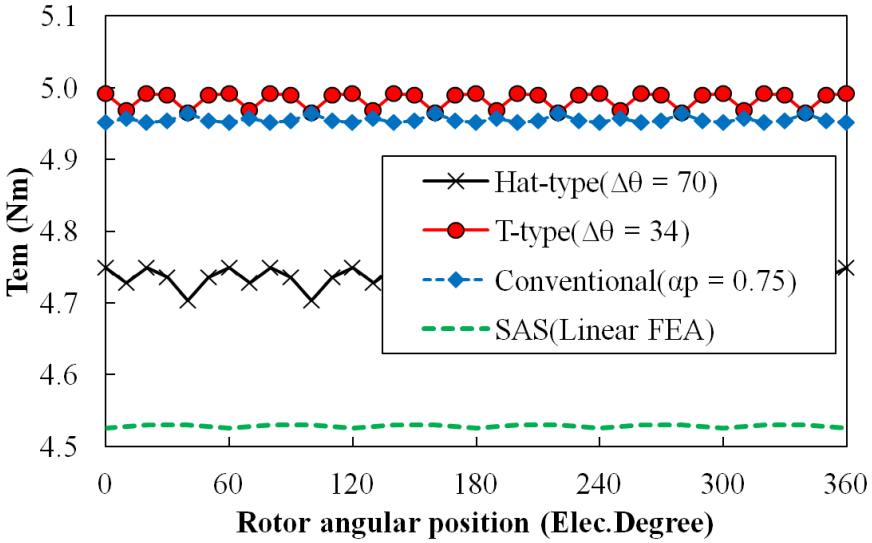

(a) Versus SAS

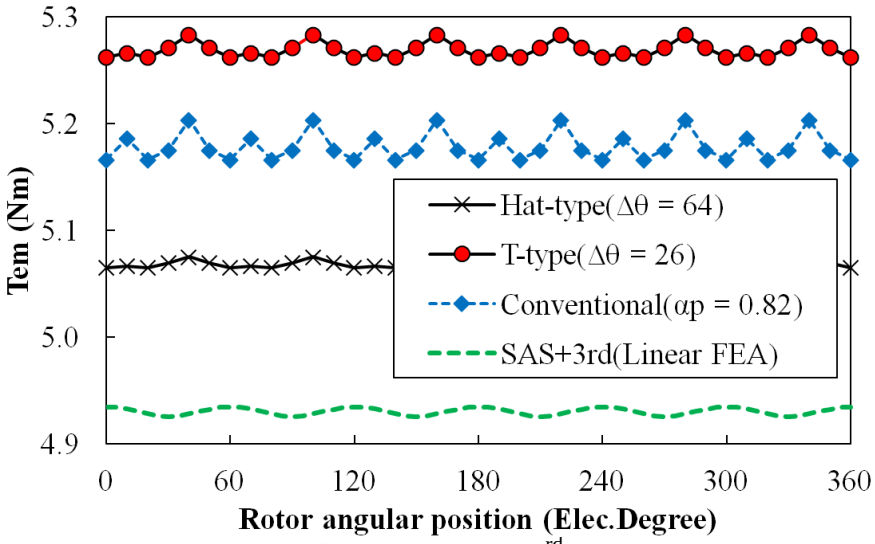

(b) Versus SAS+3rd

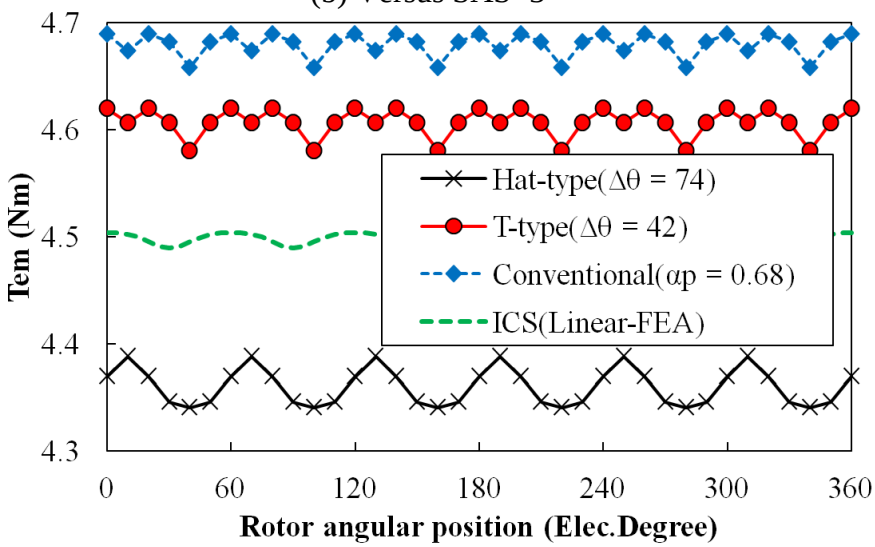

(c) Versus ICS

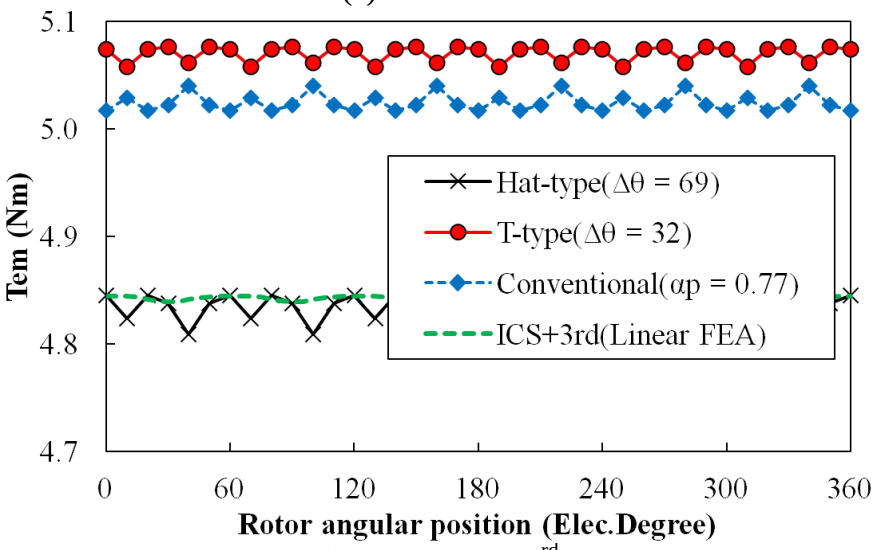

(d) Versus ICS+3rd

Fig.4.22. Comparison of analytically predicted T_{em} waveform for 12-slot/10-pole PM brushless machine having magnet pole with α_p < 1, Hat and T-type magnet poles between linear FEA predicted T_{em} for machine having SAS, SAS+3rd, ICS, and ICS+3rd shaping method, together with the same V_{pm}.

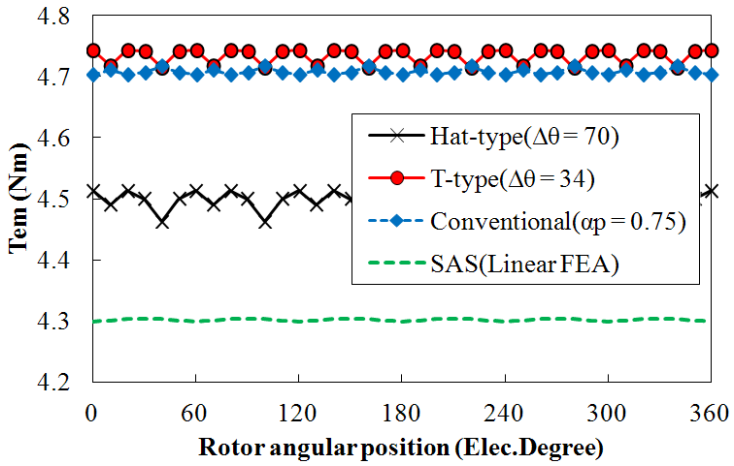

(a) Versus SAS

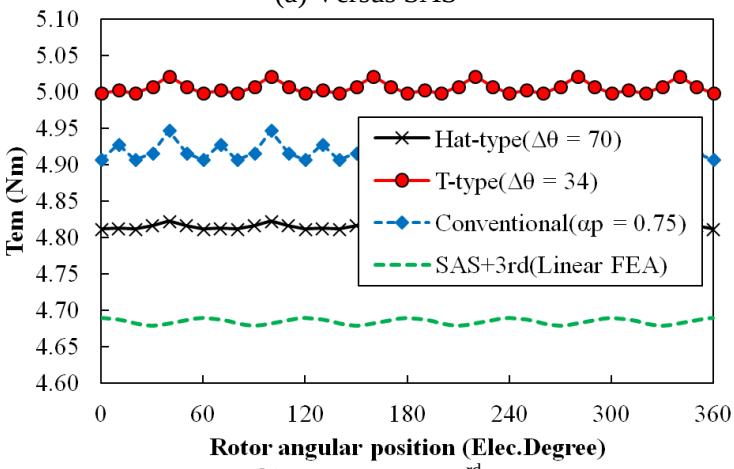

(b) Versus SAS+3rd

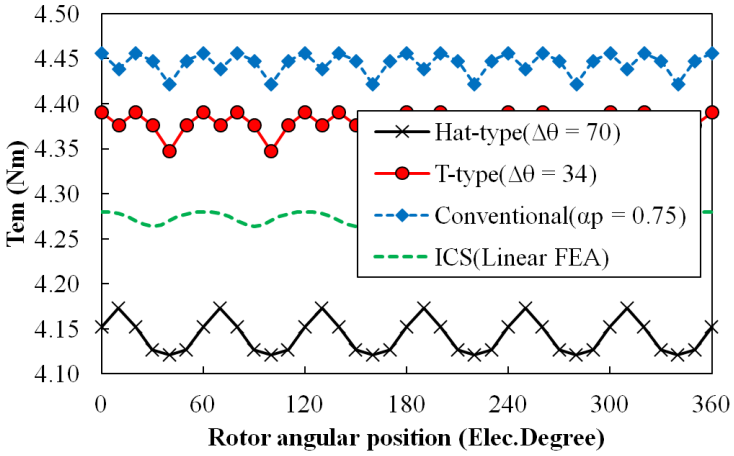

(c) Versus ICS

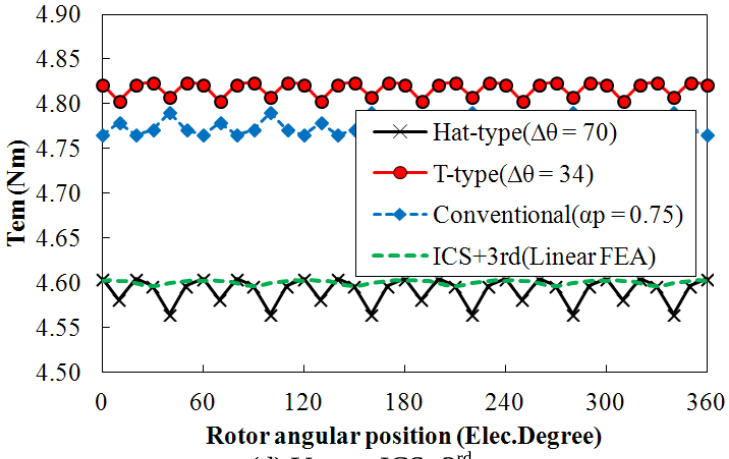

(d) Versus ICS+3rd

Fig.4.23. Comparison of non-linear FEA predicted T_{em} waveform for 12-slot/10-pole PM brushless machine having magnet pole with $\alpha_p < 1$, Hat and T-type magnet poles between linear FEA predicted T_{em} for machine having SAS, SAS+3rd, ICS, and ICS+3rd shaping method, together with the same V_{pm}.

TABLE.4-VI COMPARISON OF ELECTROMAGNETIC TORQUE (NM), CORRESPONDING PEAK-TO-PEAK TORQUE RIPPLE RATIO (%) AND MAGNET USAGE EFFICIENCY (X10^5NM/M^3)

		Magnet pole			
Designated V_{pm}		Hat-type	T-type	Conventional	SAS
SAS	T_{em}	4.73	4.98	4.96	4.53
	T_{pp}	0.97%	0.53%	0.25%	0.09%
	η_{PM}	2.57	2.70	2.69	2.46
Designated V_{pm}		Hat-type	T-type	Conventional	SAS+3rd
SAS+3rd	T_{em}	5.07	5.27	5.18	4.93
	T_{pp}	0.20%	0.40%	0.72%	0.19%
	η_{PM}	2.51	2.61	2.56	2.44
Designated V_{pm}		Hat-type	T-type	Conventional	ICS
ICS	T_{em}	4.36	4.61	4.68	4.50
	T_{pp}	1.09%	0.85%	0.67%	0.32%
	η_{PM}	2.63	2.78	2.82	2.71
Designated V_{pm}		Hat-type	T-type	Conventional	ICS+3rd
ICS+3rd	T_{em}	4.83	5.07	5.03	4.84
	T_{pp}	0.75%	0.38%	0.46%	0.11%
	η_{PM}	2.56	2.68	2.66	2.56

TABLE.4-VII COMPARISON OF NON-LINEAR FEA PREDICTED ELECTROMAGNETIC TORQUE (NM), CORRESPONDING PEAK-TO-PEAK TORQUE RIPPLE RATIO (%) AND MAGNET USAGE EFFICIENCY (X10^5NM/M^3)

		Magnet pole			
Designated V_{pm}		Hat-type	T-type	Conventional	SAS
SAS	T_{em}	4.49	4.73	4.71	4.30
	T_{pp}	1.07%	0.58%	0.28%	0.10%
	η_{PM}	2.44	2.57	2.56	2.34
Designated V_{pm}		Hat-type	T-type	Conventional	SAS+3rd
SAS+3rd	T_{em}	4.82	5.01	4.92	4.68
	T_{pp}	0.22%	0.44%	0.79%	0.21%
	η_{PM}	2.39	2.48	2.43	2.32
Designated V_{pm}		Hat-type	T-type	Conventional	ICS
ICS	T_{em}	4.14	4.38	4.45	4.28
	T_{pp}	1.20%	0.94%	0.74%	0.35%
	η_{PM}	2.50	2.64	2.68	2.58
Designated V_{pm}		Hat-type	T-type	Conventional	ICS+3rd
ICS+3rd	T_{em}	4.59	4.82	4.78	4.60
	T_{pp}	0.83%	0.42%	0.51%	0.12%
	η_{PM}	2.43	2.55	2.53	2.43

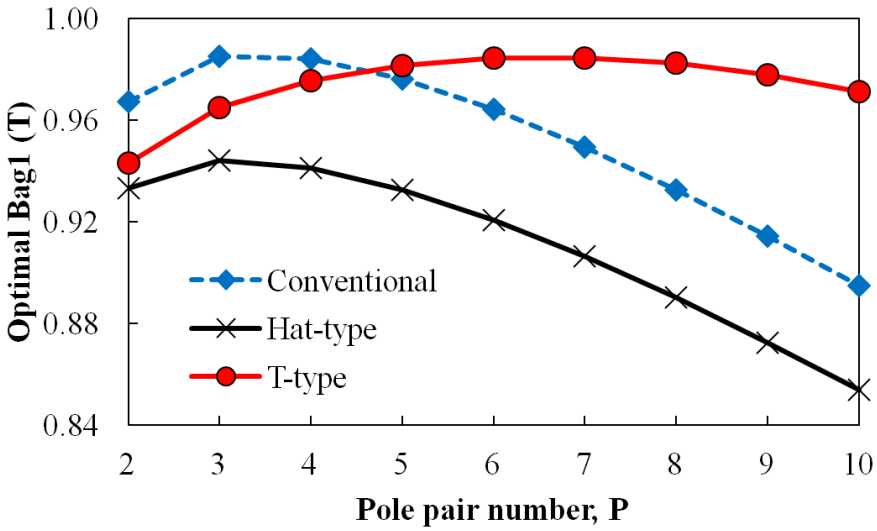

(a) V_{pm} equal to SAS when p = 5

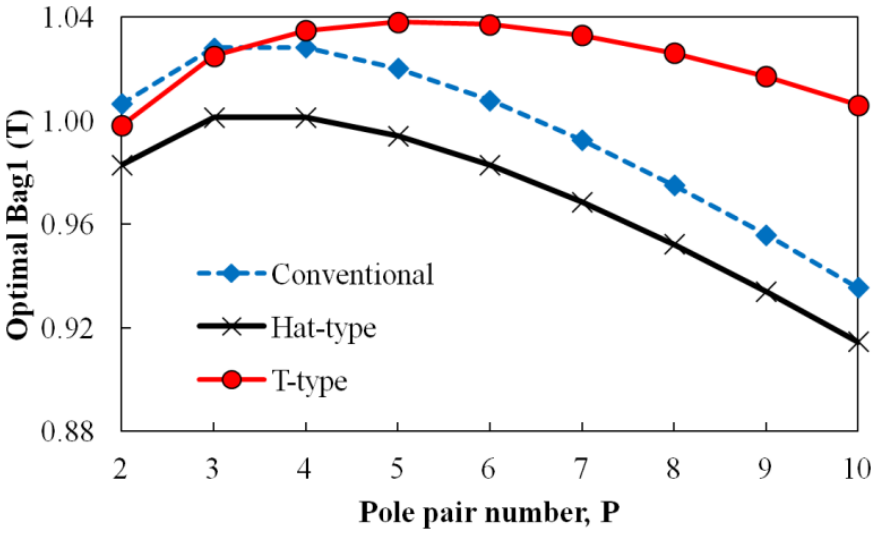

(b) V_{pm} equal to SAS+3rd when p = 5

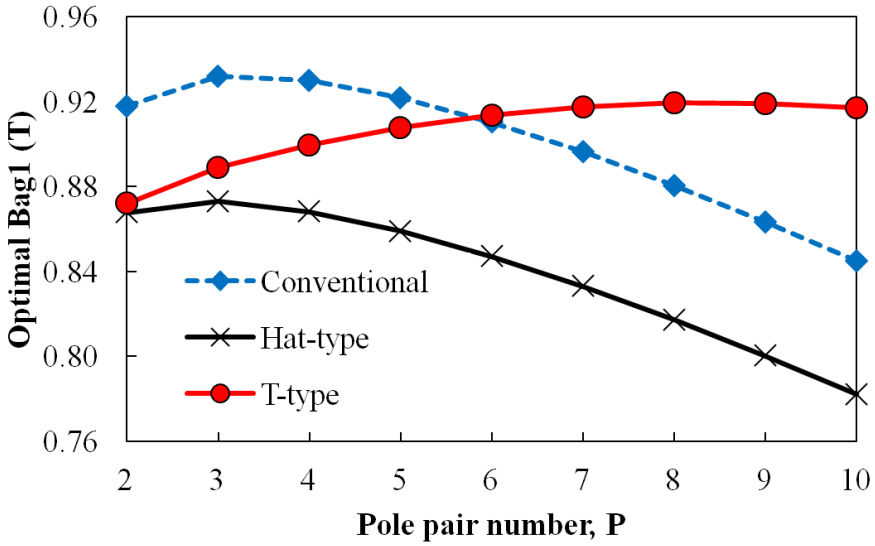

(c) V_{pm} equal to ICS when p = 5

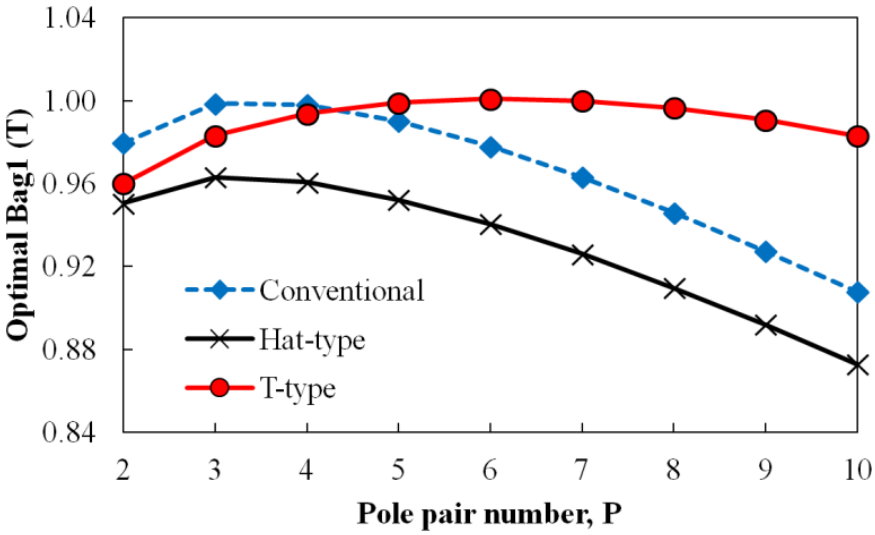

(d) V_{pm} equal to ICS+3rd when p = 5

Fig.4.24. Comparison of analytically predicted optimal B_{ag1} with the variation of both $\Delta\theta$ and p for slotless model under four V_{pm} conditions.

4.7 Summary

This chapter proposes magnet poles having unequal-magnet height, i.e. the Hat- and T-type magnets, together with optimized Halbach magnetization. An analytical model based on sub-domain technique is developed and validated by FEA for investigation. It shows that T-type magnet pole exhibits significant potential to achieve low torque ripple, high electromagnetic torque, and low magnet usage simultaneously. T-type magnet pole presents relative larger ratio of average output torque to PM volume in contrast with conventional 3-segment Halbach array. By adopting T-type magnet pole, the inherent large inter-pole leakage flux is significantly reduced in contrast with Hat-type magnet pole and traditional magnet shaping techniques.

4.8 Appendix

According to (4.2), the expression of M_{rn} can be fully expanded and deduced as:

$$
\begin{aligned}
M_{rn} = \frac{\mathrm{p}}{\pi}\Bigg\{ & -\frac{B_{rs}}{2\mu_0}\cos\Delta\theta\left[\frac{\cos\left[(1+np)\left(-\frac{R_{mp}\pi}{2p}\right)+\delta\right]}{1+np}-\frac{\cos\left[(1+np)\left(-\frac{\alpha_p\pi}{2p}\right)+\delta\right]}{1+np}\right. \\
& \left.+\frac{\cos\left[(1-np)\left(-\frac{R_{mp}\pi}{2p}\right)+\delta\right]}{1-np}-\frac{\cos\left[(1-np)\left(-\frac{\alpha_p\pi}{2p}\right)+\delta\right]}{1-np}\right]+ \\
& \frac{B_{rm}}{2\mu_0}\left[\frac{\sin\left[(1+np)\frac{R_{mp}\pi}{2p}\right]}{1+np}-\frac{\sin\left[(1+np)\left(-\frac{R_{mp}\pi}{2p}\right)\right]}{1+np}+\right. \\
& \left.\frac{\sin\left[(1-np)\frac{R_{mp}\pi}{2p}\right]}{1-np}-\frac{\sin\left[(1-np)\left(-\frac{R_{mp}\pi}{2p}\right)\right]}{1-np}\right]+ \\
& \frac{B_{rs}}{2\mu_0}\cos\Delta\theta\left[\frac{\cos\left[(1+np)\frac{\alpha_p\pi}{2p}-\delta\right]}{1+np}-\frac{\cos\left[(1+np)\frac{R_{mp}\pi}{2p}-\delta\right]}{1+np}+\right.
\end{aligned}
$$

$$\left.\frac{cos\left[(1-np)\frac{\alpha_p\pi}{2p}-\delta\right]}{1-np}-\frac{cos\left[(1-np)\frac{R_{mp}\pi}{2p}-\delta\right]}{1-np}\right]+$$

$$\frac{B_{rs}}{2\mu_0}cos\,\Delta\theta\left[\frac{cos\left[(1+np)\left(1-\frac{R_{mp}}{2}\right)\frac{\pi}{p}-\frac{\pi}{p}+\delta\right]}{1+np}-\frac{cos\left[(1+np)\left(1-\frac{\alpha_p}{2}\right)\frac{\pi}{p}-\frac{\pi}{p}+\delta\right]}{1+np}+\right.$$

$$\left.\frac{cos\left[(1-np)\left(1-\frac{R_{mp}}{2}\right)\frac{\pi}{p}-\frac{\pi}{p}+\delta\right]}{1-np}-\frac{cos\left[(1-np)\left(1-\frac{\alpha_p}{2}\right)\frac{\pi}{p}-\frac{\pi}{p}+\delta\right]}{1-np}\right]-$$

$$\frac{B_{rm}}{2\mu_0}\left[\frac{sin\left[(1+np)\left(1+\frac{R_{mp}}{2}\right)\frac{\pi}{p}-\frac{\pi}{p}\right]}{1+np}-\frac{sin\left[(1+np)\left(1-\frac{R_{mp}}{2}\right)\frac{\pi}{p}-\frac{\pi}{p}\right]}{1+np}+\right.$$

$$\left.\frac{sin\left[(1-np)\left(1+\frac{R_{mp}}{2}\right)\frac{\pi}{p}-\frac{\pi}{p}\right]}{1-np}-\frac{sin\left[(1-np)\left(1-\frac{R_{mp}}{2}\right)\frac{\pi}{p}-\frac{\pi}{p}\right]}{1-np}\right]-$$

$$\frac{B_{rs}}{2\mu_0}cos\,\Delta\theta\left[\frac{cos\left[(1+np)\left(1+\frac{\alpha_p}{2}\right)\frac{\pi}{p}-\frac{\pi}{p}-\delta\right]}{1+np}-\frac{cos\left[(1+np)\left(1+\frac{R_{mp}}{2}\right)\frac{\pi}{p}-\frac{\pi}{p}-\delta\right]}{1+np}+\right.$$

$$\left.\left.\frac{cos\left[(1-np)\left(1+\frac{\alpha_p}{2}\right)\frac{\pi}{p}-\frac{\pi}{p}-\delta\right]}{1-np}-\frac{cos\left[(1-np)\left(1+\frac{R_{mp}}{2}\right)\frac{\pi}{p}-\frac{\pi}{p}-\delta\right]}{1-np}\right]\right\}+$$

$$\frac{p}{\pi}\left\{\frac{2B_{rs}}{\mu_0}sin\,\Delta\theta\left[-\frac{sin\left[(1+np)\frac{R_{mp}\pi}{2p}-\delta\right]}{1+np}+\frac{sin\left[(1+np)\frac{\alpha_p\pi}{2p}-\delta\right]}{1+np}-\right.\right.$$

$$\left.\left.\frac{sin\left[(1-np)\frac{R_{mp}\pi}{2p}-\delta\right]}{1-np}+\frac{sin\left[(1-np)\frac{\alpha_p\pi}{2p}-\delta\right]}{1-np}\right]\right\} \tag{4.10}$$

Similarly, according to (4.3), the circumferential air-gap flux density component $M_{\theta n}$ can be deduced as:

$$M_{\theta n} = \frac{\mathrm{p}}{\pi}\left\{-\frac{B_{rs}}{2\mu_0}\cos\Delta\theta\left[\frac{\cos\left[(1+np)\left(-\frac{R_{mp}\pi}{2p}\right)+\delta\right]}{1+np}-\frac{\cos\left[(1+np)\left(-\frac{\alpha_p\pi}{2p}\right)+\delta\right]}{1+np}\right.\right.$$

$$\left.-\frac{\cos\left[(1-np)\left(-\frac{R_{mp}\pi}{2p}\right)+\delta\right]}{1-np}+\frac{\cos\left[(1-np)\left(-\frac{\alpha_p\pi}{2p}\right)+\delta\right]}{1-np}\right]+$$

$$\frac{B_{rm}}{2\mu_0}\left[\frac{\sin\left[(1+np)\frac{R_{mp}\pi}{2p}\right]}{1+np}-\frac{\sin\left[(1+np)\left(-\frac{R_{mp}\pi}{2p}\right)\right]}{1+np}-\right.$$

$$\left.\frac{\sin\left[(1-np)\frac{R_{mp}\pi}{2p}\right]}{1-np}+\frac{\sin\left[(1-np)\left(-\frac{R_{mp}\pi}{2p}\right)\right]}{1-np}\right]+$$

$$\frac{B_{rs}}{2\mu_0}\cos\Delta\theta\left[\frac{\cos\left[(1+np)\frac{\alpha_p\pi}{2p}-\delta\right]}{1+np}-\frac{\cos\left[(1+np)\frac{R_{mp}\pi}{2p}-\delta\right]}{1+np}-\right.$$

$$\left.\frac{\cos\left[(1-np)\frac{\alpha_p\pi}{2p}-\delta\right]}{1-np}+\frac{\cos\left[(1-np)\frac{R_{mp}\pi}{2p}-\delta\right]}{1-np}\right]+$$

$$\frac{B_{rs}}{2\mu_0}\cos\Delta\theta\left[\frac{\cos\left[(1+np)\left(1-\frac{R_{mp}}{2}\right)\frac{\pi}{p}-\frac{\pi}{p}+\delta\right]}{1+np}-\frac{\cos\left[(1+np)\left(1-\frac{\alpha_p}{2}\right)\frac{\pi}{p}-\frac{\pi}{p}+\delta\right]}{1+np}-\right.$$

$$\left.\frac{\cos\left[(1-np)\left(1-\frac{R_{mp}}{2}\right)\frac{\pi}{p}-\frac{\pi}{p}+\delta\right]}{1-np}+\frac{\cos\left[(1-np)\left(1-\frac{\alpha_p}{2}\right)\frac{\pi}{p}-\frac{\pi}{p}+\delta\right]}{1-np}\right]-$$

$$\frac{B_{rm}}{2\mu_0}\left[\frac{\sin\left[(1+np)\left(1+\frac{R_{mp}}{2}\right)\frac{\pi}{p}-\frac{\pi}{p}\right]}{1+np}-\frac{\sin\left[(1+np)\left(1-\frac{R_{mp}}{2}\right)\frac{\pi}{p}-\frac{\pi}{p}\right]}{1+np}-\right.$$

$$\left.\frac{\sin\left[(1-np)\left(1+\frac{R_{mp}}{2}\right)\frac{\pi}{p}-\frac{\pi}{p}\right]}{1-np}+\frac{\sin\left[(1-np)\left(1-\frac{R_{mp}}{2}\right)\frac{\pi}{p}-\frac{\pi}{p}\right]}{1-np}\right]-$$

$$\frac{B_{rs}}{2\mu_0}\cos\Delta\theta\left[\frac{\cos\left[(1+np)\left(1+\frac{\alpha_p}{2}\right)\frac{\pi}{p}-\frac{\pi}{p}-\delta\right]}{1+np}-\frac{\cos\left[(1+np)\left(1+\frac{R_{mp}}{2}\right)\frac{\pi}{p}-\frac{\pi}{p}-\delta\right]}{1+np}-\right.$$

$$\left.\frac{\cos\left[(1-np)\left(1+\frac{\alpha_p}{2}\right)\frac{\pi}{p}-\frac{\pi}{p}-\delta\right]}{1-np}+\frac{\cos\left[(1-np)\left(1+\frac{R_{mp}}{2}\right)\frac{\pi}{p}-\frac{\pi}{p}-\delta\right]}{1-np}\right]\Bigg\}+$$

$$\frac{p}{\pi}\left\{\frac{2B_{rm}}{\mu_0}\sin\Delta\theta\left[-\frac{\sin\left[(1+np)\frac{R_{mp}\pi}{2p}-\delta\right]}{1+np}+\frac{\sin\left[(1+np)\frac{\alpha_p\pi}{2p}-\delta\right]}{1+np}+\right.\right.$$

$$\left.\left.\frac{\sin\left[(1-np)\frac{R_{mp}\pi}{2p}-\delta\right]}{1-np}-\frac{\sin\left[(1-np)\frac{\alpha_p\pi}{2p}-\delta\right]}{1-np}\right]\right\} \qquad (4.11)$$

CHAPTER 5 ANALYSIS OF ELECTROMAGNETIC PERFORMANCE OF HALBACH PM BRUSHLESS MACHINES HAVING MIXED GRADE AND UNEQUAL HEIGHT OF MAGNETS

The PM brushless machine having mixed high cost NdFeB and low cost ferrite magnets with modular unequal height pole, i.e. the modular Hat- and T-type poles, together with optimized Halbach magnetization are proposed in this chapter. The electromagnetic performances of proposed magnet poles are analytically investigated, together with the finite element analyses.

5.1 Introduction

Since the Neodymium Iron Baron (NdFeB) magnets were developed in early 1980s [1][2], they are becoming increasingly popular across a wide range of products, such as high performance motors and generators for aerospace, automotive, renewable energy, and domestic appliances etc. However, the price of NdFeB magnets has been raised rapidly over the last few years, which has increased the awareness of cost-effective design and leads the magnet usage efficiency η_{pm}, to be an important design concern for industry applications. Meanwhile, low torque ripple and sinusoidal air-gap flux density are desirable for many applications. As regards to foregoing discussions, the employment of magnet shaping and Halbach magnetization may be difficult to achieve high η_{pm}. It is therefore the Hat- and T-type magnet poles are proposed in chapter 4, which combined merits of both shaping and Halbach magnetization. Recently, apart from those magnet poles, the modular pole technique is introduced by adopting different magnet materials to create magnet pole [175]-[177].With the aid of proper design, high η_{pm} for machines having modular pole technique can be achievable. This chapter aims to combine the merits of previous proposed Hat- and T-type magnet pole and modular pole technique to achieve low ripple and high η_{pm}, while avoid the negative impact of inter-pole leakage on output torque.

The magnet poles having unequal-magnet height, modular high cost NdFeB (white part) and low cost ferrite (grey part) magnets, together with Halbach magnetization are proposed in this chapter, as illustrated in Fig.5.1(c)-(f), which are designated as modular Hat-type with equal side-magnet height (modular Hat-type ESMH, Fig.5.1(c)), modular T-type with equal side-magnet height (modular T-type ESMH, Fig.5.1(d)), modular Hat-type with unequal side-magnet height and magnet grade (modular Hat-type USMH, Fig.5.1(e)) and modular T-type

with unequal side-magnet height and magnet grade (modular T-type USMH, Fig.5.1(f)) magnet poles, respectively. Further, Fig.5.1 also shows the conventional Hat-type and T-type magnet poles (Fig.5.1(a) and (b)) in which the side magnets have the same material as the mid-magnet segment but different height. It should be noted that, in the modular Hat- and T-type magnet poles, where each magnet pole is constructed by a mid-magnet, plus a side-magnet on left and right sides which may exhibit different magnetization direction, magnet grade, or height. In each magnet, the magnet segment is parallel magnetized. In order to facilitate a comparative study and design optimization, a 2-D field model with SD method is developed for predicting the magnetic field distribution and electromagnetic torque, while its accuracy is examined by FEA. The comparison study between 12-slot/10-pole PM brushless machine having conventional and modular Hat- and T-type magnet poles and conventional 3-segments Halbach array is carried out. The demagnetization withstand capabilities are also examined. Moreover, the influence of rotor pole pair number is investigated.

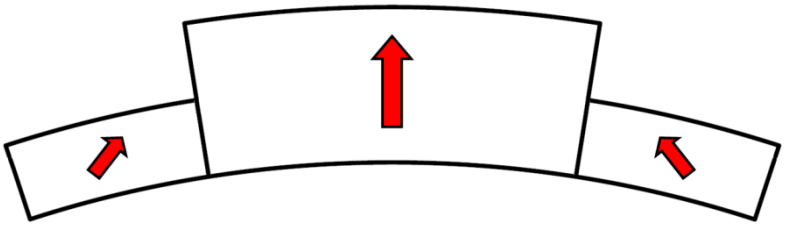

(a) Conventional Hat-type

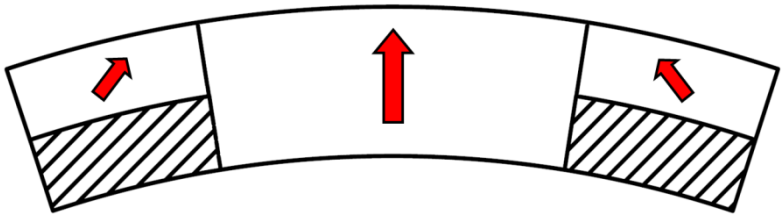

(b) Conventional T-type

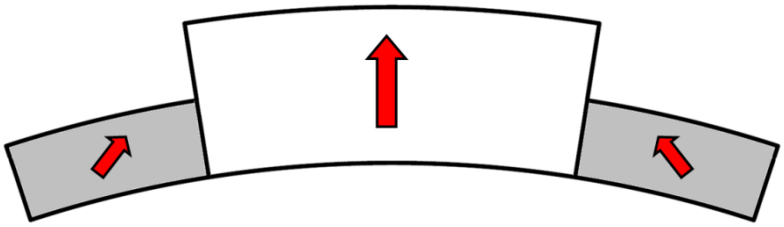

(c) Modular Hat-type ESMH

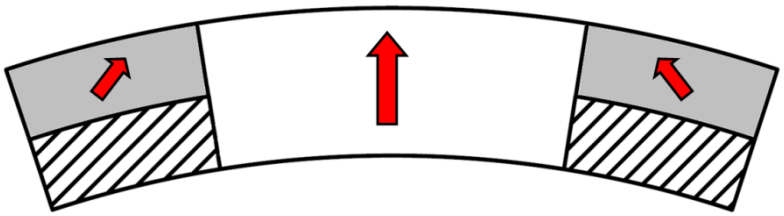

(d) Modular T-type ESMH

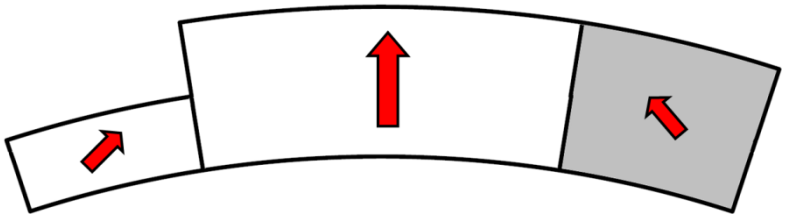

(e) Modular Hat-type USMH

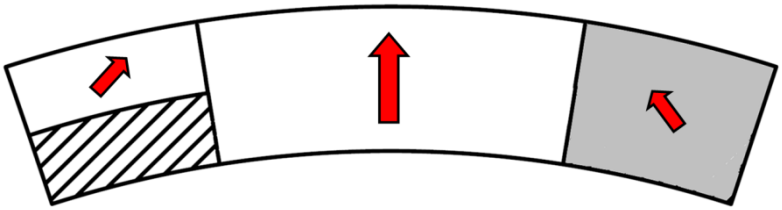

(f) Modular T-type USMH

Fig.5.1. Configurations of conventional and modular Hat- and T-type magnet poles.

5.2 Analytical Sub-Domain Models for Modular Hat- and T-Type PM Machines

Similar to foregoing developed SD model, the symbols and cross-sectional diagram of proposed T-type USMH is illustrated in Fig.5.2, where the straight stator tooth and non-magnetic base in used again to simplify the analysis.

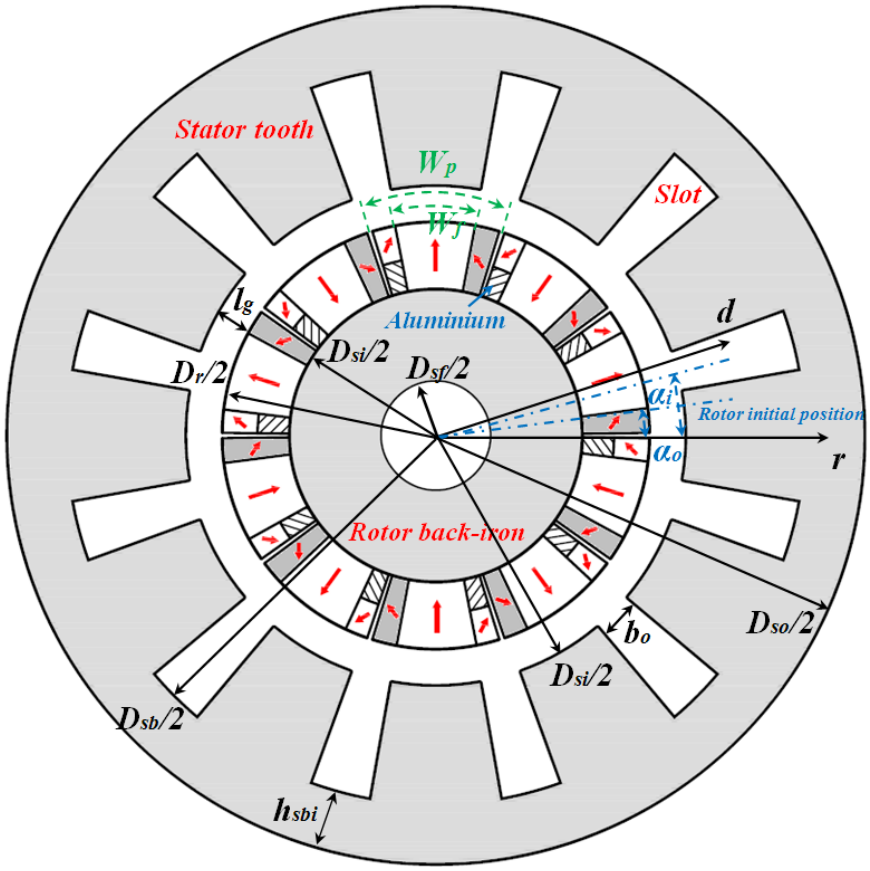

Fig.5.2. Symbols and cross-section of PM brushless machine having modular T-type USMH magnet pole in SD model.

For each magnet segment, if its magnetization is parallel and the magnet height is equal to each other, these magnetization components with design parameters shown in Fig.5.3(c) are fully described in TABLE.5-I over one pole pair, where B_{rm} is the remanence of mid-magnet, B_{rsL} is the remanence of left side-magnet, B_{rsR} is the remanence of right side-magnet, h_{pm} is the magnet height for mid-magnet, h_{pmL} is the magnet heights of left side-magnet, h_{pmR} is the magnet height of right side-magnet. The magnetization directions for both left and right side-magnet are represented as $\Delta\theta_L$ and $\Delta\theta_R$, respectively. Moreover, it should be noted that the side-magnet thickness for USMH poles needs to be adjusted to avoid even-harmonic contents due to asymmetric distributed air-gap flux density waveform.

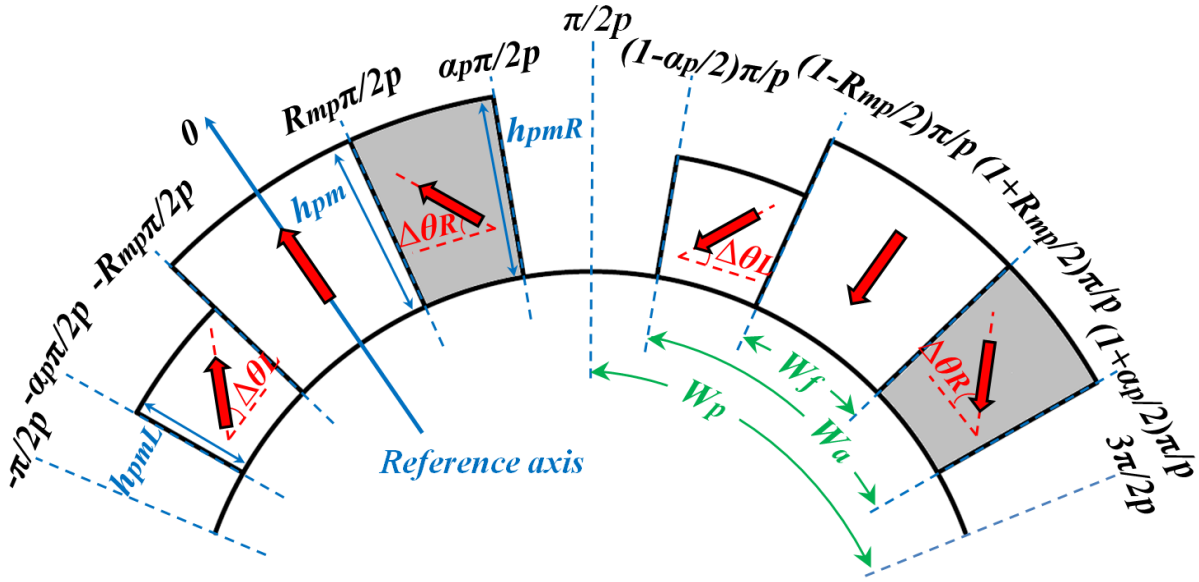

(a) Modular Hat-type USMH

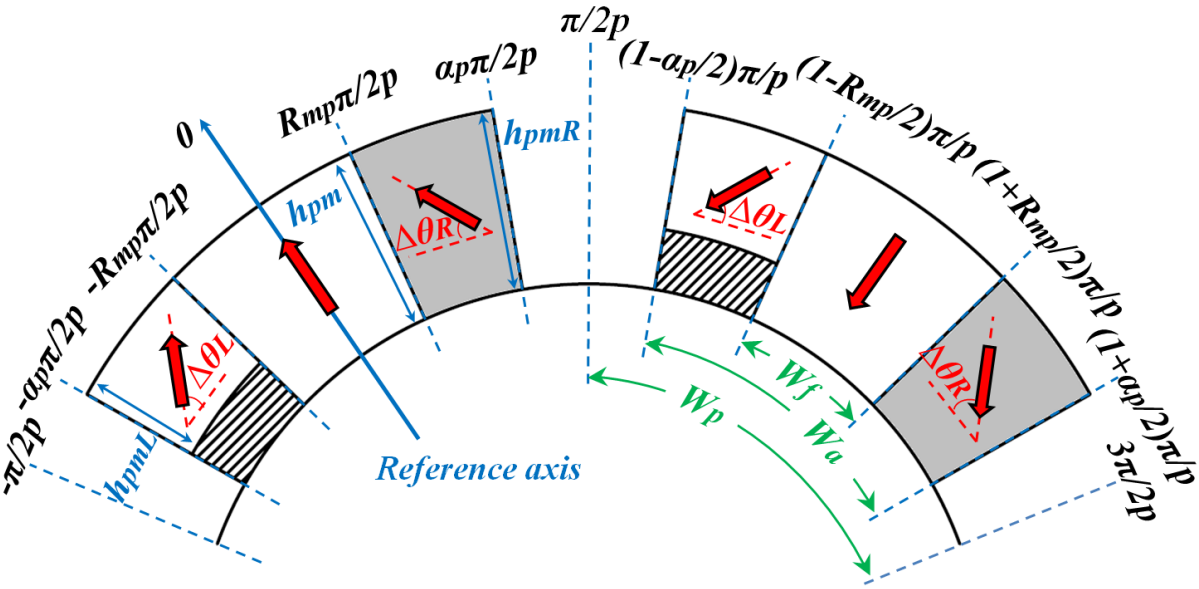

(b) Modular T-type USMH with non-magnetic base

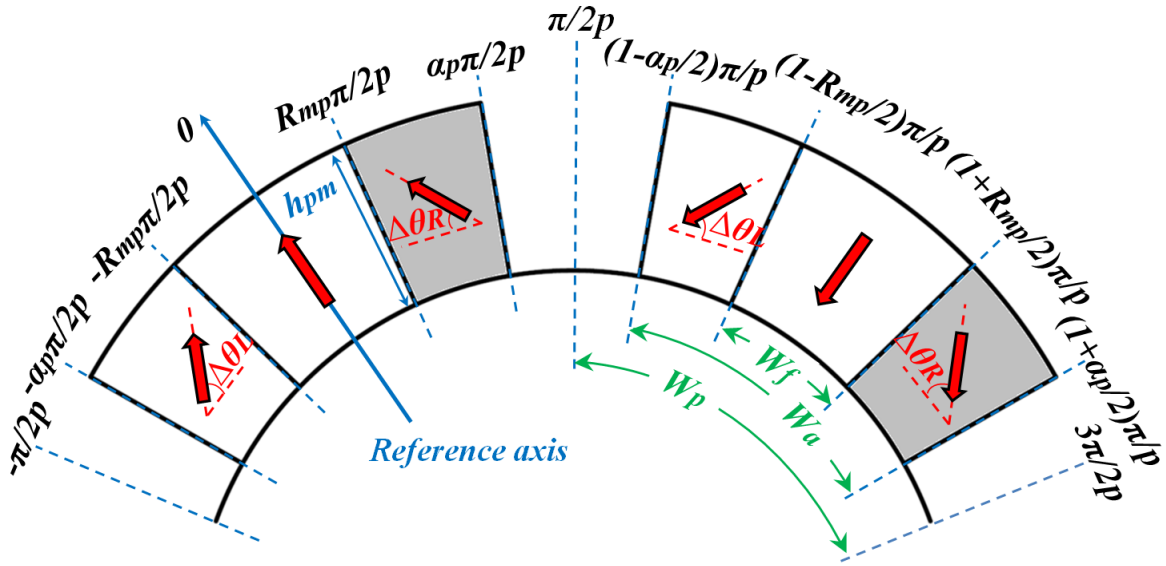

(c) General model with equal-magnet height

Fig.5.3. Design parameter identification for modular Hat- and T-type USMH magnet pole.

TABLE.5-I Magnetization Components for Hat- and T-type Magnet Pole Over One Pole Pair

Magnetization component	***Position***
$M_r = 0$ $M_\theta = 0$	$-\frac{\pi}{2p} \le \theta \le -\frac{\alpha_p \pi}{2p}$
$M_r = \frac{B_{rsL}}{\mu_0}[\sin\Delta\theta_L \cos(\theta+\delta) + \cos\Delta\theta_L \sin(\theta+\delta)]$ $M_\theta = -\frac{B_{rsL}}{\mu_0}[\sin\Delta\theta_L \sin(\theta+\delta) - \cos\Delta\theta_L \cos(\theta+\delta)]$	$-\frac{\alpha_p \pi}{2p} \le \theta \le -\frac{R_{mp}\pi}{2p}$
$M_r = \frac{B_{rm}}{\mu_0}\cos\theta$ $M_\theta = -\frac{B_{rm}}{\mu_0}\sin\theta$	$-\frac{R_{mp}\pi}{2p} \le \theta \le \frac{R_{mp}\pi}{2p}$
$M_r = \frac{B_{rsR}}{\mu_0}[\sin\Delta\theta_R \cos(\theta-\delta) - \cos\Delta\theta_R \sin(\theta-\delta)]$ $M_\theta = -\frac{B_{rsR}}{\mu_0}[\sin\Delta\theta_R \sin(\theta-\delta) + \cos\Delta\theta_R \cos(\theta-\delta)]$	$\frac{R_{mp}\pi}{2p} \le \theta \le \frac{\alpha_p \pi}{2p}$
$M_r = 0$ $M_\theta = 0$	$\frac{\alpha_p \pi}{2p} \le \theta \le \left(1-\frac{\alpha_p}{2}\right)\frac{\pi}{p}$
$M_r = -\frac{B_{rsL}}{\mu_0}\left[\sin\Delta\theta_L \cos\left(\theta-\frac{\pi}{p}+\delta\right) + \cos\Delta\theta_L \sin\left(\theta-\frac{\pi}{p}+\delta\right)\right]$ $M_\theta = \frac{B_{rsL}}{\mu_0}\left[\sin\Delta\theta_L \sin\left(\theta-\frac{\pi}{p}+\delta\right) - \cos\Delta\theta_L \cos\left(\theta-\frac{\pi}{p}+\delta\right)\right]$	$\left(1-\frac{\alpha_p}{2}\right)\frac{\pi}{p} \le \theta \le \left(1-\frac{R_{mp}}{2}\right)\frac{\pi}{p}$
$M_r = -\frac{B_{rm}}{\mu_0}\cos\left(\theta-\frac{\pi}{p}\right)$ $M_\theta = \frac{B_{rm}}{\mu_0}\sin\left(\theta-\frac{\pi}{p}\right)$	$\left(1-\frac{R_{mp}}{2}\right)\frac{\pi}{p} \le \theta \le \left(1+\frac{R_{mp}}{2}\right)\frac{\pi}{p}$

$\left.\begin{aligned} M_r &= -\frac{B_{rsR}}{\mu_0}\left[\sin\Delta\theta_R\cos\left(\theta-\frac{\pi}{p}-\delta\right)-\cos\Delta\theta_R\sin\left(\theta-\frac{\pi}{p}-\delta\right)\right] \\ M_\theta &= \frac{B_{rsR}}{\mu_0}\left[\sin\Delta\theta_R\sin\left(\theta-\frac{\pi}{p}-\delta\right)+\cos\Delta\theta_R\cos\left(\theta-\frac{\pi}{p}-\delta\right)\right] \end{aligned}\right\}$	$\left(1+\frac{R_{mp}}{2}\right)\frac{\pi}{p}\le\theta\le\left(1+\frac{\alpha_p}{2}\right)\frac{\pi}{p}$
$\left.\begin{aligned} M_r &= 0 \\ M_\theta &= 0 \end{aligned}\right\}$	$\left(1+\frac{\alpha_p}{2}\right)\frac{\pi}{p}\le\theta\le\frac{3\pi}{2p}$

Furthermore, based on asymmetrically distributed magnetization components over one pole pitch, such as those shown in Fig.5.3(a)-(c), the general expression of M_r and M_θ which can be also used for symmetrically distributed cases are written as

$$M_r = \sum_{n=1,3,5,\cdots} M_{rn(\cos np\theta)}\cos np\theta + M_{rn(\sin np\theta)}\sin np\theta \tag{5.1}$$

$$M_\theta = \sum_{n=1,3,5,\cdots} M_{\theta n(\cos np\theta)}\cos np\theta + M_{\theta n(\sin np\theta)}\sin np\theta \tag{5.2}$$

where the cosine and sine components of magnetization M_{rn} can be calculated as:

$$\begin{aligned} M_{rn(\cos np\theta)} = \frac{p}{\pi}\Bigg\{ & \int_{-\frac{\alpha_p\pi}{2p}}^{-\frac{R_{mp}\pi}{2p}} \left\{\frac{B_{rsL}}{\mu_0}\left[\sin\Delta\theta_L\cos(\theta+\delta)+\cos\Delta\theta_L\sin(\theta+\delta)\right]\right\}\cos np\theta\, d\theta \\ & + \int_{-\frac{R_{mp}\pi}{2p}}^{\frac{R_{mp}\pi}{2p}} \frac{B_{rm}}{\mu_0}\cos\theta\cos np\theta\, d\theta \\ & + \int_{\frac{R_{mp}\pi}{2p}}^{\frac{\alpha_p\pi}{2p}} \left\{\frac{B_{rsR}}{\mu_0}\left[\sin\Delta\theta_R\cos(\theta-\delta)-\cos\Delta\theta_R\sin(\theta-\delta)\right]\right\}\cos np\theta\, d\theta \\ & + \int_{\left(1-\frac{\alpha_p}{2}\right)\frac{\pi}{p}}^{\left(1-\frac{R_{mp}}{2}\right)\frac{\pi}{p}} \left\{-\frac{B_{rsL}}{\mu_0}\left[\sin\Delta\theta_L\cos\left(\theta-\frac{\pi}{p}+\delta\right)+\cos\Delta\theta_L\sin\left(\theta-\frac{\pi}{p}+\delta\right)\right]\right\}\cos np\theta\, d\theta \\ & + \int_{\left(1-\frac{R_{mp}}{2}\right)\frac{\pi}{p}}^{\left(1+\frac{R_{mp}}{2}\right)\frac{\pi}{p}} \left[-\frac{B_{rm}}{\mu_0}\cos\left(\theta-\frac{\pi}{p}\right)\right]\cos np\theta\, d\theta \\ & + \int_{\left(1+\frac{R_{mp}}{2}\right)\frac{\pi}{p}}^{\left(1+\frac{\alpha_p}{2}\right)\frac{\pi}{p}} \left\{-\frac{B_{rsR}}{\mu_0}\left[\sin\Delta\theta_R\cos\left(\theta-\frac{\pi}{p}-\delta\right)-\cos\Delta\theta_R\sin\left(\theta-\frac{\pi}{p}-\delta\right)\right]\right\}\cos np\theta\, d\theta \Bigg\} \end{aligned} \tag{5.3}$$

and,

$$M_{rn(\sin np\theta)} = \frac{p}{\pi}\left\{\int_{-\frac{\alpha_p\pi}{2p}}^{-\frac{R_{mp}\pi}{2p}} \left\{\frac{B_{rsL}}{\mu_0}\left[\sin\Delta\theta_L\cos(\theta+\delta)+\cos\Delta\theta_L\sin(\theta+\delta)\right]\right\}\sin np\theta\, d\theta\right.$$

$$+\int_{-\frac{R_{mp}\pi}{2p}}^{\frac{R_{mp}\pi}{2p}} \frac{B_{rm}}{\mu_0}\cos\theta\,\sin np\theta\, d\theta$$

$$+\int_{\frac{R_{mp}\pi}{2p}}^{\frac{\alpha_p\pi}{2p}} \left\{\frac{B_{rsR}}{\mu_0}\left[\sin\Delta\theta_R\cos(\theta-\delta)-\cos\Delta\theta_R\sin(\theta-\delta)\right]\right\}\sin np\theta\, d\theta$$

$$+\int_{\left(1-\frac{\alpha_p}{2}\right)\frac{\pi}{p}}^{\left(1-\frac{R_{mp}}{2}\right)\frac{\pi}{p}} \left\{-\frac{B_{rsL}}{\mu_0}\left[\sin\Delta\theta_L\cos\left(\theta-\frac{\pi}{p}+\delta\right)+\cos\Delta\theta_L\sin\left(\theta-\frac{\pi}{p}+\delta\right)\right]\right\}\sin np\theta\, d\theta$$

$$+\int_{\left(1-\frac{R_{mp}}{2}\right)\frac{\pi}{p}}^{\left(1+\frac{R_{mp}}{2}\right)\frac{\pi}{p}} \left[-\frac{B_{rm}}{\mu_0}\cos\left(\theta-\frac{\pi}{p}\right)\right]\sin np\theta\, d\theta$$

$$\left.+\int_{\left(1+\frac{R_{mp}}{2}\right)\frac{\pi}{p}}^{\left(1+\frac{\alpha_p}{2}\right)\frac{\pi}{p}} \left\{-\frac{B_{rsR}}{\mu_0}\left[\sin\Delta\theta_R\cos\left(\theta-\frac{\pi}{p}-\delta\right)-\cos\Delta\theta_R\sin\left(\theta-\frac{\pi}{p}-\delta\right)\right]\right\}\sin np\theta\, d\theta\right\} \tag{5.4}$$

Similarly, the cosine and sine components of $M_{\theta n}$ can be calculated,

$$M_{\theta n(\cos np\theta)} = \frac{p}{\pi}\left\{\int_{-\frac{\alpha_p\pi}{2p}}^{-\frac{R_{mp}\pi}{2p}} \left\{-\frac{B_{rsL}}{\mu_0}\left[\sin\Delta\theta_L\sin(\theta+\delta)-\cos\Delta\theta_L\cos(\theta+\delta)\right]\right\}\cos np\theta\, d\theta\right.$$

$$+\int_{-\frac{R_{mp}\pi}{2p}}^{\frac{R_{mp}\pi}{2p}} \left(-\frac{B_{rm}}{\mu_0}\sin\theta\right)\cos np\theta\, d\theta$$

$$+\int_{\frac{R_{mp}\pi}{2p}}^{\frac{\alpha_p\pi}{2p}} \left\{-\frac{B_{rsR}}{\mu_0}\left[\sin\Delta\theta_R\sin(\theta-\delta)+\cos\Delta\theta_R\cos(\theta-\delta)\right]\right\}\cos np\theta\, d\theta$$

$$+\int_{\left(1-\frac{\alpha_p}{2}\right)\frac{\pi}{p}}^{\left(1-\frac{R_{mp}}{2}\right)\frac{\pi}{p}} \left\{\frac{B_{rsL}}{\mu_0}\left[\sin\Delta\theta_L\sin\left(\theta-\frac{\pi}{p}+\delta\right)-\cos\Delta\theta_L\cos\left(\theta-\frac{\pi}{p}+\delta\right)\right]\right\}\cos np\theta\, d\theta$$

$$+\int_{\left(1-\frac{R_{mp}}{2}\right)\frac{\pi}{p}}^{\left(1+\frac{R_{mp}}{2}\right)\frac{\pi}{p}} \left[\frac{B_{rm}}{\mu_0}\sin\left(\theta-\frac{\pi}{p}\right)\right]\cos np\theta\, d\theta$$

$$\left.+\int_{\left(1+\frac{R_{mp}}{2}\right)\frac{\pi}{p}}^{\left(1+\frac{\alpha_p}{2}\right)\frac{\pi}{p}} \left\{\frac{B_{rsR}}{\mu_0}\left[\sin\Delta\theta_R\sin\left(\theta-\frac{\pi}{p}-\delta\right)+\cos\Delta\theta_R\cos\left(\theta-\frac{\pi}{p}-\delta\right)\right]\right\}\cos np\theta\, d\theta\right\}$$

(5.5)

and,

$$M_{\theta n(\sin npθ)}=\frac{p}{\pi}\left\{\int_{-\frac{\alpha_p\pi}{2p}}^{-\frac{R_{mp}\pi}{2p}}\left\{-\frac{B_{rsL}}{\mu_0}[\sin\Delta\theta_L\sin(\theta+\delta)-\cos\Delta\theta_L\cos(\theta+\delta)]\right\}\sin npθ\,d\theta\right.$$
$$+\int_{-\frac{R_{mp}\pi}{2p}}^{\frac{R_{mp}\pi}{2p}}\left(-\frac{B_{rm}}{\mu_0}\sin\theta\right)\sin npθ\,d\theta$$
$$+\int_{\frac{R_{mp}\pi}{2p}}^{\frac{\alpha_p\pi}{2p}}\left\{-\frac{B_{rsR}}{\mu_0}[\sin\Delta\theta_R\sin(\theta-\delta)+\cos\Delta\theta_R\cos(\theta-\delta)]\right\}\sin npθ\,d\theta$$
$$+\int_{\left(1-\frac{\alpha_p}{2}\right)\frac{\pi}{p}}^{\left(1-\frac{R_{mp}}{2}\right)\frac{\pi}{p}}\left\{\frac{B_{rsL}}{\mu_0}\left[\sin\Delta\theta_L\sin\left(\theta-\frac{\pi}{p}+\delta\right)-\cos\Delta\theta_L\cos\left(\theta-\frac{\pi}{p}+\delta\right)\right]\right\}\sin npθ\,d\theta$$
$$+\int_{\left(1-\frac{R_{mp}}{2}\right)\frac{\pi}{p}}^{\left(1+\frac{R_{mp}}{2}\right)\frac{\pi}{p}}\left[\frac{B_{rm}}{\mu_0}\sin\left(\theta-\frac{\pi}{p}\right)\right]\sin npθ\,d\theta$$
$$\left.+\int_{\left(1+\frac{R_{mp}}{2}\right)\frac{\pi}{p}}^{\left(1+\frac{\alpha_p}{2}\right)\frac{\pi}{p}}\left\{\frac{B_{rsR}}{\mu_0}\left[\sin\Delta\theta_R\sin\left(\theta-\frac{\pi}{p}-\delta\right)+\cos\Delta\theta_R\cos\left(\theta-\frac{\pi}{p}-\delta\right)\right]\right\}\sin npθ\,d\theta\right\}$$

(5.6)

The fully derived expressions of $M_{rn\cos(npθ)}$, $M_{rn\sin(npθ)}$, $M_{θn\cos(npθ)}$ and $M_{θn\sin(npθ)}$ are given in (5.7)-(5.10) in Appendix of this chapter.

In order to solve the overall air-gap flux density for the modular Hat- and T-type magnet pole shown in Fig.5.3(a)-(b), the superposition theory is applied as illustrated in TABLE.5-II. It reveals that the overall air-gap flux density distribution for Hat-type magnet pole is calculated by initially setting B_{rm} = 0 T and B_{rsR} = 0 T in (5.3)-(5.6), while changing B_{rsL} together with left side-magnet height h_{pmL} to the desired values (Part A) when the calculating air-gap path is fixed. After that, the air-gap flux density for right side-magnet is deduced by setting B_{rsR} and h_{pmR} into desired value, while B_{rsL} = 0 T and B_{rm} = 0 T (Part B). Then, the air-gap flux density distribution for mid-magnet is predicted by setting B_{rm} and mid-magnet height h_{pm} to the desired values, while setting B_{rsL} = 0 T and B_{rsR} = 0 T (Part C). Ultimately, the overall air-gap flux density distribution for Hat-type magnet pole is calculated by summing up the foregoing predicted value of Part A, Part B and Part C. In the similar manner, the overall air-gap flux density distribution of T-type magnet pole is calculated by summing up the value of Part 1, Part 3 and Part 4, then minus Part 2, as illustrated in TABLE.5-II. It should be noted that aforementioned superposition methods in TABLE.5-II

can be also applied to conventional and modular Hat- and T-type ESMH magnet pole cases, in Fig.5.1.

Then, the air-gap flux density distribution accounting for slotting effect can be predicted by using SD model. Since the entire SD model was elaborately discussed and fully derived in APPENDIX III and the simplified expression of SD model was given in chapter 3, it will not be duplicated again in this chapter. By solving the air-gap flux density distribution, the electromagnetic performances, including flux-linkage, back-EMF, and electromagnetic torque waveforms of PM brushless machine having proposed magnet pole structures can be predicted by adopting similar expressions of flux-linkage, back-EMF and electromagnetic torque waveforms in (3.22) and (3.23).

TABLE.5-II SUPERPOSITION THEORY FOR MODULAR HAT AND T-TYPE MAGNET

Modular Hat-type	***Modular T-type***
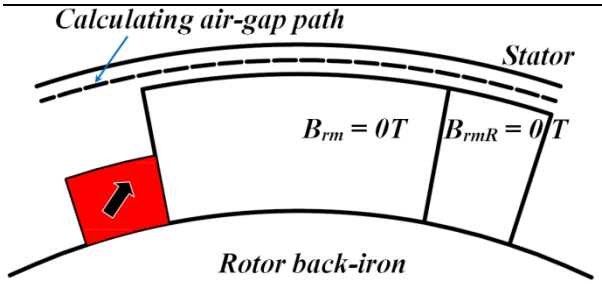	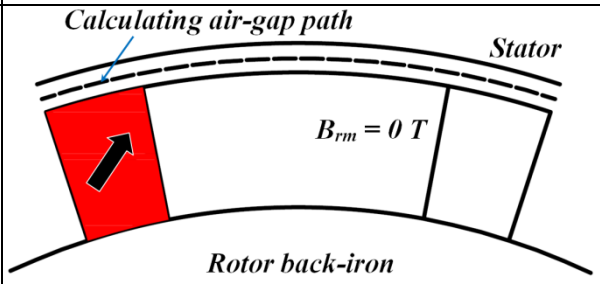
Part A	Part 1
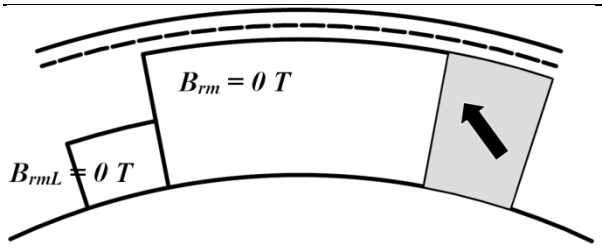	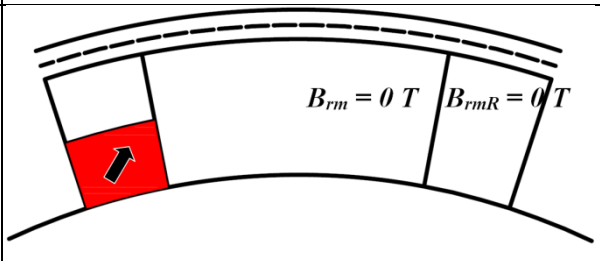
Part B	Part 2
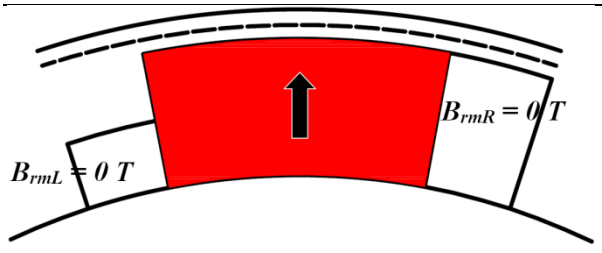	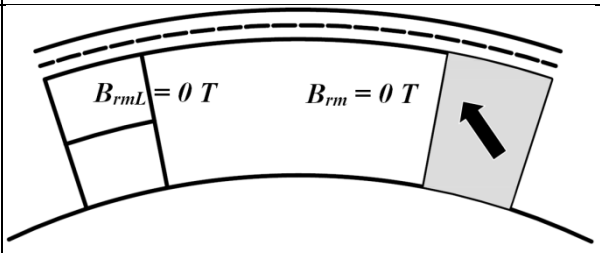
Part C	Part 3

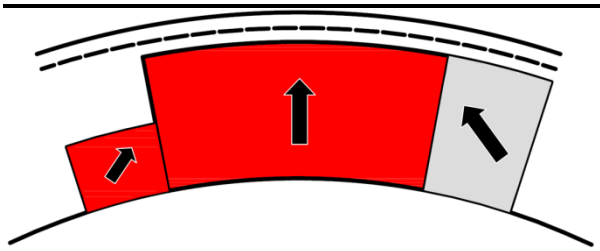

Hat-type = Part A + Part B + Part C

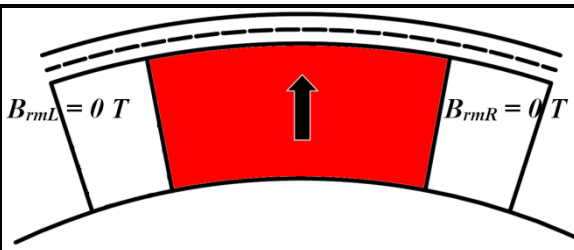

Part 4

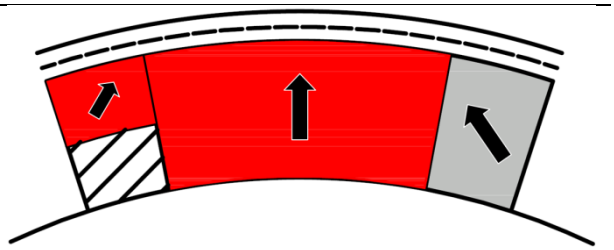

T-type = Part 1 – Part 2 + Part 3 +Part 4

5.3 Finite-Element Validation

The analytical model is validated by linear FEA on a prototype 12-slot/10-pole PM brushless machine whose design parameters (where the design parameters of rotor part is not optimized) are shown in TABLE.5-III.

TABLE.5-III MACHINES DESIGN PARAMETER (DEFAULT UNIT: MM)

Rated speed, rpm	400	Slot opening, b_o	2.0
Pole number, $2p$	10	Air-gap length, l_g	1.0
Stator slot number, N_s	12	Active length, l_a	50
Tooth-tip height, h_t	1.5	Stator back-iron thickness, h_{sbi}	3.7
Tooth body width,	-	Stator outer diameter, D_{so}	100
Stator inner diameter, D_{si}	57	Rotor outer diameter, D_{ro}	55
Rotor inner diameter, D_{ri}	49	Shaft diameter, D_{sf}	34
No. of series turns per phase, N	132	Peak phase current, I (A)	10
NdFeB, B_r (T)	1.2	NdFeB μ_r	1.05
Ferrite, B_r (T)	0.4	Ferrite μ_r	1.05
Magnet ratio, R_{mp}	0.50	Pole-arc to pole-pitch ratio, α_p	1.00
Magnetization angle of left side-magnet, $\Delta\theta_L$	60	Magnetization angle of right side-magnet, $\Delta\theta_R$	40
Magnet height of mid- magnet, h_{pm}	3.0	Magnet height of left side- magnet, h_{pmL}	1.5
Magnet height of Right side- magnet, h_{pmR}	3.0	Remanence of left side-magnet, B_{rsL} (T)	1.2

Remanence of right side-magnet, B_{rsR} (T)	0.4	Remanence of mid-magnet, B_{rm} (T)	1.2

In order to correspond to the foregoing developed analytical model, the stator with straight tooth-tips is also applied to the linear FEA model with exactly the same geometry parameters. The analytically and FEA predicted air-gap flux density distributions, phase back-EMF, and electromagnetic torque waveforms are compared in Fig.5.4-8 for the prototype machine having modular Hat- and T-type USMH magnet poles, respectively, and excellent agreement is achieved.

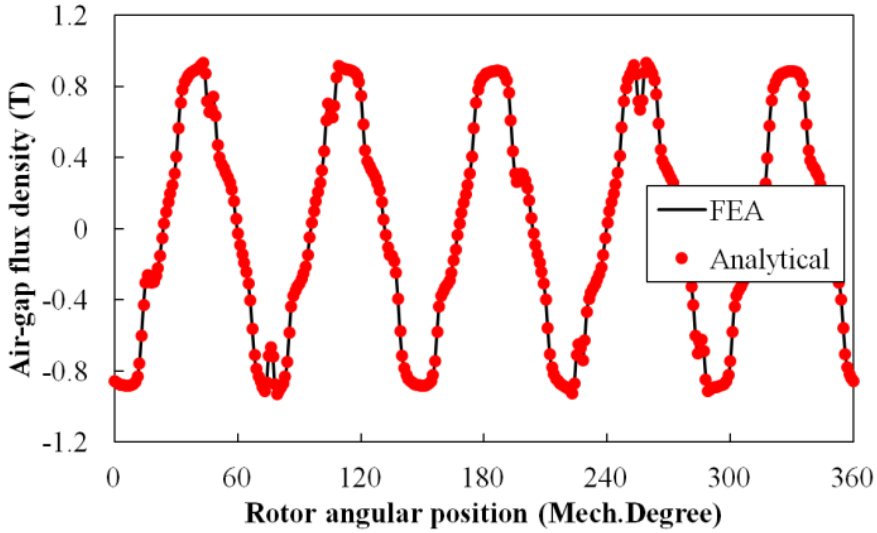

(a) Radial

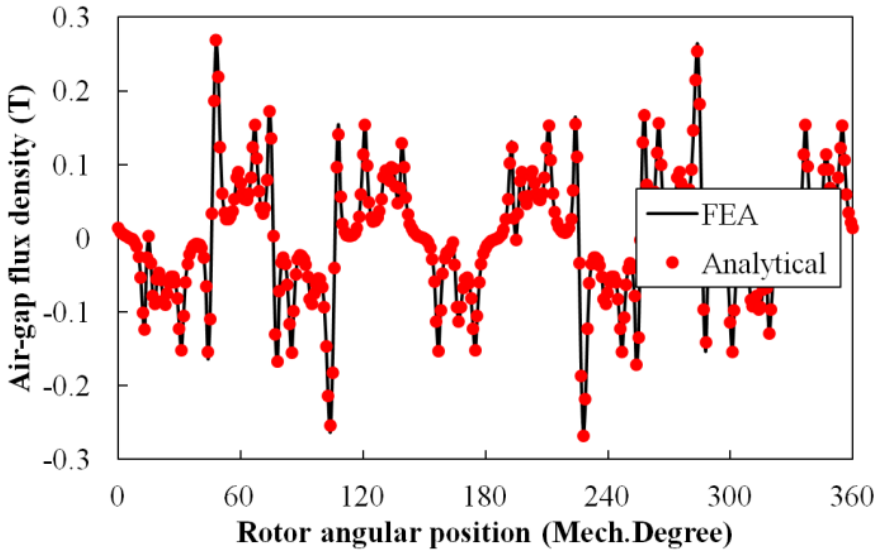

(b) Circumferential

Fig.5.4. Comparison of analytical and FEA predicted air-gap flux density components for 12-slot/10-pole PM brushless machine having modular Hat-type USMH magnet pole.

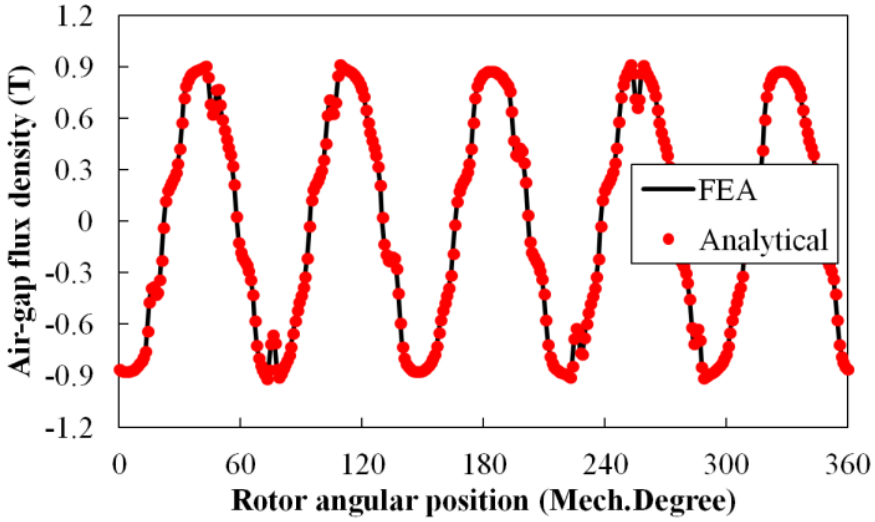

(a) Radial

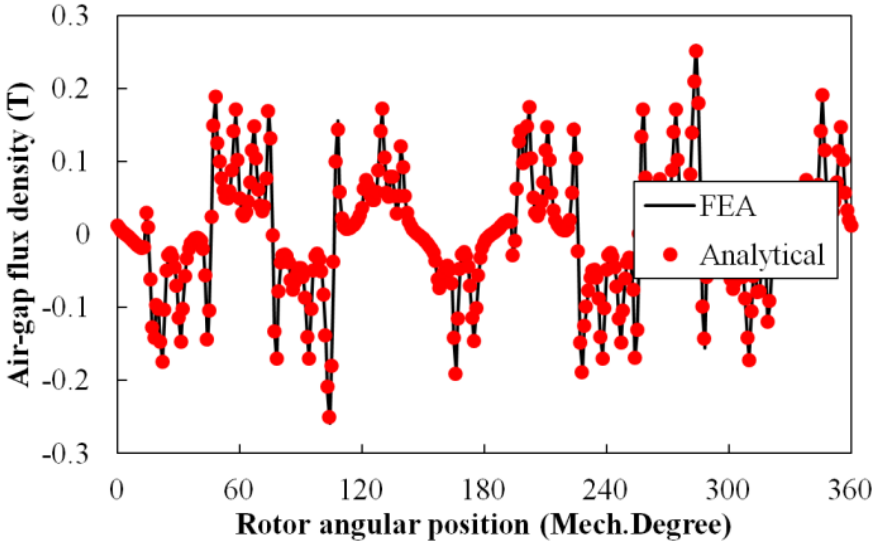

(b) Circumferential

Fig.5.5. Comparison of analytical and FEA predicted air-gap flux density components for 12-slot/10-pole PM brushless machine having modular T-type USMH magnet pole.

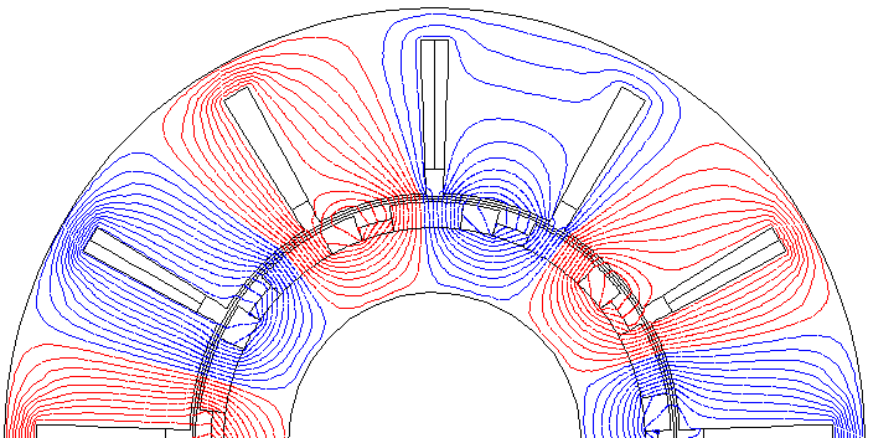

(a) Hat-type

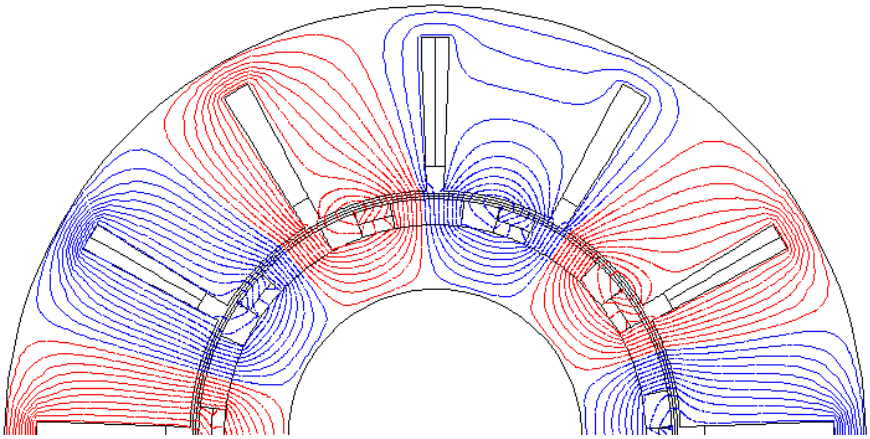

(b) T-type

Fig.5.6. FEA predicted vector potential distributions for 12-slot/10-pole PM brushless machines having modular Hat- and T-type USMH magnet pole.

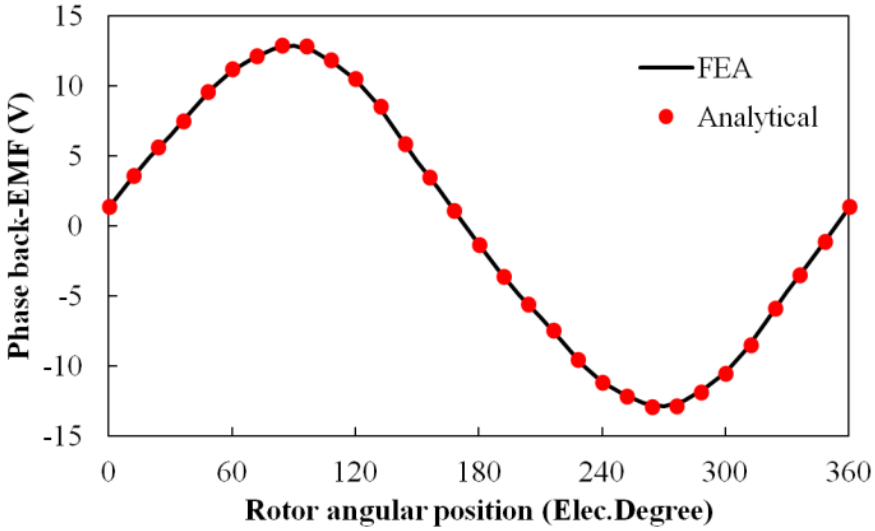

(a) Phase back-EMF, 400 rpm

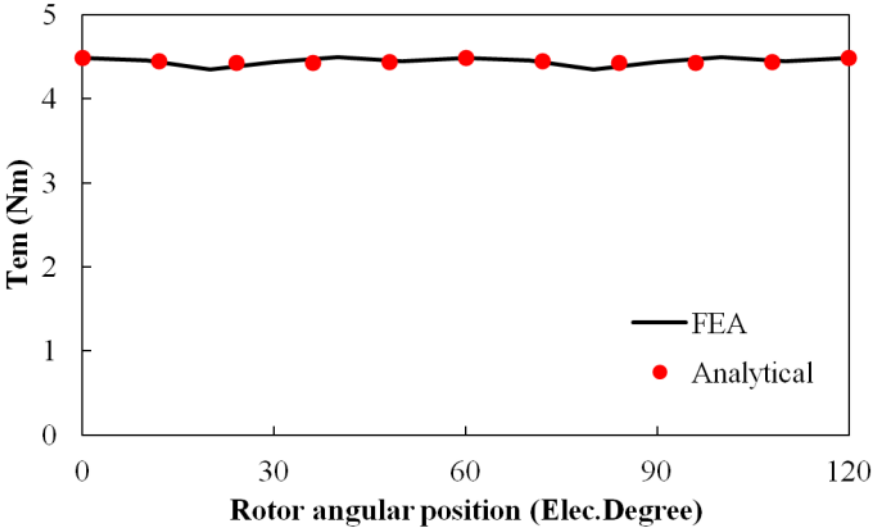

(b) Electromagnetic torque

Fig.5.7. Comparison of analytical and FEA predicted phase back-EMF at 400 rpm and electromagnetic torque waveforms for 12-slot/10-pole PM brushless machine having modular Hat-type USMH magnet pole.

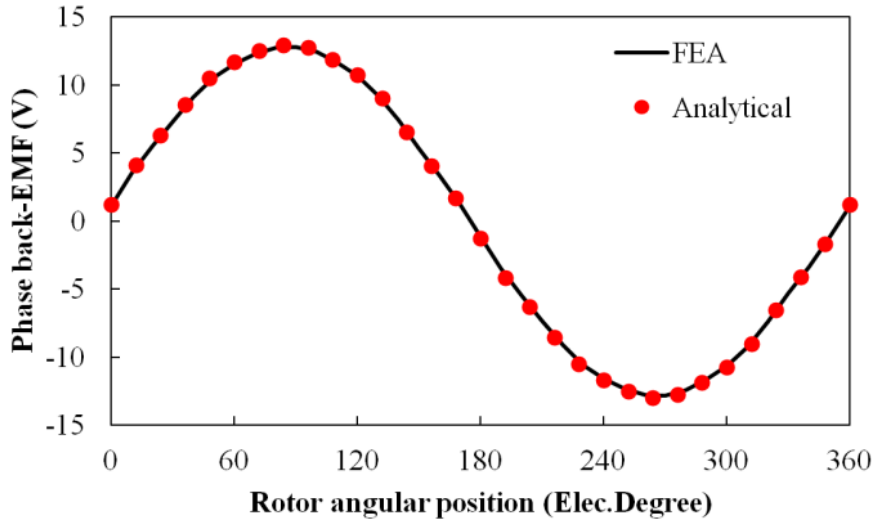

(a) Phase back-EMF, 400 rpm

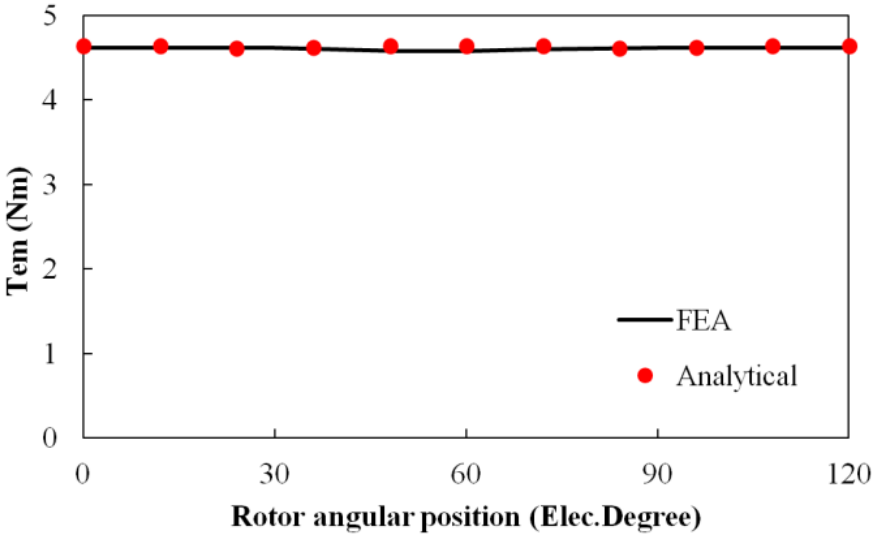

(b) Electromagnetic torque

Fig.5.8. Comparison of analytical and FEA predicted phase back-EMF at 400 rpm and electromagnetic torque waveforms for 12-slot/10-pole PM brushless machine having modular T-type USMH magnet pole.

5.4 Comparison of Conventional and Modular Hat- and T-Type Magnet Poles

Since the amplitude of T_{em} in the Halbach magnetized machine can be optimized by varying both magnet arc ratio R_{mp} and magnetization angle $\Delta\theta$ ($\Delta\theta_L = \Delta\theta_R$, if two side-magnets having the same magnet height-to-width ratio), T_{em} for the 12-slot/10-pole PM brushless machine having a conventional (same magnet height and same magnet material) 3-segment Halbach array has been globally optimized in [24]. The overall optimized T_{em} for prototype machine having conventional 3-segment Halbach array is obtained when α_p = 1.0, R_{mp} = 0.70 and $\Delta\theta$ = 40, respectively, while the machine having a conventional T-type ESMH

magnet pole can exhibit significantly larger optimal T_{em} than a conventional Hat-type ESMH magnet pole when $h_{pmL} = h_{pmR} = h_{pm}/2$. Moreover, it is commonly accepted that there is no overall optimal result for magnet pole having mixed grade magnet materials since the higher the remanence used the better performance will be obtained. Therefore, the mixed grade magnet pole is developed upon an optimized conventional magnet pole structure, but aims to achieve higher magnet usage efficiency η_{pm}, which is equal to the average torque divided by the magnet volume. Thus, to form the modular Hat- and T-type USMH based on the foregoing global optimized conventional 3-segment Halbach array, the right side-magnet of a conventional Hat- and T-type magnet pole is replaced by ferrite magnet with fully used rotor volume, e.g. h_{pmR} = 3.0 mm, on the basis of its low price, nearly negligible asymmetric influence on air-gap flux density and away from on-load field (one way rotating case). Fig.5.9 compares the optimal T_{em} and η_{pm} (since the price of NdFeB magnet is much higher than that of Ferrite magnet, η_{pm} in this section will only consider V_{pm} of NdFeB magnet) for the machines having conventional and modular Hat- and T-type magnet poles as illustrated in Fig.5.1 when the remanence ratio of two PM materials B_{rs}/B_{rm} = 0.4/1.2 = 1/3. It reveals that the modular T-type USMH exhibit relative large optimal T_{em}, plus the largest η_{pm} but relative small NdFeB usage when h_{pmL} is chosen between 1.5mm and 2.0mm in contrast to other magnet poles.

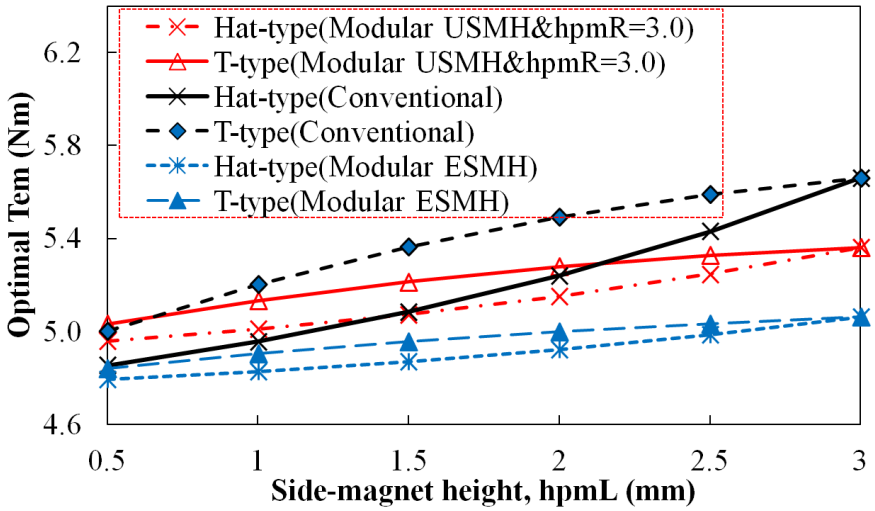

(a) Optimal T_{em}

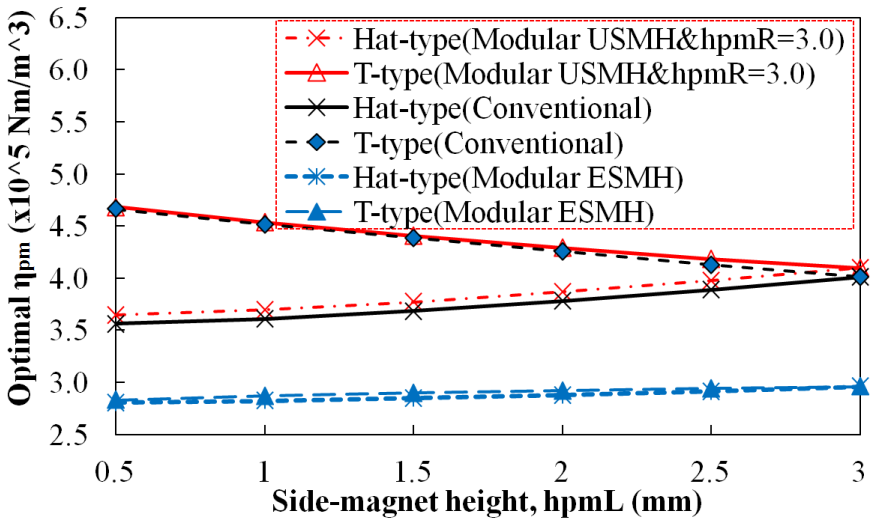

(b) Optimal η_{PM}

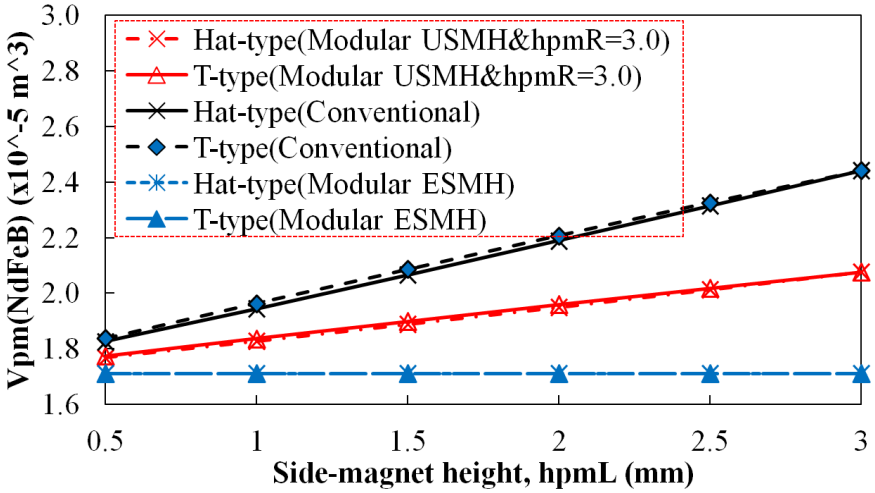

(c) Optimal NdFeB usage

Fig.5.9. Analytically predicted optimal T_{em}, η_{PM} and NdFeB usage for 12-slot/10-pole PM brushless machines having optimized conventional and modular Hat- and T-type magnet poles with the variation of side-magnet height and magnetization angles when B_{rs}/B_{rm} = *0.4/1.2 = 1/3*.

As regards to the foregoing analysis, side-magnet height for T-type magnet pole towards to half of the mid-magnet height together with NdFeB material can exhibit good performance in contrast to Hat-type, conventional pole and conventional 3-segment Halbach array. On the other hand, h_{pmL} = 1.5 mm is also suitable for modular T-type with unequal side-magnet height, since the asymmetric distortion of phase back-EMF is relative small, Fig.5.10. The analytically predicted T_{em} between 12-slot/10-pole PM brushless machines having conventional pole, optimized 3-segment Halbach array, conventional Hat- and T-type magnet pole, modular Hat- and T-type ESMH magnet pole, together with modular Hat- and T-type USMH magnet pole, are compared in Fig.5.11. The linear FEA predicted vector potential

distributions of those machines with the optimal magnetization angle are illustrated in Fig.5.12.

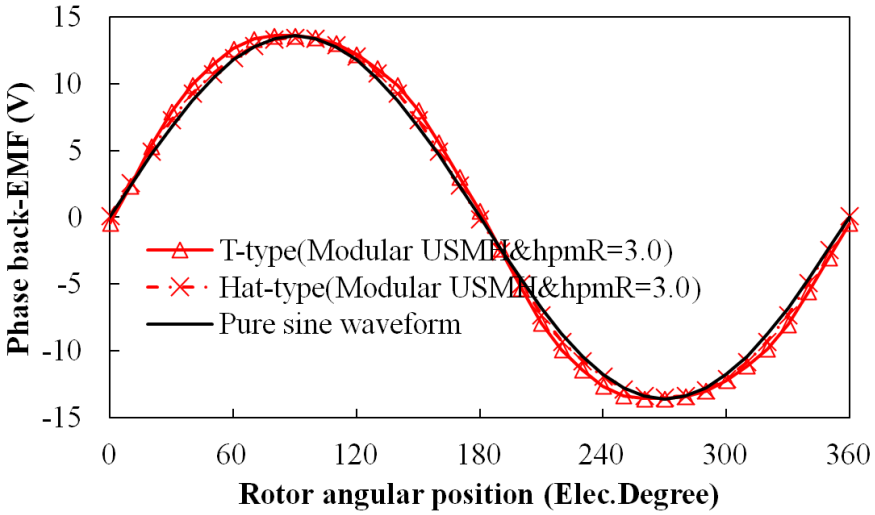

(a) Phase back-EMF, at 400 rpm

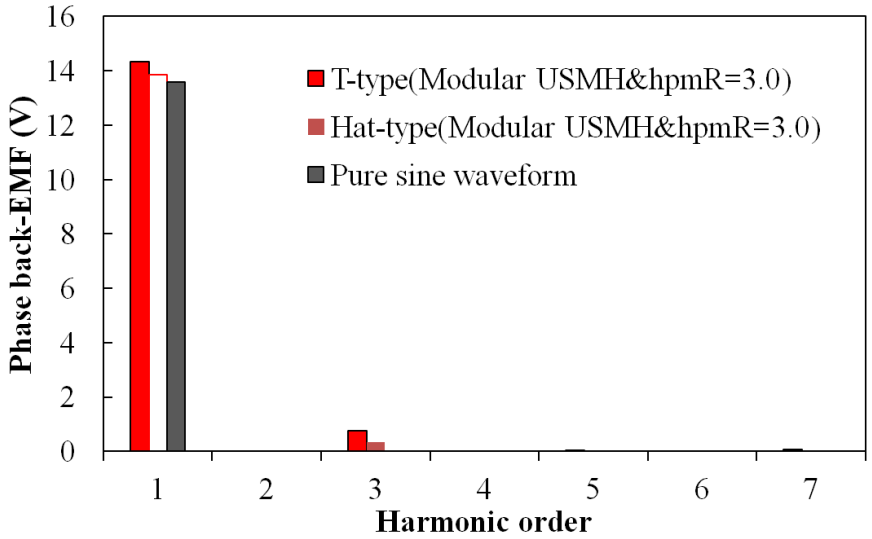

(b) Spectra

Fig.5.10. Comparison of analytically predicted phase back-EMF waveform and spectra between 12-slot/10-pole PM brushless machines having optimized modular Hat- and T-type magnet pole with R_{mp} = 0.7, B_{rsL} = 1.2T, B_{rsR} = 0.4T, h_{pmL} = 1.5mm and h_{pmR} = 3.0mm.

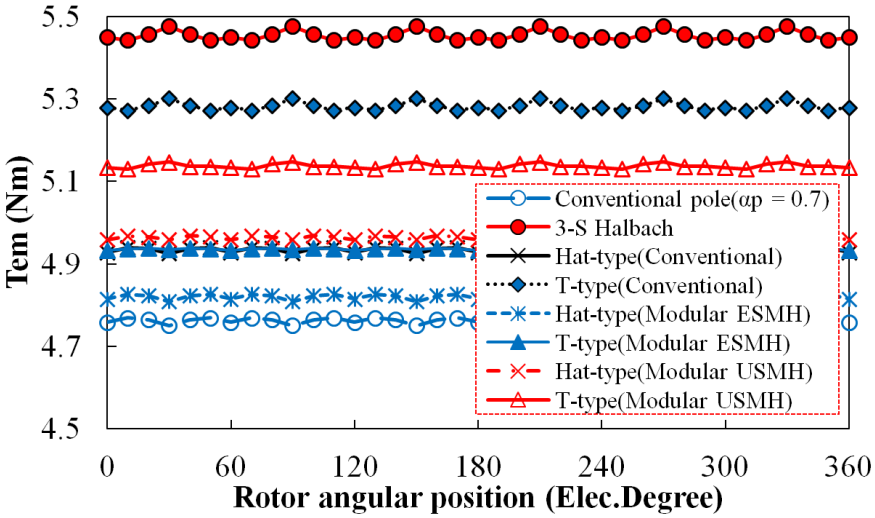

Fig.5.11. Comparison of analytically predicted T_{em} waveform between 12-slot/10-pole PM brushless machines having conventional, optimized 3-segment Halbach, conventional Hat- and T-type magnet pole, modular Hat- and T-type magnet poles.

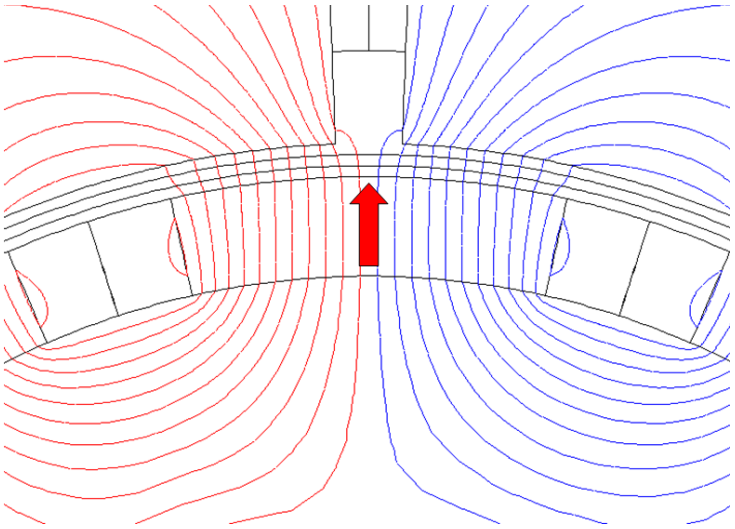

(a) Conventional pole (α_p = 0.70)

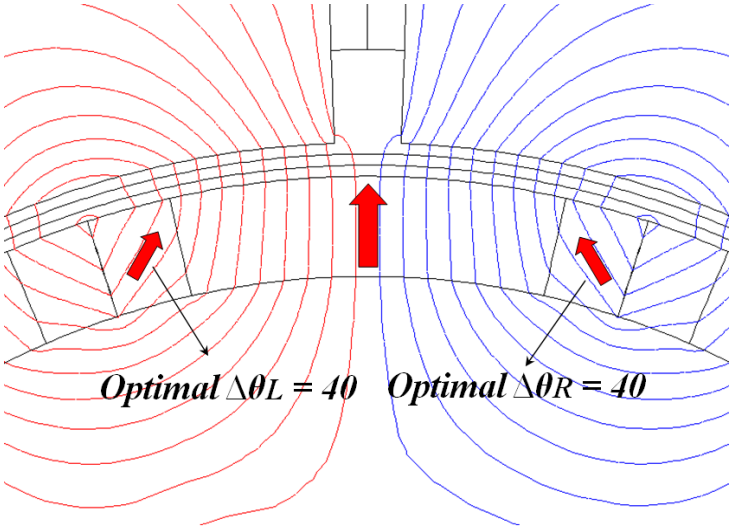

(b) Conventional 3-segment Halbach

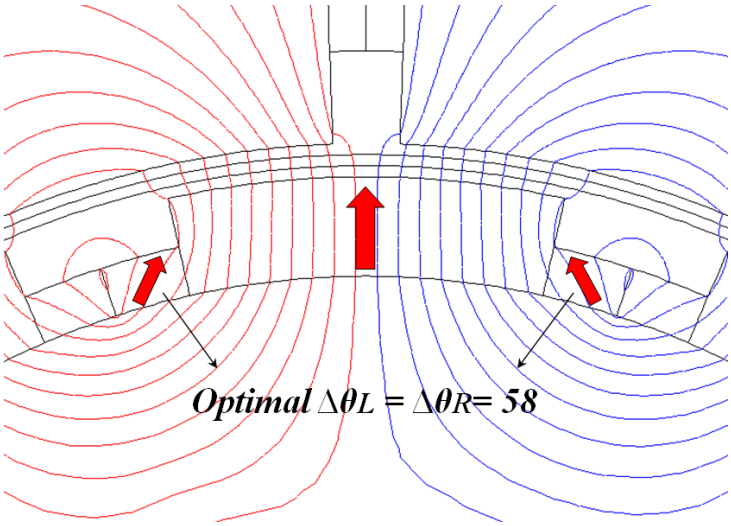

(c) Hat-type (Conventional)

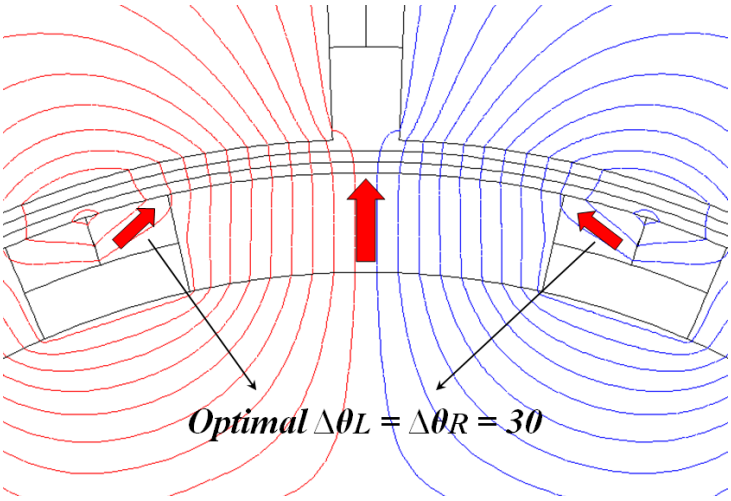

(d) T-type (Conventional)

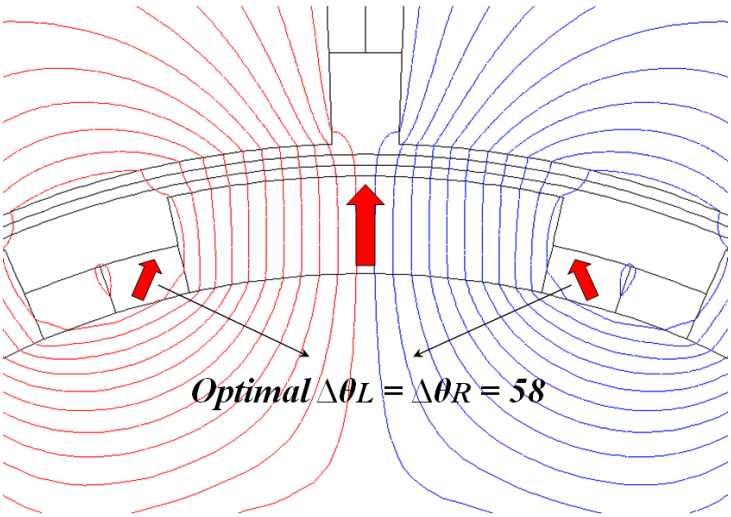

(e) Modular Hat-type ESMH

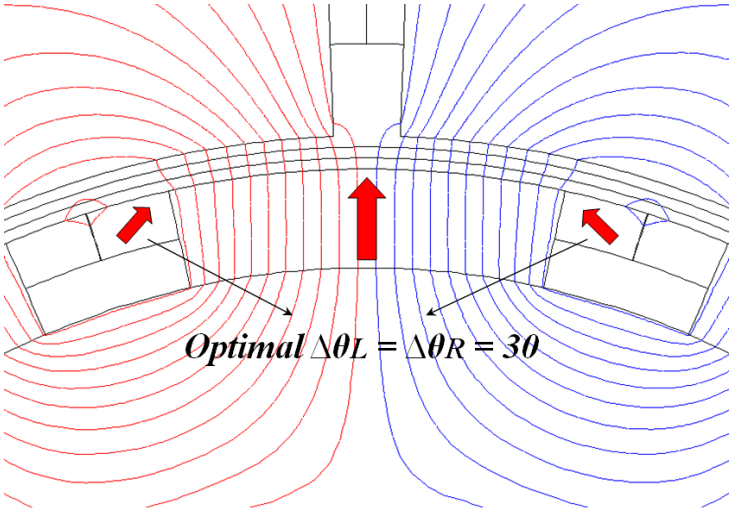

(f) Modular T-type ESMH

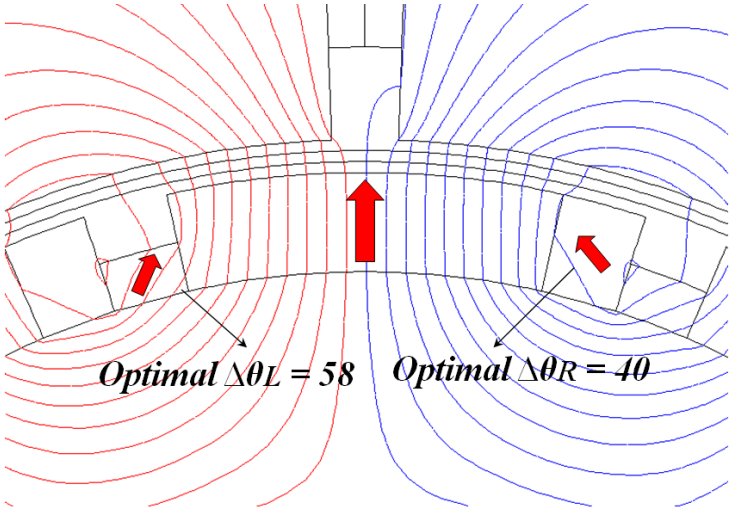

(g) Modular Hat-type USMH

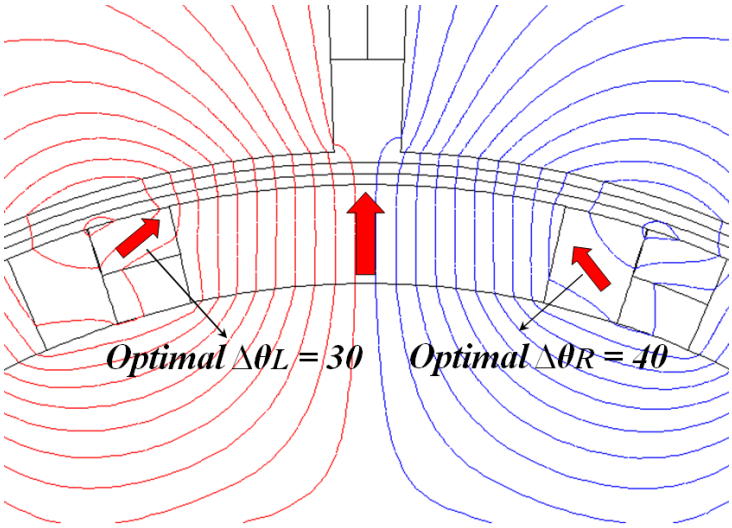

(h) Modular T-type USMH

Fig.5.12. Linear FEA predicted vector potential distribution of 12-slot/10-pole PM brushless machines having conventional pole, optimized conventional 3-segment Halbach array, conventional Hat- and T-type, modular Hat- and T-type magnet poles.

5.5 Investigation on Machine Having Modular Hat- and T-Type USMH Magnet Pole

According to the foregoing analysis, the machines having conventional T-type magnet pole exhibit significantly higher T_{em} than that with conventional Hat-type magnet pole, which can be explained by the reduced inter-pole leakage flux, as highlighted in Fig.5.13(a)-(b). Moreover, the amount of inter-pole leakage flux for conventional Hat-type magnet pole can be also effectively reduced by adopting modular Hat-type USMH magnet pole (h_{pmL} = 1.5 mm and h_{pmR} = 3.0 mm which are also applied to T-type USMH), Fig.5.13(d). As a consequence, the flux-linkage of modular Hat-type USMH magnet pole is higher than that of conventional Hat-type magnet pole as compared in Fig.5.14(a) and Fig.5.14(c), which in turn leads to the modular Hat-type USMH magnet pole to produce slightly higher T_{em} than the conventional Hat-type magnet pole (Fig.5.11) but lower NdFeB usage (Fig.5.9(c)). The demagnetization withstand capability (DWC) for the conventional and modular Hat- and T-type USMH magnet poles is examined, as illustrated in Fig.5.15, where only the application of one way rotating, such as fan and wind power generation etc., are considered. The position is determined as the worst case (the peak torque condition in this chapter) only for a single magnet pole by observing its flux density distribution during one electrical period. However, this specific worst position is only suitable for a single magnet pole, meanwhile the rest of magnet poles are not suffering from the worst case during this time. Since the irreversible demagnetization of the given NdFeB (N42H) and ferrite (FB9H) magnet happens when minimum flux density (B) in the magnetization direction of magnet is lower than ~0.1T and ~0T with the working temperature around 60 degree, respectively, thus all the conventional and modular Hat- and T-type USMH magnet pole cases are sustainable and therefore feasible for the designed maximum on-load condition (TABLE.5-III). However, it can be noted that Hat-type magnet pole presents much better DWC performance than T-type magnet pole due to side-magnets being away from on-load field. It should be noted that the irreversible demagnetization of side-magnet by using ferrite magnet will not happen even when prototype machine is working around -20 degree condition. However, in order to save the space, the detailed flux density distribution figures with the minimum amplitude marks in their magnetization direction are not presented here.

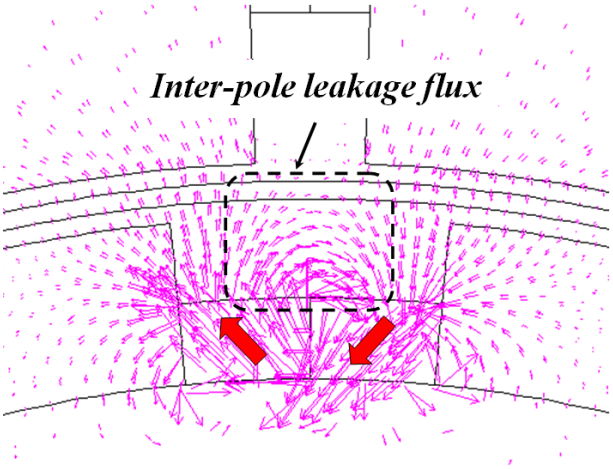

(a) Conventional Hat-type

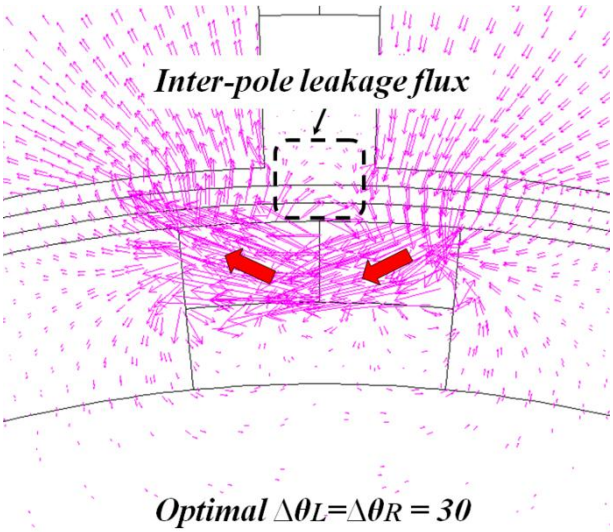

(b) Conventional T-type

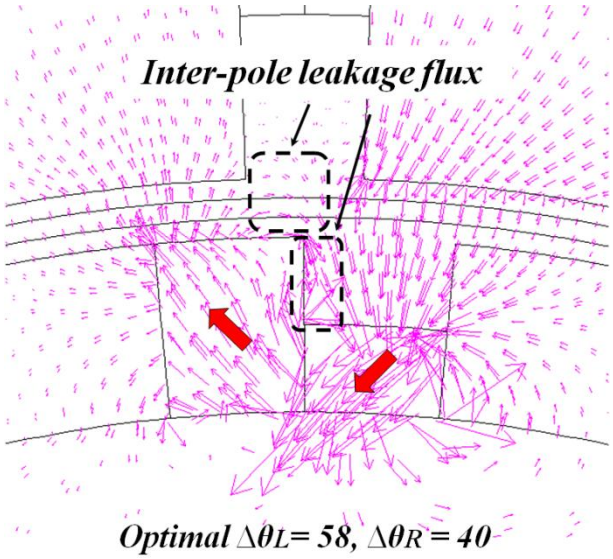

(c) Modular Hat-type USMH

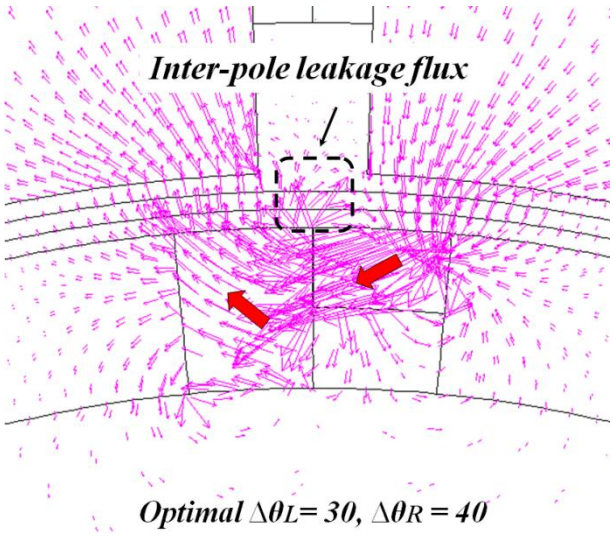

(d) Modular T-type USMH

Fig.5.13. Comparison of FEA predicted inter-pole leakage flux between optimized conventional and modular Hat- and T-type USMH magnet poles when B_{rm} = 0 T.

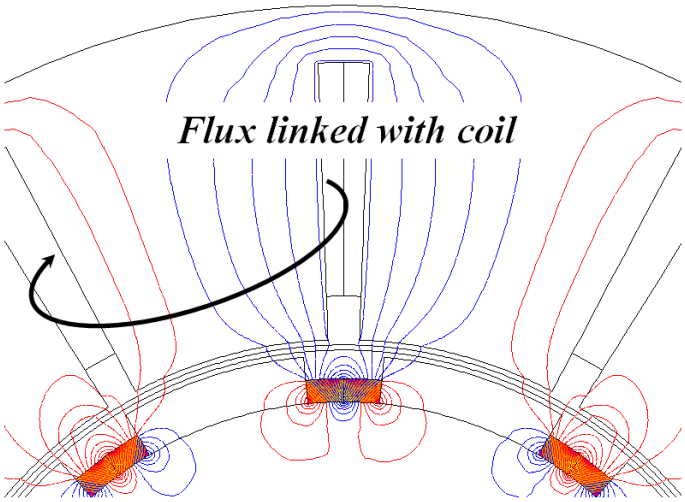

(a) Conventional Hat-type

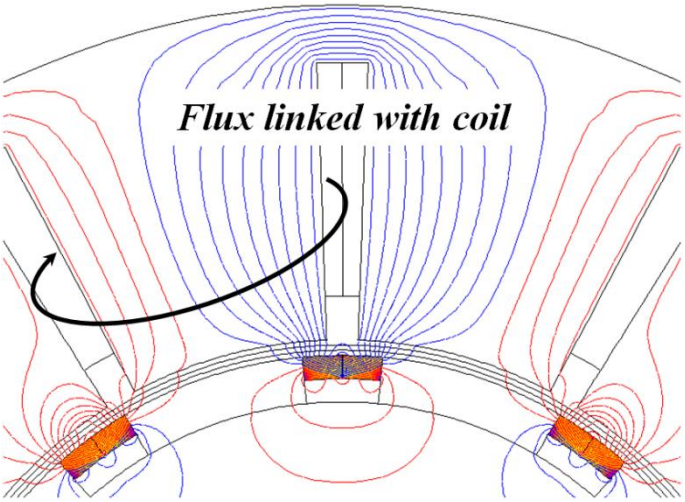

(b) Conventional T-type

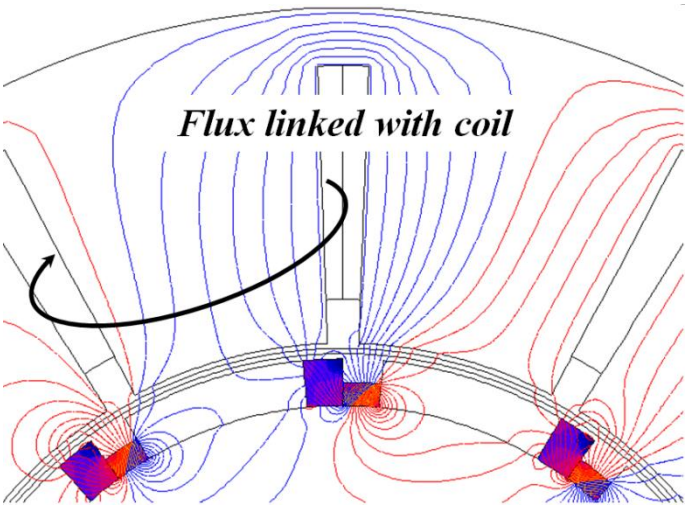

(c) Modular Hat-type USMH

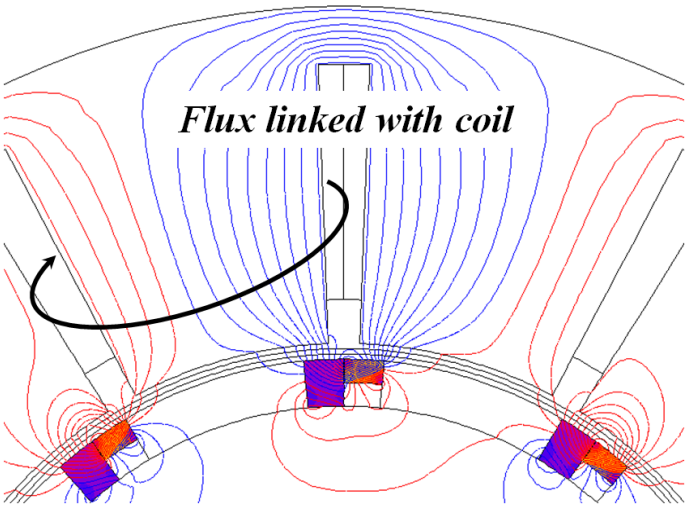

(d) Modular T-type USMH

Fig.5.14. Comparison of FEA predicted flux which can be linked with the coil between optimized conventional and modular Hat-and T-type USMH magnet poles when B_{rm} = 0 T.

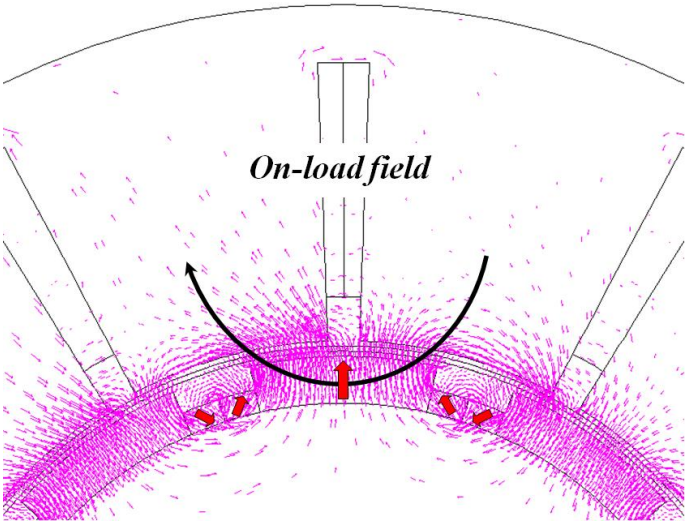

(i). On-load field

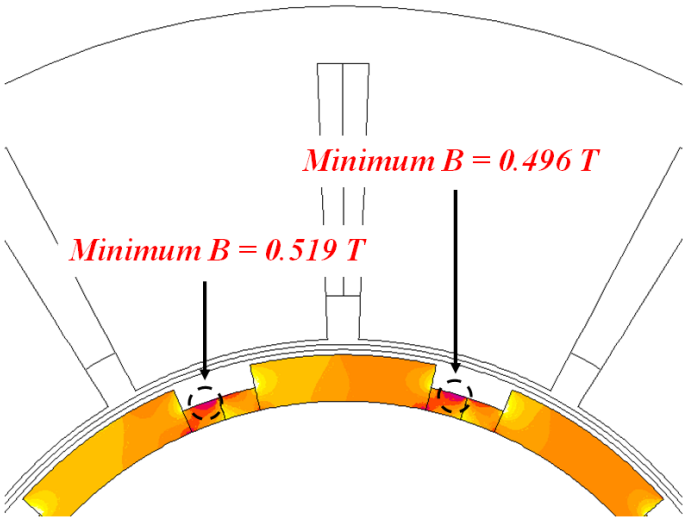

(ii). Potential demagnetization area

(a) Conventional Hat-type

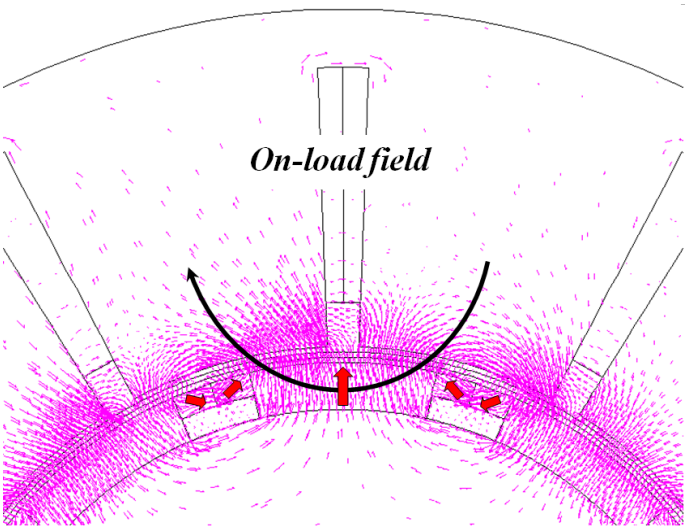

(i). On-load field

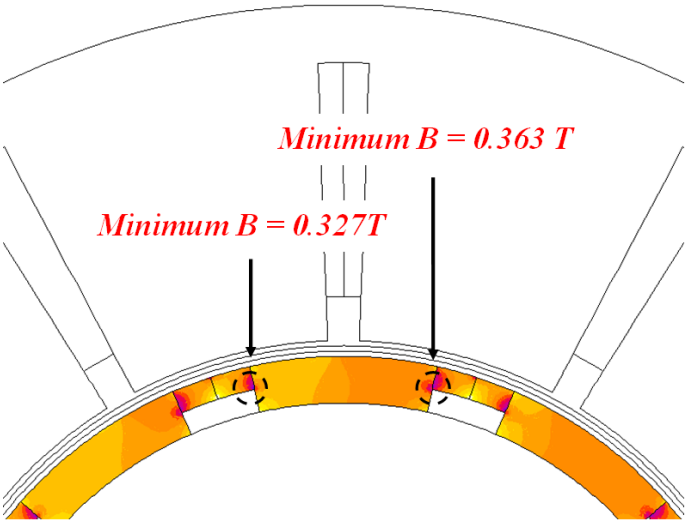

(ii). Potential demagnetization area

(b) Conventional T-type

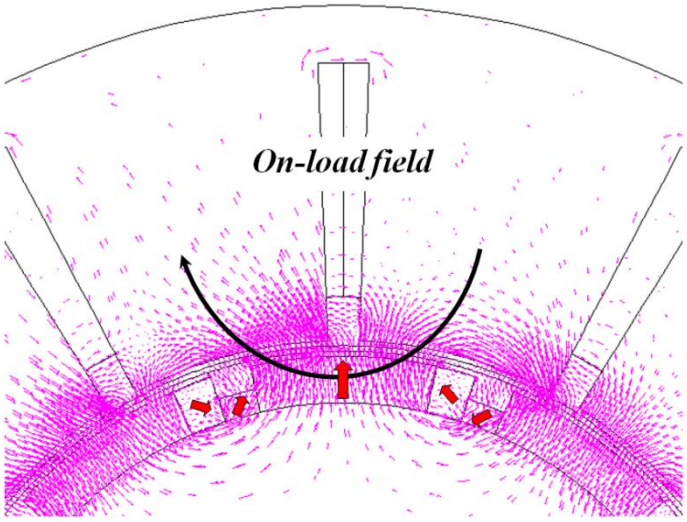

(i). On-load field

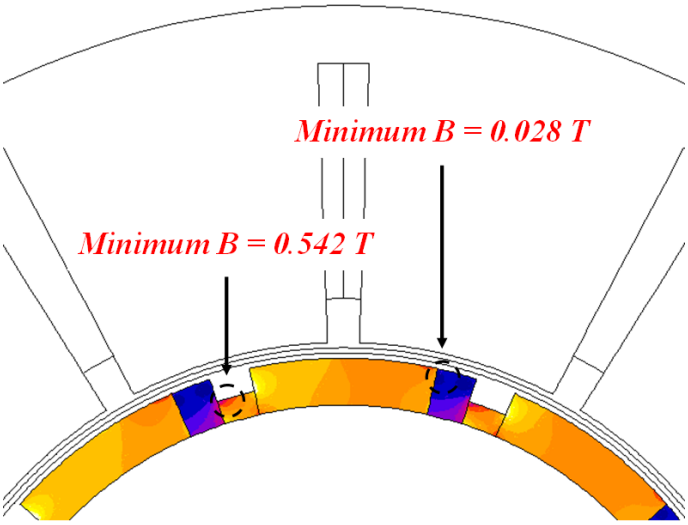

(ii). Potential demagnetization area

(c) Modular Hat-type USMH

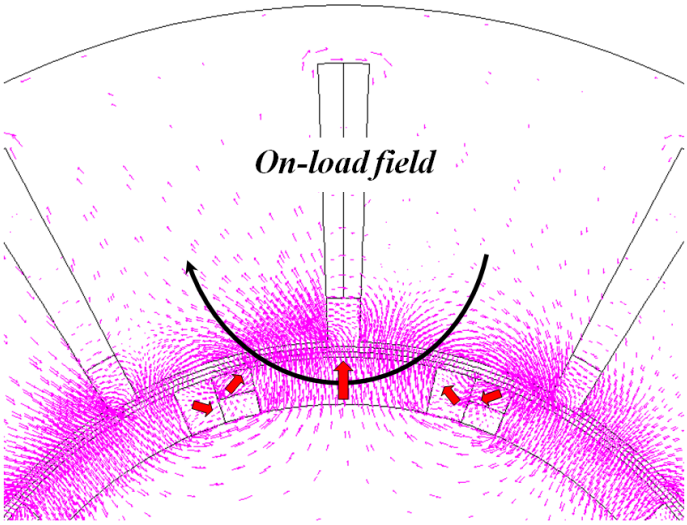

(i). On-load field

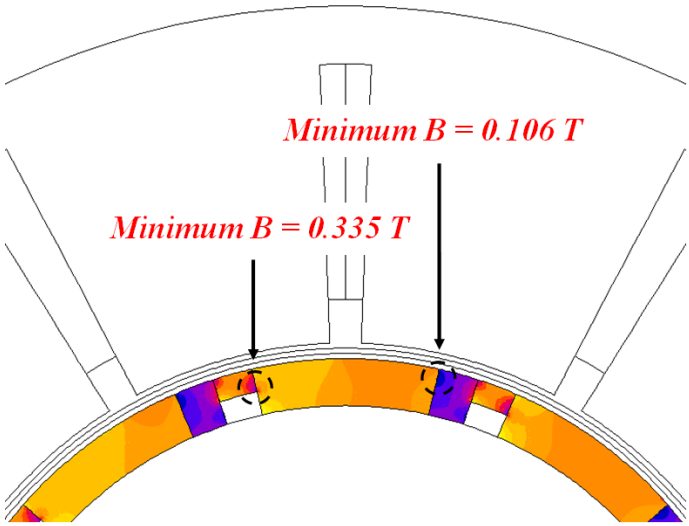

(ii). Potential demagnetization area

(d) Modular T-type USMH

Fig.5.15. Demagnetization investigation on 12-slot/10-pole PM brushless machines having conventional and modular Hat- and T-type USMH magnet pole when q-axis current is maximized.

Furthermore, the investigation on the curvature effect in accordance to rotor pole pair variation is examined by adopting slotless model with given rotor outer diameter and air-gap length in Table II. In this slotless model, the variation of the air-gap flux density waveform with p is analytically global optimized, while the fundamental air-gap flux density B_{ag1} is calculated by using Fast Fourier Transform (FFT) from the obtained flux density waveforms. Further, in this case, B_{ag1} is used instead of T_{em} for slotless model, since its amplitude can directly reflect the magnitude of T_{em}. Therefore, B_{ag1}/V_{pm} can be used to represent the foregoing magnet usage $\eta_{pm} = T_{em}/V_{pm}$. Fig.5.16 reveals that although conventional 3-segment Halbach array exhibits the highest amplitude of B_{ag1}, the similar magnet usage efficiency which is defined as B_{ag1}/V_{pm}*(NdFeB)* still demonstrates the relative merits of modular T-type, modular Hat- and T-type USMH magnet poles when p increases.

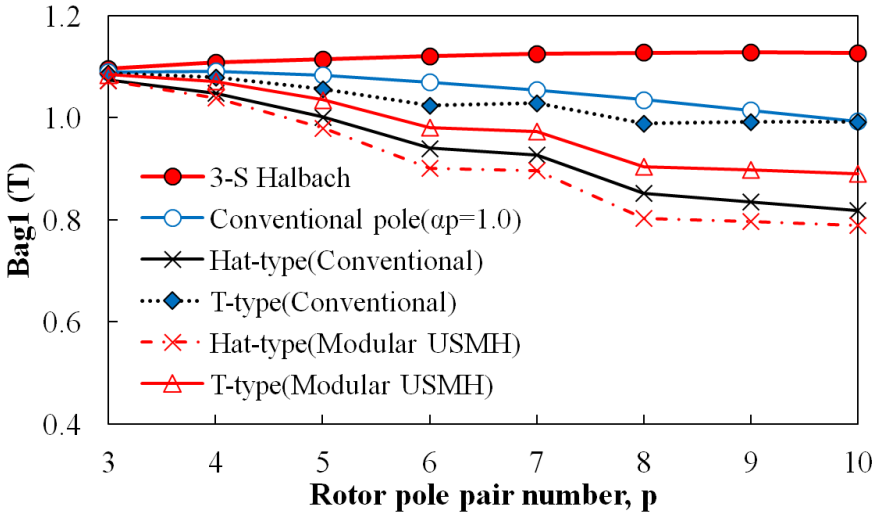

(a) B_{ag1}

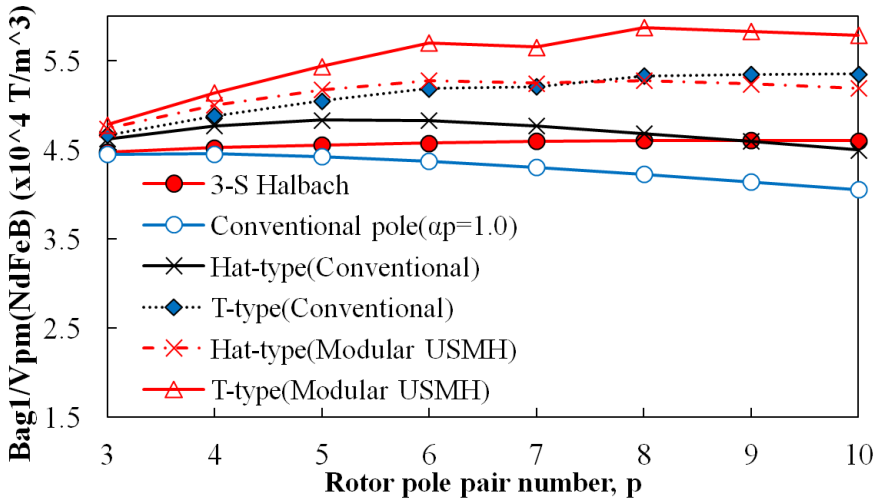

(b) B_{ag1}/V_{pm}*(NdFeB)*

Fig.5.16. Comparison of analytically predicted B_{ag1} and ratio of B_{ag1}/V_{pm}(NdFeB) for slotless machines having conventional pole (α_p = 1), 3-segment Halbach array, conventional Hat- and T-type magnet pole, and modular Hat- and T-type USMH magnet pole with overall optimized R_{mp} and magnetization angles.

5.6 Summary

This chapter proposes the permanent magnet machines having mixed high cost NdFeB magnets and low cost ferrite magnets to form modular unequal side-magnet height pole, i.e. the modular Hat- and T-type magnets with either equal or unequal side-magnet height, together with optimized Halbach magnetizations. The investigation shows that a modular T-type magnet pole with unequal side-magnet height and different magnet materials exhibits significant potential to achieve low torque ripple, relative high electromagnetic torque, and

low NdFeB usage simultaneously. Meanwhile, it also presents a high ratio of average electromagnetic torque to PM volume in contrast to a conventional 3-segment Halbach array. By adopting the T-type magnet pole, the inherent large inter-pole leakage flux is reduced in contrast to the Hat-type magnet pole. Further, the modular technique can also reduce the inter-pole leakage flux in the conventional Hat-type magnet pole. Due to side-magnet being away from on-load field, both conventional and modular Hat-type magnet poles present better demagnetization withstand capability than conventional and modular T-type magnet pole.

5.7 Appendix

According to (5.3) and (5.4), the expressions of $M_{rn(\cos np\theta)}$ and $M_{rn(\sin np\theta)}$ can be fully expanded and derived as:

$$M_{rn(\cos np\theta)}\ \frac{\mathrm{p}}{\pi}\Bigg\{-\frac{B_{rsL}}{2\mu_0}\cos\Delta\theta_L\Bigg[\frac{\cos\left[(1+np)\left(-\frac{R_{mp}\pi}{2p}\right)+\delta\right]}{1+np}-\frac{\cos\left[(1+np)\left(-\frac{\alpha_p\pi}{2p}\right)+\delta\right]}{1+np}$$
$$+\frac{\cos\left[(1-np)\left(-\frac{R_{mp}\pi}{2p}\right)+\delta\right]}{1-np}-\frac{\cos\left[(1-np)\left(-\frac{\alpha_p\pi}{2p}\right)+\delta\right]}{1-np}\Bigg]+$$
$$\frac{B_{rm}}{2\mu_0}\Bigg[\frac{\sin\left[(1+np)\frac{R_{mp}\pi}{2p}\right]}{1+np}-\frac{\sin\left[(1+np)\left(-\frac{R_{mp}\pi}{2p}\right)\right]}{1+np}+$$
$$\frac{\sin\left[(1-np)\frac{R_{mp}\pi}{2p}\right]}{1-np}-\frac{\sin\left[(1-np)\left(-\frac{R_{mp}\pi}{2p}\right)\right]}{1-np}\Bigg]+$$
$$\frac{B_{rsR}}{2\mu_0}\cos\Delta\theta_R\Bigg[\frac{\cos\left[(1+np)\frac{\alpha_p\pi}{2p}-\delta\right]}{1+np}-\frac{\cos\left[(1+np)\frac{R_{mp}\pi}{2p}-\delta\right]}{1+np}+$$
$$\frac{\cos\left[(1-np)\frac{\alpha_p\pi}{2p}-\delta\right]}{1-np}-\frac{\cos\left[(1-np)\frac{R_{mp}\pi}{2p}-\delta\right]}{1-np}\Bigg]+$$

$$\frac{B_{rsL}}{2\mu_0}\cos\Delta\theta_L\left[\frac{\cos\left[(1+np)\left(1-\frac{R_{mp}}{2}\right)\frac{\pi}{p}-\frac{\pi}{p}+\delta\right]}{1+np}-\frac{\cos\left[(1+np)\left(1-\frac{\alpha_p}{2}\right)\frac{\pi}{p}-\frac{\pi}{p}+\delta\right]}{1+np}+\right.$$

$$\left.\frac{\cos\left[(1-np)\left(1-\frac{R_{mp}}{2}\right)\frac{\pi}{p}-\frac{\pi}{p}+\delta\right]}{1-np}-\frac{\cos\left[(1-np)\left(1-\frac{\alpha_p}{2}\right)\frac{\pi}{p}-\frac{\pi}{p}+\delta\right]}{1-np}\right]-$$

$$\frac{B_{rm}}{2\mu_0}\left[\frac{\sin\left[(1+np)\left(1+\frac{R_{mp}}{2}\right)\frac{\pi}{p}-\frac{\pi}{p}\right]}{1+np}-\frac{\sin\left[(1+np)\left(1-\frac{R_{mp}}{2}\right)\frac{\pi}{p}-\frac{\pi}{p}\right]}{1+np}+\right.$$

$$\left.\frac{\sin\left[(1-np)\left(1+\frac{R_{mp}}{2}\right)\frac{\pi}{p}-\frac{\pi}{p}\right]}{1-np}-\frac{\sin\left[(1-np)\left(1-\frac{R_{mp}}{2}\right)\frac{\pi}{p}-\frac{\pi}{p}\right]}{1-np}\right]-$$

$$\frac{B_{rsR}}{2\mu_0}\cos\Delta\theta_R\left[\frac{\cos\left[(1+np)\left(1+\frac{\alpha_p}{2}\right)\frac{\pi}{p}-\frac{\pi}{p}-\delta\right]}{1+np}-\frac{\cos\left[(1+np)\left(1+\frac{R_{mp}}{2}\right)\frac{\pi}{p}-\frac{\pi}{p}-\delta\right]}{1+np}+\right.$$

$$\left.\left.\frac{\cos\left[(1-np)\left(1+\frac{\alpha_p}{2}\right)\frac{\pi}{p}-\frac{\pi}{p}-\delta\right]}{1-np}-\frac{\cos\left[(1-np)\left(1+\frac{R_{mp}}{2}\right)\frac{\pi}{p}-\frac{\pi}{p}-\delta\right]}{1-np}\right]\right\}+$$

$$\frac{p}{\pi}\left\{\frac{B_{rsL}}{2\mu_0}\sin\Delta\theta_L\left[\frac{\sin\left[(1+np)\left(-\frac{R_{mp}\pi}{2p}\right)+\delta\right]}{1+np}-\frac{\sin\left[(1+np)\left(-\frac{\alpha_p\pi}{2p}\right)+\delta\right]}{1+np}+\right.\right.$$

$$\left.\frac{\sin\left[(1-np)\left(-\frac{R_{mp}\pi}{2p}\right)+\delta\right]}{1-np}-\frac{\sin\left[(1-np)\left(-\frac{\alpha_p\pi}{2p}\right)+\delta\right]}{1-np}\right]+$$

$$\frac{B_{rsR}}{2\mu_0}\sin\Delta\theta_R\left[\frac{\sin\left[(1+np)\frac{\alpha_p\pi}{2p}-\delta\right]}{1+np}-\frac{\sin\left[(1+np)\frac{R_{mp}\pi}{2p}-\delta\right]}{1+np}+\right.$$

$$\left.\frac{\sin\left[(1-np)\frac{\alpha_p\pi}{2p}-\delta\right]}{1-np}-\frac{\sin\left[(1-np)\frac{R_{mp}\pi}{2p}-\delta\right]}{1-np}\right]-$$

$$\frac{B_{rsL}}{2\mu_0}\sin\Delta\theta_L\left[\frac{\sin\left[(1+np)\left(1-\frac{R_{mp}}{2}\right)\frac{\pi}{p}+\delta-\frac{\pi}{p}\right]}{1+np}-\frac{\sin\left[(1+np)\left(1-\frac{\alpha_p}{2}\right)\frac{\pi}{p}+\delta-\frac{\pi}{p}\right]}{1+np}+\right.$$

$$\left.\frac{\sin\left[(1-np)\left(1-\frac{R_{mp}}{2}\right)\frac{\pi}{p}+\delta-\frac{\pi}{p}\right]}{1-np}-\frac{\sin\left[(1-np)\left(1-\frac{\alpha_p}{2}\right)\frac{\pi}{p}+\delta-\frac{\pi}{p}\right]}{1-np}\right]-$$

$$\frac{B_{rsR}}{2\mu_0}\sin\Delta\theta_R\left[\frac{\sin\left[(1+np)\left(1+\frac{\alpha_p}{2}\right)\frac{\pi}{p}-\delta-\frac{\pi}{p}\right]}{1+np}-\frac{\sin\left[(1+np)\left(1+\frac{R_{mp}}{2}\right)\frac{\pi}{p}-\delta-\frac{\pi}{p}\right]}{1+np}+\right.$$

$$\left.\left.\frac{\sin\left[(1-np)\left(1+\frac{\alpha_p}{2}\right)\frac{\pi}{p}-\delta-\frac{\pi}{p}\right]}{1-np}-\frac{\sin\left[(1-np)\left(1+\frac{R_{mp}}{2}\right)\frac{\pi}{p}-\delta-\frac{\pi}{p}\right]}{1-np}\right]\right\} \qquad (5.7)$$

and

$$M_{rn(\sin np\theta)} = \frac{\mathrm{p}}{\pi}\left\{-\frac{B_{rsL}}{2\mu_0}\cos\Delta\theta_L\left[\frac{\sin\left[(1+np)\left(-\frac{R_{mp}\pi}{2p}\right)+\delta\right]}{1+np}-\frac{\sin\left[(1+np)\left(-\frac{\alpha_p\pi}{2p}\right)+\right.\right.\right.$$

$$\left.\left.\left.-\frac{\sin\left[(1-np)\left(-\frac{R_{mp}\pi}{2p}\right)+\delta\right]}{1-np}+\frac{\sin\left[(1-np)\left(-\frac{\alpha_p\pi}{2p}\right)+\delta\right]}{1-np}\right]-\right.\right.$$

$$\left.\frac{B_{rm}}{2\mu_0}\left[\frac{\cos\left[(1+np)\frac{R_{mp}\pi}{2p}\right]}{1+np}-\frac{\cos\left[(1+np)\left(-\frac{R_{mp}\pi}{2p}\right)\right]}{1+np}-\right.\right.$$

$$\left.\left.\frac{\cos\left[(1-np)\frac{R_{mp}\pi}{2p}\right]}{1-np}+\frac{\cos\left[(1-np)\left(-\frac{R_{mp}\pi}{2p}\right)\right]}{1-np}\right]+\right.$$

$$\left.\frac{B_{rsR}}{2\mu_0}\cos\Delta\theta_R\left[\frac{\sin\left[(1+np)\frac{\alpha_p\pi}{2p}-\delta\right]}{1+np}-\frac{\sin\left[(1+np)\frac{R_{mp}\pi}{2p}-\delta\right]}{1+np}-\right.\right.$$

$$\left.\left.\frac{\sin\left[(1-np)\frac{\alpha_p\pi}{2p}-\delta\right]}{1-np}+\frac{\sin\left[(1-np)\frac{R_{mp}\pi}{2p}-\delta\right]}{1-np}\right]+\right.$$

$$\frac{B_{rsL}}{2\mu_0}\cos\Delta\theta_L\left[\frac{\sin\left[(1+np)\left(1-\frac{R_{mp}}{2}\right)\frac{\pi}{p}-\frac{\pi}{p}+\delta\right]}{1+np}-\frac{\sin\left[(1+np)\left(1-\frac{\alpha_p}{2}\right)\frac{\pi}{p}-\frac{\pi}{p}+\delta\right]}{1+np}-\right.$$

$$\left.\frac{\sin\left[(1-np)\left(1-\frac{R_{mp}}{2}\right)\frac{\pi}{p}-\frac{\pi}{p}+\delta\right]}{1-np}+\frac{\sin\left[(1-np)\left(1-\frac{\alpha_p}{2}\right)\frac{\pi}{p}-\frac{\pi}{p}+\delta\right]}{1-np}\right]-$$

$$\frac{B_{rm}}{2\mu_0}\left[-\frac{\cos\left[(1+np)\left(1+\frac{R_{mp}}{2}\right)\frac{\pi}{p}-\frac{\pi}{p}\right]}{1+np}+\frac{\cos\left[(1+np)\left(1-\frac{R_{mp}}{2}\right)\frac{\pi}{p}-\frac{\pi}{p}\right]}{1+np}+\right.$$

$$\left.\frac{\cos\left[(1-np)\left(1+\frac{R_{mp}}{2}\right)\frac{\pi}{p}-\frac{\pi}{p}\right]}{1-np}-\frac{\cos\left[(1-np)\left(1-\frac{R_{mp}}{2}\right)\frac{\pi}{p}-\frac{\pi}{p}\right]}{1-np}\right]-$$

$$\frac{B_{rsR}}{2\mu_0}\cos\Delta\theta_R\left[\frac{\sin\left[(1+np)\left(1+\frac{\alpha_p}{2}\right)\frac{\pi}{p}-\frac{\pi}{p}-\delta\right]}{1+np}-\frac{\sin\left[(1+np)\left(1+\frac{R_{mp}}{2}\right)\frac{\pi}{p}-\frac{\pi}{p}-\delta\right]}{1+np}-\right.$$

$$\left.\left.\frac{\sin\left[(1-np)\left(1+\frac{\alpha_p}{2}\right)\frac{\pi}{p}-\frac{\pi}{p}-\delta\right]}{1-np}+\frac{\sin\left[(1-np)\left(1+\frac{R_{mp}}{2}\right)\frac{\pi}{p}-\frac{\pi}{p}-\delta\right]}{1-np}\right]\right\}+$$

$$\frac{\mathrm{p}}{\pi}\left\{-\frac{B_{rsL}}{2\mu_0}\sin\Delta\theta_L\left[\frac{\cos\left[(1+np)\left(-\frac{R_{mp}\pi}{2p}\right)+\delta\right]}{1+np}-\frac{\cos\left[(1+np)\left(-\frac{\alpha_p\pi}{2p}\right)+\delta\right]}{1+np}\right.\right.$$

$$\left.-\frac{\cos\left[(1-np)\left(-\frac{R_{mp}\pi}{2p}\right)+\delta\right]}{1-np}+\frac{\cos\left[(1-np)\left(-\frac{\alpha_p\pi}{2p}\right)+\delta\right]}{1-np}\right]-$$

$$\frac{B_{rsR}}{2\mu_0}\sin\Delta\theta_R\left[\frac{\cos\left[(1+np)\frac{\alpha_p\pi}{2p}-\delta\right]}{1+np}-\frac{\cos\left[(1+np)\frac{R_{mp}\pi}{2p}-\delta\right]}{1+np}-\right.$$

$$\left.\frac{\cos\left[(1-np)\frac{\alpha_p\pi}{2p}-\delta\right]}{1-np}+\frac{\cos\left[(1-np)\frac{R_{mp}\pi}{2p}-\delta\right]}{1-np}\right]+$$

$$\frac{B_{rsL}}{2\mu_0}\sin\Delta\theta_L\left[\frac{\cos\left[(1+np)\left(1-\frac{R_{mp}}{2}\right)\frac{\pi}{p}-\frac{\pi}{p}+\delta\right]}{1+np}-\frac{\cos\left[(1+np)\left(1-\frac{\alpha_p}{2}\right)\frac{\pi}{p}-\frac{\pi}{p}+\delta\right]}{1+np}-\right.$$

$$\left.\frac{\cos\left[(1-np)\left(1-\frac{R_{mp}}{2}\right)\frac{\pi}{p}-\frac{\pi}{p}+\delta\right]}{1-np}+\frac{\cos\left[(1-np)\left(1-\frac{\alpha_p}{2}\right)\frac{\pi}{p}-\frac{\pi}{p}+\delta\right]}{1-np}\right]+$$

$$\frac{B_{rsR}}{2\mu_0}\sin\Delta\theta_R\left[\frac{\cos\left[(1+np)\left(1+\frac{\alpha_p}{2}\right)\frac{\pi}{p}-\frac{\pi}{p}-\delta\right]}{1+np}-\frac{\cos\left[(1+np)\left(1+\frac{R_{mp}}{2}\right)\frac{\pi}{p}-\frac{\pi}{p}-\delta\right]}{1+np}-\right.$$

$$\left.\left.\frac{\cos\left[(1-np)\left(1+\frac{\alpha_p}{2}\right)\frac{\pi}{p}-\frac{\pi}{p}-\delta\right]}{1-np}+\frac{\cos\left[(1-np)\left(1+\frac{R_{mp}}{2}\right)\frac{\pi}{p}-\frac{\pi}{p}-\delta\right]}{1-np}\right]\right\} \quad (5.8)$$

Similarly, according to (5.5) and (5.6), the circumferential air-gap flux density components $M_{\theta n(\sin np\theta)}$ and $M_{\theta n(\cos np\theta)}$ can be derived as:

$$M_{rn(\cos np\theta)}=\frac{\mathrm{p}}{\pi}\left\{\frac{B_{rsL}}{2\mu_0}\sin\Delta\theta_L\left[\frac{cos\left[(1+np)\left(-\frac{R_{mp}\pi}{2p}\right)+\delta\right]}{1+np}-\frac{\cos\left[(1+np)\left(-\frac{\alpha_p\pi}{2p}\right)+\right.\right.\right.$$

$$\left.\left.\left.+\frac{\cos\left[(1-np)\left(-\frac{R_{mp}\pi}{2p}\right)+\delta\right]}{1-np}-\frac{\cos\left[(1-np)\left(-\frac{\alpha_p\pi}{2p}\right)+\delta\right]}{1-np}\right]+\right.\right.$$

$$\left.\frac{B_{rm}}{2\mu_0}\left[\frac{\cos\left[(1+np)\frac{R_{mp}\pi}{2p}\right]}{1+np}-\frac{\cos\left[(1+np)\left(-\frac{R_{mp}\pi}{2p}\right)\right]}{1+np}+\right.\right.$$

$$\left.\left.\frac{\cos\left[(1-np)\frac{R_{mp}\pi}{2p}\right]}{1-np}-\frac{\cos\left[(1-np)\left(-\frac{R_{mp}\pi}{2p}\right)\right]}{1-np}\right]+\right.$$

$$\left.\frac{B_{rsR}}{2\mu_0}\sin\Delta\theta_R\left[\frac{\cos\left[(1+np)\frac{\alpha_p\pi}{2p}-\delta\right]}{1+np}-\frac{\sin\left[(1+np)\frac{R_{mp}\pi}{2p}-\delta\right]}{1+np}+\right.\right.$$

$$\frac{\cos\left[(1-np)\frac{\alpha_p\pi}{2p}-\delta\right]}{1-np}-\frac{\cos\left[(1-np)\frac{R_{mp}\pi}{2p}-\delta\right]}{1-np}\Bigg]+$$

$$\frac{B_{rsL}}{2\mu_0}\sin\Delta\theta_L\Bigg[-\frac{\cos\left[(1+np)\left(1-\frac{R_{mp}}{2}\right)\frac{\pi}{p}-\frac{\pi}{p}+\delta\right]}{1+np}+\frac{\cos\left[(1+np)\left(1-\frac{\alpha_p}{2}\right)\frac{\pi}{p}-\frac{\pi}{p}+\delta\right]}{1+np}-$$

$$\frac{\cos\left[(1-np)\left(1-\frac{R_{mp}}{2}\right)\frac{\pi}{p}-\frac{\pi}{p}+\delta\right]}{1-np}+\frac{\cos\left[(1-np)\left(1-\frac{\alpha_p}{2}\right)\frac{\pi}{p}-\frac{\pi}{p}+\delta\right]}{1-np}\Bigg]+$$

$$\frac{B_{rm}}{2\mu_0}\Bigg[-\frac{\cos\left[(1+np)\left(1+\frac{R_{mp}}{2}\right)\frac{\pi}{p}-\frac{\pi}{p}\right]}{1+np}+\frac{\cos\left[(1+np)\left(1-\frac{R_{mp}}{2}\right)\frac{\pi}{p}-\frac{\pi}{p}\right]}{1+np}-$$

$$\frac{\cos\left[(1-np)\left(1+\frac{R_{mp}}{2}\right)\frac{\pi}{p}-\frac{\pi}{p}\right]}{1-np}+\frac{\cos\left[(1-np)\left(1-\frac{R_{mp}}{2}\right)\frac{\pi}{p}-\frac{\pi}{p}\right]}{1-np}\Bigg]+$$

$$\frac{B_{rsR}}{2\mu_0}\sin\Delta\theta_R\Bigg[-\frac{\cos\left[(1+np)\left(1+\frac{\alpha_p}{2}\right)\frac{\pi}{p}-\frac{\pi}{p}-\delta\right]}{1+np}+\frac{\cos\left[(1+np)\left(1+\frac{R_{mp}}{2}\right)\frac{\pi}{p}-\frac{\pi}{p}-\delta\right]}{1+np}$$

$$-$$

$$\frac{\cos\left[(1-np)\left(1+\frac{\alpha_p}{2}\right)\frac{\pi}{p}-\frac{\pi}{p}-\delta\right]}{1-np}+\frac{\cos\left[(1-np)\left(1+\frac{R_{mp}}{2}\right)\frac{\pi}{p}-\frac{\pi}{p}-\delta\right]}{1-np}\Bigg]\Bigg\}+$$

$$\frac{\mathrm{p}}{\pi}\Bigg\{\frac{B_{rsL}}{2\mu_0}\cos\Delta\theta_L\Bigg[\frac{\sin\left[(1+np)\left(-\frac{R_{mp}\pi}{2p}\right)+\delta\right]}{1+np}-\frac{\sin\left[(1+np)\left(-\frac{\alpha_p\pi}{2p}\right)+\delta\right]}{1+np}$$

$$+\frac{\sin\left[(1-np)\left(-\frac{R_{mp}\pi}{2p}\right)+\delta\right]}{1-np}-\frac{\sin\left[(1-np)\left(-\frac{\alpha_p\pi}{2p}\right)+\delta\right]}{1-np}\Bigg]+$$

$$\frac{B_{rsR}}{2\mu_0}\cos\Delta\theta_R\left[-\frac{\sin\left[(1+np)\frac{\alpha_p\pi}{2p}-\delta\right]}{1+np}+\frac{\sin\left[(1+np)\frac{R_{mp}\pi}{2p}-\delta\right]}{1+np}-\right.$$

$$\left.\frac{\sin\left[(1-np)\frac{\alpha_p\pi}{2p}-\delta\right]}{1-np}+\frac{\sin\left[(1-np)\frac{R_{mp}\pi}{2p}-\delta\right]}{1-np}\right]+$$

$$\frac{B_{rsL}}{2\mu_0}\cos\Delta\theta_L\left[-\frac{\sin\left[(1+np)\left(1-\frac{R_{mp}}{2}\right)\frac{\pi}{p}-\frac{\pi}{p}+\delta\right]}{1+np}+\frac{\sin\left[(1+np)\left(1-\frac{\alpha_p}{2}\right)\frac{\pi}{p}-\frac{\pi}{p}+\delta\right]}{1+np}-\right.$$

$$\left.\frac{\sin\left[(1-np)\left(1-\frac{R_{mp}}{2}\right)\frac{\pi}{p}-\frac{\pi}{p}+\delta\right]}{1-np}+\frac{\sin\left[(1-np)\left(1-\frac{\alpha_p}{2}\right)\frac{\pi}{p}-\frac{\pi}{p}+\delta\right]}{1-np}\right]+$$

$$\frac{B_{rsR}}{2\mu_0}\cos\Delta\theta_R\left[\frac{\sin\left[(1+np)\left(1+\frac{\alpha_p}{2}\right)\frac{\pi}{p}-\frac{\pi}{p}-\delta\right]}{1+np}-\frac{\sin\left[(1+np)\left(1+\frac{R_{mp}}{2}\right)\frac{\pi}{p}-\frac{\pi}{p}-\delta\right]}{1+np}+\right.$$

$$\left.\left.\frac{\sin\left[(1-np)\left(1+\frac{\alpha_p}{2}\right)\frac{\pi}{p}-\frac{\pi}{p}-\delta\right]}{1-np}-\frac{\sin\left[(1-np)\left(1+\frac{R_{mp}}{2}\right)\frac{\pi}{p}-\frac{\pi}{p}-\delta\right]}{1-np}\right]\right\} \qquad (5.9)$$

and,

$$M_{\theta n(\sin np\theta)}=\frac{\mathrm{p}}{\pi}\left\{-\frac{B_{rsL}}{2\mu_0}\cos\Delta\theta_L\left[\frac{\cos\left[(1+np)\left(-\frac{R_{mp}\pi}{2p}\right)+\delta\right]}{1+np}-\frac{\cos\left[(1+np)\left(-\frac{\alpha_p\pi}{2p}\right)+\delta\right.}{1+np}\right.\right.$$

$$\left.-\frac{\cos\left[(1-np)\left(-\frac{R_{mp}\pi}{2p}\right)+\delta\right]}{1-np}+\frac{\cos\left[(1-np)\left(-\frac{\alpha_p\pi}{2p}\right)+\delta\right]}{1-np}\right]+$$

$$\frac{B_{rm}}{2\mu_0}\left[\frac{\sin\left[(1+np)\frac{R_{mp}\pi}{2p}\right]}{1+np}-\frac{\sin\left[(1+np)\left(-\frac{R_{mp}\pi}{2p}\right)\right]}{1+np}-\right.$$

$$\left.\frac{\sin\left[(1-np)\frac{R_{mp}\pi}{2p}\right]}{1-np}+\frac{\sin\left[(1-np)\left(-\frac{R_{mp}\pi}{2p}\right)\right]}{1-np}\right]+$$

$$\frac{B_{rsR}}{2\mu_0}\cos\Delta\theta_R\left[\frac{\cos\left[(1+np)\frac{\alpha_p\pi}{2p}-\delta\right]}{1+np}-\frac{\cos\left[(1+np)\frac{R_{mp}\pi}{2p}-\delta\right]}{1+np}-\right.$$

$$\left.\frac{\cos\left[(1-np)\frac{\alpha_p\pi}{2p}-\delta\right]}{1-np}+\frac{\cos\left[(1-np)\frac{R_{mp}\pi}{2p}-\delta\right]}{1-np}\right]+$$

$$\frac{B_{rsL}}{2\mu_0}\cos\Delta\theta_L\left[\frac{\cos\left[(1+np)\left(1-\frac{R_{mp}}{2}\right)\frac{\pi}{p}-\frac{\pi}{p}+\delta\right]}{1+np}-\frac{\cos\left[(1+np)\left(1-\frac{\alpha_p}{2}\right)\frac{\pi}{p}-\frac{\pi}{p}+\delta\right]}{1+np}-\right.$$

$$\left.\frac{\cos\left[(1-np)\left(1-\frac{R_{mp}}{2}\right)\frac{\pi}{p}-\frac{\pi}{p}+\delta\right]}{1-np}+\frac{\cos\left[(1-np)\left(1-\frac{\alpha_p}{2}\right)\frac{\pi}{p}-\frac{\pi}{p}+\delta\right]}{1-np}\right]-$$

$$\frac{B_{rm}}{2\mu_0}\left[\frac{\sin\left[(1+np)\left(1+\frac{R_{mp}}{2}\right)\frac{\pi}{p}-\frac{\pi}{p}\right]}{1+np}-\frac{\sin\left[(1+np)\left(1-\frac{R_{mp}}{2}\right)\frac{\pi}{p}-\frac{\pi}{p}\right]}{1+np}-\right.$$

$$\left.\frac{\sin\left[(1-np)\left(1+\frac{R_{mp}}{2}\right)\frac{\pi}{p}-\frac{\pi}{p}\right]}{1-np}+\frac{\sin\left[(1-np)\left(1-\frac{R_{mp}}{2}\right)\frac{\pi}{p}-\frac{\pi}{p}\right]}{1-np}\right]-$$

$$\frac{B_{rsR}}{2\mu_0}\cos\Delta\theta_R\left[\frac{\cos\left[(1+np)\left(1+\frac{\alpha_p}{2}\right)\frac{\pi}{p}-\frac{\pi}{p}-\delta\right]}{1+np}-\frac{\cos\left[(1+np)\left(1+\frac{R_{mp}}{2}\right)\frac{\pi}{p}-\frac{\pi}{p}-\delta\right]}{1+np}-\right.$$

$$\left.\left.\frac{\cos\left[(1-np)\left(1+\frac{\alpha_p}{2}\right)\frac{\pi}{p}-\frac{\pi}{p}-\delta\right]}{1-np}+\frac{\cos\left[(1-np)\left(1+\frac{R_{mp}}{2}\right)\frac{\pi}{p}-\frac{\pi}{p}-\delta\right]}{1-np}\right]\right\}+$$

$$\frac{p}{\pi}\left\{\frac{B_{rsL}}{2\mu_0}\sin\Delta\theta_L\left[\frac{\sin\left[(1+np)\left(-\frac{R_{mp}\pi}{2p}\right)+\delta\right]}{1+np}-\frac{\sin\left[(1+np)\left(-\frac{\alpha_p\pi}{2p}\right)+\delta\right]}{1+np}-\right.\right.$$

$$\left.\left.\frac{\sin\left[(1-np)\left(-\frac{R_{mp}\pi}{2p}\right)+\delta\right]}{1-np}+\frac{\sin\left[(1-np)\left(-\frac{\alpha_p\pi}{2p}\right)+\delta\right]}{1-np}\right]+\right.$$

$$\frac{B_{rsR}}{2\mu_0}\sin\Delta\theta_R\left[\frac{\sin\left[(1+np)\frac{\alpha_p\pi}{2p}-\delta\right]}{1+np}-\frac{\sin\left[(1+np)\frac{R_{mp}\pi}{2p}-\delta\right]}{1+np}-\right.$$

$$\left.\frac{\sin\left[(1-np)\frac{\alpha_p\pi}{2p}-\delta\right]}{1-np}+\frac{\sin\left[(1-np)\frac{R_{mp}\pi}{2p}-\delta\right]}{1-np}\right]-$$

$$\frac{B_{rsL}}{2\mu_0}\sin\Delta\theta_L\left[\frac{\sin\left[(1+np)\left(1-\frac{R_{mp}}{2}\right)\frac{\pi}{p}+\delta-\frac{\pi}{p}\right]}{1+np}-\frac{\sin\left[(1+np)\left(1-\frac{\alpha_p}{2}\right)\frac{\pi}{p}+\delta-\frac{\pi}{p}\right]}{1+np}-\right.$$

$$\left.\frac{\sin\left[(1-np)\left(1-\frac{R_{mp}}{2}\right)\frac{\pi}{p}+\delta-\frac{\pi}{p}\right]}{1-np}+\frac{\sin\left[(1-np)\left(1-\frac{\alpha_p}{2}\right)\frac{\pi}{p}+\delta-\frac{\pi}{p}\right]}{1-np}\right]-$$

$$\frac{B_{rsR}}{2\mu_0}\sin\Delta\theta_R\left[\frac{\sin\left[(1+np)\left(1+\frac{\alpha_p}{2}\right)\frac{\pi}{p}-\delta-\frac{\pi}{p}\right]}{1+np}-\frac{\sin\left[(1+np)\left(1+\frac{R_{mp}}{2}\right)\frac{\pi}{p}-\delta-\frac{\pi}{p}\right]}{1+np}-\right.$$

$$\left.\left.\frac{\sin\left[(1-np)\left(1+\frac{\alpha_p}{2}\right)\frac{\pi}{p}-\delta-\frac{\pi}{p}\right]}{1-np}+\frac{\sin\left[(1-np)\left(1+\frac{R_{mp}}{2}\right)\frac{\pi}{p}-\delta-\frac{\pi}{p}\right]}{1-np}\right]\right\} \qquad (5.10)$$

CHAPTER 6 ANALYTICAL PREDICTION OF OPTIMAL SPLIT RATIO FOR FRACTIONAL-SLOT EXTERNAL ROTOR PM BRUSHLESS MACHINES

The split ratio is one of the most important design parameters for PM brushless machines. It has been optimized for maximum torque density with both internal rotor and tubular PM brushless machines over last decades. In this chapter, the optimal split ratio for both non-overlapping and overlapping winding external rotor PM brushless machines have been derived analytically, with due account for the influence of both fixed and variable rotor back-iron thickness, pole number, slot number, winding factor, tooth-tip, and end-winding length. Moreover, the variation of optimal split ratio with slot and pole combinations, tooth-tips, and maximum flux density in the stator/rotor lamination is also investigated. The theoretical analyses are verified by FEA.

6.1 Introduction

It is well known that the split ratio between the rotor and stator outer diameters is an important design parameter of permanent magnet (PM) brushless machines. The split ratio for external rotor machine is defined as the ratio of outer stator diameter to outer rotor diameter. Previous work [200] has confirmed the existence of optimal split ratio for minimum copper loss. Although the numerical methods, such as FEA, can be used to analyse the influence of split ratio, the analytical methods are preferred as the stage of preliminary design and optimization. Analytical methods were developed in [201]-[203] for SPM machines, neglecting the influence of tooth-tips and end-winding. A recent study [204] has reported an improved analytical model accounting for the combination of slot and pole numbers, brushless DC and AC operation modes, tooth-tips and end-winding length. Furthermore, an analytical model in [205] was developed for determining the optimal split ratio of fractional-slot interior PM machines with flux focusing technique. In contrast with studies in rotary machines, the analytical approach to determine the optimal split ratio of tubular PM machines to date was subjected to two distinguished methodologies from the foregoing stated algorithm, viz. 2-D field model [207][208] and the lumped circuit model [209]. Those analytical approaches for the determination of optimal split ratio, as stated above, are only developed for internal rotor [200]-[206] and tubular [207]-[209] PM machines.

Up to date, the increasing awareness of high performance electrical vehicles (EV) stimulates the research activity to enhance the electrical machine performance. Hence, the

external rotor PM brushless machine becomes popular for in-wheel traction applications, on the basis of their short stack length and high torque density. Meanwhile, the external rotor PM brushless machines are also widely applied for wind power generation system. However, the approaches of analytical optimal split ratio prediction as stated above are not applicable for external rotor machines. Therefore, this chapter proposes an analytical model to predict the optimal split ratio for external rotor PM brushless machines.

The air-gap flux density of internal rotor machines is generally independent of the split ratio. Thus, in the analytical model for internal rotor PM machines, the optimal split ratio is obtained for a specified air-gap flux density. The optimal split ratio reduces and the torque increases correspondingly, when the air-gap flux density increases. Therefore, the proper design is based on a trade-off between magnet volume and torque density, but usually not a global optimum [205]. Nonetheless, the air-gap flux density of the external rotor PM machine is a function of the split ratio, Fig.6.1(a). It decreases as the split ratio increases due to the variation of PM thickness. The decrease of the air-gap flux density competing with the increased the slot area leads to an optimal split ratio and an optimal air-gap flux density for the maximum torque, Fig.6.1(b).

This chapter proposes a general analytical model of optimal split ratio determination for external rotor SPM machines having both fixed (due to mechanical consideration) and variable rotor back-iron thickness, together with either overlapping windings or non-overlapping windings. It accounts for the influence of end-winding length, stator back-iron thickness, and curvature effect. Its validity is confirmed by FEA on an overlapping winding (24-slot/8-pole) machine and a non-overlapping winding (24-slot/28-pole) machine, in Fig.6.2.

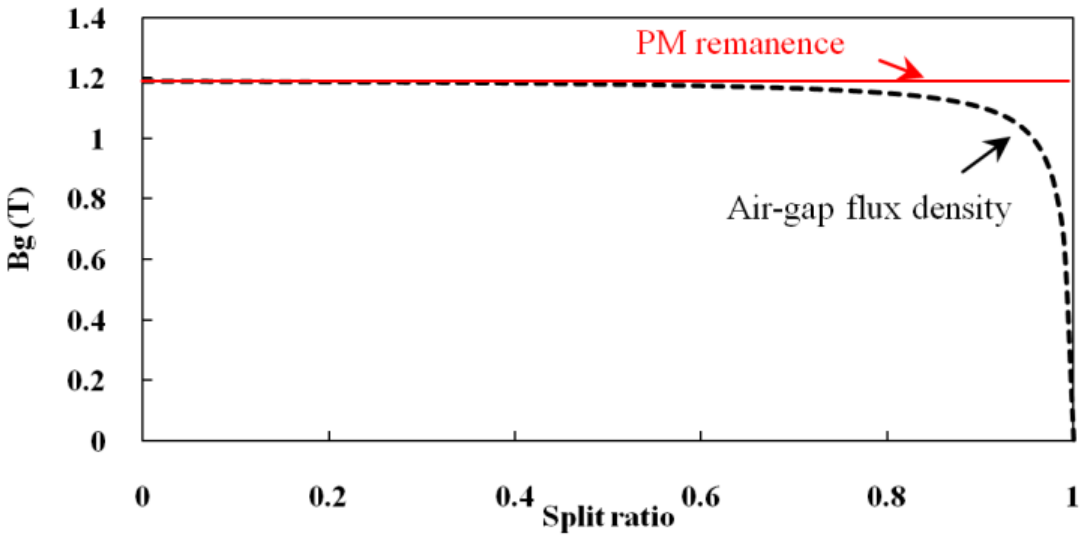

(a) Air-gap flux density versus split ratio

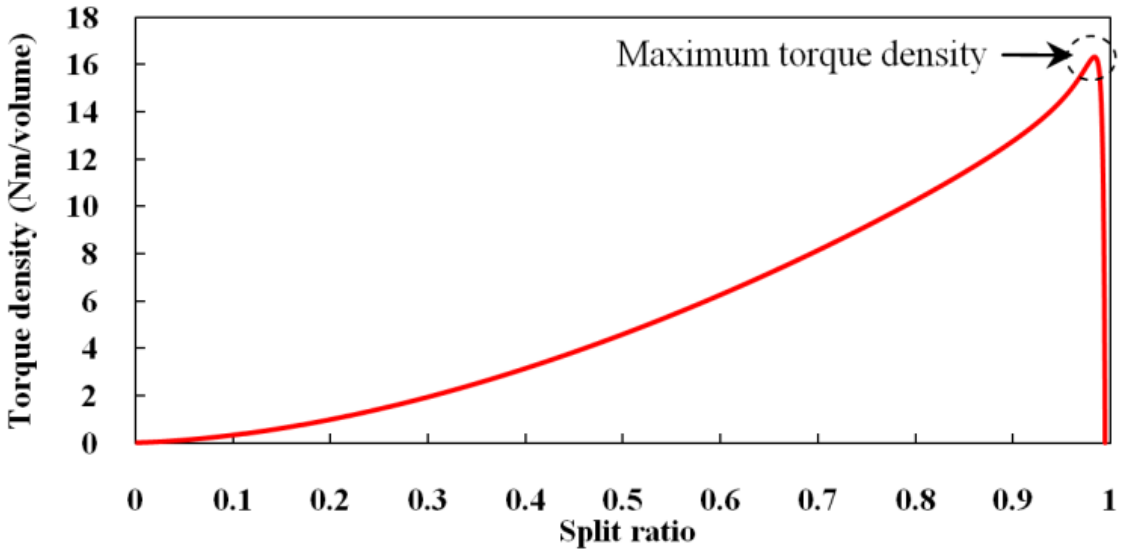

(b) Torque density versus split ratio

Fig.6.1. Variation of air-gap flux density and torque density with split ratio.

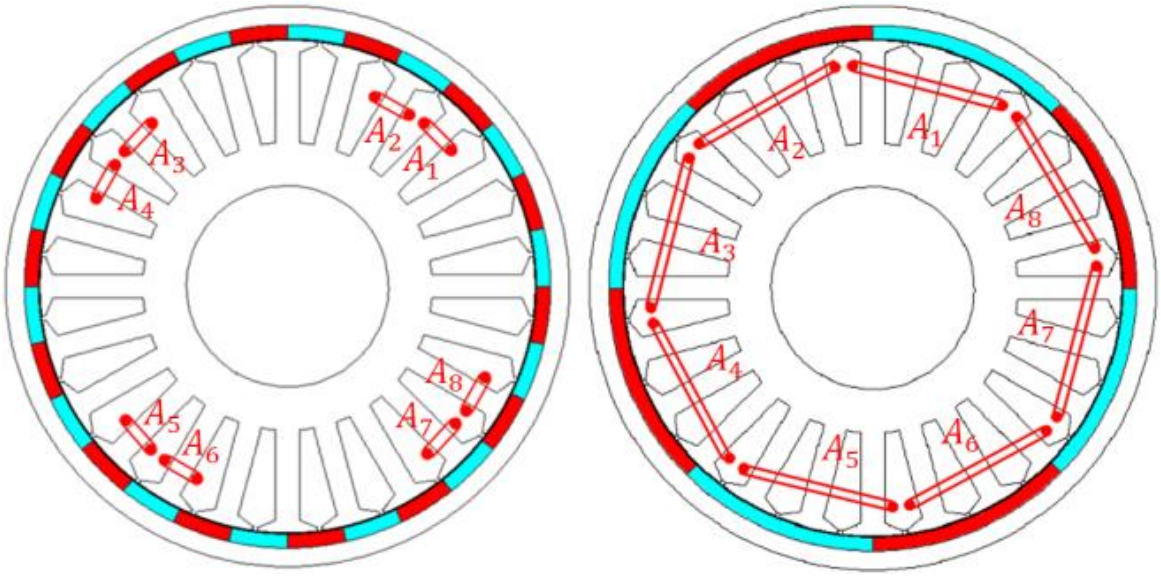

(a) 24-slot/28-pole machine (b) 24-slot/8-pole machine

Fig.6.2. Geometries of 24-slot/28-pole and 24-slot/8-pole external rotor SPM machines.

TABLE 6-I. MAIN PARAMETER OF PROTOTYPE 24-SLOT MACHINES

Stator slot number, N_s	24	Slot opening, b_o (mm)	2.0
Tooth-tips height, h_t (mm)	1.5	Air-gap length, l_g (mm)	1.0
Rotor outer diameter, D_{ro} (mm)	240	Active length, l_a (mm)	59.5
PM remanence, B_r (T)	1.22	Copper loss (W)	58
PM relative permeability,μ_r	1.05	Shaft diameter, D_{sf} (mm)	100

6.2 Analytical Determination of Optimal Split Ratio

The optimal split ratio for a three-phase brushless DC motor with a non-overlapping winding will be derived, by assuming

- trapezoidal air-gap flux density distribution
- 120° electrical conduction
- parallel side stator teeth, without tooth tips
- neglecting end windings
- rotor cage diameter is fixed

6.2.1 Fixed Rotor Back-Iron Thickness

The rotor back-iron thickness h_{rbi} is fixed initially. The schematic view of two non-overlapping and overlapping winding 24-slot hub machines are shown in Fig.6.2 and their main design parameters are defined and can be found in TABLE 6-I.

The PM thickness (h_m) can be determined as:

$$H_m h_m + H_g l_g = 0$$

$$h_m = -\frac{H_g l_g}{H_m}$$

where, h_m is the magnet thickness, l_g is the air-gap length, H_m and H_g are the magnetic intensities of magnet and air-gap, respectively. Further, if

$$B_m = B_g$$

Thus,

$$B_m = B_r + \mu_0 \mu_m H_m$$

$$B_{ag} = B_r - \mu_0 \mu_m \cdot \frac{H_g l_g}{h_m}$$

$$= B_r - \mu_m \cdot \frac{l_g}{h_m} \cdot \mu_0 H_g$$

$$= B_r - \mu_m \cdot \frac{l_g}{h_m} \cdot B_g$$

$$= \frac{B_r}{\frac{A_m}{A_g} + \mu_m \frac{l_g}{h_m}} \tag{6.1}$$

where, B_m is the flux density in magnet and B_g is the air-gap flux density. Then, the amplitude of air-gap flux density $B_{ag(\lambda)}$ which can be treated as a function of the split ratio λ and derived as:

$$B_{ag(\lambda)} = \frac{B_r}{\frac{A_g}{A_m} + \mu_r \cdot \frac{l_g}{\frac{D_{ro}}{2} - \frac{D_{so}}{2} - h_{rbi} - l_g}}$$

$$= \frac{B_r}{\left(\frac{D_{so} + l_g}{D_{so} + 2l_g}\right)^2 + \mu_r \cdot \frac{l_g}{\frac{D_{ro}}{2} - \frac{D_{so}}{2} - h_{rbi} - l_g}}$$

$$= \frac{B_r}{\left(\frac{\frac{D_{so}}{D_{ro}} + \frac{l_g}{D_{ro}}}{\frac{D_{so}}{D_{ro}} + \frac{2l_g}{D_{ro}}}\right)^2 + \mu_r \cdot \frac{l_g}{D_{ro} \cdot \left(\frac{1}{2} - \frac{D_{so}}{2D_{ro}} - \frac{h_{rbi}}{D_{ro}} - \frac{l_g}{D_{ro}}\right)}}$$

$$= \frac{B_r}{\left(\frac{\lambda + \frac{l_g}{D_{ro}}}{\lambda + \frac{2l_g}{D_{ro}}}\right)^2 + \mu_r \cdot \frac{l_g}{D_{ro} \cdot \left(\frac{1}{2} - \frac{\lambda}{2} - \frac{h_{rbi}}{D_{ro}} - \frac{l_g}{D_{ro}}\right)}}$$

$$= \frac{B_r}{\left(\frac{\lambda + \tau}{\lambda + 2\tau}\right)^2 + \mu_r \cdot \frac{l_g}{D_{ro} \cdot \left(\frac{1}{2} - \frac{\lambda}{2} - \frac{h_{rbi}}{D_{ro}} - \tau\right)}} \quad (6.2)$$

Thus,

$$B_{ag(\lambda)} = \frac{B_r}{\eta + \mu_r l_g / \left[D_{ro}\left(\frac{1}{2} - \frac{h_{rbi}}{D_{ro}} - \frac{\lambda}{2} - \tau\right)\right]} \quad (6.3)$$

where the split ratio is:

$$\lambda = D_{so}/D_{ro} \quad (6.4)$$

where D_{so} is the stator outer diameter and

$$\tau = l_g/D_{ro} \quad (6.5)$$

$$\eta = \left(\frac{\lambda + \tau}{\lambda + 2\tau}\right)^2 \quad (6.6)$$

The electromagnetic torque under brushless DC operation mode (Since the air-gap flux density is assumed to be trapezoidally distributed, the BLDC operation mode is chosen as desired operation mode in this chapter. However, the BLAC operation can be also applied to proposed analytical model which has no influence on optimal split ratio prediction in contrast to the BLDC operation, but only varies the amplitude of average torque), when the air-gap

flux density is uniformly distributed and the armature reaction effect is ignored, can be obtained as:

$$T = 2k_w N_{ph}(D_{so} + l_g) l_a B_{ag(\lambda)} I_a \tag{6.7}$$

where N_{ph} is the number of turns per phase and I_a is the amplitude of phase current.

By taking account of the end-winding length, the calculation of is extra copper loss that affects torque density variation may be separated into two cases, viz. non-overlapping and overlapping winding machines, Fig.6.3. The average end-winding length as shown in Fig.6.3 can be estimated by:

$$l_e = \pi r_{ew} \tag{6.8}$$

$$r_{ew} = (r_{oew} + r_{iew})/2 \tag{6.9}$$

where r_{ew}, r_{oew} and r_{iew} are the average, outer and inner radii of end-winding, respectively.

By considering the effect of end-winding length, the motor copper loss is derived as:

$$P_{cu} = 24 N_{ph}^2 I_a^2 \rho \frac{l_a + l_e}{A_s K_p N_s} \tag{6.10}$$

Thus,

$$I_a = \sqrt{\frac{P_{cu} A_s K_p N_s}{24 N_{ph}^2 \rho (l_a + l_e)}} \tag{6.11}$$

where A_s is the slot area, K_p is the winding packing factor, and ρ is the resistivity of the winding.

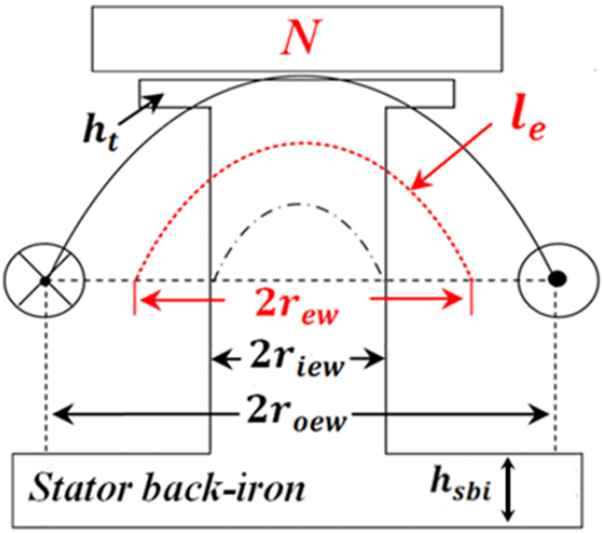

(a) Non-overlapping winding

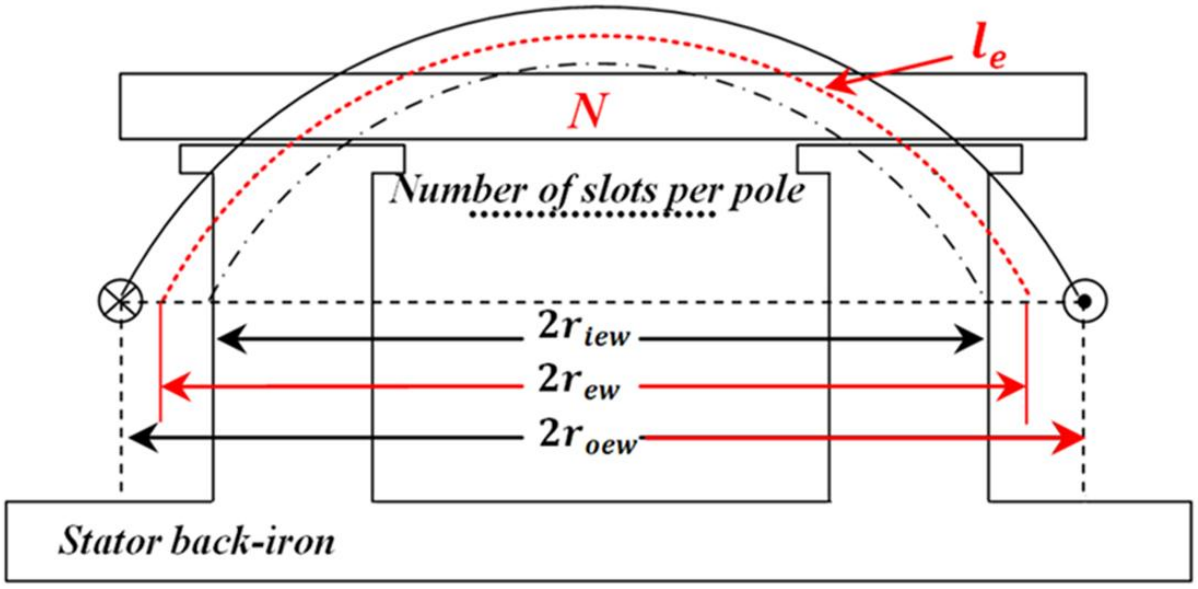

(b) Overlapping winding

Fig.6.3. Illustration of end-winding length.

By simplifying the expression of parameters independent of the split ratio variation as a constant, the torque density can be expressed in terms of λ as:

$$TD = \frac{4T}{\pi D_{ro}^2 l_a} = C \cdot k_w \sqrt{\frac{l_a}{l_a + l_e}} \gamma_{(\lambda)} \lambda \sqrt{\frac{4A_s N_s}{\pi D_{ro}^2}} \tag{6.12}$$

where the flux density ratio $\gamma_{(\lambda)}$ is:

$$\gamma_{(\lambda)} = B_{ag(\lambda)} / B_{smax} \tag{6.13}$$

and

$$C = \sqrt{\frac{2P_{cu}K_p}{3\rho l_a \pi}} B_{smax} \tag{6.14}$$

where C is a constant value for a given copper loss, B_{smax} is the maximum flux density in the stator lamination accounting for the magnetic saturation, and normally is chosen around the knee point of the specific lamination B-H curve on the open-circuit condition [205].

The nominal torque density is deduced as:

$$TD^* = TD/C \tag{6.15}$$

It should be emphasized that the slot area A_s in (6.12) varies with the split ratio. Consequently, the variations of both stator tooth body thickness and stator back-iron thickness with λ are necessary to be understood. It is assumed that the flux passing the air-gap per slot-pitch completely flows into the stator tooth body if the leakage flux is neglected for both overlapping and non-overlapping winding machines. Hence, the stator tooth body

width is written by:

$$b_t = \frac{\pi D_{ro}(\lambda + \tau)\gamma_{(\lambda)}}{N_s} \tag{6.16}$$

In addition, the required stator back-iron thickness h_{sbi} to keep B_{smax} is equal to half of the tooth body width b_t for machines with the number of slots per pole $Q \leq 1.5$ [204]. However, for machines with $Q > 1.5$, the required h_{sbi} is obtained assuming that the flux in the stator back-iron is equal to half of the flux per pole [205]. Eventually, the required h_{sbi} is derived according to two cases:

For $Q \leq 1.5$

$$h_{sbi} = \frac{\pi D_{ro}(\lambda + \tau)\gamma_{(\lambda)}}{2N_s} \tag{6.17}$$

For $Q > 1.5$

$$h_{sbi} = \frac{\pi D_{ro}(\lambda + \tau)\gamma_{(\lambda)}}{4N_p} \tag{6.18}$$

where N_p is the number of pole pair. Moreover, machines having non-overlapping windings exhibit both $Q \leq 1.5$ and $Q > 1.5$ cases, while machines having overlapping windings have only $Q > 1.5$ case.

In practice, the real h_{sbi} can be thicker than required value due to mechanical constraint, as shown in Fig.6.4(c) where D_{si} and D_{si1} indicate the required slot inner diameter to achieve B_{smax} and the real slot inner diameter, respectively. b_t is initially increasing as λ increases, Fig.6.4(a). Then, two stator tooth bodies contact each other as long as b_t is increased to a certain thickness, Fig.6.4(b), and keep contact for a range of the split ratio, Fig.6.4(c). Further, b_t is reduced significantly when λ is near to 1, which causes two stator bodies to be separated, Fig.6.4(d). Therefore, in accordance with Fig.6.4, the analytical expression of nominal torque density TD^* is derived based on two conditions, viz. (1) $\alpha \leq \theta$; (2) $\alpha > \theta$, where the angles α and θ are defined as:

For $Q \leq 1.5$

$$\alpha = arcsin\left[\frac{\pi(\lambda + \tau)\gamma_{(\lambda)}}{\pi(\lambda + \tau)\gamma_{(\lambda)} + \varepsilon N_s}\right] \tag{6.19}$$

For $Q > 1.5$

$$\alpha = arcsin\left[\frac{2\pi N_p(\lambda + \tau)\gamma_{(\lambda)}}{\pi N_s(\lambda + \tau)\gamma_{(\lambda)} + 2\varepsilon N_s N_p}\right] \tag{6.20}$$

$$\theta = \frac{180}{N_s} \tag{6.21}$$

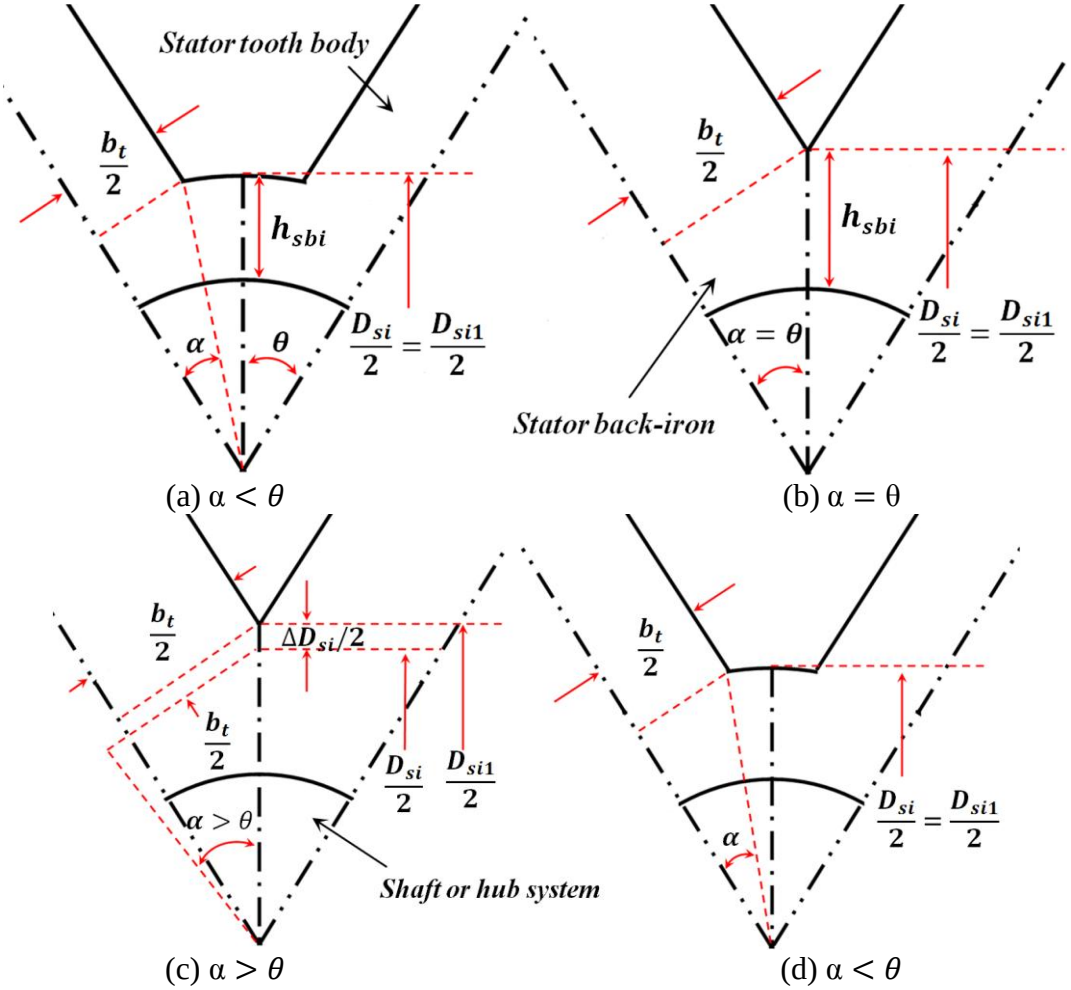

Fig.6.4.Variation of stator tooth body width and stator inner area including stator back-iron and hub system areas with split ratio λ. The split ratio increases from (a)-(d).

Ultimately, the TD^*expressions of the proposed model based on different Q numbers are summarized in Tables II-III and IV for three cases. The symbols ε and σ in the tables are the shaft and tooth-tip ratios, and given by $\varepsilon = D_{sf}/D_{ro}$ and $\sigma = 2h_t/D_{ro}$. Those foregoing equations reveal TD^* is only depending on the split ratio for external rotor machine. However, TD^* is a function of two independent variables, viz. B_g and split ratio, for internal rotor machine.

It is important to notice that an expression of optimal split ratio for the maximum TD^* can be derived but it is mathematically complicated. Instead, the optimal split ratio can be easily determined by scanning TD^* with the split ratio.

6.2.2 Variable Rotor Back-Iron Thickness

For the majority machine design, h_{rbi} should be varied to avoid the saturation in the rotor back iron, i.e. keeping a desired maximum flux density level, B_{rmax}, in the rotor lamination. As can be seen in Fig.6.5, the flux leaving from one magnet pole ϕ_{pm} are separated into two

equal parts of opposite direction in the rotor back-iron ϕ_{rbi}. This phenomenon can be mathematically expressed as:

$$\phi_{pm} = 2\phi_{rbi}$$

$$\frac{\pi(D_{ro} - 2h_{rbi})\eta B_{ag(\lambda)}}{2N_p} = 2h_{rbi}B_{rmax} \tag{6.22}$$

where N_p is the pole pair number.

By substituting (6.3) into (6.22), the h_{rbi} can be obtained by solving the quadratic formula as:

$$h_{rbi} = \frac{-b \pm \sqrt{b^2 - 4ac}}{2a} \tag{6.23}$$

where

$$a = 2\pi\beta\eta - 4N_p\eta \tag{6.24}$$

$$b = 2N_p\eta D_{ro}(2\tau + \lambda - 1) - 4N_p\mu_r l_g \ + \pi\eta\beta D_{ro}(2\tau + \lambda - 1) \tag{6.25}$$

$$c = 1/2 \cdot \pi\beta\eta D_{ro}^2(1 - 2\tau - \lambda) \tag{6.26}$$

where the flux density ratio for rotor part is written as:

$$\beta = \frac{B_{ag(\lambda)}}{B_{rmax}} \tag{6.27}$$

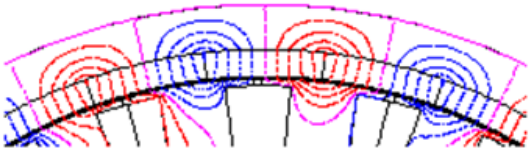

(a) 24-slot/28-pole machine

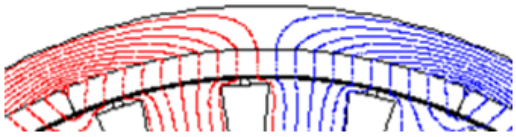

(b) 24-slot/8-pole machine

Fig.6.5. FEA predicted equal-potential distribution in rotor back-iron.

Since the slot area prediction for both fixed and variable h_{rbi} is the same, TD^* predictions in accordance with different Q numbers are the same as shown in TABLE 6-II-III and IV.

TABLE 6-II. NOMINAL TORQUE DENSITY $\boldsymbol{TD}^*$ FOR EXTERNAL ROTOR SPM MACHINE WITH NON-OVERLAPPING WINDING AND $\boldsymbol{Q \leq 1.5}$

$\alpha \le \theta$	$TD^* = k_w\sqrt{\frac{l_a}{l_a+l_e}}\gamma_{(\lambda)}(\lambda+\tau)\sqrt{\left(1-2\gamma_{(\lambda)}+\frac{2\pi\gamma_{(\lambda)}^2}{N_s}-\frac{\pi^2\gamma_{(\lambda)}^2}{N_s^2}\right)\lambda^2+\left(2\varepsilon\gamma_{(\lambda)}-2\tau\gamma_{(\lambda)}+\frac{4\pi\tau\gamma_{(\lambda)}^2}{N_s}-\frac{2\pi^2\gamma_{(\lambda)}^2\tau}{N_s^2}-\frac{2\pi\varepsilon\gamma_{(\lambda)}}{N_s}+2\sigma\gamma_{(\lambda)}-2\sigma\right)\lambda+2\varepsilon\tau\gamma_{(\lambda)}+\frac{2\pi\tau^2\gamma_{(\lambda)}^2}{N_s}-\frac{\tau^2\pi^2\gamma_{(\lambda)}^2}{N_s^2}-\frac{2\pi\varepsilon\gamma_{(\lambda)}\tau}{N_s}-\varepsilon^2+\sigma^2+2\tau\sigma\gamma_{(\lambda)}}$
	$l_e = \frac{\pi^2 D_{ro}}{4N_s}\left[\left(\frac{\pi}{2N_s}+1\right)(\lambda+\tau)\gamma_{(\lambda)}+\frac{\lambda}{2}+\frac{\varepsilon}{2}-\frac{\sigma}{2}\right]$
$\alpha > \theta$	$TD^* = k_w\sqrt{\frac{l_a}{l_a+l_e}}\gamma_{(\lambda)}(\lambda+\tau)\sqrt{\left(1-2\gamma_{(\lambda)}+\frac{2\pi\gamma_{(\lambda)}^2}{N_s sin\theta}-\frac{\pi^2\gamma_{(\lambda)}^2}{N_s^2 sin^2\theta}\right)\lambda^2+\left(\frac{4\tau\pi\gamma_{(\lambda)}^2}{N_s sin\theta}-2\gamma_{(\lambda)}\tau-\frac{2\pi^2\gamma_{(\lambda)}^2\tau}{N_s^2 sin^2\theta}+2\sigma\gamma_{(\lambda)}-2\sigma\right)\lambda+\frac{2\pi\gamma_{(\lambda)}^2\tau^2}{N_s sin\theta}-\frac{\pi^2\gamma_{(\lambda)}^2\tau^2}{N_s^2 sin^2\theta}+\sigma^2+2\tau\sigma\gamma_{(\lambda)}}$
	$l_e = \frac{\pi^2 D_{ro}}{4N_s}\left[\left(\frac{\pi}{2N_s sin\theta}+1\right)(\lambda+\tau)\gamma_{(\lambda)}+\frac{\lambda}{2}-\frac{\sigma}{2}\right]$

TABLE 6-III. NOMINAL TORQUE DENSITY $\boldsymbol{TD}^*$ FOR EXTERNAL ROTOR SPM MACHINE WITH NON-OVERLAPPING WINDING AND $\boldsymbol{Q} > 1.5$

$\alpha \le \theta$	$TD^* = k_w\gamma_{(\lambda)}\sqrt{\frac{l_a}{l_a+l_e}}(\lambda+\tau)\sqrt{\left(1-2\gamma_{(\lambda)}+\frac{\gamma_{(\lambda)}^2}{N_p}-\frac{\pi^2\gamma_{(\lambda)}^2}{4N_p^2}\right)\lambda^2+\left(\frac{2\tau\gamma_{(\lambda)}^2}{N_p}-2\tau\gamma_{(\lambda)}+2\varepsilon\gamma_{(\lambda)}-\frac{\tau\pi^2\gamma_{(\lambda)}^2}{2N_p^2}-\frac{\pi\varepsilon\gamma_{(\lambda)}}{N_p}+2\sigma\gamma_{(\lambda)}-2\sigma\right)\lambda+\frac{\tau^2\gamma_{(\lambda)}^2}{N_p}+2\varepsilon\tau\gamma_{(\lambda)}-\frac{\pi^2\gamma_{(\lambda)}^2\tau^2}{4N_p^2}-\frac{\pi\varepsilon\tau\gamma_{(\lambda)}}{N_p}-\varepsilon^2+\sigma^2+2\sigma\tau\gamma_{(\lambda)}}$
	$l_e = \frac{\pi^2 D_{ro}}{4N_s}\left[\left(\frac{\pi}{4N_p}+1\right)(\lambda+\tau)\gamma_{(\lambda)}+\frac{\lambda}{2}+\frac{\varepsilon}{2}-\frac{\sigma}{2}\right]$
$\alpha > \theta$	$TD^* = k_w\gamma_{(\lambda)}\sqrt{\frac{l_a}{l_a+l_e}}(\lambda+\tau)\sqrt{\left(1-2\gamma_{(\lambda)}+\frac{2\pi\gamma_{(\lambda)}^2}{N_s sin\theta}-\frac{\pi^2\gamma_{(\lambda)}^2}{N_s^2 sin^2\theta}\right)\lambda^2+\left(\frac{4\tau\pi\gamma_{(\lambda)}^2}{N_s sin\theta}-2\gamma_{(\lambda)}\tau-\frac{2\pi^2\gamma_{(\lambda)}^2\tau}{N_s^2 sin^2\theta}+2\sigma\gamma_{(\lambda)}-2\sigma\right)\lambda+\frac{2\pi\gamma_{(\lambda)}^2\tau^2}{N_s sin\theta}-\frac{\pi^2\gamma_{(\lambda)}^2\tau^2}{N_s^2 sin^2\theta}+\sigma^2+2\sigma\tau\gamma_{(\lambda)}}$
	$l_e = \frac{\pi^2 D_{ro}}{4N_s}\left[\left(\frac{\pi}{2N_s sin\theta}+1\right)(\lambda+\tau)\gamma_{(\lambda)}+\frac{\lambda}{2}-\frac{\sigma}{2}\right]$

TABLE 6-IV. NOMINAL TORQUE DENSITY $\boldsymbol{TD}^*$ FOR EXTERNAL ROTOR SPM MACHINE WITH OVERLAPPING WINDING AND $\boldsymbol{Q} > 1.5$

$\alpha \le \theta$	$TD^* = k_w\gamma_{(\lambda)}\sqrt{\frac{l_a}{l_a+l_e}}(\lambda+\tau)\sqrt{\left(1-2\gamma_{(\lambda)}+\frac{\gamma_{(\lambda)}^2}{N_p}-\frac{\pi^2\gamma_{(\lambda)}^2}{4N_p^2}\right)\lambda^2+\left(\frac{2\tau\gamma_{(\lambda)}^2}{N_p}-2\tau\gamma_{(\lambda)}+2\varepsilon\gamma_{(\lambda)}-\frac{\tau\pi^2\gamma_{(\lambda)}^2}{2N_p^2}-\frac{\pi\varepsilon\gamma_{(\lambda)}}{N_p}+2\sigma\gamma_{(\lambda)}-2\sigma\right)\lambda+\frac{\tau^2\gamma_{(\lambda)}^2}{N_p}+2\varepsilon\tau\gamma_{(\lambda)}-\frac{\pi^2\gamma_{(\lambda)}^2\tau^2}{4N_p^2}-\frac{\pi\varepsilon\tau\gamma_{(\lambda)}}{N_p}-\varepsilon^2+\sigma^2+2\sigma\tau\gamma_{(\lambda)}}$
	$l_e = \frac{\pi^2 D_{ro}}{4}\left\{\left[\frac{\pi\gamma_{(\lambda)}(\lambda+\tau)}{4N_p}+\frac{\lambda}{2}+\frac{\varepsilon}{2}-\frac{\sigma}{2}\right]\cdot\left[\frac{1}{2N_p}+\frac{1}{N_s}\left(\frac{N_s}{2N_p}-1\right)\right]+\frac{\gamma_{(\lambda)}(\lambda+\tau)}{N_s}\right\}$
$\alpha > \theta$	$TD^* = k_w\gamma_{(\lambda)}\sqrt{\frac{l_a}{l_a+l_e}}(\lambda+\tau)\sqrt{\left(1-2\gamma_{(\lambda)}+\frac{2\pi\gamma_{(\lambda)}^2}{N_s sin\theta}-\frac{\pi^2\gamma_{(\lambda)}^2}{N_s^2 sin^2\theta}\right)\lambda^2+\left(\frac{4\tau\pi\gamma_{(\lambda)}^2}{N_s sin\theta}-2\gamma_{(\lambda)}\tau-\frac{2\pi^2\gamma_{(\lambda)}^2\tau}{N_s^2 sin^2\theta}+2\sigma\gamma_{(\lambda)}-2\sigma\right)\lambda+\frac{2\pi\gamma_{(\lambda)}^2\tau^2}{N_s sin\theta}-\frac{\pi^2\gamma_{(\lambda)}^2\tau^2}{N_s^2 sin^2\theta}+\delta^2+2\sigma\tau\gamma_{(\lambda)}}$

$$l_e = \frac{\pi^2 D_{ro}}{4}\left\{\left[\frac{\pi\gamma_{(\lambda)}(\lambda+\tau)}{2N_s sin\theta}+\frac{\lambda}{2}-\frac{\sigma}{2}\right]\cdot\left[\frac{1}{2N_p}+\frac{1}{N_s}\left(\frac{N_s}{2N_p}-1\right)\right]+\frac{\gamma_{(\lambda)}(\lambda+\tau)}{N_s}\right\}$$

6.3 FEA Validation

The comparison between FEA and analytically predicted average torque of the 24-slot/28-pole and 24-slot/8-pole external rotor PM brushless machines with variable rotor back-iron thickness are shown in Fig.6.6(a) and (b), respectively. The analytically predicted optimal split ratio agrees with FEA results very well for both machines, although the average torque obtained by proposed analytical model is higher than that by FEA due to the simplifications in the analytical model, such as neglected leakage flux and armature reaction, etc. It should be mentioned that the focus of this paper is to predict the optimal split ratio for a given machine envelop dimension. Therefore, although the foregoing simplifications lead to an imprecision torque prediction, they do not have a significant effect on optimal split ratio determination. The vector potential distributions in both machines having optimal split ratios are shown in Fig.6.7.

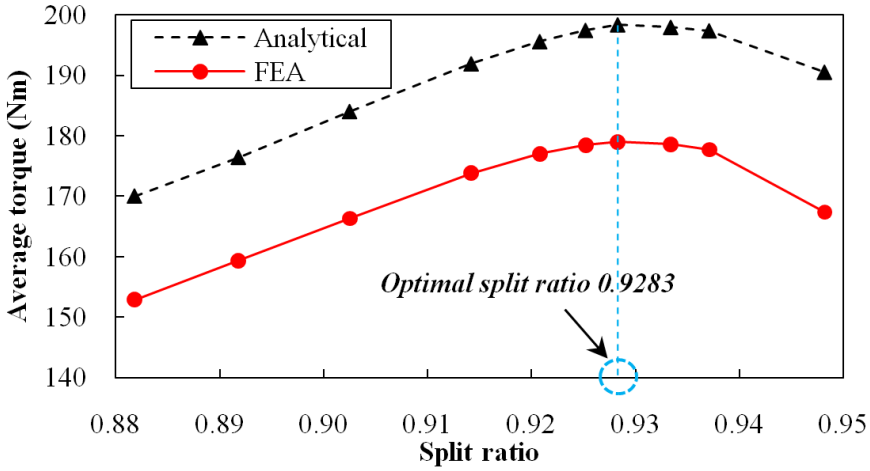

(a) 24-slot/28-pole machine

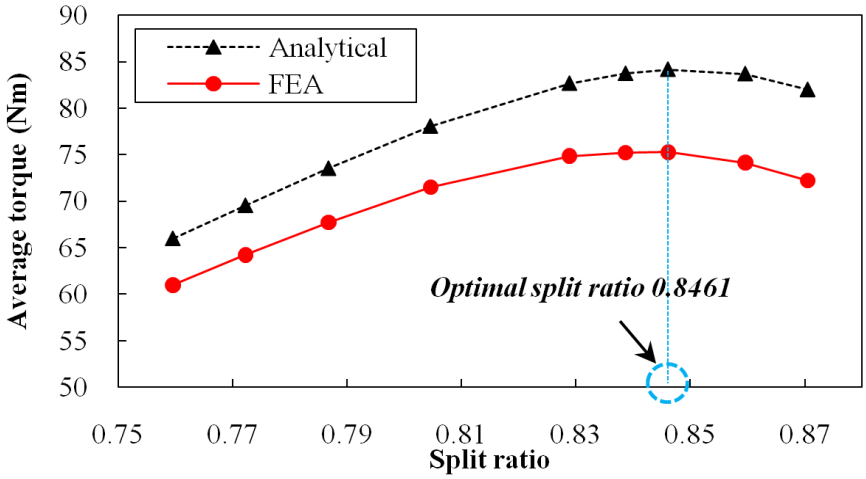

(b) 24-slot/8-pole machine

Fig.6.6. Comparison of analytically and FEA predicted average torque variation with split ratio where both B_{smax} and B_{rmax} are equal to 1.8 T.

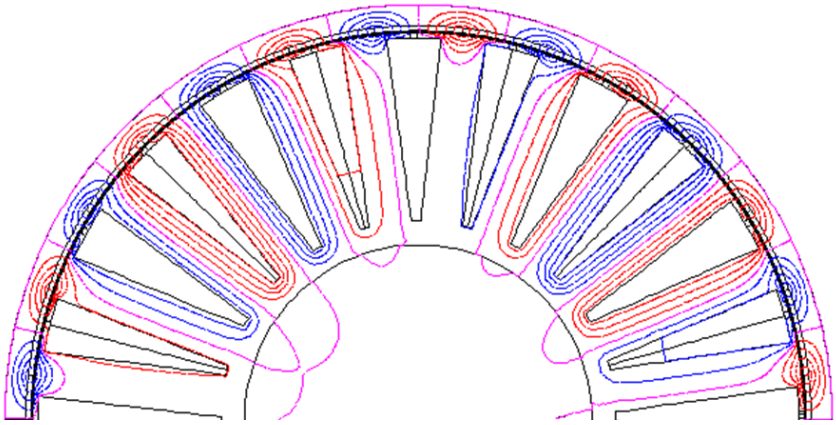

(a) 24-slot/28-pole machine

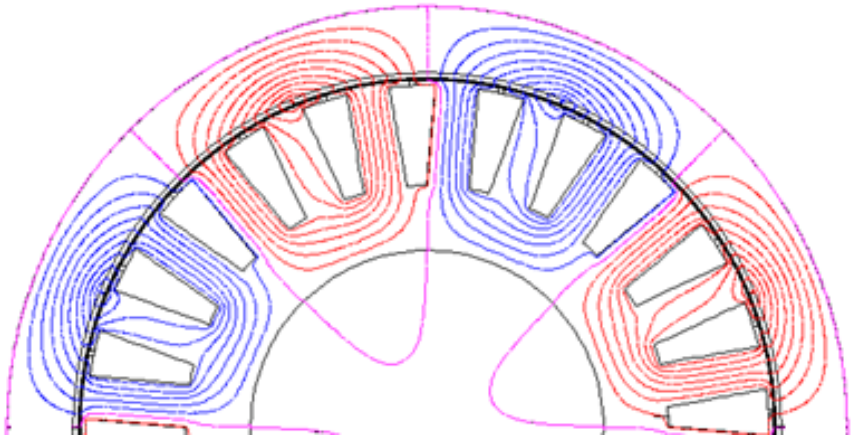

(b) 24-slot/8-pole machine

Fig.6.7. Vector potential distributions of machines having optimal split ratios.

6.4 Influence of Design Parameters on Split Ratio

The influence of the combination of slot and pole numbers on optimal split ratio is

investigated when the rotor back-iron thickness is either fixed or variable. As can be seen in Fig.6.8(a), the optimal split ratio of the machine having variable h_{rbi} exhibit significant increase with the variation of pole number than that of the machine having fixed h_{rbi}. Since the rotor back-iron thickness decreases as rotor pole pair number increasing, hence the optimal split ratio increases proportionally to the rotor pole pair number for variable rotor back-iron case. The variation of optimal split ratio of the 3-phase 10-pole machines with the slot number is also significant for variable h_{rbi} case, Fig.6.8(b). However, the slot number has less influence on optimal split ratio variation in contrast with the pole number.

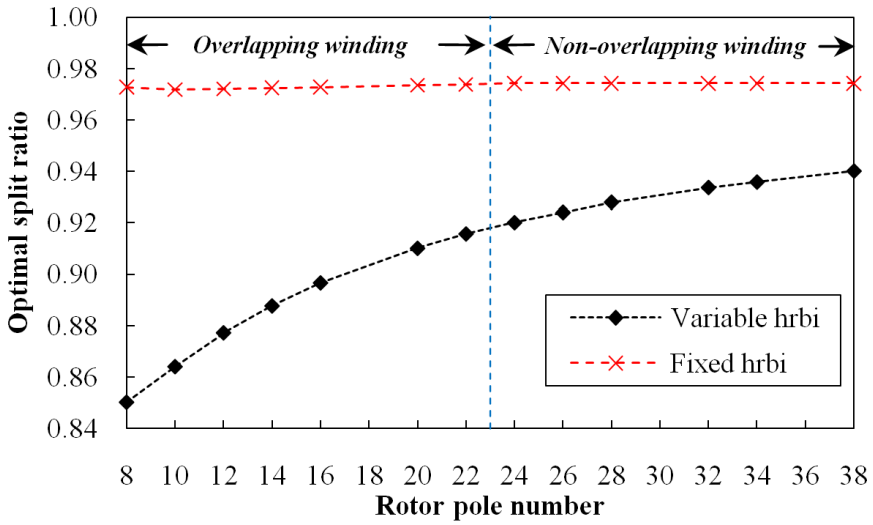

(a) 3-phase 72-slot machines

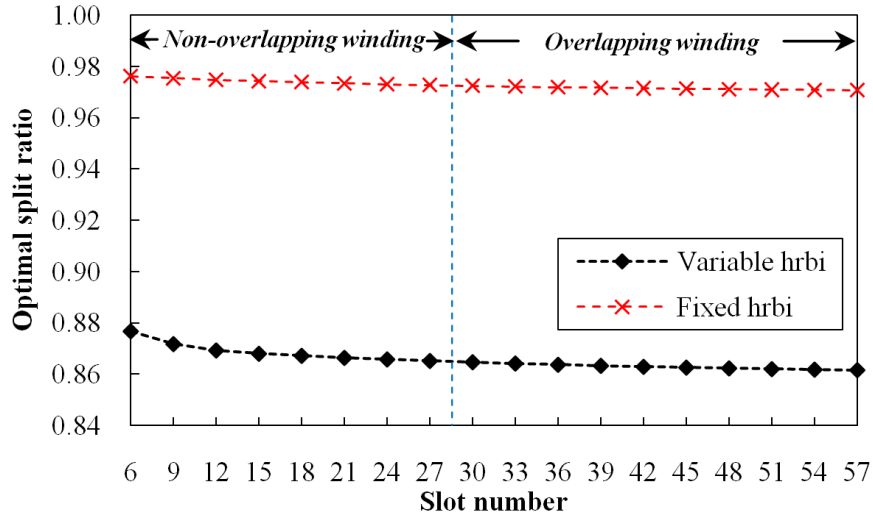

(b) 3-phase 10-pole machines

Fig.6.8. Variation of optimal split ratio in 3-phase 72-slot and 10-pole machines where $h_{rbi} = 6$ mm for fixed h_{rbi} case.

Since the machine design with variable h_{rbi} is more common than that with fixed h_{rbi}, the following parameter investigation and FEA validation are focused on analytical model with

variable h_{rbi}. Fig.6.9 and Fig.6.10 compare the variation of optimal split ratio with h_t, B_{rmax} and B_{smax} for the 24-slot/28-pole and 24-slot/8-pole machines, respectively. As can be seen, the higher the B_{smax}, the lower the optimal split ratio due to the reduction of h_{sbi}. In addition, the higher the B_{rmax}, the higher the optimal split ratio due to reduction of h_{rbi} for both machines. Further, the increase of tooth-tip thickness will result in an increase of optimal split ratio.

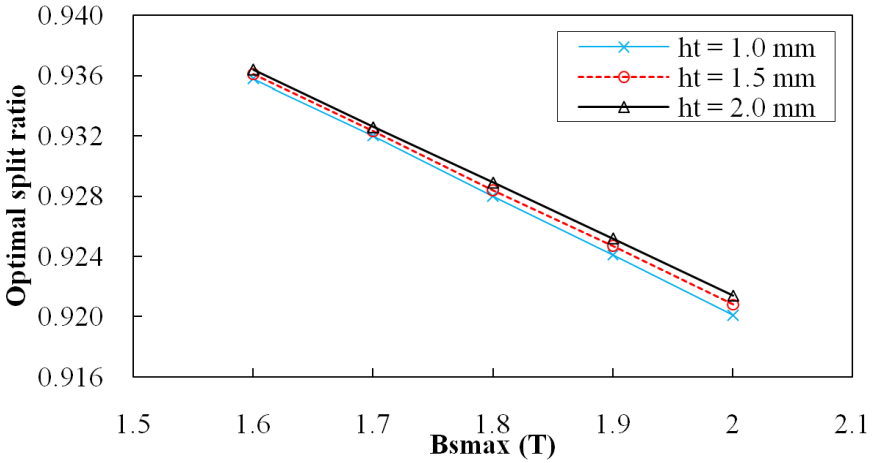

(a) $B_{rmax} = 1.8$ T

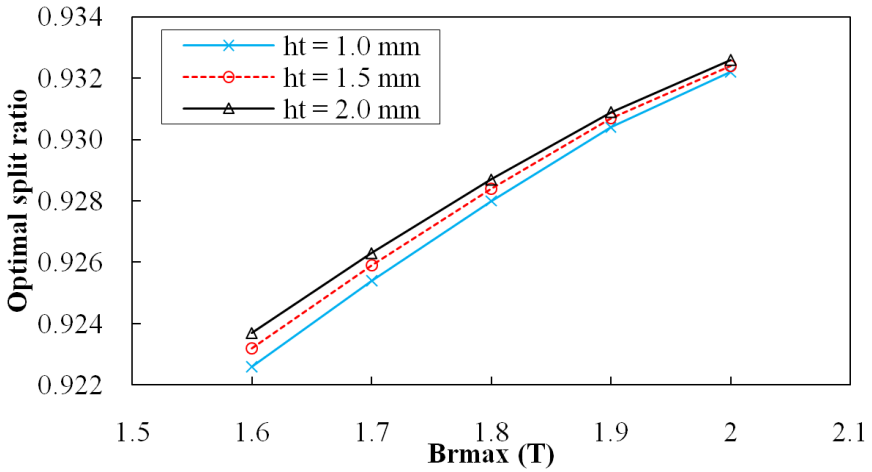

(b) $B_{smax} = 1.8$ T

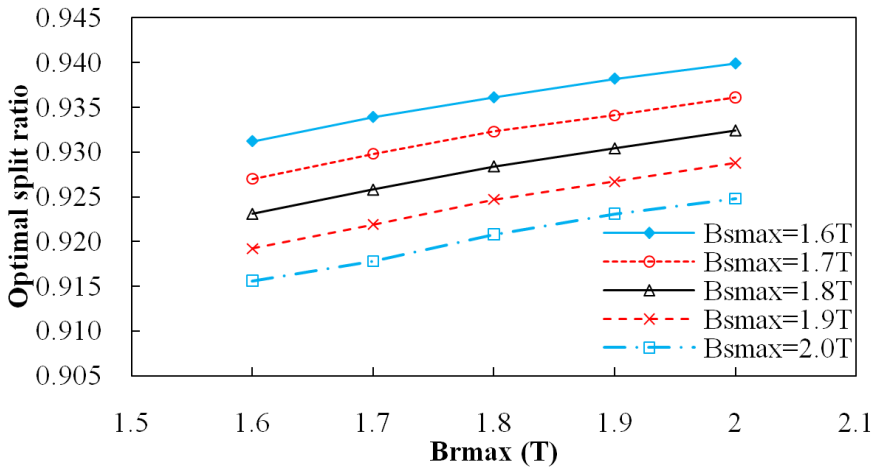

(c) $h_t = 1.5\ mm$

Fig.6.9. Variation of optimal split ratio with h_t, B_{rmax} and B_{smax} for 24-slot/28-pole machine.

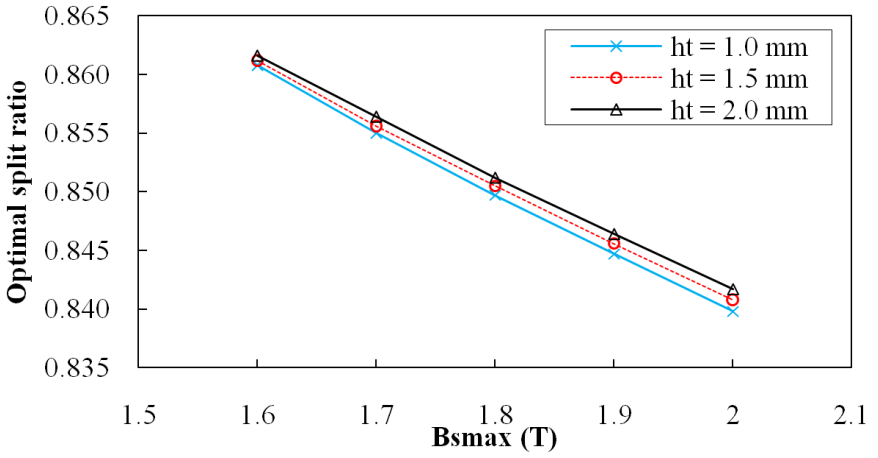

(a) $B_{rmax} = 1.8$ T

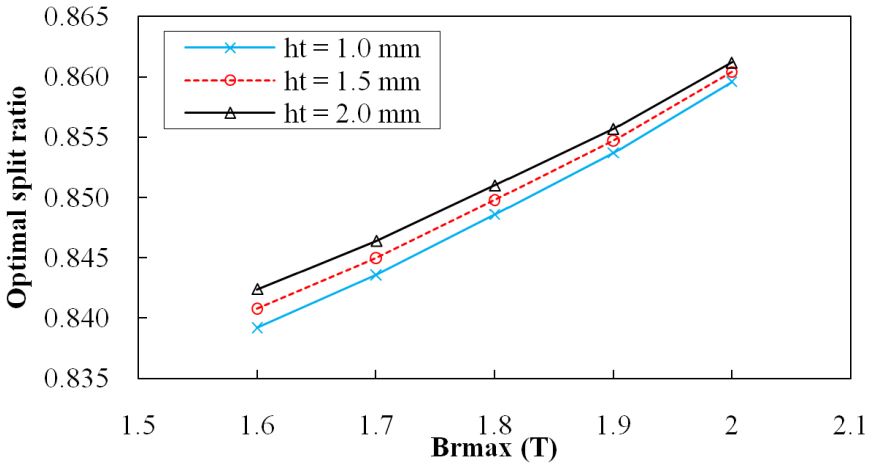

(b) $B_{smax} = 1.8$ T

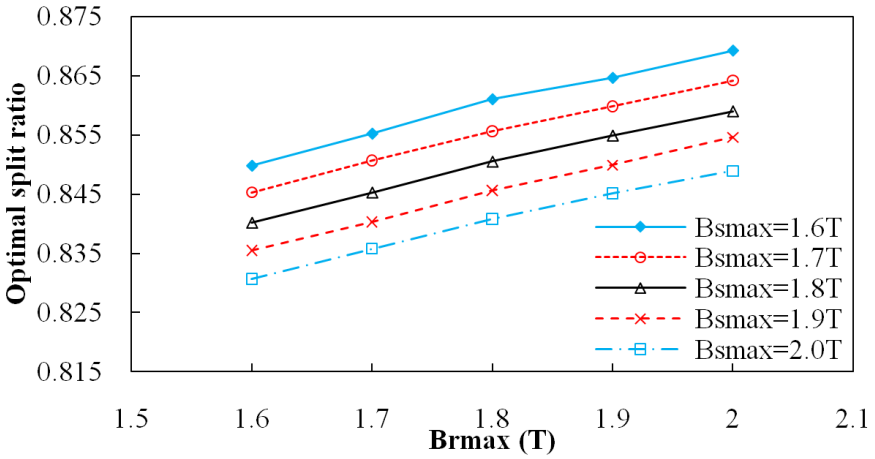

(c) $h_t = 1.5\ mm$

Fig.6.10. Variation of optimal split ratio with h_t, B_{rmax} and B_{smax} for 24-slot/8-pole machine.

Moreover, the optimal split ratio for external rotor PM brushless machine having Halbach array with fixed rotor back-iron thickness can be directly obtained by adopting equation

$$\lambda_{Halbach} = \frac{\lambda_{Conv} \cdot D_{ro} + \left[h_{pm(Conv)} - h_{pm(Halbach)}\right]}{D_{ro}} \tag{6.28}$$

where, λ_{conv} and $\lambda_{Halbach}$ represent the optimal split ratio for conventional pole and Halbach array, respectively. The $h_{pm(conv)}$ is the corresponding magnet thickness for optimal λ_{conv}, while the $h_{pm(Halbach)}$ is the magnet thickness for Halbach array to achieve the same amplitude of $B_{ag(\lambda)}$ for $h_{pm(Conv)}$. It has already been investigated in foregoing chapters that the magnet pole having Halbach array can exhibit significant higher B_{ag} than conventional magnet pole when magnet thickness is equal to each other, which in turn, means the thinner $h_{pm(Halbach)}$ is capable of obtaining the same amplitude of $B_{ag(\lambda)}$. Consequently, the optimal outer stator diameter is increased for external rotor machine having Halbach array to maintain the B_{smax} in a desired level. For fixed rotor back-iron cases, it can be concluded that external rotor PM machine having Halbach array exhibit larger optimal split ratio than conventional pole rotor. In general, it is also true for variable rotor back-rion thickness cases, since the self-shielding characteristic lead Halbach array to exhibit thinner rotor back-iron than machine having conventional pole.

6.4 Measurement

The proposed analytical model is validated with experimental measurement on a prototype 54-slot/60-pole fractional-slot external rotor PM brushless machine having a fixed rotor back-iron thickness (as required by mechanical consideration) and fixed copper loss (constant

thermal condition) for in-wheel traction application as an example. Fig.6.11 shows the schematic view of a 54-slot/60-pole fractional-slot external rotor PM brushless machine with non-overlapping winding, whose main design parameters are defined in TABLE 6-V.

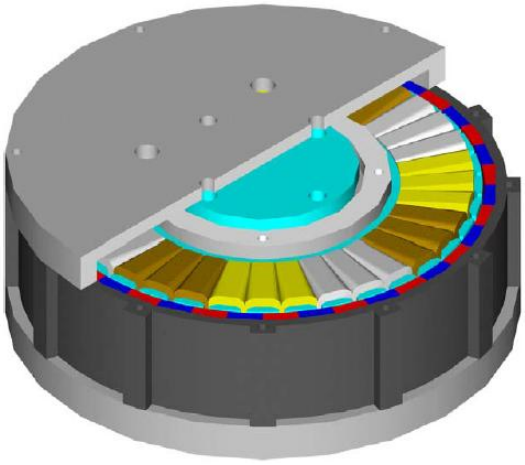

Fig.6.11. 54-slot/60-pole external rotor surface-mounted PM machine.

TABLE 6-V MAIN PARAMETER OF PROTOTYPE MOTOR

Pole number, $2N_p$	60	Slot opening, b_o (mm)	2.0
Stator slot number, N_s	54	Air-gap length, l_g (mm)	0.8
Tooth-tip height, h_t (mm)	1.3	Active length, l_a (mm)	44.1
Rotor outer diameter, D_{ro} (mm)	240	Shaft or hub diameter, D_{sf} (mm)	160
PM remanence, B_r (T)	1.2	Maximum flux density, B_{smax}(T)	1.8
PM relative permeability,μ_r	1.05	Rotor back-iron thickness, h_{rbi} (mm)	3.1
Copper loss (P_{cu})	36.2		

Fig.6.12 compares the average torque predicted by FEA and analytical model for the 54-slot/60-pole PM brushless machine. The analytically predicted optimal split ratio agrees well with the FEA result, although it can be noticed that the amplitude of average torque obtained by the proposed analytical model is higher than that by FEA, due to the simplifications made in the derivation of analytical model, such as neglected leakage flux and armature reaction, etc. It should be mentioned that the focus of this paper is to predict the optimal split ratio for a given space envelop of the machine. Hence, although the foregoing simplifications which lead to an imprecision torque calculation, they do not have a significant effect on the optimal split ratio determination.

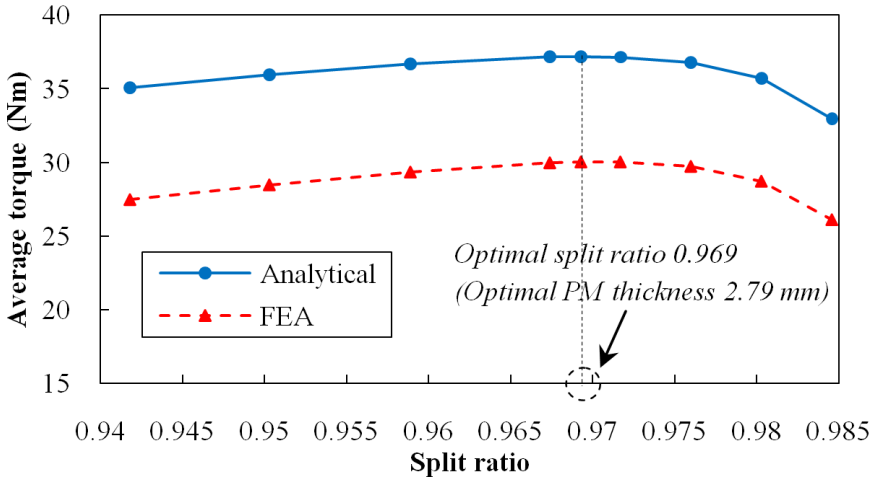

Fig.6.12. Comparison of analytically and FEA predicted average torque variation with split ratio for 54-slot/60-pole fractional-slot external rotor brushless machine.

Furthermore, the permanent magnet thickness corresponding to the optimal split ratio is equal to 2.79 mm. However, PM thickness of 3 mm exhibits similar average torque, but improves the demagnetization withstand capability and also easier to be manufactured. Vector potential distribution for the machine having a 3 mm PM thickness and related dimensions is shown in Fig.6.13. Moreover, a three phase 54-slot/60-pole prototype machine equipped with non-overlapping winding and having main design parameters shown in Table I, together with the optimal split ratio of 0.9674 (3 mm PM thickness) and corresponding dimensions, viz. $b_t = 5.7$ mm, $h_{sbi} = 2.9$ mm and $D_{si} = 165.8$ mm by considering the required winding packing factor, is shown in Fig.6.14. TABLE 6-VI compares the analytical, FEA and measured average torque (The torque is simply measured by fixing a beam to the rotor and its one end being rested on a scale. The torque acting on the rotor is transferred to the beam and acts on the scale. Hence, the torque is obtained by multiplying the reading from the scale with the arm distance. The stator which is fixed in lathe is clamped by an indexing head so that the stator can be rotated to an accurate position with respect to the stationary rotor. Since the prototype machine is controlled by $I_d = 0$, then the maximum static torque is obtained by rotating the rotor when the stator is fixed in lathe, meanwhile one phase coil is connected with a positive DC current while other two phase coils are parallel connected with negative current.) from the prototype machine.

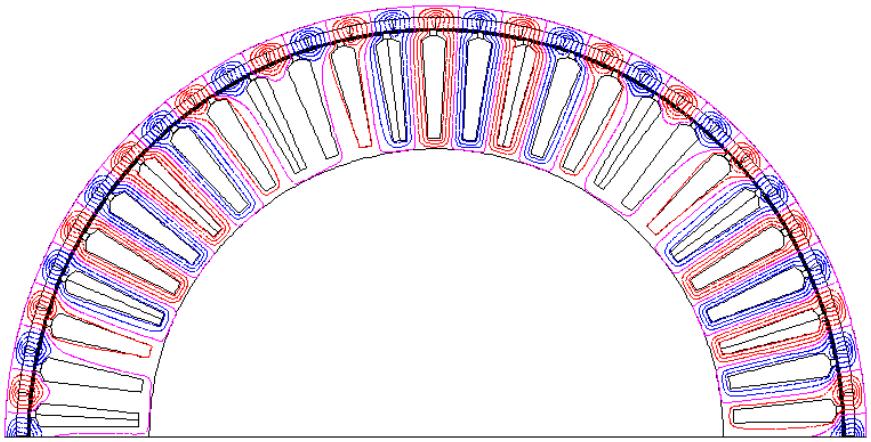

Fig.6.13. Vector potential distribution for 54-slot/60-pole external rotor PM brushless machine with 3 mm PM thickness.

(a) Rotor and hub system (b) Stator with winding

Fig.6.14. Prototype 54-slot/60-pole external rotor PM brushless machine with proposed optimal split ratio and PM thickness.

TABLE 6-VI COMPARISON OF MEASURED, AND PREDICTED AVERAGE TORQUE

Analytical	FEA	Measured
37.2 Nm	29.4 Nm	27.9 Nm

6.5 Summary

The optimal split ratio for both non-overlapping and overlapping winding external rotor PM brushless machines have been developed analytically, considering the influence of the fixed and variable rotor back-iron thickness, slot and pole combination, curvature effect, tooth-tips, and end-winding length. The analytical predictions of optimal split ratios for an overlapping and a non-overlapping winding machines have been verified by FEA, and the results matched very well. The influence of slot and pole combinations, tooth-tip, and the maximum flux density in the stator lamination on the optimal slot ratio is investigated, respectively. The

proposed analytical model to predict optimal split ratio is derived based on torque maximization. Therefore, it is useful for machine initial design. However, the design parameters can be further adjusted if thermal or other requirements are need to consider.

CHAPTER 7 GENERAL CONCLUSION AND FUTURE WORK

7.1 Conclusions

This thesis develops a general analytical model which is capable of predicting the electromagnetic performance of slotted/slotless permanent magnet brushless machines with both even- and odd-segment Halbach array, having different magnet remanence, magnetization angle and arc for each single magnet segment. The developed analytical models and corresponding investigations are examined by finite element analyses. They are summarized as follows.

7.1.1 Developed Analytical Model

Analytical models are powerful tools for the design and research of PM brushless machines. This thesis has developed a package of analytical models, TABLE 7-I, of both high accuracy and physical understanding. The developed analytical models are applicable to permanent magnet brushless machines having segmented Halbach array and proposed Hat- and T-type magnet poles, while an analytical model is developed to predict optimal split ratio for external rotor PM machines. Their accuracies have been extensively verified by finite element analysis and partially by experimental results.

TABLE 7-I DEVELOPED ANALYTICAL MODELS

Chapter	Model	Papers	Features
2	2-D field slotless model and SDE	[J]	Directly predict optimal R_{mp} for 2-segment Halbach array
3	2-D field model with SD method	[J]	General analytical model for machine having segmented Halbach array
4	Magnetization vectors	[J][J]	Magnetization vectors for proposed Hat- and T-type magnet poles
5	1-D field model	[J][C3][C4]	Predict optimal split ratio for external rotor PM machines
APPENDIX I and II	LPC Model	[C1][C2]	Brushless claw-pole rotor and stator machines

A. *Analytical model of slotless PM brushless machine having 2-segment Halbach array*

This is developed based on 2-D field slotless model accounting for both radial and parallel magnetizations. A simple determination equation is derived by simplifying 2-D field slotless model with radial magnetization, which is capable of directly predict the optimal magnet ratio R_{mp} for a 2-segment Halbach array with either radial or parallel magnetization. (Chapter 1)

B. General 2-D field model with sub-domain method of PM brushless machine having segmented Halbach array

This is developed based on sub-domain method which can account for slotting effect by solving governing equations in each sub-domain with the boundary conditions to the interfaces between sub-domains. Meanwhile, the magnetization vectors for even and odd segment Halbach arrays are deduced and cooperated with developed 2-D field SD model. (Chapter 3)

C. *Magnetization vectors of proposed Hat- and T-type magnet poles*

Since the proposed Hat- and T-type magnet poles exhibit non-uniformly distributed air-gap, the overall magnetization vectors over one pole pair can be obtained by using superposition theory. On the basis of unsymmetrical distributed modular Hat- and T-type magnet poles, the magnetization vectors which account for both sine and cosine components are deduced. (Chapter 4-5)

D. *Analytical model of optimal split ratio determination for external rotor PM brushless machine*

The optimal split ratio for external PM brushless machine having fixed- and variable rotor back-iron, non-overlapping and overlapping windings can be predicted by using developed 1-D field model. (Chapter 6)

7.1.2 Investigation

The electromagnetic torque and magnet usage efficiency for between PM brushless machine having conventional pole, optimized 2- and 3-segment Halbach arrays and proposed magnet poles have been comparatively studied. The influences of design parameters on electromagnetic performances are also extensively studied.

A. *Comparison of slotless PM brushless machine having 2-segment Halbach array*

- Parallel magnetized 2-segment Halbach array exhibits higher fundamental air-gap flux density than radial magnetized case, especially when the magnet is thick.

- Although the optimal magnet ratio R_{mp} for parallel magnetized 2-segment Halbach array is slightly higher than that for radially magnetized 2-segment Halbach array, the simple determination equation which is derived based on the radially magnetized Halbach array is still capable to predict the optimal R_{mp} for parallel magnetized case, although small but acceptable error may exist.
- By using proposed simple determination equation, it is found that for maximized average torque, the optimal magnet ratio R_{mp} is only a function of pole pair number, magnet thickness, and permeability of permanent magnet.
- It is found that the thicker the magnet, the smaller the optimal R_{mp} for machines having iron-cored rotor.
- In contrast to the iron-cored rotor, the optimal magnet ratio R_{mp} increases as the magnet thickness increases for the air-core rotor.
- The optimal R_{mp} for the machines having an iron-cored rotor is always greater than 0.5, while the machines having an air-cored rotor is always lower than 0.5.
- For a particular case, i.e. when p = 1, the optimal R_{mp} is constant and equal to 0.5 for both iron- and air-cored rotor.

B. *Comparison of globally optimized magnet cylinder having conventional pole, 2- and 3-segment Halbach array*

- The magnet cylinder having 3-segment Halbach array exhibits significant higher fundamental air-gap flux density than the magnet cylinder having conventional pole and 2-segment Halbach array, due to increased effective magnet length.
- The 3-segment Halbach array exhibits the lowest THD value due to improved self-shielding property.

B. *Comparison of PM brushless machine having conventional pole, 3-segment Halbach array, proposed Hat- and T-type magnet pole*

- Machine having T-type magnet pole can exhibit higher ratio of average output torque to PM volume than other magnet poles when the rotor pole-pair number increases.
- By adopting T-type magnet pole, the inherent large inter-pole leakage flux is significantly reduced in contrast with Hat-type magnet pole and traditional

sinusoidal arc and inverse cosine shaping techniques. Therefore, T-type magnet pole exhibits great potential to achieve low torque ripple, high electromagnetic torque, and low magnet usage simultaneously

C. *Comparison of PM brushless machine having conventional and modular Hat- and T-type magnet pole with equal and unequal magnet height.*

- The investigation shows that a modular T-type magnet pole with unequal side-magnet height and different magnet materials exhibits significant potential to achieve low torque ripple, relative high electromagnetic torque, and low NdFeB usage simultaneously. Meanwhile, it also presents a high ratio of average electromagnetic torque to PM volume in contrast to a conventional 3-segment Halbach array and other magnet poles.
- The modular technique can also reduce the inter-pole leakage flux in the conventional Hat-type magnet pole.
- The optimal magnetization angle is related to the magnet-arc to height ratio, but independent of the magnet material.
- The variation trend of fundamental air-gap flux density with rotor pole pair number for the T-type magnet pole is similar to Halbach array, while such trend for the Hat-type magnet pole is similar to the conventional pole. Therefore, the higher the pole pair number, the larger the average torque for the machine having a T-type magnet pole will be obtained than the Hat- and conventional pole.
- With a proper design, the asymmetric distortion in the back-EMF waveform can be minimized for the machine having modular Hat- and T-type magnet poles.
- Due to side-magnet being away from on-load field, both conventional and modular Hat-type magnet poles present better demagnetization withstand capability than the conventional and modular T-type magnet pole.

D. *Influence of design parameters on optimal split ratio for external rotor PM brushless machine.*

- The optimal split ratio of the machine having variable rotor back-iron thickness exhibit significant increase with the variation of pole pair number than that of the machine having fixed rotor back-iron cases.

- Compared with the pole number, the stator slot number has less influence on optimal split ratio variation .
- The higher the amplitude of maximum flux density in the stator tooth, the lower the optimal split ratio due to the reduction of stator back-iron thickness. Meanwhile, the higher the amplitude of maximum flux density in the rotor lamination, the higher the optimal split ratio due to reduction of rotor back-iron thickness.
- The higher the magnet segment in Halbach array, the higher the optimal split ratio will be on the basis of reduced magnet thickness to maintain the same saturation level in the stator lamination.

7.2 Future Work

Following the research work in this thesis, future research includes:

- Extending the 2-D field model with SD method accounting for parasitic loss and force for PM brushless machine having Hat- and T-type magnet pole.
- Extending the Hat- and T-type magnet pole for permanent magnet plate and tubular linear machines

References

[1] L. Yang, "Twenty five years development of global NdFeB magnet industry," *J. Magn. Mater Devices*, vol. 39, no.6, pp. 9-18, December 2008.

[2] M. Sagawa, S. Fujimura, N. Togawa, H. Yamamoto, and Y. Matsuura, "New material for permanent magnets on base of Nd and Fe," *J. Appl. Phys*., vol. 55, Part IIA, pp. 2083-2087, 1985.

[3] D. C. McDonald, "Magnetizing and measuring B & H in high energy product rare earth permanent magnets," *IEEE Trans. Magn*., vol. MAG-22, no. 5, pp. 1075-1077, September 1986.

[4] L. Chang, T. Eastham, and G. Dawson, "In-situ magnetization of NdFeB magnets for permanent magnet machines," *IEEE Trans. Magn*., vol. 27, no. 5, pp. 4355-4359, September 1991.

[5] G. W. Jewell, and D. Howe, "Computer-aided design of magnetizing fixtures for the post-assembly magnetization of rare-earth permanent magnet brushless DC motors," *IEEE Trans. Magn*., vol. 28, no. 5, pp. 3036-3038, September 1992.

[6] P. Zheng, Y. Liu, Y. Wang, and S. Cheng, "Magnetization analysis of the brushless DC motor used for hybrid electrical vehicle," *IEEE Trans. Magn*., vol. 41, no. 1, pp. 522-524, January 2005.

[7] D. G. Dorrell, M. F. Hsieh, and Y. C. Hsu, "Post assembly magnetization patterns in rare-earth permanent-magnet motors," *IEEE Trans. Magn*., vol. 43, no. 6, pp. 2489-2491, June 2007.

[8] M. F. Hsieh, Y. C. Hsu, and D. G. Dorrell, "Design of large-power surface-mounted permanent-magnet motors using postassembly " *IEEE Trans. Ind. Electron*., vol. 57, no. 10, pp. 3376-3384, October 2010.

[9] M. F. Hsieh, Y. M. Lien, and D. G. Dorrell, "Post-assembly magnetization of rare-earth fractional-slot surface permanent-magnet machines using a two-shot method," *IEEE Trans. Ind Appl.*, vol. 47, no. 6, pp. 2478-2486, November/December 2011.

[10] K. Ng, Z. Q. Zhu, and D. Howe, "Open-circuit field distribution in a brushless motor with diametrically magnetized PM rotor, accounting for slotting and eddy current effecrs," *IEEE Trans. Magn*., vol. 32, no. 5, pp. 5070-5072, September 1996.

[11] K. Halbach, "Design of permanent multipole magnets with oriented rare earth cobalt material," *Nucl. Instrum. Meth*., 1980, 169, pp. 1-10

[12] P. Pillay, and R. Krishnan, "Application characteristics of permanent magnet synchronous and brushless dc motors for servo drives," *IEEE Trans. Ind. Appl*., vol. 27, no. 5, pp. 986-996, September/October 1991.

[13] A. Borisavljevic, H. Polinder, and J. A. Ferreira, "On the speed limits of permanent-magnet machines," *IEEE Trans. Ind. Electron*., vol. 57, no. 1, pp. 230-227, January 2010.

[14] A. Binder, T. Schneider, and M. Klohr, "Fixation of buried and surface-mounted magnets in high-speed permanent-magnet synchronous machines," *IEEE Trans. Ind. Electron*., vol. 42, no. 4, pp. 1031-1037, July/August 2006.

[15] N. Bianchi, S. Bolognani, and F. Luise, "Potentials and limits of high-speed PM motors," *IEEE Trans. Ind. Appl*., vol. 40, no. 6, pp. 1570-1578, November/December 2004.

[16] A. R. Munoz, and T. A. Lipo, "Dual stator winding induction machine drive," *IEEE Trans. Ind Appl.*, vol. 36, no. 5, pp. 1369-1379, Spetember/October 2000.

[17] J. Cros, and P. Viarouge, "Synthesis of high performance PM motors with concentrated windings," *IEEE Trans. Energy Convers*., vol. 17, no. 2, pp. 248-253, June 2002.

[18] A. M. El-Refaie, and T. M. Jahns, "Optimal flux weakening in surface PM machines using fractional-slot concentrated windings," *IEEE Trans. Ind. Appl*., vol. 41, no. 3, pp.

790-800, May/June 2005.
[19] D. Ishak, Z. Q. Zhu, and D. Howe, "Comparison of PM brushless motors, having either all teeth or alternate teeth wound," *IEEE Trans. Energy Convers*., vol. 21, no. 1, pp. 95-103, March 2006.
[20] A. M. El-Refaie, T. M. Jahns, and D. W. Novotny, "Analysis of surface permanent magnet machines with fractional-slot concentrated windings," *IEEE Trans Energy Convers*., vol. 21, no. 1, pp. 34-43, March 2006.
[21] R. Wrobel, and P. H. Mellor, "Design considerations of a direct drive brushless machine with concentrated windings," *IEEE Trans. Energy Convers*., vol. 23, no. 1, pp. 1-8, March 2008.
[22] F. Magnussen, and H. Lendenmann, "Parasitic effects in PM machines with concentrated windings," *IEEE Trans. Ind. Appl*., vol. 43, no. 5, pp. 1223-1232, September/October 2007.
[23] M. J. Kamper, A. J. Rix, D. A. Wills, and R. Wang, "Formulation, finite-element modeling and winding factors of non-overlap winding permanent magnet machines," in *Proc. ICEM*, Vilamonra, Portugal, September 2008, pp. 1-5.
[24] J. Wang, K. Atallah, Z. Q. Zhu, and D. Howe, "Modular three-phase permanent-magnet brushless machines for in-wheel applications," *IEEE Trans. Veh. Technol*., vol. 57, no. 5, pp. 2714-2720, September 2008.
[25] J. J. Germishuizen, and M. J. Kamper, "IPM taction machine with single layer non-overlapping concentrated windings," *IEEE Trans. Ind. Appl*., vol. 45, no. 4, pp. 1387-1394, July/August 2009.
[26] Z. Q. Zhu, "Fractional slot permanent magnet brushless machines and drives for electric and hybrid propulsion systems," *Int. Journal for Computation and Mathematics in Electrical and Electronic Engineering*, vol. 30, no. 1, pp. 9-31, 2011
[27] T. Fukami, Y. Matsuura, M. Momiyama, and M. Kawamura, "A multipole synchronous machine with nonoverlapping concentrated armature and field windings on the stator," *IEEE Trans. Ind. Electron*., vol. 59, no. 6, pp. 2583-2591, June 2012.
[28] G. D. Donato, F. G. Capponi, and F. Caricchi, "Fractional-slot concentrated-winding axial-flux permanent-magnet machine with core-wound coils," *IEEE Trans. Ind. Appl*., vol. 48, no. 2, pp. 630-641, March/April 2012.
[29] J. H. J. Potgieter, and M. J. Kamper, "Torque and voltage quality in design optimization of low-cost non-overlap single layer winding permanent magnet wind generator," *IEEE Trans. Ind. Electron*., vol. 59, no. 5, pp. 2147-2156, May 2012.
[30] A. J. Rix, and M. J. Kamper, "Radial-flux permanent-magnet hub drives: a comparison based on stator and rotor topologies," *IEEE Trans. Ind. Electron*., vol. 59, no. 6, pp. 2475-2483, June 2012.
[31] G. Dajaku, and D. Gerling, "A novel 24-slots/10-poles winding topology for electic machines," *Int. IEMDC, 2011*, Niagara Fall, Canada.
[32] F. Deng, "An improved iron loss estimation for permanent magnet brushless machines," *IEEE Trans. Energy Convers*., vol. 14, no. 4, pp. 1391-1395, December 1999.
[33] B. Stumberger, A. Hamler, and B. Hribernik, "Analysis of iron loss in interior permanent magnet synchronous motor over a wide-speed range of constant output power operation," *IEEE Trans. Magn*., vol. 36, no. 4, pp. 1846-1849, July 2000.
[34] C. Mi, G. R. Slemon, and R. Bonert, "Modeling of iron losses of permanent-magnet synchronous motors," *IEEE Trans. Ind Appl*., vol. 39, no. 3, pp. 734-742, May/June 2003.
[35] H. Domeki, Y. Ishihara, C. Kaido, Y. Kawase, S. Kitamura, T. Shimomura, N. Takahashi, T. Yamada, and K. Yamazaki, "Investigation of benchmark model for estimating iron loss in rotating machine," *IEEE Trans. Magn*., vol. 40, no. 2, pp. 794-

797, May 2005.
[36] A. Fukuma, S. Kanazawa, D. Miyagi, and N. Takahashi, "Investigation of AC loss of permanent magnet of SPM motor considering hysteresis and eddy-current losses," *IEEE Trans. Magn*., vol. 41, no. 5, pp. 1964-1967, May 2005.
[37] Y. Amara, J. Wang, and D. Howe, "Stator iron loss of tubular permanent-magnet machines," *IEEE Trans. Ind Appl*., vol. 41, no. 4, pp. 989-995, July/August 2005.
[38] K. Yamazaki, and Y. Seto, "Iron loss analysis of interior permanent-magnet synchronous motors – variation of main loss factors due to driving condition," *IEEE Trans. Ind Appl*., vol. 42, no. 4, pp. 1045-1052, July/August 2006.
[39] D. M. Ionel, M. Popescu, M. I. McGilp, T. J. E. Miller, S. J. Dellinger, and R. J. Heideman, "Computation of core looses in electrical machines using improved models for laminated steel," *IEEE Trans. Ind Appl*., vol. 43, no. 6, pp. 1554-1564, November/December 2007.
[40] J. Seo, T. Chung, C. Lee, S. Jung, and H. Jung, "Harmonic iron loss analysis of electrical machines for high-speed operation consideration driving condition," *IEEE Trans. Magn*., vol. 45, no. 10, pp. 4656-4659, October 2009.
[41] K. Yamazaki, and N. Fukushima, "Iron loss model for rotating machines using direct eddy current analysis in electrical steel sheets," *IEEE Trans. Energy Convers*., vol. 25, no. 3, pp. 633-641, September 2010.
[42] N. Kondrath, M. K. Kazimierczuk, "Inductor winding loss owing to skin and proximity effects including harmonics in non-isolated pulse-width modulated dc-dc converters operating in continuous conduction mode," *IET Power Electron*., vol. 3, iss. 6, pp. 989-1000, 2010.
[43] S. Iwasaki, R. P. Deodhar, Y. Liu, A. Pride, Z. Q. Zhu, and J. J. Bremner, "Influence of PWM on the proximity loss in permanent-magnet brushless AC machines," *IEEE Trans. Ind Appl*., vol. 45, no. 4, pp. 1359-1367, July/August 2009.
[44] P. B. Reddy, T. M. Jahns, T. P. Bohn, "Transposition effects on bundle proximity losses in high-speed PM machines," in *Proc. 2009 IEEE Energy Conversion and Exposition*, pp. 1919-1926.
[45] R. Wrobel, A. Mlot, and P. H. Mellor, "Contribution of end-winding proximity losses to temperature variation in electromagnetic devices," *IEEE Trans. Ind Electron*., vol. 59, no. 2, pp. 848-857, February 2012.
[46] L. J. Wu, Z. Q. Zhu, D. Staton, M. Popescu, and D. Hawkins, "Analytical model of eddy current loss in windings of permanent-magnet machines accounting for load," *IEEE Trans. Magn*., vol. 48, no. 7, pp. 2138-2151, July 2012.
[47] H. Polinder and M. J. Hoeijakers, "Eddy-current losses in the segmented surface-mounted magnets of a PM machine," *IEE Proc.-Electr. Power Appl*., vol. 146, no. 3, pp. 261-266, May 1999.
[48] J. D. Ede, K. Atallah, G. W. Jewell, J. B. Wang, and D. Howe, "Effect of axial segmentation of permanent magnets on rotor loss in modular permanent-magnet brushless machines," *IEEE Trans. Ind Appl*., vol. 43, no. 5, pp. 1207-1213, September/October 2007.
[49] K. Yamazaki, Y. Fukushima, and M. Sato, "Loss analysis of permanent-magnet motors with concentrated windings-variation of magnet eddy-current loss due to stator and rotor shapes," *IEEE Trans. Ind Appl*., vol. 45, no. 4, pp. 1334-1342, July/August 2009.
[50] G. C. D. Sousa, B. K. Bose, J. Cleland, R. J. Spiegel and P. J. Chappell, "Loss modeling of converter induction machine system for variable speed drive," in *Proc. 1992 Intern. Conf. on Ind. Electron., Contr., Instrumentation and Automation (IECON'92),* 1992, pp. 114-120.
[51] J. Holtz, and L. Springob, "Identification and compensation of torque ripple in high-

precision permanent magnet motor drives," *IEEE Trans. Ind Electron*., vol. 43, no. 2, pp. 309-320, April 1996.
[52] T. M. Jahns, and W. L. Soong, "Pulsating torque minimization techniques for permanent magnet AC motor drives-a review," *IEEE Trans. Ind Electron*., vol. 43, no. 2, pp. 321-330, April 1996.
[53] Z. Q. Zhu, and D. Howe, "Influence of design parameters on cogging torque in permanent magnet machines," *IEEE Trans. Energy Convers*., vol. 15, no. 4, pp. 407-412, December 2000.
[54] E. Faver, L. Cardoletti, and M. Jufer, "Permanent-magnet synchronous motors: a comprehensive approach to cogging torque suppression," *IEEE Trans. Ind Appl*., vol. 29, no. 6, pp. 1141-1149, November/December 1993.
[55] N. Bianchi, and S. Bolognani, "Design techniques for reducing the cogging torque in surface-mounted PM motors," *IEEE Trans. Ind Appl*., vol. 38, no. 5, pp. 1259-1265, September/October 2002.
[56] L. Dosiek, and P. Pillay, "Cogging torque reduction in permanent magnet machines," *IEEE Trans. Ind Appl*., vol. 43, no. 6, pp. 1565-1571, November/December 2007.
[57] K. Kim, K. Kim, S. Hwang, T. Kim, and Y. Jung, "Comparison of magnetic forces for IPM and SPM motor with rotor eccentricity," *IEEE Trans. Magn*., vol. 37, no. 5, pp. 3448-3451, September 2001.
[58] Z. Q. Zhu, D. Ishak, D. Howe, and J. Chen, "Unbalanced magnetic forces in permanent-magnet brushless machines with diametrically asymmetric phase windings," *IEEE Trans. Ind Appl*., vol. 43, no. 6, pp. 1544-1553, November/December 2007.
[59] L. J. WU, Z. Q. Zhu, J. T. Chen, and Z. P. Xia, "An analytical model of unbalanced magnetic force in fractional-slot surface-mounted permanent magnet machines," IEEE Trans. Magn., vol. 46, no. 7, pp. 2686-2700, July 2010.
[60] Z. Q. Zhu, D. Howe, E. Bolte, and B. Ackermann, "Instantaneous magnetic field distribution in brushless permanent magnet dc motors. Part I: Open-circuit field," *IEEE Trans. Magn*., vol. 29, no. 1, pp. 124-135, January 1993.
[61] Z. Q. Zhu, and D. Howe, "Instantaneous magnetic field distribution in brushless permanent magnet dc motors. Part II: Armature-reaction field," *IEEE Trans. Magn*., vol. 29, no. 1, pp. 136-142, January 1993.
[62] Z. Q. Zhu, and D. Howe, "Instantaneous magnetic field distribution in brushless permanent magnet dc motors. Part III: Effect of stator slotting," *IEEE Trans. Magn*., vol. 29, no. 1, pp. 143-151, January 1993.
[63] Z. Q. Zhu, and D. Howe, "Instantaneous magnetic field distribution in brushless permanent magnet dc motors. Part IV: Magnetic field on load," *IEEE Trans. Magn*., vol. 29, no. 1, pp. 152-158, January 1993.
[64] Z. Q. Zhu, D. Howe, and C. C. Chan, "Improved analytical model for predicting the magnet field distribution in brushless permanent-magnet machines," *IEEE Trans. Magn*., vol. 38, no. 1, pp. 229-238, January 2002.
[65] D. Zarko, D. Ban, and T. A. Lipo, "Analytical calculation of magnetic field distribution in the slotted air gap of a surface permanent-magnet motor using complex relative air-gap permeance," *IEEE Trans. Magn*., vol. 42, no. 7, pp. 1828-1837, July 2006.
[66] D. Zarko, D. Ban, and T. A. Lipo, "Analytical solution for cogging torque in surface permanent-magnet motors using conformal mapping," *IEEE Trans. Magn*., vol. 44, no. 1, pp. 52-65, January 2008.
[67] Z. J. Liu, and J. T. Li, "Analytical solution of air-gap field in permanent-magnet motors taking into account the effect of pole transition over slots," *IEEE Trans. Magn*., vol. 43, no. 10, pp. 3872-3883, October 2007.
[68] Z. J. Liu, and J. T. Li, "Accurate prediction of magnetic field and magnetic forces in

permanent magnet motors using an analytical solution," *IEEE Trans. Energy Convers*., vol. 23, no. 3, pp. 717-726, September 2008.
[69] Z. J. Liu, J. T. Li, and Q. Jiang, "An improved analytical solution for predicting magnetic forces in permanent magnet motors," *J. Appl. Phys*., vol. 103, no. 7, pp. 07F135-07F135, 2008.
[70] J. C. Mallinson, "One-sided fluxes – a magnetic curiosity?" *IEEE Trans. Magn*., vol. mag-9, no. 4, pp. 678-682, December 1973.
[71] Z. Q. Zhu, and D. Howe, "Halbach permanent magnet machines and applications: a review," *IEE Proc. Electrical Power Applications*, vol. 148, no. 4, pp. 299-308, 2001.
[72] Z. Q. Zhu, "Recent development of Halbach permanent magnet machines and applications," in *Proc. Power Conversion Conf*., April 2007.
[73] .J F. Gieras, R. Wang, M. J. Kamper, *Axial Flux Permanent Magnet Brushless Machines*, 2nd ed. New York: Springer-Verlag, 2008.
[74] S. Jang and S. Lee, "Comparison of two types of PM linear synchronous servo and miniature motor with air-cored film coil," *IEEE Trans. Magn*., vol. 38, no. 5, pp. 3264-3266, September 2002.
[75] S. Jang, S. Lee, and I. Yoon, "Design criteria for detent force reduction of permanent-magnet linear synchronous motors with Halbach array," *IEEE Trans Magn*., vol. 38, no. 5, pp. 3261-3263. September 2002.
[76] L. Li, M. Ma, B. Kou, and Q. Chen, "Analysis and optimization of slotless electromagnetic linear launcher for space use," *IEEE Trans. Plasma. Sci.*, vol. 39, no. 1, pp. 127-132, Jan. 2011.
[77] Z. Q. Zhu, Z. P. Xia, and D. Howe, "Comparison of Halbach magnetized brushless machines based on discrete magnet segments or a single ring magnet," *IEEE Trans. Magn*, vol. 38, no. 5, pp. 2997-2999, September 2002.
[78] Z. Q. Zhu, Z. P. Xia, Y. F. Shi, D. Howe, A. Pride, and X. J. Chen, "Performance of Halbach magnetized brushless AC motors," *IEEE Trans. Magn*., vol. 39, no. 5, pp. 2992-2994, September 2003.
[79] R. Wrobel, and P. H. Mellor, "Particle swarm optimization for design of brushless permanent magnet machines," in *Proc. 41st IEEE IAS Annu. Meeting*, Tampa, FL, 2006, vol. 4, pp. 1891-1897.
[80] M. Fazil, and K. R, Rajagopal, "Nonlinear dynamic modeling of a single-phase permanent-magnet brushless DC motor using 2-D static finite-element results," *IEEE Trans. Magn*., vol. 47, no. 4, pp. 781-786, April 2011.
[81] S. Dwari, and L. Parsa, "Design of Halbch-array-based permanent-magnet motors with high acceleration," *IEEE Trans. Ind. Electron*., vol. 58, no. 9, pp. 3768-3775, September 2011.
[82] S. Jang, S. Jeong, D. Ryu, and S. Choi, "Design and analysis of high speed slotless PM machine with Halbach array," *IEEE Trans. Magn*., vol. 37, no. 4, pp. 2827-2830, July 2001.
[83] S. Jang, S. Lee, H. Cho, and S. Cho, "Analysis of unbalanced force for high-speed slotless permanent magnet machine with Halbach array," *IEEE Trans. Magn*., vol. 39, no. 5, pp. 3265-3267, September 2003.
[84] R. P. Praveen, M. H. Ravichandran, V. T. Sadasivan Achari, V. P. Jagathy Raj, G. Madhu, G. R. Bindu, "A novel slotless Halbach-array permanent-magnet brushless DC motor for spacecraft applications," *IEEE Trans. Ind. Electron*., vol. 59, no. 9, pp. 3553-3560, September 2012.
[85] W. J. Kim, M. T. Berhan, and J. H. Lang, "Analysis and implementation of a tubular motor with Halbach magnet array," in *Proc. IEEE Industry Application Soc., 31th Annu. Meeting*, vol. 1, 1996, pp. 471-478.

[86] S. Jang, J. Choi, S. Lee, H. Cho, and W. Jang, "Analysis and experimental verification of moving-magnet linear actuator with cylindrical Halbach array," *IEEE Trans. Magn.*, vol. 40, no. 4, pp. 2068-2070, July 2004.
[87] S. Jang, J. Choi, H. Cho, and S. Lee, "Thrust analysis and measurements of tubular linear actuator with cylindrical Halbach array," *IEEE Trans. Magn*., vol. 41, no. 5, pp. 2028-2031, May 2005.
[88] J. Wang, and D. Howe, "Tubular modular permanent-magnet machines equipped with quasi-Halbach magnetized magnets-part I: magnetic field distribution, EMF, and thrust force," *IEEE Trans. Magn.*, vol. 41, no. 9, pp. 2470-2478, September 2005.
[89] J. Wang, and D. Howe, "Tubular modular permanent-magnet machines equipped with quasi-Halbach magnetized magnets-part II: armature reaction and design optimization," *IEEE Trans. Magn.*, vol. 41, no. 9, pp. 2479-2489, September 2005.
[90] J. Wang, Z. Lin, and D. Howe, "Analysis of a short-stroke, single phase, quasi-Halbach magnetized tubular permanent magnet motor for linear compressor applications," *IET Electr. Power Appl*., vol. 2, no. 3, pp. 193-200, May 2008.
[91] J. Wang, W. Wang, K. Atallah, and D. Howe, "Demagnetization assessment for three-phase tubular brushless permanent magnet machines," *IEEE Trans. Magn*., vol. 44, no. 9, pp. 2195-2203, September 2008.
[92] Z. Q. Zhu, X. Chen, D. Howe, and S. Iwasaki, "Electromagnetic modeling of a novel linear oscillating actuator," *IEEE Trans. Magn*., vol. 44, no. 11, pp. 3855-3858, November 2008.
[93] J. Choi, H. Kim, S. Jang, and S. Lee, "Thrust calculations and measurements of cylindrical linear actuator using transfer relations theorem," *IEEE Trans. Magn*., vol. 44, no. 11, pp. 4081-4084, November 2008.
[94] T. Ibrahim, J. Wang, and D. Howe, "Analysis and experimental verification of a single-phase, quasi-Halbach magnetized tubular permanent magnet motor with non-ferromagnetic support tube," *IEEE Trans. Magn*., vol. 44, no. 11, pp. 4361-4364, November 2008.
[95] X. Chen, Z. Q. Zhu, and D. Howe, "Modeling and analysis of a tubular oscillating permanent-magnet actuator," *IEEE Trans. Ind. Appl.*, vol. 45, no. 6, pp. 1961-1970, November/December 2009.
[96] J. Wang, D. Howe, and Z. Lin, "Design optimization of short-stroke single-phase tubular permanent-magnet motor for refrigeration applications," *IEEE Trans. Ind. Electron*., vol. 57, no. 1, pp. 327-334, January 2010.
[97] J. Wang, T. Ibrahim, and D. Howe, "Prediction and measurement of iron loss in a short-stroke, single-phase, tubular permanent magnet machine," *IEEE Trans. Magn*., vol. 46, no. 6, pp. 1315-1318, June 2010.
[98] C. Liu, C. Lin, C. Hwang, and C. Tu, "Compact model of a slotless tubular linear generator for renewable energy performance assessments," *IEEE Trans. Magn*., vol. 46, no. 6, pp. 1467-1470, June 2010.
[99] X. Chen, and Z. Q. Zhu, "Analytical determination of optimal split ratio of e-core permanent magnet linear oscillating actuators," *IEEE Trans. Ind. Appl.*, vol. 47, no. 1, pp. 25-33, January/February 2011.
[100] Y. Son, Y. You, and B. Kwon, "Optimal design to increase thrust force in electro-magnetic linear actuator for fatigue and durability test machine," *IEEE Trans. Magn.*, vol. 47, no. 10, pp. 4294-4297, October 2011.
[101] H. A. Leupold, A. Tilak, and E. Potenziani, "Permanent magnet spheres: design, construction, and application," *J. Appl. Phys*., vol. 87, pp. 4730 (2000).
[102] C. Xia, H. Li, and T. Shi, "3-D magnetic field and torque analysis of a novel Halbach array permanent-magnet spherical motor," *IEEE Trans. Magn*., vol. 44, no. 8, pp. 2016-

2020, August 2008.
[103]J. C. Compter, "Electro-dynamic planar motor," *Precison Eng*., vol. 28, no.2, pp. 171-180, Apr. 2004.
[104]J. Jansen, C. M. M. Van Lierop, E. A. Lomonova, A. J. A. Vandenput, "Modeling of magnetically levitated planar actuators with moving magnets," *IEEE Trans. Magn*., vol. 43, no. 1, pp. 15-25, January 2007.
[105]Y. Ueda, and H. Ohsaki, "A planar actuator with a small mover traveling over large yaw and translational displacements," IEEE Trans. Magn., vol. 44, no. 5, pp. 609-616, May 2008.
[106]J. Boeij, E. Lomonova, and J. A. Vandenput, "Optimization of contactless plannar actuator with manipulator," *IEEE Trans. Magn*., vol. 44, no. 6, pp. 1118-1121, June 2008.
[107]Y. Ueda, and H. Ohsaki, "Six-degree-of-freedom motion analysis of a planar actuator with a magnetically levitated mover by six-phase current controls," *IEEE Trans. Magn*., vol. 44, no. 11, pp. 4301-4304, November 2008.
[108]H. Jiang, X. Huang, G. Zhou, Y. Wang, and Z. Wang, "Analytical force calculations for high-precision planar actuator with Halbach magnet array," *IEEE Trans. Magn*., vol. 45, no. 10, pp. 4543-4546, October 2009.
[109]W. Min, M. Zhang, Y. Zhu, B. Chen, G. Duan, J. Hu, and W. Yin, "Analysis and optimization of a new 2-D magnet array for planar motor," *IEEE Trans. Magn*., vol. 46, no. 5, pp. 1167-1171, May 2010.
[110]W. Min, M. Zhang, Y. Zhu, F. Liu, G. Duan, J. Hu, and W. Yin, "Analysis and design of novel overlapping ironless windings for planar motors," *IEEE Trans. Magn*., vol. 47, no. 11, pp. 4635-4642, November 2011.
[111]R. Post, K. Fowler, and S. Post, "A high efficiency electromechanical battery," *Proc. IEEE*, vol. 81, no. 3, pp. 462-474, Mar. 1993.
[112]B. Merritt, R. Post, G. Dreifuerst, and D. Bender, "Halbahc array motor/Generators – a novel generalized electric machine," Lawrence Livermore National Laboratory, Univ. of California, CA, 1995.
[113]J. Hull, S. SenGupta, and J. R. Gaines, "Trapped-flux internal-dipole superconducting motor/generator," *IEEE Trans. Appl. Supercond*., vol. 9, no. 2, pp. 1229-1232, June 1999.
[114]J. Hull, and L. Turner, "Magnetomechanics of internal-dipole, Halbach-array motor/generators," *IEEE Trans. Magn*., vol. 36, no. 4, pp. 2004-2011, July 2000.
[115]S. Jang, S. Jeong, D. Ryu, and S. Choi, "Comparison of three types of PM brushless machines for an electro-mechanical battery," *IEEE Trans. Magn*., vol. 36, no. 5, pp. 3540-3543, September 2000.
[116]G. Sotelo, A. Ferreira, and R. Jr, "Halbach array superconducting magnetic bearing for a flywheel energy storage system," *IEEE Trans. Appl. Supercond*., vol. 15, no. 2, pp. 2253-2256, June 2005.
[117]S. M. Jang, D. Youm K. Ko, and S. Choi, "Design and experimental evaluation of synchronous machine without iron loss using double-side Halbach magnetized PM rotor in high power FESS," *IEEE Trans. Magn*., vol. 44, no. 11, pp. 4337-4340, November 2008.
[118]J. Yonnet, G. Lemarquand, S. Hemmerlin, and E. OlivierRulliere, "Stacked structures of passive magnetic bearings," *J. Appl. Phys*., 1991, 70, (10), pp. 6633-6635.
[119]M. C. Marin-Pera and J. P. Yonnet, "Study of permanent magnet arrangements for superconducting passive bearings," *IEEE Trans. Magn*., vol. 30, no. 6, pp. 4743-4745, November 1994.
[120]R. F. Post, and D. D. Ryutov, "Ambient-temperature passive magnetic bearing: theory

and design equations," in *Proc. Sixth Int. Symp. Magnetic Bearings*. Lancaster, PA: Technomic Publishing Co., 1998, p. 109.
[121]J. F. Charpentier, and G. Lemarquand, "Optimal design of cylindrical air-gap synchronous permanent magnet couplings," *IEEE Trans. Magn*., vol. 35, no. 2, pp. 1037-1046, March 1999.
[122]J. F. Charpentier, and G. Lemarquand, "Study of permanent-magnet couplings with progressive magnetization using an analytical formulation," *IEEE Trans. Magn*., vol. 35, no. 5, pp. 4206-4217, September 1999.
[123]R. Moser and H. Bleuler, "Precise positioning using electrostatic glass motor with diamegnetically suspended rotor," *IEEE Trans. Appl. Supercond., vol. 12*, no. 1, pp. 937-939, March 2002.
[124]J. Chen, J. Zhou, G. Meng, and W. Zhang, "Evaluation of eddy-current effects on diamagnetic bearings for microsystems," *IEEE Trans. Ind. Electron.*, vol. 56, no. 4, pp. 964-972, April 2009.
[125]G. G. Sotelo, D. H. N. Dias, R. de Andrade. Jr., and R. M. Stephan, "Test on a superconductor linear magnetic bearing of a full-scale maglev vehicle," *IEEE Trans. Appl. Supercond*., vol. 21, no. 3, pp. 1464-1468, June 2011.
[126]Y. Choi, and D. Gweon, "A high-precision dual-servo stage using Halbach linear active magnetic bearings," *IEEE Trans. Magn*., vol. 16, no. 5, pp. 925-931, October 2011.
[127]G. Kustler, "Extraordinary levitation height in a weight compensated diamagnetic levitation system with permanent magnets," *IEEE Trans. Magn*., vol. 48, no. 6, pp. 2044-2048, June 2012.
[128]K. Bachovchin, J. Hobury, and R. Post, "Magnetic fields and forces in permanent magnet levitated bearings," *IEEE Trans. Magn*., in publishing 2012.
[129]L. Jian, K. T. Chau, Y. Gong, J. Z. Jiang, C. Yu, and W. Li, "Comparison of coaxial magnetic gears with different topologies," *IEEE Trans. Magn*., vol. 45, no. 10, pp. 4526-4529, October 2009.
[130]T. Ohji, Y. Katsuda, K. Amei, and M. Sakui, "Structure of one-axis controlled repulsive type magnetic beraring system with surface permanent magnets installed and its levitation and rotation tests," *IEEE Trans. Magn*., vol. 47, no. 12, pp. 4734-4739, December 2011.
[131]F. Bloch, O. Cugat, G. Meunier, and J. C. Toussaint, "Innovating approaches to the generation of intense magnetic fields: design and optimization of 4 Tesla permanent magnet flux source," *IEEE Trans. Magn*., vol. 34, no. 5, pp. 2465-2468, September 1998.
[132]Z. Q. Zhu, Z. P. Xia, K. Atallah, G. W. Jewell, and D. Howe, "Power alignment system for anisotropic bonded NdFeB Halbach cylinders," *IEEE Trans. Magn*., vol. 36, no. 5, pp. 3349-3352, September 2000.
[133]Z. Q. Zhu, Z. P. Xia, K. Atallah, G. W. Jewell, and D. Howe, "Analysis of anisotropic bonded NdFeB Halbach cylinders accounting for partial powder alignment," *IEEE Trans. Magn*., vol. 36, no. 5, pp. 3575-3577, September 2000.
[134]P. Rochette, F. Vadeboin, and L. Clochard, "Rock magnetic application of Halbach cylinders," *Phys. Earth Planet. Inter*. 4026 (2001). pp. 1-9.
[135]Q. Peng, S. M. McMurry, and J. M. D. Coey, "Cylindrical permanent-magnet structures using images in an iron shield," *IEEE Trans. Magn*., vol. 39, no. 1, pp. 1983-1989, July 2003.
[136]H. Shute, and J. Mallinson, "Magnetostatic energy of structures with rotating vector magnetizations," *IEEE Trans. Magn*., vol. 39, no. 5, pp. 2146-2148, September 2003.
[137]J. E. Hilton, S. M. McMurry, "Halbach cylinders with improved field homogeneity and tailored gradient fields," *IEEE Trans. Magn*., vol. 43, no. 5, pp. 1898-1902, May 2007.

[138]J. Choi, and J. Yoo, "Design of a Halbach array based on optimization techniques," *IEEE Trans. Magn.*, vol. 44, no. 10, pp. 2361-2366, October 2008.
[139]J. Paulsen, J. Franck, V. Demas, and L. Bouchard, "Least squares magnetic-field optimization for portable nuclear magnetic resonance magnet design," *IEEE Trans. Magn.*, vol. 44, no. 12, pp. 4582-4590, December 2008.
[140]G. Kustler, "Computation of NdFeB-Halbach cylinders with circular and elliptical cross sections in three dimensions," *IEEE Trans. Magn.*, vol. 46, no. 9, pp. 3601-3607, September 2010.
[141]R. Bjork, "The ideal dimensions of a Halbach cylinder of finite length," *J. Appl. Phys.* 109, 013915(2011)
[142]S. J. Lee, J. M. Kenkel, V. K. Pecharsky, and D. C. Jiles, "Permanent magnet array for the magnetic refrigerator," *J. Appl. Phys.* 91, 8894 (2002)
[143]S. J. Lee, J. M. Kenkel, and D. C. Jiles, "Design of permanent-magnet field source for rotary-magnetic refrigeration systems," *IEEE Trans. Magn.*, vol. 38, no. 5, pp. 2991-2993, September 2002.
[144]X. N. Xu, D. W. Lu, G. Q. Yuan, and X. Jin, "Numerical simulations of vector field distributions generated by circular permanent-magnet arrays with side-openings," *IEEE Trans. Magn.*, vol. 42, no. 5, pp. 1512-1517, May 2006.
[145]M. W. Poole, and R. P. Walker, "Periodic magnets for undulartors and free electron lasers – a review of performance features," *IEEE Trans. Magn.*, vol. mag-17, no. 5, pp. 1978-1981, September 1981.
[146]R. D. Schlueter, and S. Marks, "Three-dimensional pure permanent magnet undulator design theory," *IEEE Trans. Magn.*, vol. 32, no. 4, pp. 2710-2713, July 1996.
[147]R. D. Schlueter, S. Marks, and S. Prestemon, "Elliptically polarizing undulator end designs," *IEEE Trans. Appl. Supercond.*, vol. 16, no. 2, pp.1582-1585, June 2006.
[148]R. Post, and D. Ryntov, "The Inductrack: a simpler approach to magnetic levitation," *IEEE Trans. Appl. Supercond.*, vol. 10, no. 1, pp. 901-904, March 2000.
[149]S. Jang, S. Jeong, and S. Cha, "The application of linear Halbach array to eddy current rail brake system," *IEEE Trans. Magn.*, vol. 37, no. 4, pp. 2627-2629, July 2001.
[150]R. Kratz, and R. Post, "A null-current electro-dynamic levitation system," *IEEE Trans. Appl. Supercond.*, vol. 12, no. 1, pp. 930-932, March 2002.
[151]S. Jang, S. Lee, and S. Jeong, "Characteristic analysis of eddy-current brake system using the linear Halbach array," *IEEE Trans. Magn.*, vol/ 38, no. 5, pp. 2994-2996, September 2002.
[152]Q. Han, C. Ham, and R. Phillips, "Four- and eight-piece Halbach array analysis and geometry optimization for maglev," in *IEE Proc. –Electro. Power Appl.*, May 2005, vol. 152, no. 3, pp. 535-542, 2005.
[153]W. Ko and C. Ham, "A novel approach to analyze the transient dynamics of an electrodynamics suspension maglev," *IEEE Trans. Magn.*, vol. 43, no. 6, pp. 2603-2605, Jun 2007.
[154]J. Zhang, Y. Zeng, J. Cheng, and X. Tang, "Optimization of permanent magnet guideway for HTS maglev vehicle with numerical methods," *IEEE Trans. Appl. Supercond.*, vol. 18, no. 3, pp. 1681-1686, September 2008.
[155]N. Del-Valle, A. Sanchez, C. Navau, and D. Chen, "Theoretical hints for optimizing force and stability in actual devices," *IEEE. Trans. Appl. Supercond.*, vol. 19, no. 3, pp. 2070-2073, June 2009.
[156]J. Wang, S. Wang, and J. Zheng, "Recent development of high temperature superconducting maglev system in China," *IEEE Trans. Appl. Supercond.*, vol. 19, no. 3, pp. 2142-2147, June 2009.
[157]J. Bird and T. A. Lipo, "Modeling the 3-D rotational and translational motion of a

Halbach rotor above split-sheet guideway," *IEEE Trans. Magn*., vol. 45, no. 9, pp. 3233-3242, September 2009.
[158]M. T. Thompson, "Practical issues in the use of NdFeB permanent magnets in maglev, motors, bearings, and eddy current brakes," *Proc. IEEE*, vol. 97, no. 11, pp. 1758-1767, November 2009.
[159]Z. Long, G. He, and S. Xue, "Study of EDS & EMS hybrid suspension system with permanent-magnet Halbach array," *IEEE Trans. Magn.*, vol. 47, no. 12, pp. 4717-4724, December 2011.
[160]W. J. Jeon, H. Watanabe, A. Nakamoto, Y. Kamiya, and T. Onuki, "Dynamic characteristic of synchronous motors applying a plural sub-magnets scheme to the rotor," *IEEE Trans Magn*., vol. 35, no. 5, pp. 3574-3576, September 1999.
[161]S. Chaithongsuk, N. Takorabet, and F. Meibody-Tabar, "On the use of pulse width modulation method for the elimination of flux density harmonics in the air-gap of surface PM motors," *IEEE Trans. Magn*., vol. 45, no. 3, pp. 1736-1739, March 2009.
[162]R. Lateb, N. Takorabet, and F. Meibody-Tabar, "Effect of magnet segmentation on the cogging torque in surface-mounted permanent-magnet motors," *IEEE Trans. Magn*., vol. 42, no. 3, pp. 442-445, March 2006.
[163]M. Ashabani, and Y. Abdel-Rady I. Mohamed, "Multiobjective shape optimization of segmented pole permanent-magnet synchronous machines with improved torque characteristics," *IEEE Trans. Magn*., vol. 47, no. 4, pp. 795-804, April 2011.
[164]A. H. Isfahani, "Analytical framework for thrust enhancement in permanent-magnet (PM) linear synchronous motors with segmented PM poles" *IEEE Trans. Magns*., vol. 46, no. 4, April 2010.
[165]Y. Li, J. B. Zou, and Y. P. Lu, "Optimum design of magnet shape in permanent-magnet synchronous motors," *IEEE Trans. Magn*., vol. 39, no. 6, pp. 3523-3526, November 2003.
[166]Y. Li, J. W. Xin, T. B. Wang, and Y. P. Lu, "Programmable design of magnet shape for permanent-magnet synchronous motors with sinusoidal back emf waveform," *IEEE Trans. Magn*, vol. 41, no. 10, pp. 2163-2167, September 2008.
[167]M. R. Dubois, H. Polinder, and J. A. Ferreira, "Contribution of permanent-magnet volume elements of no-load voltage in machines," *IEEE Trans. Magn*., vol. 39, no. 3, pp. 1784-1792, May 2003.
[168]M. F. Hsieh, and Y. S. Hsu, "An investigation on influence of magnet arc shaping upon back electromagnetic force waveforms for design of permanent-magnet brushless motors," *IEEE Trans. Magn*., vol. 41, no. 10, pp. 3949-3951, March 2005.
[169]M. Islam, S. Mir, T. Sebastian, and S. Underwood, "Design consideration of sinusoidally excited permanent-magnet machines for low-torque-ripple applications," *IEEE Trans. Ind. Appl*., vol. 41, no. 4, pp. 955-962, July/August 2005.
[170]P. Zheng, J. Zhao, J. Q. Han, J. Wang, Z. Y. Yao, and R. R. Liu, "Optimization of the magnetic pole shape of a permanent-magnet synchronous motor," *IEEE Trans. Magn*., vol. 43, no. 6, pp. 2531-2533, June 2007.
[171]N. R. Tavana, and A. Shoulaie, "Analysis and design of magnetic pole shape in linear permanent-magnet machine," *IEEE Trans. Magn*., vol. 46, no. 4, pp. 1000-1006, April 2010.
[172]H. K. Hong, and J. H. Yoo, "Shape design of the surface mounted permanent magnet in a synchronous machine," *IEEE Trans. Magn*., vol. 47, no. 8, pp. 2109-2117, August 2011.
[173]K. I. Lskaris, and A. G. Kladas, "Permanent-magnet shape optimization effects on synchronous motor performance," *IEEE Trans. Ind. Electron*., vol. 58, no. 9, pp. 3776-3783, September 2011.

[174]M. R. Dubois, and G. Mailloux, "Analytical calculation of no-load voltage waveforms in machines based on permanent-magnet volume integration," *IEEE Trans. Magn*., vol. 44, no. 5, pp. 581-589, May 2008.
[175]M. R. Dubois, H. Polinder, and J. A. Ferreira, "Varying magnetization orientation for permanent-magnet volume reduction in machines," *IEEE Trans. Magn*., vol. 39, no. 3, pp. 1793-1799, May 2003.
[176]A. H. Isfahani, S. Vaez-Zadeh, and M. A. Rahman, "Using modular poles for shape optimization of flux density distribution in permanent magnet machines," *IEEE Trans. Magn*., vol. 44, no. 8, pp. 2009-2014, August 2008.
[177]A. H. Isfahani, S. Vaez-Zadeh, and M. A. Rahman, "Performance improvement of permanent magnet machines by modular poles," *Proc. IET Electric Power Appl*., vol. 3, iss. 4, pp. 343-351, July 2009.
[178]Y. Pang, Z. Q. Zhu, and Z. J. Feng, "Cogging torque in cost-effective surface-mounted permanent-magnet nachines," *IEEE Trans. Magn*., vol. 47, no. 9, pp. 2269-2276, September 2011.
[179]J. De La Ree, and N. Boules, "Magnet shaping to reduce induced voltage harmonics in PM machines with surface mounted magnets," *IEEE Trans. Energy Conver*., vol. 6, no. 1, pp. 155-161, March 1999.
[180]K. J. Binnes, P. J. Lawrenson, and C. W. Trowbridge, *The analytical and numerical solution of electric and magnetic fields*: John Wiley & Sons Ltd, 1992.
[181]B. Ackermann, J. H. H. Janssen, R. Sottek, and R. I. van Steen, "New technique for reducing cogging torque in a class of brushless DC motors," *IEE Proceedings B of Electric Power Applications*., vol. 139, no. 4, pp. 315-320, July 1992.
[182]S. M. Hwang, J. B. Eom, G. B. Hwang, W. B. Jeong, and Y. H. Jung, "Cogging torque and acoustic noise reduction in permanent magnet motors by teeth pairing," *IEEE Trans. Magn*., vol. 36, no. 5, pp. 3144-3146, September 2000.
[183]Z. Q. Zhu, and D. Howe, "Instantaneous magnetic field distribution in brushless permanent magnet dc motors. Part III: Effect of stator slotting," *IEEE Trans Magn*., vol. 29, no. 1, pp. 143-151, January 1993.
[184]D. Zarko, D. Ban, and T. A. Lipo, "Analytical calculation of magnetic field distribution in the slotted air gap of a surface permanent-magnet motor using complex relative air-gap permeance," *IEEE Trans Magn*., vol .42, no. 7, pp. 1828-1837, July 2006.
[185]Z.Q. Zhu, L. J. Wu, and Z. P. Xia, "An accurate sub-domain model for magnetic field computation in slotted surface-mounted permanent magnet machines," *IEEE Trans. Magn*., vol. 46, no. 4, pp. 1100-1115, April 2010.
[186]R. Bjork, A. Smith, C. R. H. Bahl, "Analysis of the magnetic field, force, amd torque for two-dimensional Halbach cylinders," *J. Magn. Magn. Mater*., vol. 322, p. `33, 2010.
[187]H. Shute, J. Mallinson, D. Wilton, and D. Mapps, "One-sided fluxes in planar, cylindrical, and spherical magnetized structures," *IEEE Trans. Magn*., vol. 36, no. 2, pp. 440-451, March 2000.
[188]Z. P. Xia, Z. Q. Zhu, and D. Howe, "Analytical magnetic field analysis of Halbach magnetized permanent-magnet machines," *IEEE Trans. Magn*., vol. 40, no. 4, pp. 1864-1872, July 2004.
[189]M. Marinescu and N. Marinescu, "New concept of permanent magnet excitation for electrical machines: analytical and numerical computation," *IEEE Trans. Magn*., vol. 28, no. 2, pp. 1390-1393, March 1992.
[190]L. Jian, and K. T. Chau, "A coaxial magnetic gear with Halbach permanent-magnet arrays," *IEEE Trans. Energy Convers*., vol. 25, no. 2, pp. 319-328, June 2010.
[191]T. Shi, Z. Qiao, C. Xia, H. Li, Z. Song, "Modeling, analyzing and parameter designing of the magnetic field of a segmented Halbach cylinder," *IEEE Trans. Magn*., vol. 48, no.

5, pp. 1890-1898, May 2012.
[192] P. H. Mellor, and R. Wrobel, “Optimization of a multipolar permanent-magnet rotor comprising two arc segments per pole,” *IEEE Trans. Ind. Appl.*, vol. 43, no. 4, pp. 942-951, July/August 2007.
[193] M. Markovic, and T. Perriard, “Optimization design of a segmented Halbach permanent-magnet motor using an analytical model,” *IEEE Trans. Magn*., vol. 45, no. 7, pp. 2955-2960, July 2009.
[194] K. Boughrara, B. L. Chikouche, R. Ibtiouen, D. Zarko, and O. Touhami, “Analytical model of slotted air-gap surface mounted permanent-magnet synchronous motor with magnet bars magnetized in the shifting direction,” *IEEE Trans. Magn*., vol. 45, no. 2, pp. 747-758, February 2009.
[195] K. J. Meessen, J. J. H. Paulides, and E. A. Lomonova, “Analysis of 3-D effects in segmented cylindrical quasi-Halbach magnet arrays,” *IEEE Trans. Magn*., vol. 47, no. 4, pp. 727-733, April 2011.
[196] K. J. Meessen, B. L. J. Gysen, J. J. H. Paulides, and E. A. Lomonova, “Halbach permanent magnet shape selection for slotless tubular actuators,” *IEEE Trans. Magn*., vol. 44, no. 11, pp. 4305-4308, November 2008.
[197] A. Rahideh, and T. Korakianitis, “Analytical open-circuit magnetic field distribution of slotless brushless permanent-magnet machines with rotor eccentricity,” *IEEE Trans. Magn*., vol. 47, no. 12, pp. 4791-4808, December 2011.
[198] N. Bianchi, and M. Dai Pre, “Use of the star of slots in designing fractional-slot single-layer synchronous motors,” *Proc. IEE-Electr. Power Appl*., vol. 153, no. 3, pp. 459-466, May 2006.
[199] Z. Q. Zhu, K. Wang, and G. Ombach, “Optimal magnet shaping with third order harmonic for maximum torque in brushless AC machines,” *IET Int. Conf. on Power Electronics, Machines and Drives, PEMD 2012*, CD Rom.
[200] D. E. Hesmondhalgh, D. Tipping, and M. Amrani, "Design and construction of a high-speed high-performance direct-drive handpiece," *IEE Proc. B, Elect. Power Appl*., vol. 134, pp. 286-296, 1987.
[201] F. B. Chaaban, "Determination of the optimum rotor/stator diameter ratio of permanent magnet machines," *Elect. Mach. Power Syst*., vol. 22, pp. 521-531, 1994.
[202] F. B. Chaaban, and El-Hajj, "A cost-effective design approach for permanent magnet brushless machines," *Elect. Mach. Power Syst*., 2000, 28, pp. 893-900.
[203] J. D. Ede, Z. Q. Zhu, and D. Howe, "Optimal split ratio for high-speed permanent magnet brushless DC motors," in *Int. Conf. Elect. Mach Syst.*, 2001, vol. 2, pp. 909-912.
[204] Y. Pang, Z. Q. Zhu, and D. Howe, "Analytical determination of optimal split ratio for permanent magnet brushless motors," *IEE Proc. Elect. Power Appl.*, vol. 153, pp. 7-13, 2006.
[205] L. J. Wu, Z. Q. Zhu, J. T. Chen, Z. P. Xia, and G. W. Jewell, "Optimal split ratio in fractional-slot interior permanent-magnet machines with non-overlapping windings," *IEEE Trans. Magn*., vol. 46, no. 5, pp. 1235-1242, May 2010.
[206] Y. Tang, Y. Xu, J. Hu, J, Zou, and S. Li, "Optimization of split ratio to design the PM brushless DC motor," *Int. Conf. Elect. Mach. Syst*., pp. 2009.
[207] J. Wang, and D. Howe, "Tubular modular permanent magnet machines equipped with quasi-Halbach magnetized magnets-part II: armature reaction and design optimization," *IEEE Trans. Magn*., vol. 41, no. 9, pp. 2479-2489, 2005.
[208] X. Chen, Z. Q. Zhu, and D. Howe, "Modeling and analysis of a tubular oscillating permanent magnet actuator," *IEEE Trans. Ind. Appl*., vol. 45, no. 6, pp. 1961-1970, Nov/Dec 2009.
[209] X. Chen and Z.Q. Zhu, “Analytical determination of optimal split ratio of E-core

permanent magnet linear oscillatory actuators," *IEEE Trans. on Industry Applications*, vol.47, no.1, pp.25-33, January 2011.

APPENDIX I – ANALYSIS OF CLAW-POLE ROTOR BRUSHLESS MACHINE WITH DC EXCITATION BY LUMPED-PARAMETER MAGNETIC CIRCUIT MODEL

Nowadays, the replacement of rare-earth permanent magnet is one of the primary targets to enhance the cost-effective design for electrical machines. A claw-pole rotor brushless machine with DC excitation is desirable as a magnetless machine because it is reliable, low-cost, and does not need slip ring etc. However, the inherent 3D structure makes numerical analysis very time-consuming. In this paper, a lumped-parameter magnetic circuit model is developed to model and design an 18-slot/6-pole claw-pole rotor brushless machine with DC excitation, while its validity is examined by using 3D finite-element analysis. The optimization is also carried out, together with optimal skew and unequal rotor pole thickness

I.1 Introduction

High reliability, high efficiency, and easier mass production of electrical machines have been the key objectives of industrial, automotive and domestic applications over the past decades. Recently, although the performance of electrical machine is significantly improved with the aid of permanent magnets (PM), the rising cost of PM has renewed attention to adopting magnetless machines. Hence, considering all of these aspects together with the increasing concern of cost-effective design, the claw-pole machine which is one of the oldest type three-phase electrical machines [I1] becomes increasingly attractive.

A typical claw-pole rotor machine consists of a conventional stator which is equipped with a three phase overlapping or non-overlapping winding and two sets of claw shaped poles are nested to form rotor pole pairs [I2-I4]. The rotor coil is supplied with direct current (DC) via a slip ring to produce intrinsic field [I5-I6]. However, the inherent problems of slip ring such as poor maintenance-free capability and unreliability lead this construction unfeasible for modern design requirements in contrast to machines with PM excitation. Hence, a two-stator structure with a claw-pole rotor radially sandwiched between is shown in Fig.I.1, where the outer stator is equipped with armature winding, while the inner stator holds a DC excitation coil. It is observed that the proposed claw-pole machine exhibits a 3D structure with complex flux paths and two air-gap regions which, in turn, makes numerical analysis, such as 3D finite-element analysis (FEA), extremely time-consuming. Therefore, a lumped-parameter magnetic circuit model (LMC model) is developed to model and design the claw-pole rotor brushless machine with DC excitation. The developed LMC model is validated by adopting

3D FEA for an 18-slot/6-pole claw-pole rotor machine, while the design parameters and the shape of claw-pole are also optimized.

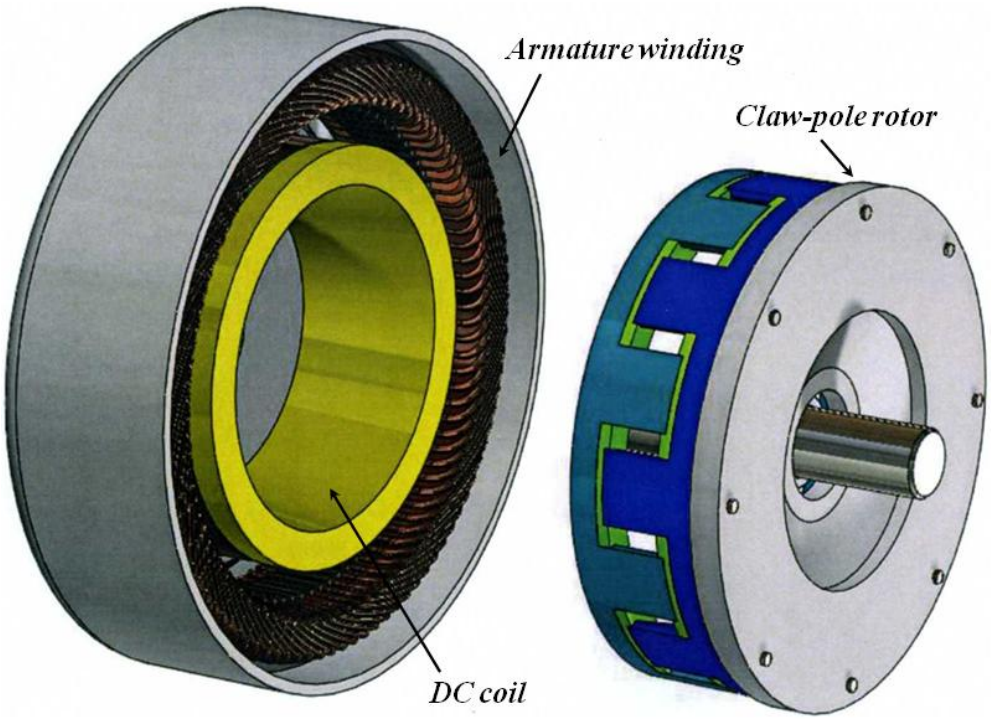

Fig.I.1. Illustration of claw-pole rotor machine.

I.2 Lumped-Parameter Magnetic Circuit Model

The basic principle of LMC model is developed by adopting a magnetic circuit which can be analogous to electrical circuit, and written as

$$\Phi = FP \tag{I.1}$$

where Φ, F and P represent flux, magnetomotive force and permeance, respectively. The Maxwell equations are used to establish the mathematical expressions of four typical permeances which can be used to summarize all kinds of permenaces in electrical machines on the basis of material property, cross-section and flux paths. These typical permeances are named as the permeance of nonlinear region, tooth to tooth air-gap permeance, slot leakage permeance, and permeance of half-cylinder and half-ring, respectively. The detailed derivation and expressions of these permeances are elaborately discussed and can be found in [I7]. As regards to Kirchhoff's law, the LMC model of proposed claw-pole rotor machine, which has *s*-stator slot and *p*-rotor pole, is built and illustrated in Fig.I.2. Furthermore, the meaning of each permeance in LMC model are explained as shown in Fig.I.3, where P_{bi} is the permeance of outer stator back-iron, P_{lt} is the permeance outer stator teeth, P_{ls} is the slot leakage permeance in outer stator, P_{smrn} (m is the number of stator tooth, and n is the number

of rotor pole) is the air-gap permeance between the stator tooth and rotor pole, P_{rt} is the permeance of rotor pole, P_{rr} is the permeance between two adjacent rotor poles, P_{fl} is the leakage permeance of field winding, P_{er} and P_{es} are the permeance of end plate of rotor and stator, P_{eres} is the air-gap permeance between the rotor and inner stator, and P_{sb} is the permeance of inner stator back-iron. All of these permeances shown in Fig.I.2-3 can be described by adopting one of aforementioned typical permeance whose expressions are given in [I7].

According to the developed LMC model, the node potential is calculated as

$$PF^T = \Phi^T \tag{I.2}$$

where F is the node potential determinant, and the subscript T is the operator of matrix transpose. Therefore, by determining the node potentials, all branch magnetic fluxes can be subsequently obtained. The developed LMC model is applicable to any slot/pole combinations for claw-pole rotor machines, since the modeling and solving are accomplished in terms of matrix transformation. Finally, the phase flux linkage (λ_{ph}), back-EMF (E_{ph}) and electromagnetic torque (T_{em}) waveform can be easily obtained as

$$\lambda_{ph} = N\Phi_{ph} \tag{I.3}$$

$$E_{ph} = \frac{d\lambda_{ph}}{dt} \tag{I.4}$$

$$T_{em} = \frac{(E_A I_A + E_B I_B + E_C I_C)}{\omega_r} \tag{I.5}$$

where N is the number of turns and ω_r is the mechanical angular speed.

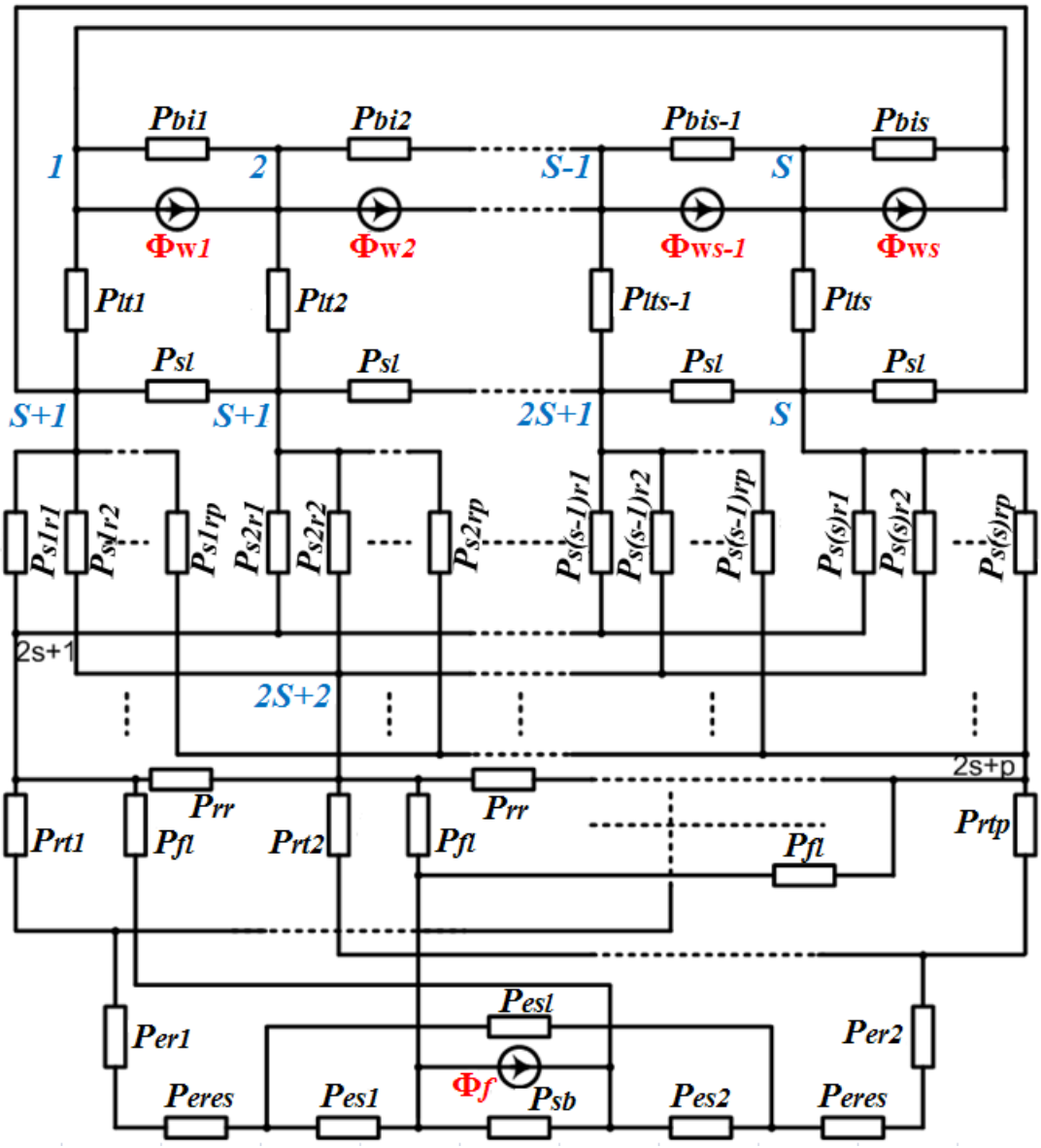

Fig.I.2. Lumped-parameter magnetic circuit model for claw-pole rotor brushless machine with DC excitation.

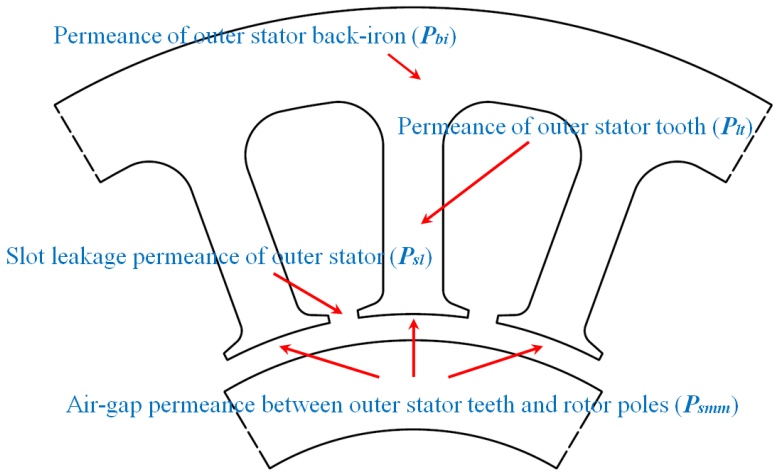

(a) Permeance of outer stator and outer air-gap

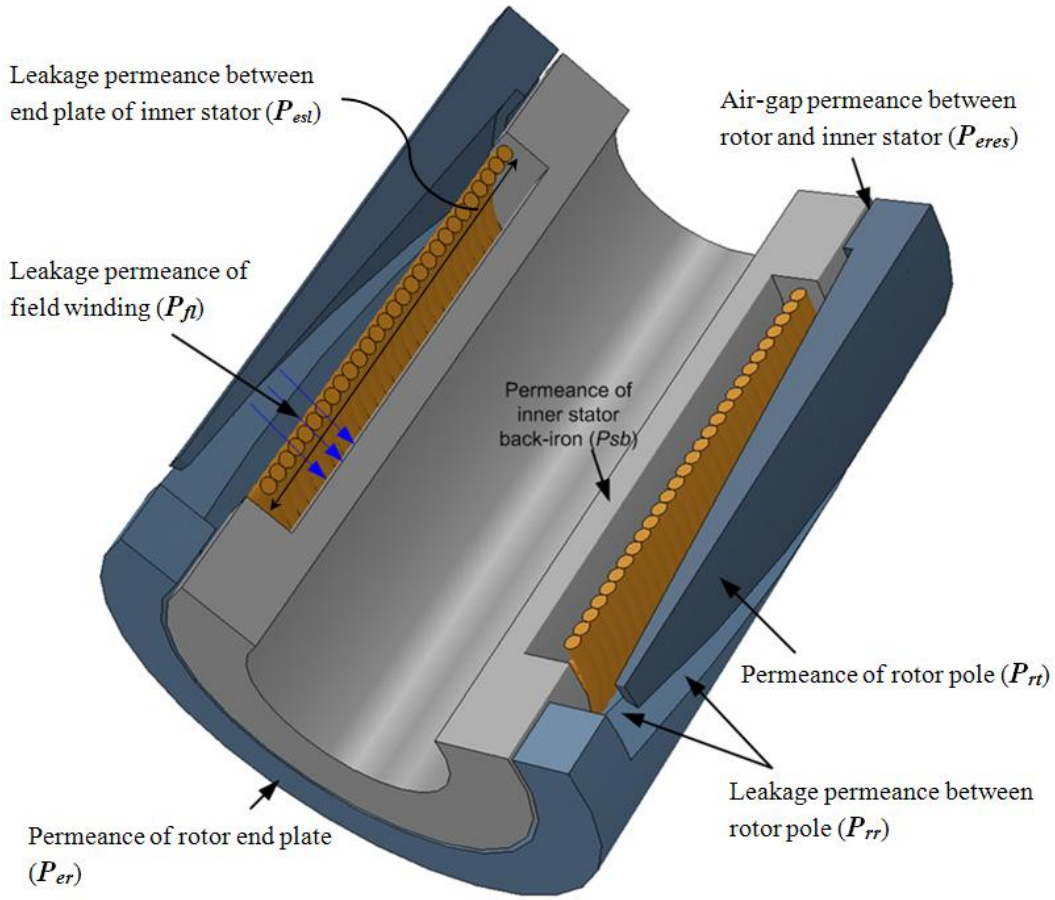

(b) Permeance of inner stator and rotor

Fig.I.3. Illustration of permeance in developed lumped-parameter magnetic circuit for claw-pole rotor brushless machine with DC excitation.

The FEA model of 18-slot/6-pole claw-pole rotor brushless machine with DC excitation is built in consistence with the foregoing developed LMC model, as shown in Fig.I.4 with the design parameters list in TABLE I-I. The analytical and FEA predicted phase flux-linkage, back-EMF and electromagnetic torque waveforms using both linear and nonlinear magnetic properties are compared in Fig.I.5, where reasonable agreements are achieved, especially for the average torque.

TABLE I-I Main Parameters of Prototype Motor

Number of phases	3	Thickness of rotor pole (end part)	6 mm
Number of stator slots	18	Thickness of rotor pole (active part)	5 mm
Number of rotor poles	6	Thickness of rotor back-iron (end part)	6 mm
Outer diameter of outer stator	70 mm	Length of rotor	63 mm

Inner diameter of outer stator	50 mm	Inner airgap length	0.5 mm
Axial length of outer stator	45 mm	Depth of inner stator slot	5 mm
Outer stator tooth width	3 mm	Thickness of inner stator back-iron	10 mm
Outer stator back-iron thickness	4 mm	Number of turns per phase	72
Outer stator tooth-tips thickness	1.5 mm	Number of turns of field winding	100
Slot opening of outer stator	3 mm	Rated field current	15A
Outer air-gap length	0.5 mm	Rated armature current (peak)	12 A
Outer diameter of rotor	49 mm	Rated speed	3300 rpm
Distance between two adjacent poles	3 mm	Lamination : SIL300 and 0.35mm for each single sheet	

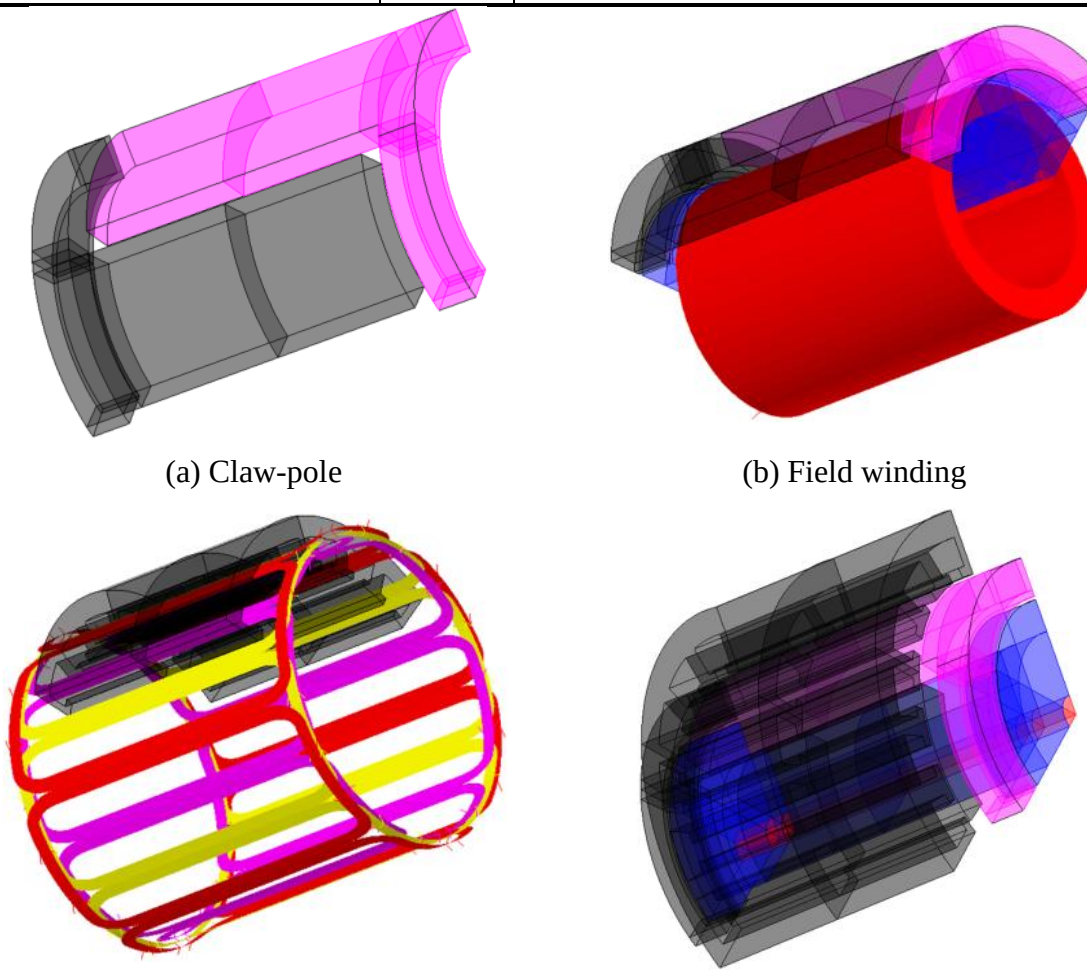

(a) Claw-pole (b) Field winding

(c) Armature winding (d) Whole machine

Fig.I.4. FEA model of 18-slot/6-pole claw-pole rotor brushless machine with DC excitation.

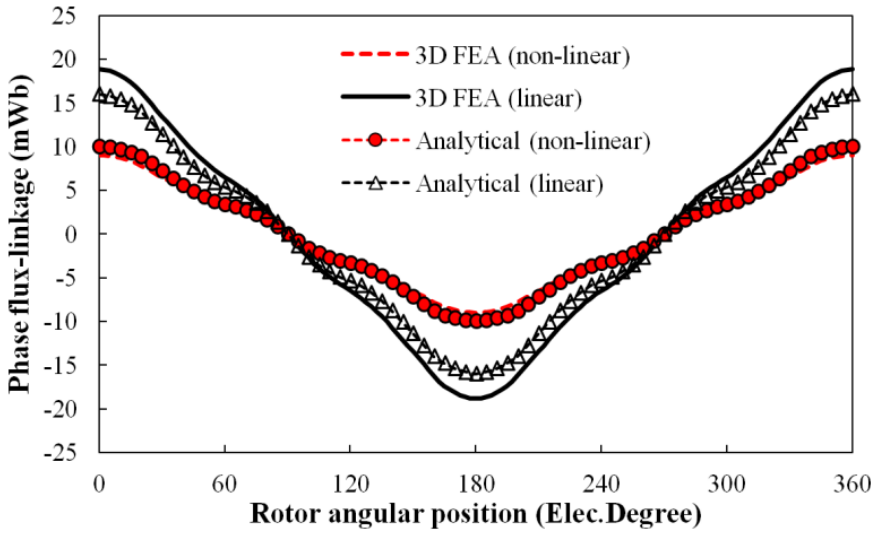

(a)Phase flux-linkage

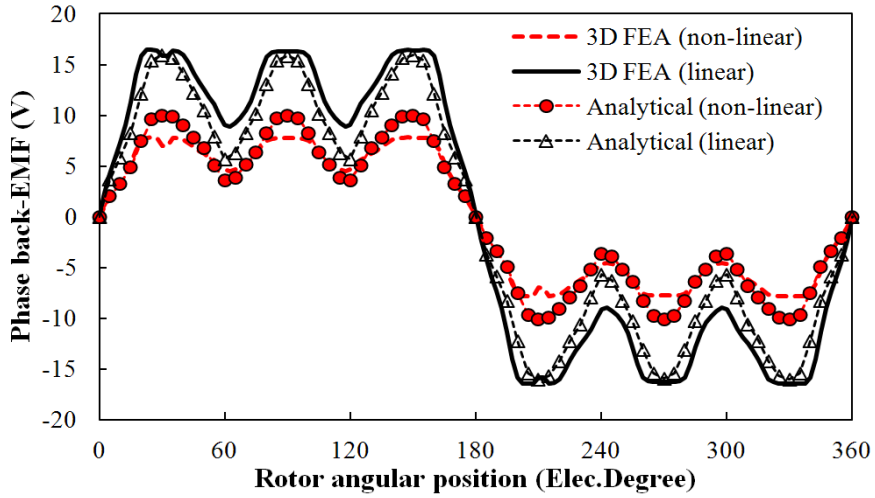

(b) Phase back-EMF, 3300 rpm

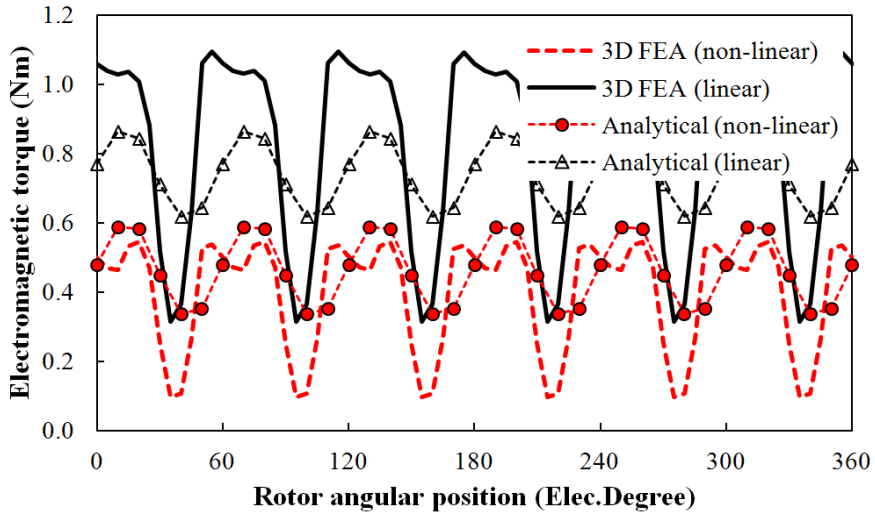

(c) Output torque

Fig.I.5. Comparison of linear and nonlinear lumped-parameter magnetic circuit model and 3D FEA predicted phase flux-linkage, phase back-EMF and electromagnetic torque waveforms.

I.3 Optimization of Claw-Pole Machine

In order to minimize the torque ripples, the claw-pole having skewed pole shape is often required. On the other hand, since the flux paths are very complicated in claw-pole region, the amounts of leakage flux are significant, where the leakage flux, especially the inter-pole leakage flux between two neighboring claw-poles and pole-tip to end plate leakage flux are dominant. Consequently, both method of skew and unequal rotor pole thickness are applied to claw-poles as shown in Fig.I.6. However, in order to reduce the computational time, the claw-pole is axially step skewed by 5 steps (n = 5), and in each step, the axial length of claw-pole (l_r) is equally stretched into l_r/n. Meanwhile, the corresponding thickness of the claw-pole (t_b) is equal to t_b*m/n (m denotes the step sequence, and $m = n, n\text{-}1, \ldots, 1$), in Fig.I.6. Consequently, the permeances in the rotor region are varied with foregoing geometry parameters correspondingly. The 3D FEA model is also made consistent with changes in LMC model as shown in Fig.I.7.

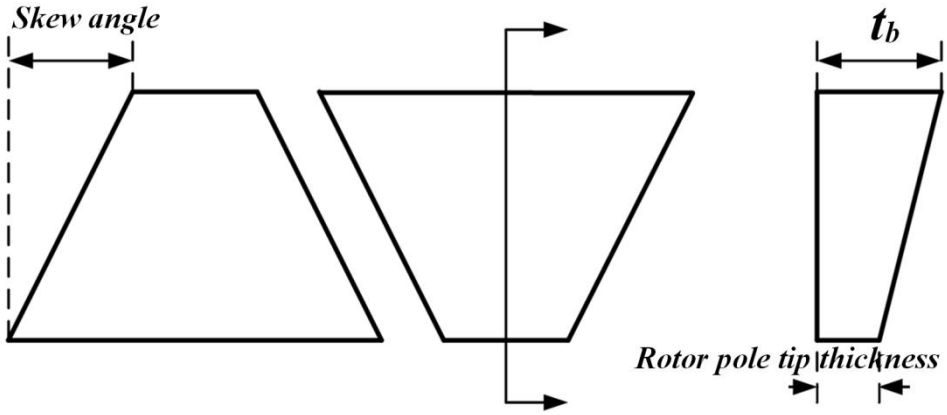

(a) Ideal skew

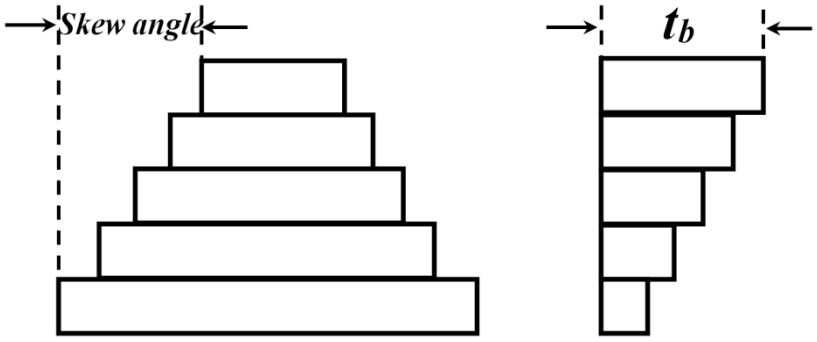

(b) Axially stepped skew

Fig.I.6. Parameters for claw-pole having skew and unequal rotor pole thickness.

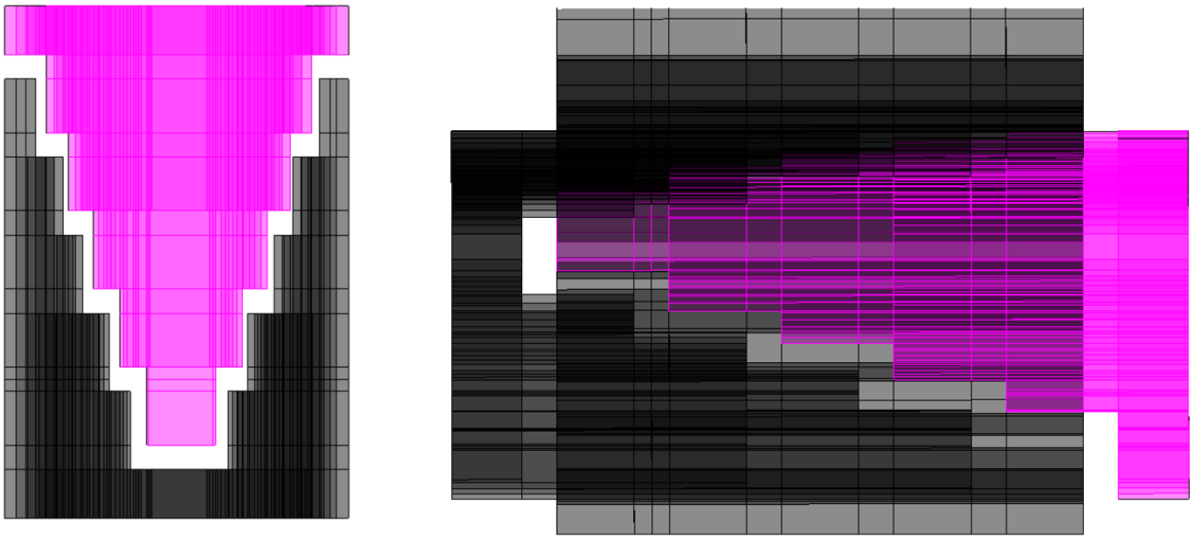

(a) Axially step skewed rotor (b) Whole machine

Fig.I.7. Axially step skewed claw-pole rotor with unequal rotor pole thickness in 3D FEA model.

Fig.I.8 shows the variation of phase flux-linkage, back-EMF, fundamental amplitude of phase back-EMF, electromagnetic torque, amplitude of average electromagnetic torque and corresponding peak-to-peak torque ripple with claw-pole skew angle for the 18-slot/6-pole claw-pole rotor brushless machine with DC excitation. It is observed that although skew angle equal to 42.5 electrical degree exhibit largest fundamental amplitude of phase back-EMF, the skew angle equal to 60 electrical degree can exhibit both relative large average electromagnetic torque and relative small peak-to-peak torque ripple. Thus, it has been chosen as the optimal skew angle.

Since the leakage flux is the major source to generate negative impact on the claw-pole machine performance, the unequal rotor pole thickness is adopted. Based on the foregoing optimized skew angle, the top thickness of rotor pole is optimized with the consideration of manufacturing tolerance, where 1 mm is selected as the preferable value, in Fig.I.9(a). Further, the split ratio is one of the most important design parameters for electrical machines and defined as the ratio between rotor and stator outer diameter. Thus, it is optimized when the copper loss is fixed and the foregoing optimized parameters are also employed, together with fixed rotor pole thickness and inner stator structure. As can be seen in Fig.I.9(b), the optimal split ratio is equal to 0.7. Moreover, due to skewed rotor structure, the middle pole-arc to pole-pitch ratio along machine axial direction is used as the standard for optimization, where the electromagnetic torque is maximized when the middle pole-arc to pole-pitch ratio is equal to 0.6. Then, the stator tooth width and stator back-iron thickness are optimized in order to achieve maximum torque capability, where the optimal result is obtained when stator

tooth width and stator back-iron thickness equal to 2.4 mm and 2.0 mm, respectively, in Fig.I.10.

Ultimately, with the aid of optimized design parameters, the electromagnetic torque is significantly improved in contrast to the original designed 18-slot/6-pole claw-pole rotor brushless machine with DC excitation, in Fig.I.11. However, it should be mentioned that the developed LMC model can be coupled with more powerful global optimization methods, e.g. the genetic algorithm and evolutionary algorithm [I6], to obtain more precise optimal results.

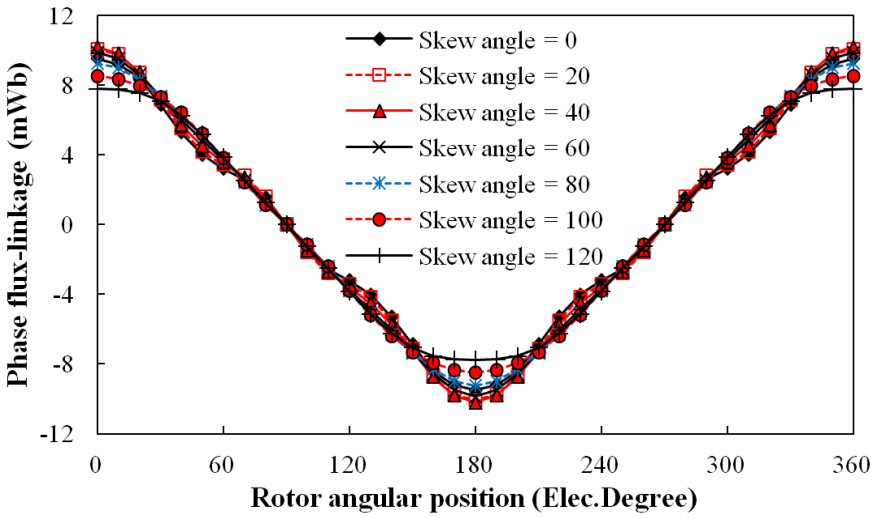

(a) Phase flux-linkage

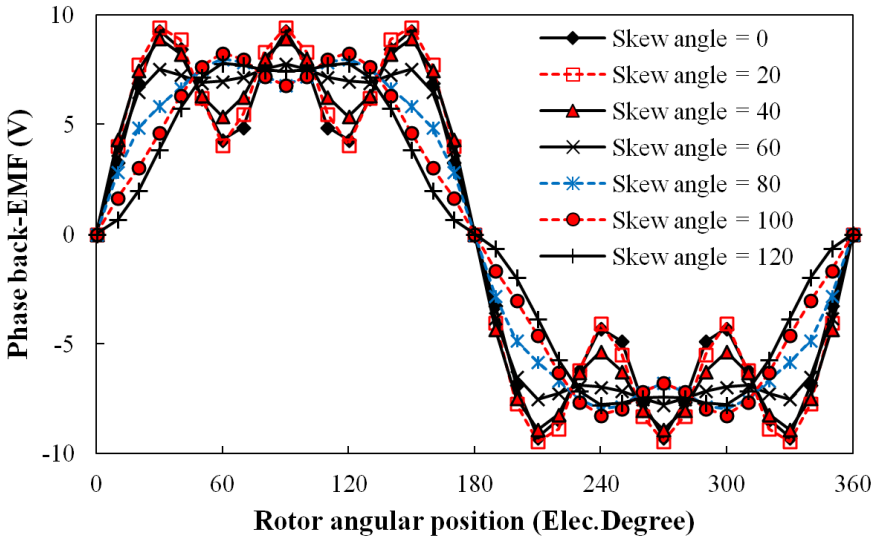

(b) Phase back-EMF, 3300 rpm

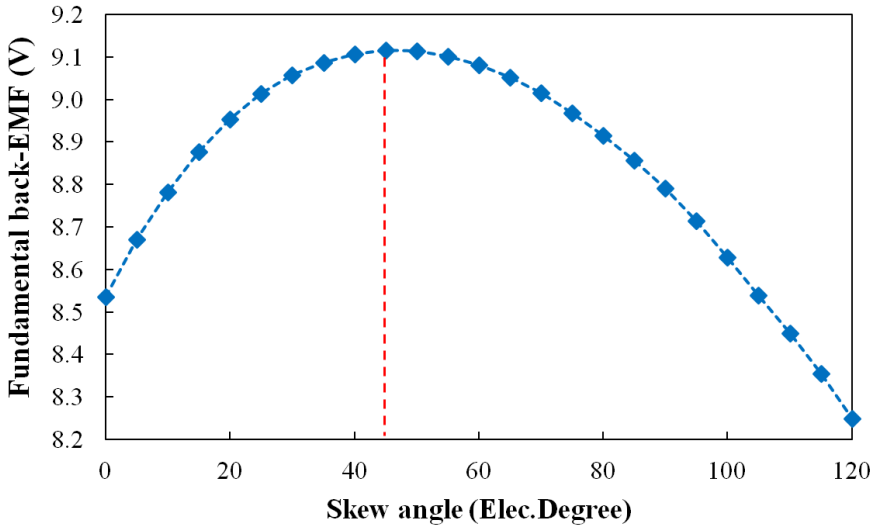

(c) Fundamental amplitude of phase back-EMF

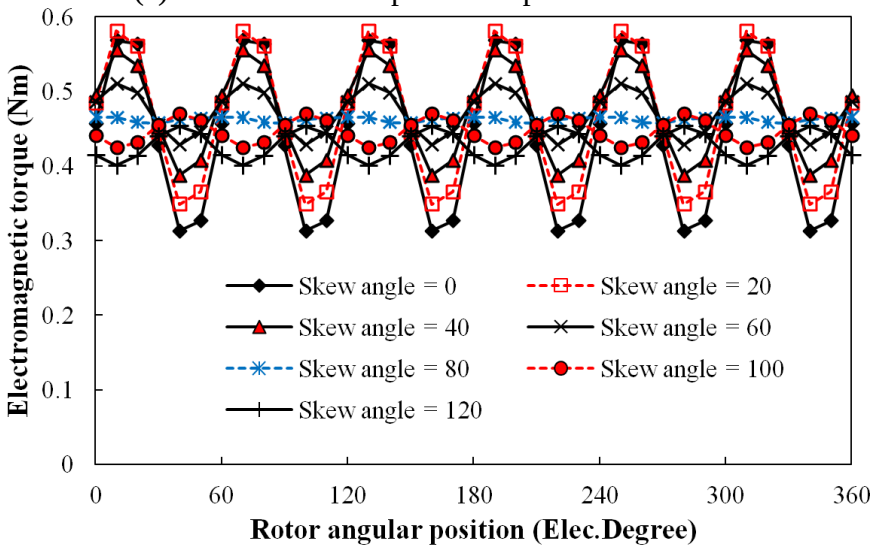

(d) Electromagnetic torque

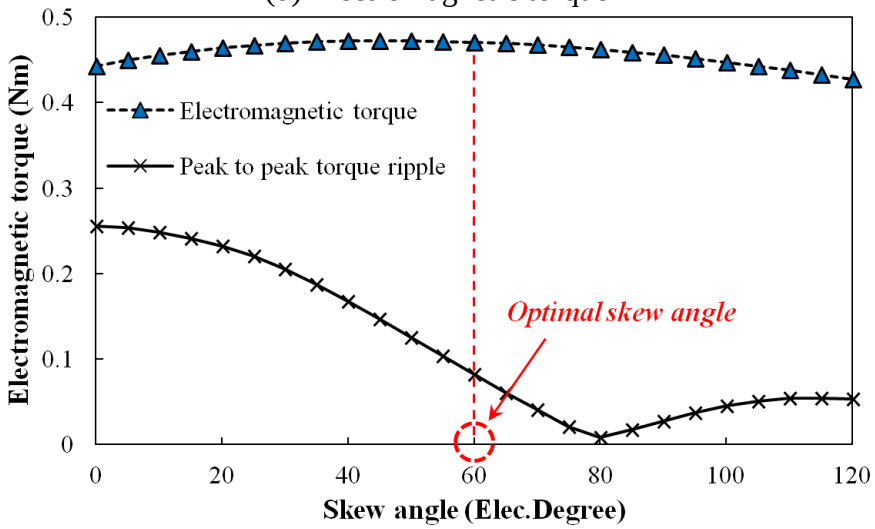

(e) Average electromagnetic torque and corresponding peak-to-peak torque ripple

Fig.I.8. Variation of phase flux-linkage, back-EMF, fundamental amplitude of phase back-EMF, electromagnetic torque, amplitude of average electromagnetic torque and corresponding peak-to-peak ripple with claw-pole skew angle for 18-slot/6-pole claw-pole rotor brushless machine with DC excitation.

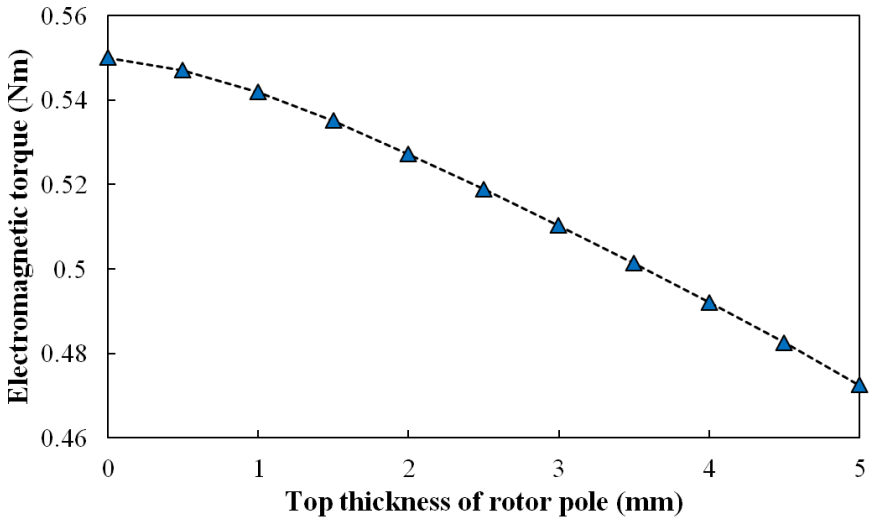

(a) Top thickness of rotor pole

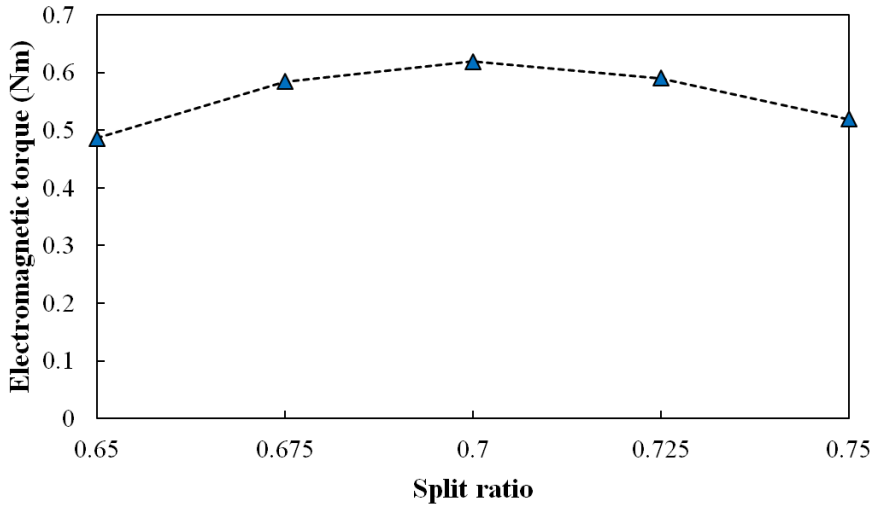

(b) Split ratio

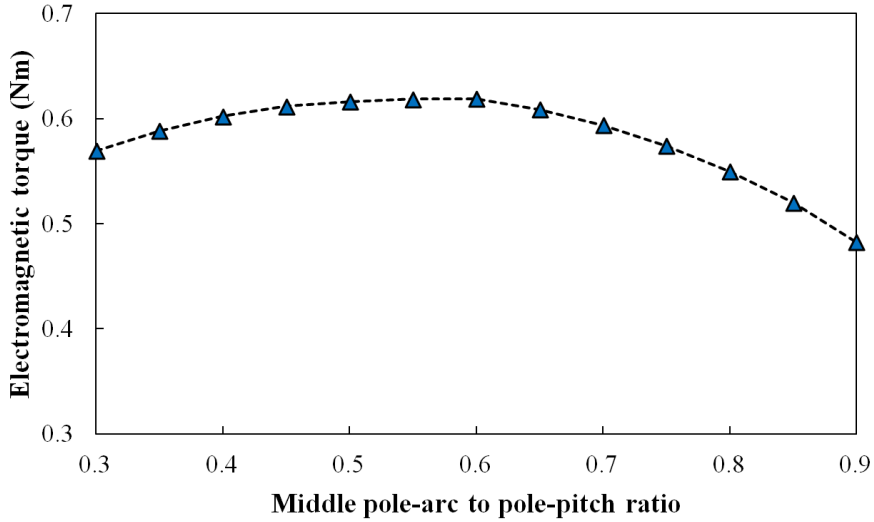

(c) Pole-arc to pole-pitch ratio

Fig.I.9. Optimization of electromagnetic torque with variation of top thickness of rotor pole, split ratio, and pole-arc to pole-pitch ratio for 18-slot/6-pole claw-pole rotor brushless machine with DC excitation.

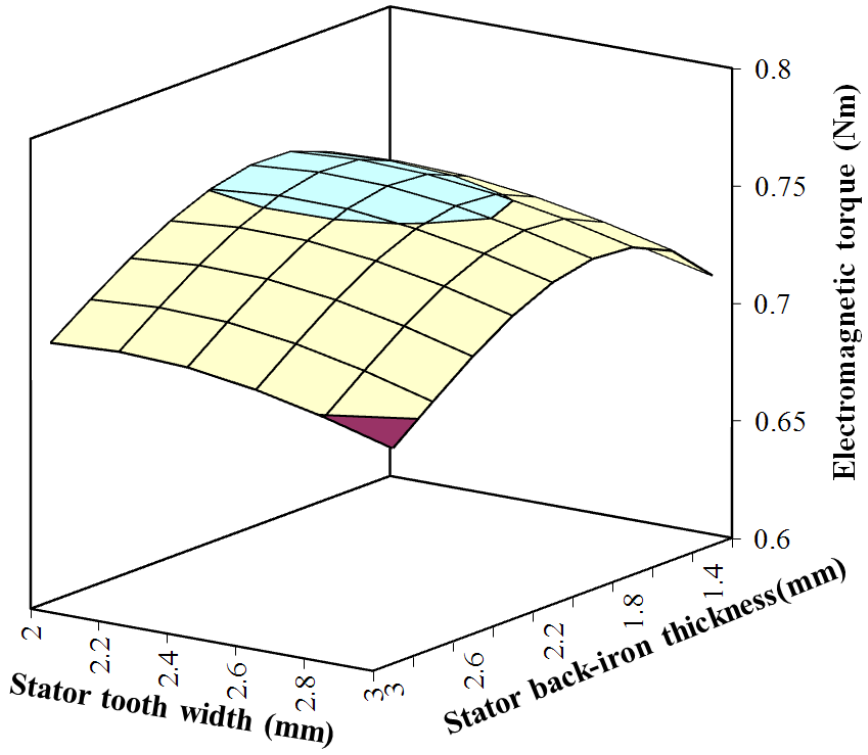

Fig.I.10. Optimization of electromagnetic torque with variation of stator tooth width and stator back-iron for 18-slot/6-pole claw-pole rotor machine with DC excitation.

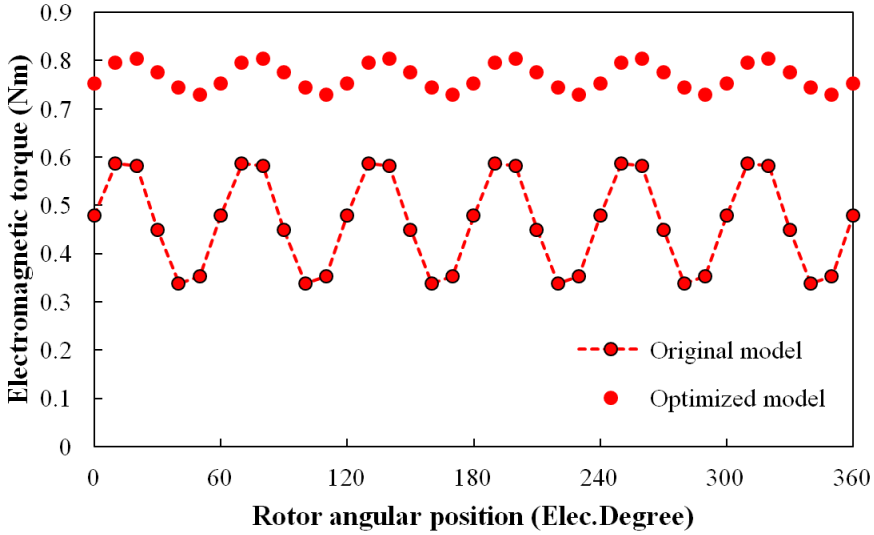

Fig.I.11. Comparison of original and optimized 18-slot/6-pole claw-pole rotor brushless machine with DC excitation.

I.4 Further FEA Validation

The capability of modeling claw-pole machine having skew and unequal rotor pole thickness for developed LMC model is validated by 3D FEA with the foregoing local optimized 18-slot/6-pole claw-pole rotor brushless machine with DC excitation. The

analytical and 3D FEA predicted phase flux-linkage, back-EMF and electromagnetic torque waveforms are compared and good agreement is obtained, Fig.I.12. The 3D FEA predicted flux density distribution in the original and optimized claw-pole regions are shown in Fig.I.13.

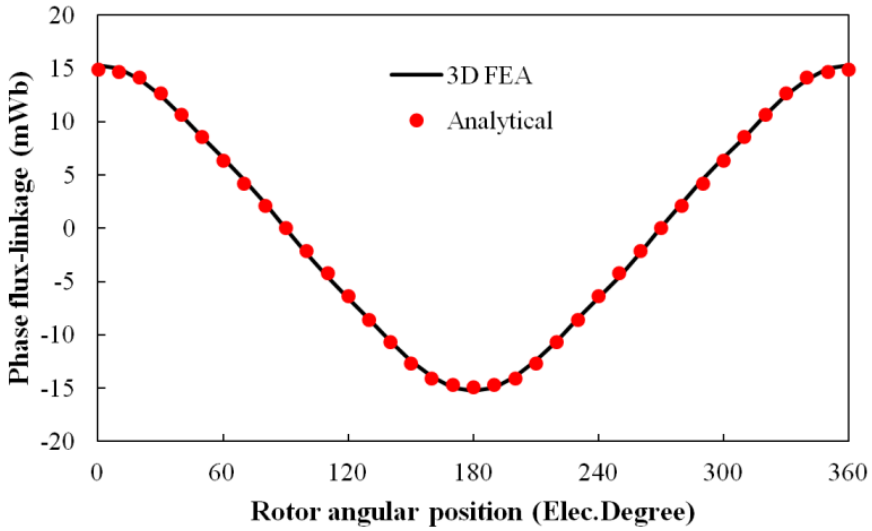

(a) Phase flux-linkage

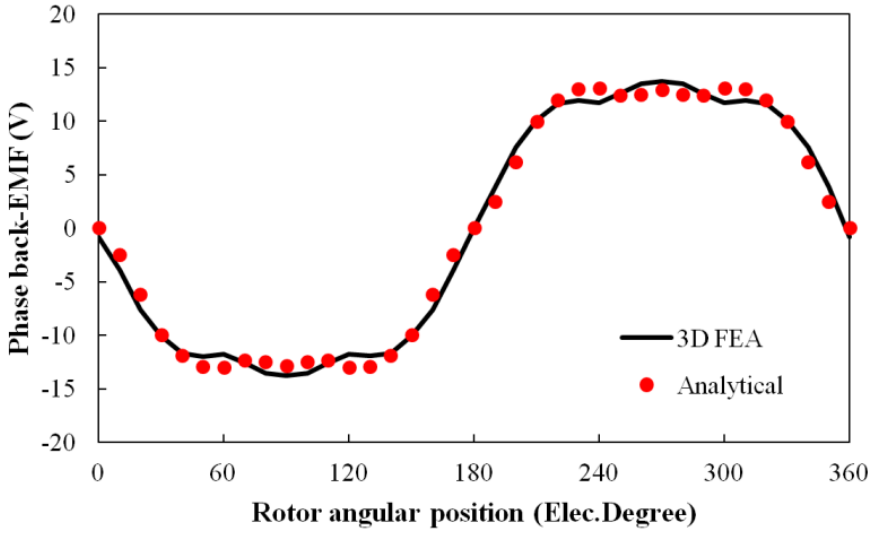

(b) Phase back-EMF, 3300 rpm

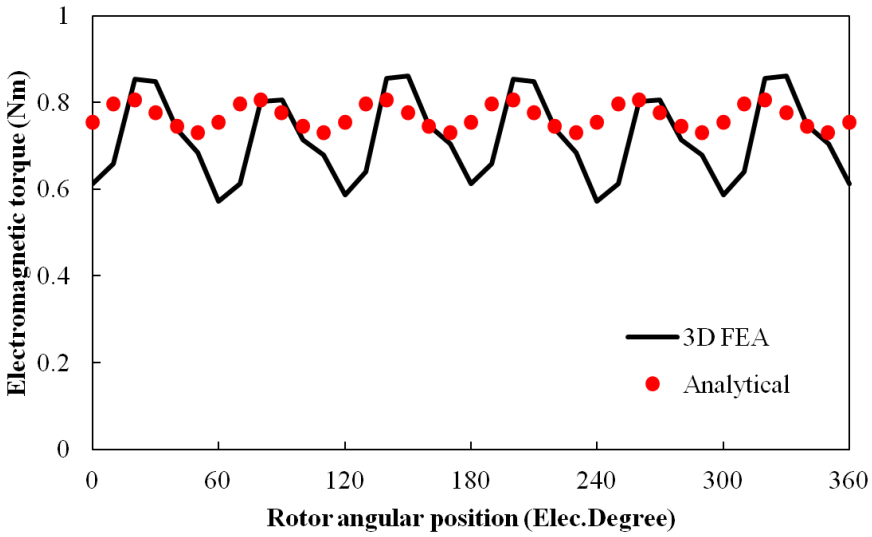

(c) Electromagnetic torque

Fig.I.12. Comparison of analytical and 3D FEA predicted phase flux-linkage, back-EMF, and electromagnetic torque waveforms for local optimized 18-slot/6-pole claw-pole rotor brushless machine with DC excitation.

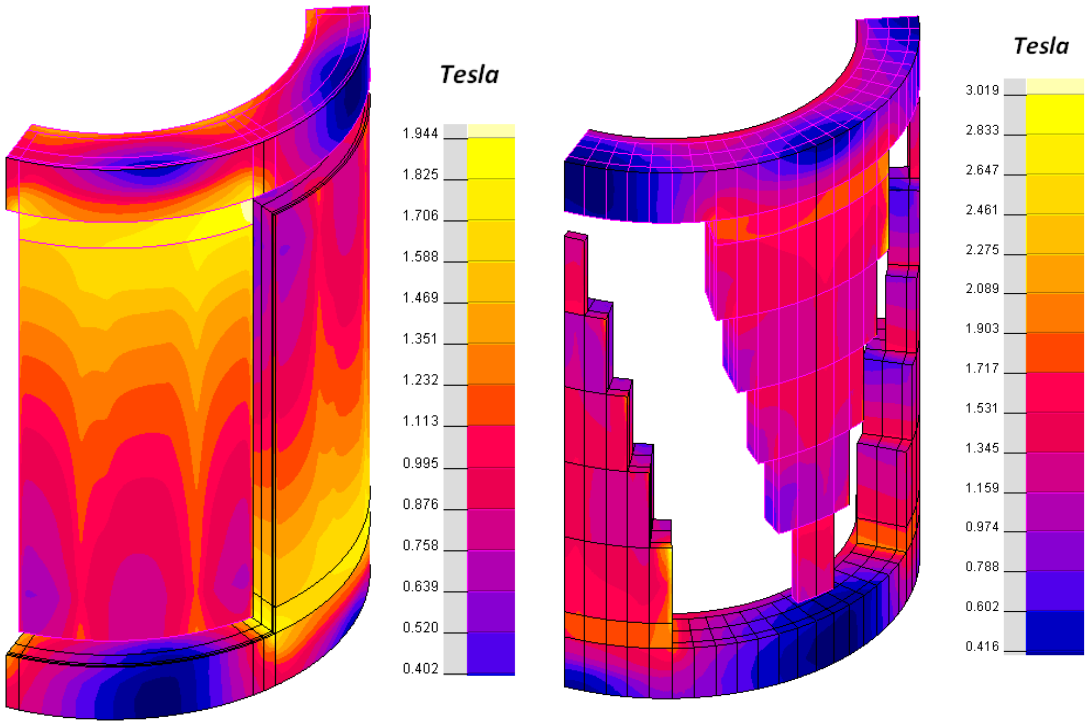

(a) Original claw-pole (b) Modified claw-pole

Fig.I.13. 3D FEA predicted flux density distribution in original and optimized claw-pole region.

I.5 Summary

In this appendix, a claw-pole rotor brushless machine with DC excitation is described with two (outer and inner) stators and one middle claw-pole rotor structure. Thus, the inherent problem of slip ring is eliminated. In order to fast optimize the 18-slot/6-pole claw-pole rotor brushless machine with DC excitation, a lumped-parameter magnetic circuit model is developed, while its validity is examined by 3D finite-element analysis. The overall optimized machine with the adoption of skew and unequal pole thickness exhibits significant improvement in terms of electromagnetic torque waveform.

I.6 References

[II1] H. Roisse, M. Hecquet, and P. Brochet, "Simulations of synchronous machines using a electric-magnetic coupled network model," *IEEE Trans. Magn*., vol. 34, no. 5, pp. 3656-3659, September 1998.

[II2] S. Kuppers, and G. Henneberger, "Numerical procedures for the calculation and design of automotive alternators," *IEEE Trans. Magn*., vol. 33, no. 2, pp. 2022-2025, March 1997.

[II3] L. Li, and Y. Xiang, "Finite element computation of 3-D nonlinear magnetic field in claw-pole electric machine using two scalar potentials, hybrid elements & automatic mesh generation," *IEEE Trans. Magns*, vol. 26, no. 2, pp. 371-374, March 1990.

[II4] A. Koenig, J. Williams, and S. Pekarek, "Evaluation of alternative evolutionary programming techniques for optimization of an automotive alternator," *IEEE Trans. Veh. Technol*., vol. 55, no. 3, pp. 933-942, May 2006.

[II5] F. Zhang, H. Bai, H. Gruenberger, and E. Nolle, "Comparative study on claw pole electrical machine with different structure," in *2nd IEEE Conf. Industrical Electronic and Applications, ICIEA*, Harbin, China, May 23-27, 2007, pp. 636-640.

[II6] B. Fahimi, and T. Sebastian, "Guest editorial special section on automotive electromechanical converters," *IEEE Trans. Veh. Technol*., vol. 56, no. 4, pp. 1470-1476, July 2007.

[II7] J. T. Chen, and Z. Q. Zhu, "Influence of the rotor pole number on optimal parameters in flux-switching PM brushless AC machines by the lumped-parameter magnetic circuit model," *IEEE Trans. Ind Appl*., vol. 46, no. 4, pp. 1381-1388, July/August 2010.

APPENDIX II – ANALYTICAL MODELLING OF CLAW-POLE STATOR SPM BRUSHLESS MACHINE HAVING SMC STATOR CORE

Since the claw-pole machines can exhibit a number of attractive features, they have been widely applied to automotive and domestic markets. Nowadays, with the development of rare-earth permanent magnet (PM) and powder metallurgy techniques, high performance and cost-effective design of a multiphase claw-pole stator SPM brushless machine becomes achievable. However, the inherent 3D structure makes finite-element analysis very time-consuming. Thus, a lumped-parameter magnetic circuit model is developed and validated by 3D finite element analysis in this appendix to design 3-phase 10-pole claw-pole stator surface-mounted PM brushless machine having soft magnetic composite made stator core. A prototype machine is built and tested in accordance with analytically optimized overall design parameters

B.1 Introduction

Easier mass production, high reliability, and low cost, etc. are among some attractive features of claw-pole machines. Consequently, claw-pole machines are widely applied to automotive and domestic markets since they were firstly commercialized in 1891 [II1]. Nowadays, the incorporation of rare-earth permanent magnet (PM) and powder metallurgy techniques (PMT) leads cost-effective design to be a substantial challenge and opportunity for continuously developing high performance claw-pole machines.

Generally, the claw shaped pole structure can be adopted in either stator or rotor, i.e. the claw-pole rotor and claw-pole stator machines. A typical claw-pole rotor machine consists of a conventional stator which is equipped with a multiphase overlapping or non-overlapping winding and two sets of claw-pole are nested to form rotor pole pairs [II2-4]. The ring PM or rotor coil, which is supplied with direct current (DC) via a slip ring to produce intrinsic field [II5-6], is embedded beneath the claw-poles. On the other hand, the claw-pole stator machine exhibits a conventional surface-mounted PM (SPM) rotor, while the stator is formed by two sets of claw-pole, together with a stator coil inside it to produce armature field, in Fig.II.1. The multiphase structure can be easily realized by connecting several single phase claw-pole stators with shifted electrical degree by means of ‘star-of-slot’ [7]. In contrast to claw-pole rotor machine, the claw-pole stator is manufactured with soft magnetic composite (SMC) material by using PMT, where the stator parts can be compacted in a mold into desired shape,

with minimal, if any, further machining [II8-12]. Thus, the cost for mass production is very low. Since the iron particles are insulated from each other due to the usage of adhesive for composite bonding, the eddy-current loss is significantly reduced for claw-pole stator machine. Moreover, the abandoned slip ring and end-winding makes it even more attractive for high performance applications. However, the design of multiphase claw-pole stator machine having such complex 3D structure by using finite-element analysis (FEA) is very complicated and time-consuming. Therefore, a lumped-parameter magnetic circuit model (LMC model) is developed to model and design the multiphase claw-pole stator SPM brushless machine. The developed LMC model is validated by adopting 3D FEA for a 10-pole claw-pole stator machine, while the design parameters and the shape of the claw-pole, plus unequal pole thickness are also optimized. A prototype machine is constructed and the measured results exhibit good agreement with LMC model predicted results.

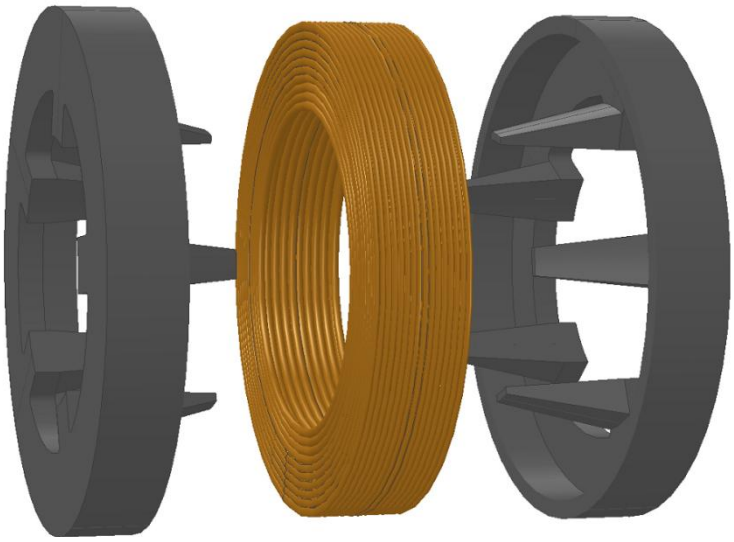

(a) One-phase claw-pole stator

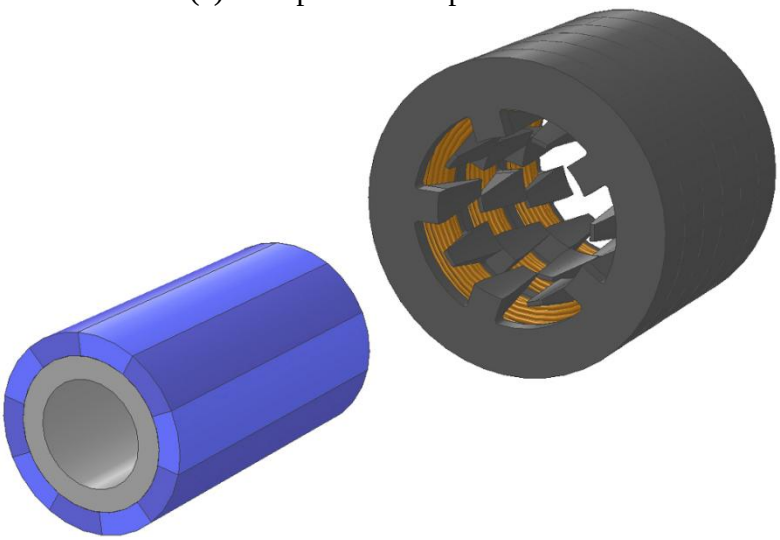

(b) Three-phase claw-pole stator SPM brushless machine

Fig.II.1. Illustration of three-phase claw-pole stator SPM brushless machine.

B.2 Lumped Parameter Magnetic Circuit Model

The basic principle of LMC model is developed by adopting a magnetic circuit and written as

$$\Phi = FP \tag{II.1}$$

where Φ, F and P represent flux, magnetomotive force and permeance, respectively. The Maxwell equations are adopted to establish the mathematical expressions of four typical permeances which can be used to describe all kinds of permenaces in electrical machine in accordance with material nonlinearity, geometries and flux paths. These typical permeances are named as the permeance of nonlinear region, tooth to tooth air-gap permeance, slot leakage permeance, and permeance of half-cylinder and half-ring, respectively. The detail derivation and expressions of these permeances are elaborately discussed and can be found in [II13]. By adopting Kirchhoff's law, the LMC model of proposed claw-pole stator SPM brushless machine, which has *s*-stator slot and *p*-rotor pole, is built and illustrated in Fig.II.2, where P_{sb} is the permeance of stator back-iron, P_{es} is the permeance of end-plate of stator, P_{er} is the permeance of end-plate of claw-pole, P_{erl} is the leakage permeance between end-plate of claw-pole, P_{sc} is the permeance of claw-pole, P_{scl} is the leakage permeance between two neighboring claw-pole, P_{fl} is the leakage permeance of field winding, P_{eres} is the air-gap permeance between the rotor and inner stator, P_{rpl} is the leakage permeance between two neighboring rotor pole, P_{pmr} is the permeance of PM, and P_{bi} is the permeance of rotor back-iron. All of these permeances in developed LMC model can be calculated by adopting one of aforementioned four typical permeances whose expressions are given in [II13].

Furthermore, the node potential in LMC model is calculated as

$$PF^T = \Phi^T \tag{II.2}$$

where F is the node potential determinant, and the subscript T is the operator of matrix transpose. By solving the node potentials, all branch magnetic fluxes can be subsequently obtained. The developed LMC model is applicable to any slot/pole combination for claw-pole stator SPM brushless machines, since the modeling and solving are accomplished in terms of matrix transformation. Ultimately, the phase flux linkage (λ_{ph}), back-EMF (E_{ph}) and electromagnetic torque (T_{em}) waveform can be easily obtained as

$$\lambda_{ph} = N\Phi_{ph} \tag{II.3}$$

$$E_{ph} = \frac{d\lambda_{ph}}{dt} \tag{II.4}$$

$$T_{em} = \frac{(E_A I_A + E_B I_B + E_C I_C)}{\omega_r} \quad \text{(II.5)}$$

where N is the number of turns and ω_r is the mechanical angular speed.

On the other hand, the complex 3D structure of claw-pole stator causes significant amounts of leakage flux, where the inter-pole and pole-tip to end-plate leakage flux are dominating. Therefore, both methods of skew and unequal claw-pole thickness, in Fig.II.3(a), are often required and applicable to reduce torque ripples and leakage fluxes. However, in order to reduce the computational time, the claw-pole stator is axially step skewed by 5 steps (n = 5), and in each step, the axial length of claw-pole (l_r) is equally stretched into l_r/n, while the tip pole thickness (t_t) is equal to t_b*m/n (m represents the step sequence, and $m = n, n-1,\ldots,1$), in Fig.II.3(b). Further, the permeances in the claw-pole stator region are varied with foregoing geometry parameters correspondingly. The 3D FEA model is also consistent with changes in LMC model as shown in Fig.II.4 for a 10-pole claw-pole stator SPM brushless machine with design parameters listed in TABLE II-I. The analytical and 3D FEA predicted phase back-EMF and electromagnetic waveforms are compared as shown in Fig.II.5, where good agreements are achieved.

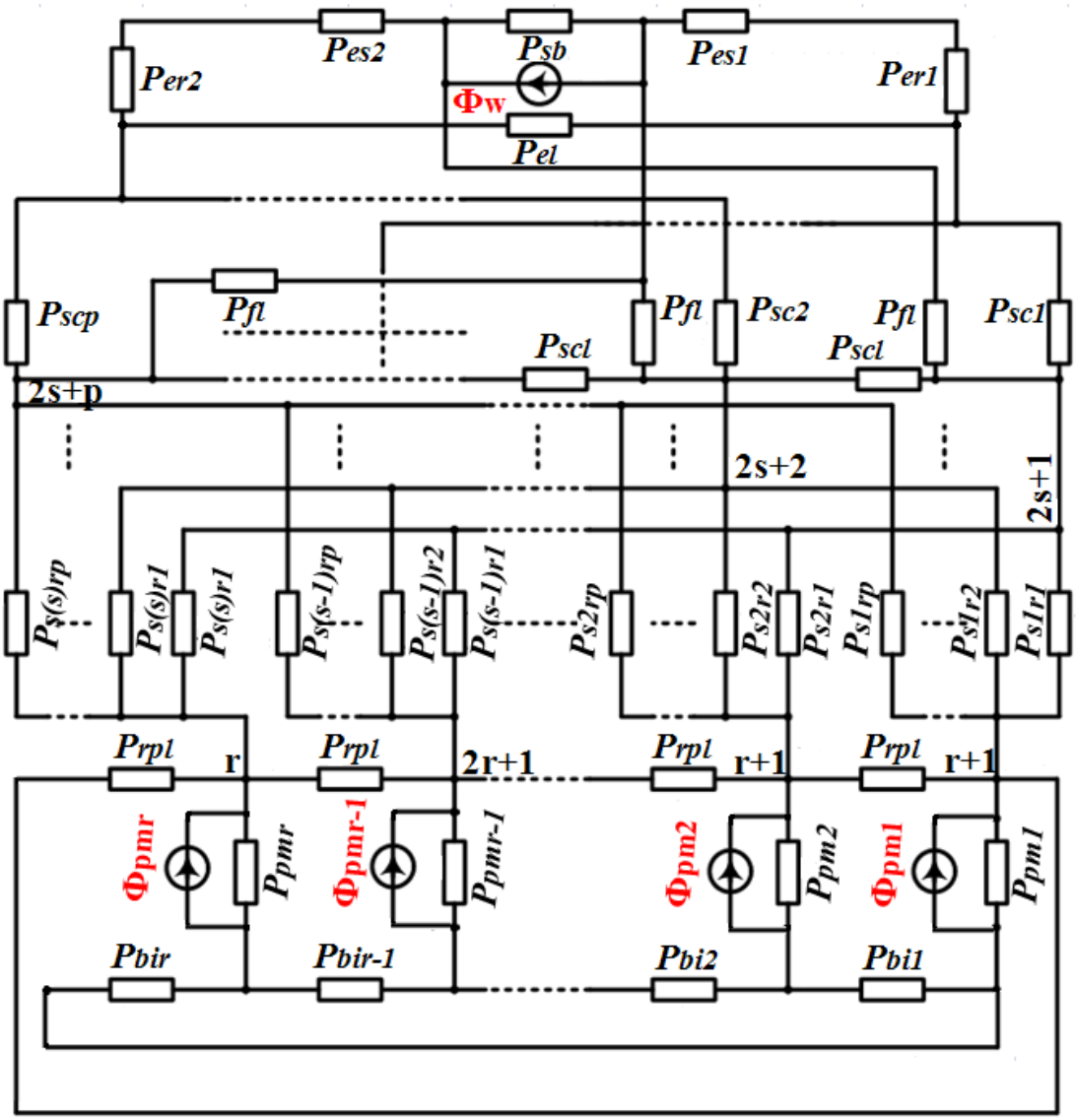

Fig.II.2. Illustration of lumped circuit model.

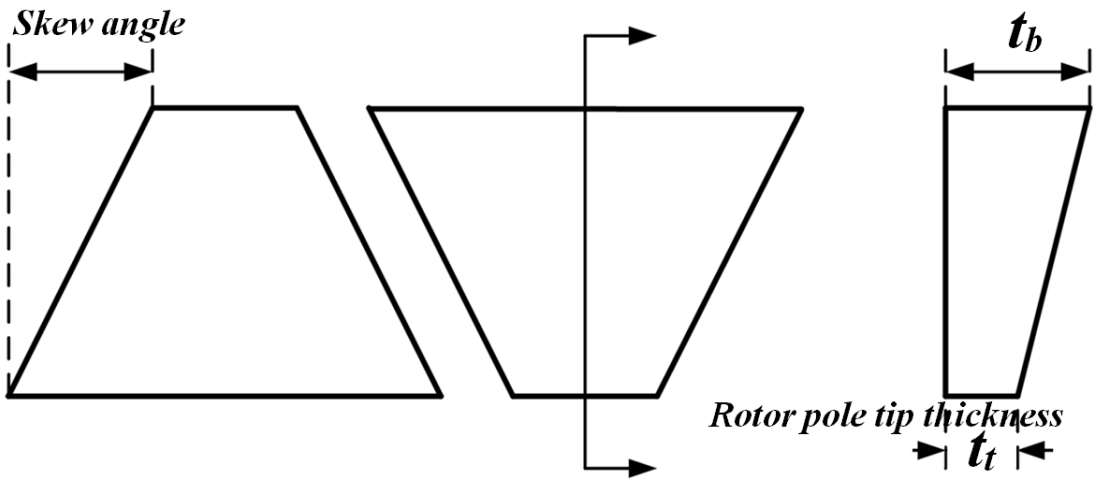

(a) Ideal skew

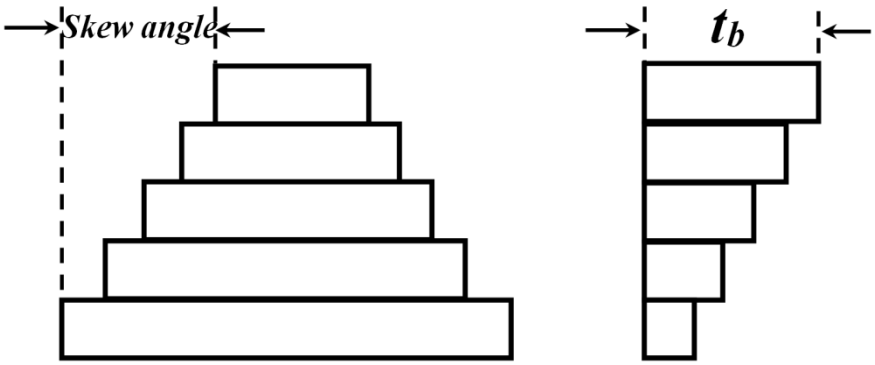

(b) Axially stepped skew

Fig.II.3. Parameters for claw-pole having skew and unequal claw-pole thickness.

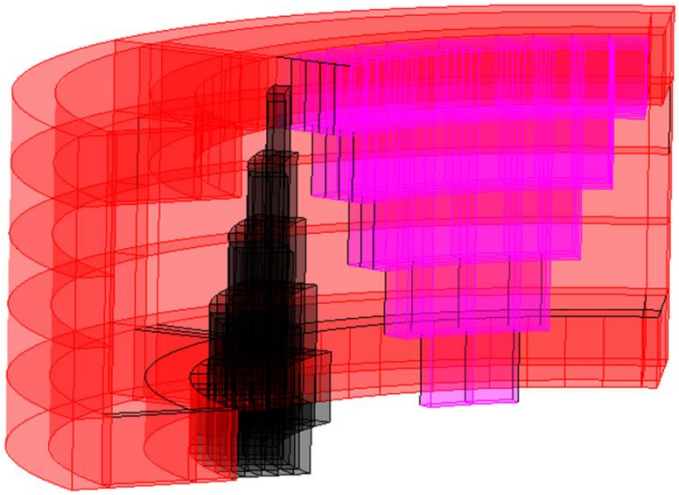

Fig.II.4. Schematic view of claw-pole stator SPM brushless machine having step skew and unequal pole thickness in 3D FEA model with one phase

TABLE II-I Main Parameter of Prototype Motor

Number of phases	3	Stator pole thickness	5 mm
Number of stator poles (same as number of rotor poles)	10	Stator middle pole-arc to pole-pitch ratio	0.6
Outer diameter of outer stator	70 mm	Air-gap length	0.5 mm
Inner diameter of outer stator	39.5 mm	Thickness of magnets	4 mm
Split ratio	0.55	Magnet remanence	0.4 T
Axial length of one segment stator	20 mm	Relative PM permeability	1.05
Axial length of rotor	20×3=60 mm	Number of turns per phase	72
Stator back-iron thickness	3 mm	Rated armature current (peak)	12 A
Thickness of stator end plate	4 mm	Rated speed	3300 rpm

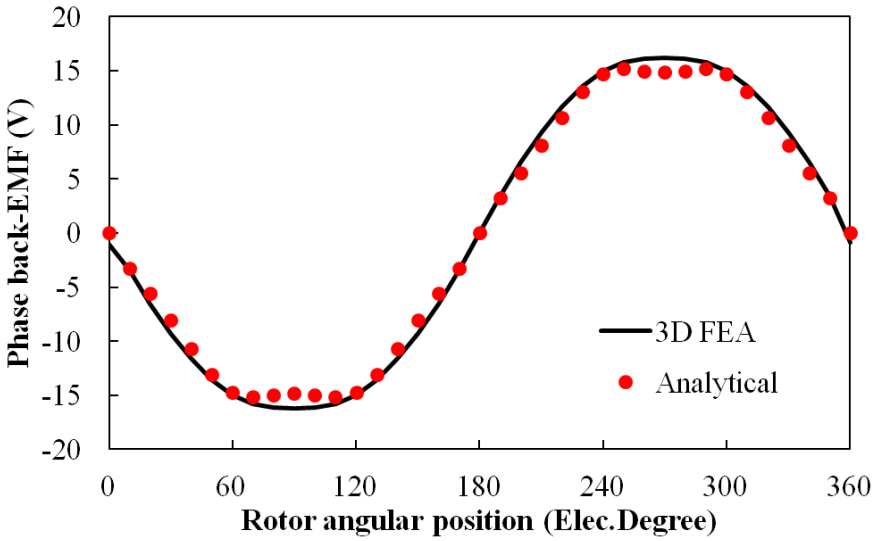

(a) Phase back-EMF, 3300 rpm

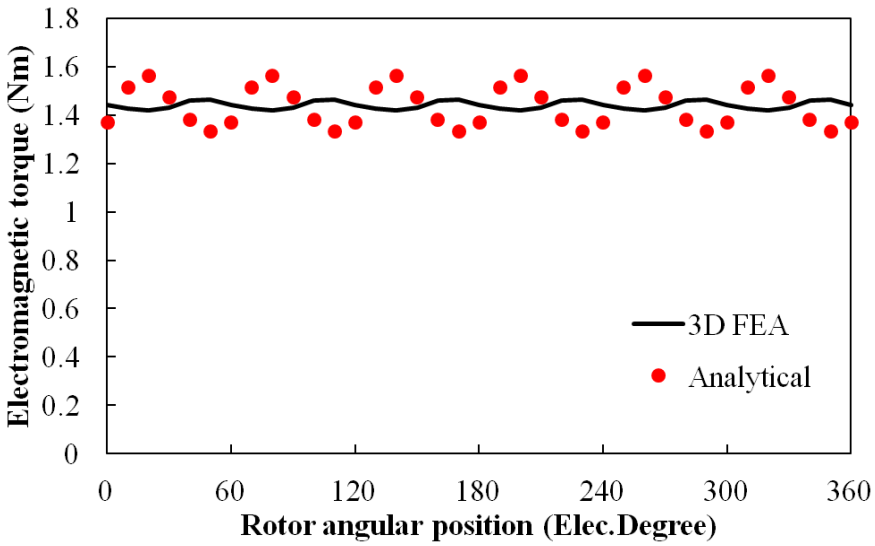

(b) Electromagnetic torque

Fig.II.5. Comparison of lumped-parameter magnetic circuit model and 3D FEA predicted phase flux-linkage, back-EMF and electromagnetic torque waveforms for 3-phase 10-pole claw-pole stator SPM brushless machine.

B.3 Optimization of Design Parameters

In contrast to initial design, a high performance NdFeB magnet (B_r = 1.2T, μ_r = 1.05) is used instead of low performance ferrite magnet. The design parameters for prototype 10-pole claw-pole stator SPM brushless machine are optimized based on electromagnetic torque maximization. However, due to increased saturation condition, a denser stepped skew where n = 20 is used. Since the leakage flux cause significant electromagnetic performance degradation, the methods of skew and unequal claw-pole thickness are firstly optimized. As can be seen in Fig.II.6(a), skew angle of 60 electrical degree exhibits the highest average

electromagnetic torque but meanwhile presents relative low peak-to-peak torque ripple. Thus, it is chosen as the optimal value. Based on this optimal skew angle, the claw-pole tip thickness (t_t) is optimized to reduce the pole tip to end-plate and inter-pole leakage fluxes, where, t_t = 1.0 mm achieves the maximum torque. Furthermore, the split ratio is one of the most important design parameter which can be defined as the ratio between rotor and stator outer diameters is also optimized as 0.5 by determining the maximum torque with foregoing optimized design parameters and fixed copper loss condition. Similarly, the optimal middle pole-arc to pole-pitch ratio (0.6), stator end-plate thickness (3.5 mm), and stator back-iron thickness (2.5 mm) are determined, respectively.

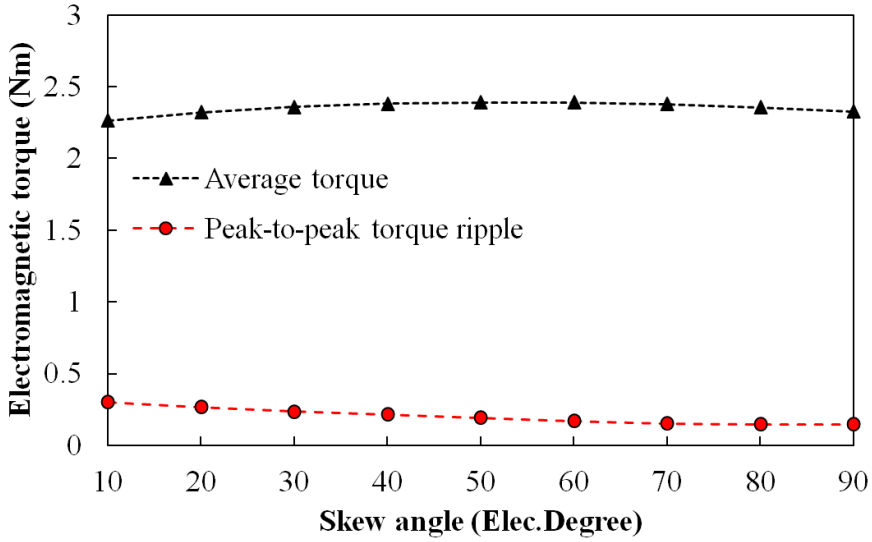

(a) skew angle optimization

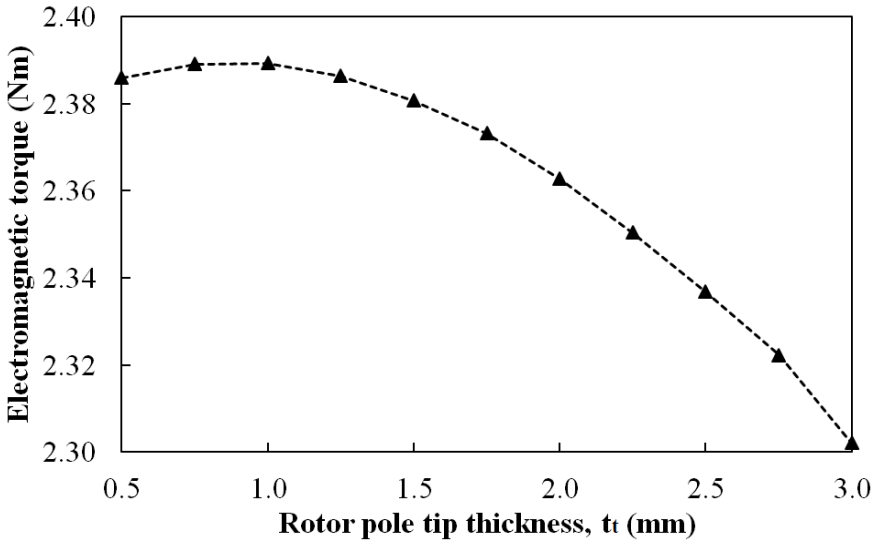

(b) Rotor pole tip thickness optimization

Fig.II.6. Variation of electromagnetic torque with skew angle and rotor pole tip thickness for 10-pole claw-pole stator SPM brushless machine.

B.4 Experimental Validation

A prototype three phase 10-pole claw-pole stator SPM brushless machine is built by employing the foregoing optimized design parameters. Fig.II.7(a) shows one set of SMC claw-pole stator which is made by compacting SMC material in a mold. A final assembled three phase claw-pole stator machine is shown in Fig.II.7(b) with the mechanical drawing to illustrate its inside structure, in Fig.II.7(c).

Fig.II.8 compares the analytically predicted and measured phase back-EMF and electromagnetic torque, where good agreement is obtained.

(a) One set of SMC claw-pole stator

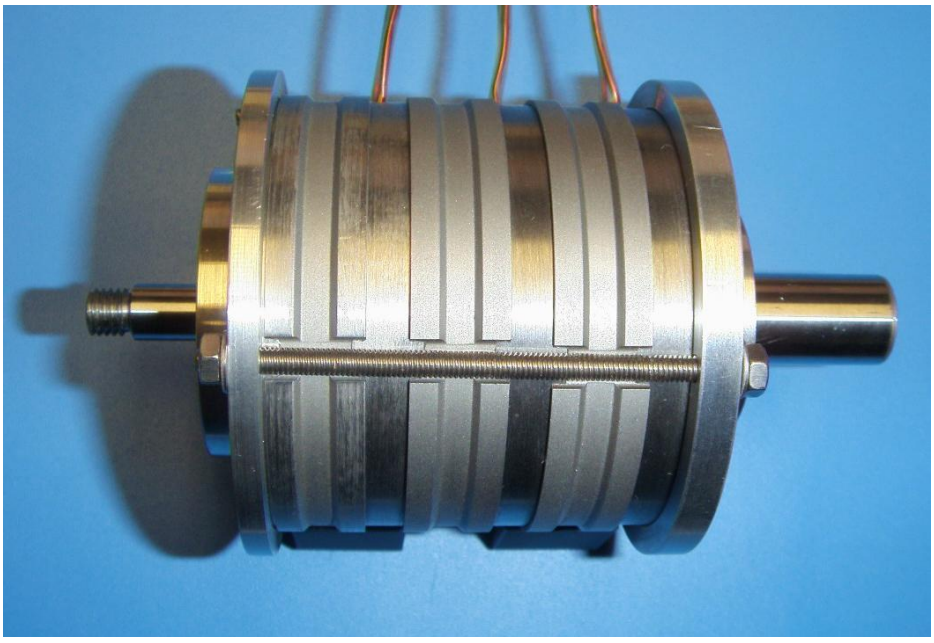

(b) Three-phase 10-pole claw-pole stator SPM brushless machine

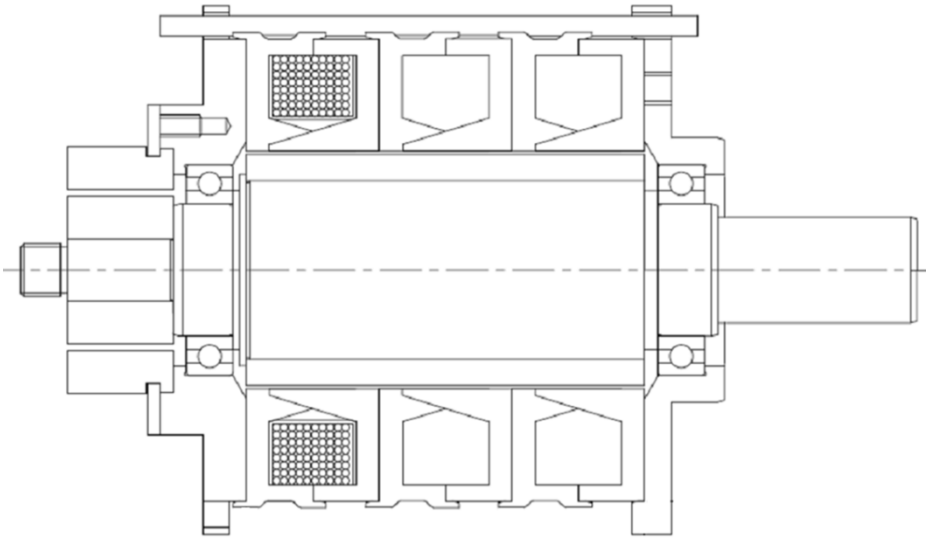

(c) Mechanical drawing of prototype machine

Fig.II.7. Prototype 10-pole claw-pole stator SPM brushless machine

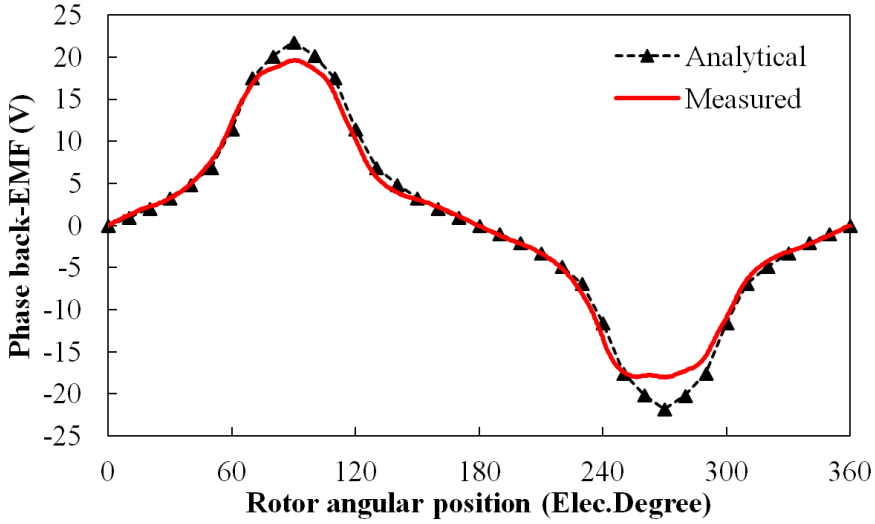

(a) Phase back-EMF, 3300 rpm

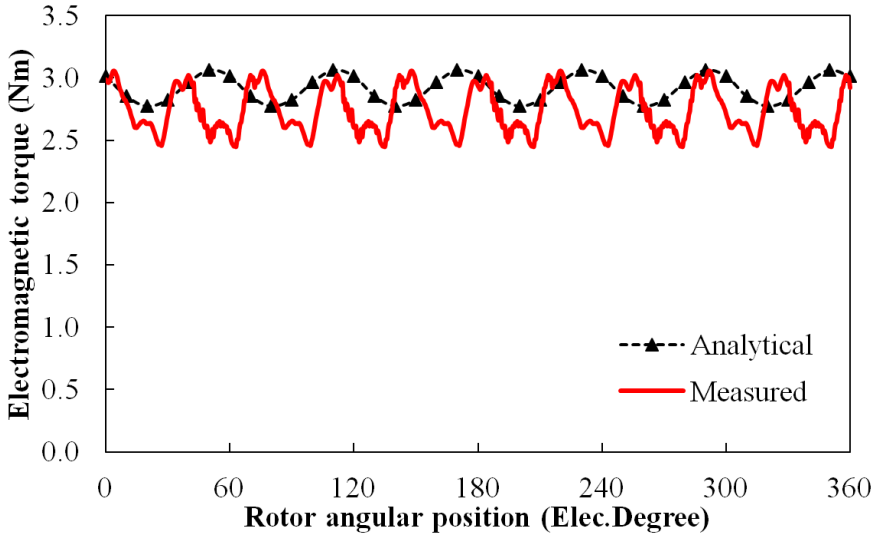

(b) Electromagnetic torque

Fig.II.8. Comparison of analytically predicted and measured phase back-EMF and electromagnetic torque waveforms.

B.5 Summary

In this appendix, a three phase claw-pole stator surface-mounted PM brushless machine with soft magnetic composite stator core is described. Due to the inherent 3D structure, a lumped-parameter magnetic circuit model is developed and validated by 3D FEA to design and optimize a three phase 10-pole claw-pole stator machine. A prototype machine is also built based on overall optimized design parameters, while good agreement is achieved between the measured and analytically predicted results.

B.6 Reference

[II8] H. Roisse, M. Hecquet, and P. Brochet, "Simulations of synchronous machines using a electric-magnetic coupled network model," *IEEE Trans. Magn*., vol. 34, no. 5, pp. 3656-3659, September 1998.

[II9] S. Kuppers, and G. Henneberger, "Numerical procedures for the calculation and design of automotive alternators," *IEEE Trans. Magn*., vol. 33, no. 2, pp. 2022-2025, March 1997.

[II10] L. Li, and Y. Xiang, "Finite element computation of 3-D nonlinear magnetic field in claw-pole electric machine using two scalar potentials, hybrid elements & automatic mesh generation," *IEEE Trans. Magns*, vol. 26, no. 2, pp. 371-374, March 1990.

[II11] A. Koenig, J. Williams, and S. Pekarek, "Evaluation of alternative evolutionary programming techniques for optimization of an automotive alternator," *IEEE Trans.Veh.Tech.*, vol.55, no.3, pp.933-942, May 2006.

[II12] F. Zhang, H. Bai, H. Gruenberger, and E. Nolle, "Comparative study on claw pole electrical machine with different structure," *2nd IEEE Conf. Industrical Electronic and Applications, ICIEA*, Harbin, China, May 23-27, 2007, pp. 636-640.

[II13] B. Fahimi, and T. Sebastian, "Guest editorial special section on automotive electromechanical converters," *IEEE Trans. Veh. Tech.*, vol. 56, no. 4, pp. 1470-1476, July 2007.

[II14] N. Bianchi, and M. Dai Pre, "Use of the star of slots in designing fractional-slot single-layer synchronous motors," *Proc. IEE-Electr. Power Appl*., vol. 153, no. 3, pp. 459-466, May 2006.

[II15] Y. Guo, J. G. Zhu, P. Watterson, and W. Wu, "Comparative study of 3-D flux electrical machines with soft magnetic composite cores," *IEEE Trans. Ind Appl.*, vol. 39, no. 6, pp. 1696-1703, Nov./Dec. 2003.

[II16] Y. G. Guo, J. G. Zhu, and H. Y. Lu, "Accurate determination of parameters of claw-pole motor with SMC stator core by finite-element magnetic-field analysis," *IEE Proc. EPA*, vol. 153, no. 4, pp. 185-195, July 2006.

[II17] Y. Huang, J. G. Zhu, Y.G. Gou, Z. Lin, and Q. Hu, "Design and analysis of a high-speed claw pole motor with soft magnetic composite core," *IEEE Trans. Magn.*, vol. 43, no. 6, pp. 2492-2494, June 2007.

[II18] Y. Guo, J. Zhu, and D. G. Dorrell, "Design and analysis of a claw pole permanent magnet motor with molded soft magnetic composite core," *IEEE Tran. Magn*., vol. 45, no.10, pp. 4582-4585, October 2009.

[II19] C. Henaux, B. Nogarede, and D. Harribey, "A new concept of modular permanent magnet and soft magnetic compound motor dedicated to widespread application," *IEEE Trans. Magn*., vol. 48, no. 6, pp. 2035-2043.

[II20] J. T. Chen, and Z. Q. Zhu, "Influence of the rotor pole number on optimal parameters in flux-switching PM brushless AC machines by the lumped-parameter magnetic circuit model," *IEEE Trans. Ind Appl*., vol. 46, no. 4, pp. 1381-1388, July/August 2010.

APPENDIX III – SUB-DOMAIN ANALYTICAL MODEL

The developed 2-D field model with sub-domain method is exactly based on [III1].

Some assumptions are made in order to simplify the problem as follows: (1) Ideal spoke-like slot shapes as shown in Fig.III.1; (2) Infinite permeability of stator/rotor iron; (3) Neglected end effect; (4) Non-conductive magnet material; (5) Radial or parallel magnetization; (6) Linear demagnetization characteristics of magnet.

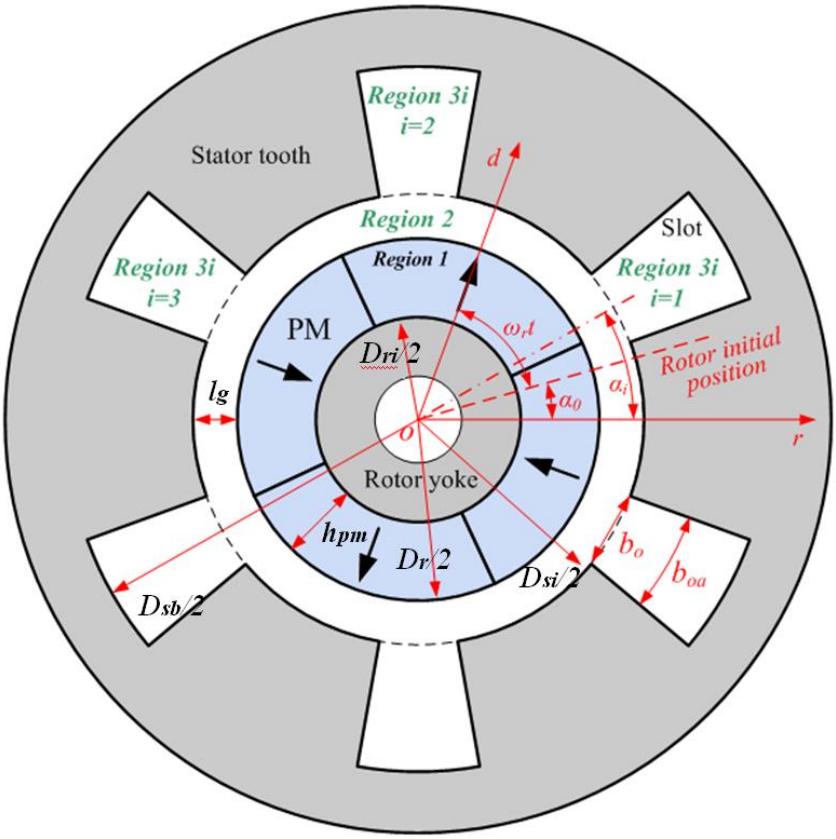

Fig.III.1. Symbols and three types of sub-regions.

As can be seen in Fig.III.1, the whole domain of the field problem can be divided into three types of sub-domains, viz. magnet (Region 1), air-gap (Region 2), and stator slots (Region 3*i*, *i*=1,2, …,N_s.). The general expressions of the scalar potential distributions in polar coordinates can be expressed by [7, 72]:

$$\begin{aligned}\phi_1(k\neq 1)=&\sum_k\left[A_1(k)r^k+B_1(k)r^{-k}+\frac{M_{ck}r}{\mu_r\left(1-k^2\right)}\right]\cos(k\alpha)\\&+\sum_n\left[C_1(k)r^k+D_1(k)r^{-k}+\frac{M_{sk}r}{\mu_r\left(1-k^2\right)}\right]\sin(k\alpha)\end{aligned}\tag{III.1}$$

and

$$\begin{aligned}\phi_1(k=1) &= \left[A_1(1)r + B_1(1)r^{-1} + \frac{1}{2}\frac{M_{c1} r \ln r}{\mu_r}\right]\cos(\alpha) \\ &+ \left[C_1(1)r + D_1(1)r^{-1} + \frac{1}{2}\frac{M_{s1} r \ln r}{\mu_r}\right]\sin(\alpha)\end{aligned} \tag{III.2}$$

for Region 1, and

$$\begin{aligned}\phi_2 &= \sum_k \left[A_2(k)r^k + B_2(k)r^{-k}\right]\cos(k\alpha) \\ &+ \sum_k \left[C_2(k)r^k + D_2(k)r^{-k}\right]\sin(k\alpha)\end{aligned} \tag{III.3}$$

for Region 2, and [72]

$$\phi_{3i} = \sum_m C_{3i}(m)\left[\left(\frac{r}{R_{sb}}\right)^{F_m} - \left(\frac{r}{R_{sb}}\right)^{-F_m}\right]\sin\left[F_m\left(\alpha + \frac{b_{oa}}{2} - \alpha_i\right)\right] \tag{III.4}$$

for i^{th} slot, Region 3i, where k, m are the harmonic orders, R_{sb} is the radius of the slot bottom, $A_1(k)$-$D_1(k)$, $A_2(k)$-$D_2(k)$, and $C_{3i}(m)$ are coefficients to be determined by the boundary conditions, α_i is the position of the i^{th} slot, b_{oa} is the slot opening angle corresponding to the slot opening width b_o, and

$$F_m = \frac{m\pi}{b_{oa}} \tag{III.5}$$

$$b_{oa} = \frac{b_o}{R_s} \tag{III.6}$$

and the magnetization of magnets can be expressed by [III2][III3]:

$$\mathbf{M} = M_r\mathbf{r} + M_\theta\boldsymbol{\alpha} \tag{III.7}$$

$$\begin{aligned}M_r &= \sum_{k=1,3,5,\cdots} M_{rk}\cos\left(k\alpha - k\omega_r t - k\alpha_0\right) \\ &= \sum_{k=1,3,5,\cdots} M_{rck}\cos k\alpha + M_{rsk}\sin k\alpha\end{aligned} \tag{III.8}$$

$$\begin{aligned}M_\alpha &= \sum_{k=1,3,5,\cdots} M_{\alpha k}\sin\left(k\alpha - k\omega_r t - k\alpha_0\right) \\ &= \sum_{k=1,3,5,\cdots} M_{\alpha ck}\cos k\alpha + M_{\alpha sk}\sin k\alpha\end{aligned} \tag{III.9}$$

$$M_{rck} = M_{rk}\cos\left(k\omega_r t + k\alpha_0\right) \tag{III.10}$$

$$M_{rsk} = M_{rk}\sin\left(k\omega_r t + k\alpha_0\right) \tag{III.11}$$

$$M_{\alpha ck} = -M_{\alpha k}\sin\left(k\omega_r t + k\alpha_0\right) \tag{III.12}$$

$$M_{\alpha sk} = M_{\alpha k}\cos\left(k\omega_r t + k\alpha_0\right) \tag{III.13}$$

$$M_k = M_{rk} + kM_{\alpha k} \tag{III.14}$$

$$M_{ck} = M_k\cos\left(k\omega_r t + k\alpha_0\right) \tag{III.15}$$

$$M_{sk} = M_k\sin\left(k\omega_r t + k\alpha_0\right) \tag{III.16}$$

For radial magnetization:

$$M_{rk} = \frac{4pB_r}{k\pi\mu_0}\sin\frac{k\pi\alpha_p}{2p} \quad k/p = 1,\ 3,\ 5,\cdots \tag{III.17}$$

$$M_{\alpha k} = 0 \quad k/p = 1,\ 3,\ 5,\cdots \tag{III.18}$$

For parallel magnetization:

$$M_{rk} = \frac{B_r}{\mu_0}\alpha_p\left(A_{1k} + A_{2k}\right) \quad k/p = 1,\ 3,\ 5,\cdots \tag{III.19}$$

$$M_{\alpha k} = \frac{B_r}{\mu_0}\alpha_p\left(A_{1k} - A_{2k}\right) \quad k/p = 1,\ 3,\ 5,\cdots \tag{III.20}$$

Where

$$A_{1k} = \frac{\sin\left[\left(k+1\right)\alpha_p\frac{\pi}{2p}\right]}{\left(k+1\right)\alpha_p\frac{\pi}{2p}} \tag{III.21}$$

$$A_{2k} = \frac{\sin\left[\left(k-1\right)\alpha_p\frac{\pi}{2p}\right]}{\left(k-1\right)\alpha_p\frac{\pi}{2p}} \tag{III.22}$$

where B_r is residual flux density of magnet and α_p is pole-arc to pole-pitch ratio, ω_r is the rotor rotational speed, α_0 is the rotor initial position, p is the number of pole pairs. It should be noted that k=1 is a singular point of A_{2k} in (III.22). Although the expression of A_{2k} when k=1 is not given, the limit of A_{2k} when $k\rightarrow1$, which is the value of $A_{2k}(k=1)$, can be easily derived. This method will be used for all singular cases in the following discussion.

According to (III.3), the scalar potential on the surface of the stator bore is:

$$\begin{aligned}\phi_2\big|_{r=R_s} = &\sum_k\left[A_2(k)R_s^{\,k} + B_2(k)R_s^{\,-k}\right]\cos(k\alpha)\\ &+\sum_k\left[C_2(k)R_s^{\,k} + D_2(k)R_s^{\,-k}\right]\sin(k\alpha)\end{aligned} \tag{III.23}$$

Moreover, according to (III.4), the scalar potential on the surface of the stator bore can also be expressed as:

$$\phi_s = \phi_{3i}\big|_{r=R_s} = \sum_m C_{3i}(m)\chi_m\sin\left[F_m\left(\alpha + \frac{b_{oa}}{2} - \alpha_i\right)\right] \tag{III.24}$$

for α_i-$b_{oa}/2\le\alpha\le\alpha_i$+$b_{oa}/2$, and for others:

$$\phi_s = 0 \tag{III.25}$$

where

$$\chi_m = \left(\frac{R_s}{R_{sb}}\right)^{F_m} - \left(\frac{R_s}{R_{sb}}\right)^{-F_m} \tag{III.26}$$

Thus, according to continuity condition:

$$\phi_2\big|_{r=R_s} = \phi_s \tag{III.27}$$

In order to solve (III.27), ϕ_s can be expanded into Fourier series as:

$$\phi_s = \sum_k \left[A_{stator}(k)\cos(k\alpha) + B_{stator}(k)\sin(k\alpha) \right] \tag{III.28}$$

where

$$A_{stator}(k) = \sum_i \sum_m C_{3i}(m)\chi_m \eta_{si}(m,k) \tag{III.29}$$

$$B_{stator}(k) = \sum_i \sum_m C_{3i}(m)\chi_m \xi_{si}(m,k) \tag{III.30}$$

where

$$\eta_{si} = \eta_s \cos k\alpha_i - \xi_s \sin k\alpha_i \tag{III.31}$$

$$\xi_{si} = \eta_s \sin k\alpha_i + \xi_s \cos k\alpha_i \tag{III.32}$$

where

$$\eta_s(m,k) = \begin{cases} \dfrac{2mb_{oa}\cos(kb_{oa}/2)\sin^2(m\pi/2)}{m^2\pi^2 - k^2 b_{oa}^{\ 2}} & m\pi \neq kb_{oa} \\ \dfrac{b_{oa}}{2\pi}\sin\left(\dfrac{m\pi}{2}\right) & m\pi = kb_{oa} \end{cases} \tag{III.33}$$

$$\xi_s(m,k) = \begin{cases} -\dfrac{2mb_{oa}\sin(kb_{oa}/2)\cos^2(m\pi/2)}{m^2\pi^2 - k^2 b_{oa}^{\ 2}} & m\pi \neq kb_{oa} \\ \dfrac{b_{oa}}{2\pi}\cos\left(\dfrac{m\pi}{2}\right) & m\pi = kb_{oa} \end{cases} \tag{III.34}$$

Then, according to (III.23)-(III.30), the following equation set can be obtained:

$$\begin{cases} A_2 R_s^{\ k} + B_2 R_s^{\ -k} = A_{stator} = \sum_i \sum_m C_{3i}(m)\chi_m \eta_{si}(m,k) \\ C_2 R_s^{\ k} + D_2 R_s^{\ -k} = B_{stator} = \sum_i \sum_m C_{3i}(m)\chi_m \xi_{si}(m,k) \end{cases} \tag{III.35}$$

It should be noted that the integration constants of the governing function in the airgap, A_2, B_2, C_2, and D_2, are related with the scalar potential distributions of all slots by the sum operation as seen from (III.35), which shows the essence of the exact sub-domain model.

By employing the boundary conditions of infinite permeability of rotor yoke and of continuous scalar potential and radial flux density at $r=R_m$, the harmonic coefficient of ϕ_2 can be derived:

$$A_2 = \frac{K_{Brc} + K_{Ba\alpha s}}{-\mu_0 k}\frac{R_m^{\ k+1}}{R_s^{\ 2k}} + B_{5k}A_{5k}\sum_i \sum_m C_{3i}(m)\chi_m \eta_{si}(m,k) \tag{III.36}$$

$$B_2 = \frac{K_{Brc} + K_{Ba\alpha s}}{\mu_0 k} R_m^{\ k+1} - B_{6k}A_{6k}\sum_i \sum_m C_{3i}(m)\chi_m \eta_{si}(m,k) \tag{III.37}$$

$$C_2 = \frac{K_{Brs} - K_{B\alpha c}}{-\mu_0 k} \frac{R_m^{\,k+1}}{R_s^{\,2k}} + B_{5k} A_{5k} \sum_i \sum_m C_{3i}(m) \chi_m \xi_{si}(m,k) \tag{III.38}$$

$$D_2 = \frac{K_{Brs} - K_{B\alpha c}}{\mu_0 k} R_m^{\,k+1} - B_{6k} A_{6k} \sum_i \sum_m C_{3i}(m) \chi_m \xi_{si}(m,k) \tag{III.39}$$

where

$$K_{Brc} = A_{4k} \gamma(k) M_{rck} \tag{III.40}$$

$$K_{Brs} = A_{4k} \gamma(k) M_{rsk} \tag{III.41}$$

$$K_{B\alpha s} = A_{4k} \zeta(k) M_{\alpha sk} \tag{III.42}$$

$$K_{B\alpha c} = A_{4k} \zeta(k) M_{\alpha ck} \tag{III.43}$$

and for the internal rotor machine:

$$A_{4k} = -\frac{1}{2} \mu_0 k \tag{III.44}$$

$$\gamma = \frac{2}{k^2 - 1} \frac{1}{\rho} \left[(1-k) - 2\left(\frac{R_r}{R_m}\right)^{k+1} + (k+1)\left(\frac{R_r}{R_m}\right)^{2k} \right] \tag{III.45}$$

$$\zeta = \frac{2}{k^2 - 1} \frac{1}{\rho} \left[(k-1) - 2k\left(\frac{R_r}{R_m}\right)^{k+1} + (k+1)\left(\frac{R_r}{R_m}\right)^{2k} \right] \tag{III.46}$$

$$\rho = (\mu_r + 1)\left[1 - \left(\frac{R_r}{R_s}\right)^{2k}\right] - (\mu_r - 1)\left[\left(\frac{R_m}{R_s}\right)^{2k} - \left(\frac{R_r}{R_m}\right)^{2k}\right] \tag{III.47}$$

$$B_{5k} = R_s^{\,-k} \tag{III.48}$$

$$B_{6k} = R_s^{\,-k} R_m^{\,2k} \tag{III.49}$$

$$A_{5k} = \frac{1}{\rho} \left[(\mu_r + 1) + (\mu_r - 1)\left(\frac{R_r}{R_m}\right)^{2k} \right] \tag{III.50}$$

$$A_{6k} = \frac{1}{\rho} \left[(\mu_r - 1) + (\mu_r + 1)\left(\frac{R_r}{R_m}\right)^{2k} \right] \tag{III.51}$$

and for the external rotor machine:

$$A_{4k} = -\frac{1}{2} \mu_0 k \left(\frac{R_s}{R_m}\right)^{2k} \tag{III.52}$$

$$\gamma = \frac{2}{k^2 - 1} \frac{1}{\rho} \left[(1-k)\left(\frac{R_m}{R_r}\right)^{2k} - 2\left(\frac{R_m}{R_r}\right)^{k-1} + (k+1) \right] \tag{III.53}$$

$$\zeta = \frac{2}{k^2 - 1} \frac{1}{\rho} \left[(k-1)\left(\frac{R_m}{R_r}\right)^{2k} - 2k\left(\frac{R_m}{R_r}\right)^{k-1} + (k+1) \right] \tag{III.54}$$

$$\rho = (\mu_r + 1)\left[\left(\frac{R_s}{R_r}\right)^{2k} - 1\right] - (\mu_r - 1)\left[\left(\frac{R_m}{R_r}\right)^{2k} - \left(\frac{R_s}{R_m}\right)^{2k}\right] \tag{III.55}$$

$$B_{5k} = R_s^{\,k} R_m^{\,-2k} \tag{III.56}$$

$$B_{6k} = R_s^{\,k} \tag{III.57}$$

$$A_{5k} = \frac{1}{\rho}\left[(\mu_r + 1)\left(\frac{R_m}{R_r}\right)^{2k} + (\mu_r - 1)\right] \tag{III.58}$$

$$A_{6k} = \frac{1}{\rho}\left[(\mu_r - 1)\left(\frac{R_m}{R_r}\right)^{2k} + (\mu_r + 1)\right] \tag{III.59}$$

Thus, the problem becomes how to calculate the harmonic coefficient $C_{3i}(m)$ of ϕ_{3i}. For this problem, another boundary condition can be applied - that the radial component flux density at stator slot opening should be continuous.

According to (III.4), the radial component flux density at the i^{th} slot opening is expressed by:

$$B_{3ir}\Big|_{r=R_s} = -\mu_0 \sum_m \delta_m C_{3i}(m) \sin\left[F_m\left(\alpha + \frac{b_{oa}}{2} - \alpha_i\right)\right] \tag{III.60}$$

where

$$\delta_m = \frac{F_m}{R_{sb}}\left[\left(\frac{R_s}{R_{sb}}\right)^{F_m - 1} + \left(\frac{R_s}{R_{sb}}\right)^{-F_m - 1}\right] \tag{III.61}$$

According to (III.3), the radial component flux density at the stator bore is also expressed by:

$$\begin{aligned} B_{2r}\Big|_{r=R_s} = &-\mu_0 \sum_k k\left[A_2(k) R_s^{\,k-1} - B_2(k) R_s^{\,-k-1}\right]\cos(k\alpha) \\ &-\mu_0 \sum_k k\left[C_2(k) R_s^{\,k-1} - D_2(k) R_s^{\,-k-1}\right]\sin(k\alpha) \end{aligned} \tag{III.62}$$

Thus,

$$B_{3ir}\Big|_{r=R_s} = B_{2r}\Big|_{r=R_s} \qquad \alpha_i - \frac{b_{oa}}{2} \le \alpha \le \alpha_i + \frac{b_{oa}}{2} \tag{III.63}$$

In order to solve (III.63), the right term, $B_{2r}|_{r=Rs}$ is expanded into Fourier series over the i^{th} slot opening:

$$\begin{aligned} B_{2r}\Big|_{r=R_s} = &-\mu_0 \sum_m C_{si}(m) \sin\left[F_m\left(\alpha + \frac{b_{oa}}{2} - \alpha_i\right)\right] \\ &\alpha_i - \frac{b_{oa}}{2} \le \alpha \le \alpha_i + \frac{b_{oa}}{2} \end{aligned} \tag{III.64}$$

where

$$\begin{aligned} C_{si}(m) = \sum_k k\left[A_2(k)R_s^{k-1} - B_2(k)R_s^{-k-1}\right]\sigma_{si}(m,k) \\ +k\left[C_2(k)R_s^{k-1} - D_2(k)R_s^{-k-1}\right]\tau_{si}(m,k) \end{aligned} \tag{III.65}$$

where

$$\sigma_{si}(m,k) = \frac{2\pi}{b_{oa}}\eta_{si}(m,k) \tag{III.66}$$

$$\tau_{si}(m,k) = \frac{2\pi}{b_{oa}}\xi_{si}(m,k) \tag{III.67}$$

Thus, by solving (III.63), the following relationship can be obtained:

$$\begin{aligned} \delta_m C_{3i}(m) = \sum_k k\left[A_2(k)R_s^{k-1} - B_2(k)R_s^{-k-1}\right]\sigma_{si}(m,k) \\ +k\left[C_2(k)R_s^{k-1} - D_2(k)R_s^{-k-1}\right]\tau_{si}(m,k) \end{aligned} \tag{III.68}$$

According to (III.36)-(III.39), the following equation set can be derived:

$$\begin{cases} A_2R_s^{k-1} - B_2R_s^{-k-1} = G_1 - \lambda\sum_i\sum_m C_{3i}(m)\chi_m\eta_{si}(m,k) \\ C_2R_s^{k-1} - D_2R_s^{-k-1} = G_2 - \lambda\sum_i\sum_m C_{3i}(m)\chi_m\xi_{si}(m,k) \end{cases} \tag{III.69}$$

where for the internal rotor machine:

$$G_1 = \left(\frac{R_m}{R_s}\right)^{k+1}\left[\gamma(k)M_{rck} + \zeta(k)M_{\alpha sk}\right] \tag{III.70}$$

$$G_2 = \left(\frac{R_m}{R_s}\right)^{k+1}\left[\gamma(k)M_{rsk} - \zeta(k)M_{\alpha ck}\right] \tag{III.71}$$

$$\lambda = -\frac{1}{R_s}\left[A_{5k} + \left(\frac{R_m}{R_s}\right)^{2k}A_{6k}\right] \tag{III.72}$$

and for the external rotor machine:

$$G_1 = \left(\frac{R_s}{R_m}\right)^{k-1}\left[\gamma(k)M_{rck} + \zeta(k)M_{\alpha sk}\right] \tag{III.73}$$

$$G_2 = \left(\frac{R_s}{R_m}\right)^{k-1}\left[\gamma(k)M_{rsk} - \zeta(k)M_{\alpha ck}\right] \tag{III.74}$$

$$\lambda = -\frac{1}{R_s}\left[\left(\frac{R_s}{R_m}\right)^{2k}A_{5k} + A_{6k}\right] \tag{III.75}$$

From (III.68) and (III.69), the harmonic coefficient $C_{3i}(m)$ can be obtained by solving:

$$\begin{aligned} \delta_m C_{3i}(m) = \sum_k k\left[G_1(k)\sigma_{si}(m,k) + G_2(k)\tau_{si}(m,k)\right] \\ -\sum_k k\lambda(k)\sigma_{si}(m,k)\sum_l\sum_j C_{3l}(j)\chi_j\eta_{sl}(j,k) \\ -\sum_k k\lambda(k)\tau_{si}(m,k)\sum_l\sum_j C_{3l}(j)\chi_j\xi_{sl}(j,k) \end{aligned} \tag{III.76}$$

where j=1,2,3…,M, l=1,2,3..., N_s, M is the highest harmonic order of scalar potential distribution along slot openings in the computation. (III.76) can be rewritten into matrix format as:

$$\mathbf{\delta C_{3i}} = \mathbf{Y_{si}} - \mathbf{P_{si}} \sum_{l=1}^{N_s} \mathbf{\eta_{sl}}^{\mathrm{T}} \mathbf{\chi C_{3l}} - \mathbf{Q_{si}} \sum_{l=1}^{N_s} \mathbf{\xi_{sl}}^{\mathrm{T}} \mathbf{\chi C_{3l}} \tag{III.77}$$

Where

$$\mathbf{\delta} = diag\left(\delta_1, \delta_2, \cdots, \delta_M\right) \tag{III.78}$$

$$\mathbf{C_{3i}} = \left[C_{3i}(1) \quad C_{3i}(2) \quad \cdots \quad C_{3i}(M)\right]^T \tag{III.79}$$

$$\mathbf{\eta_{si}} = \left(\eta_{si}(m,n)\right)_{M\times N} \tag{III.80}$$

$$\mathbf{\xi_{si}} = \left(\xi_{si}(m,n)\right)_{M\times N} \tag{III.81}$$

$$\mathbf{Y_{si}} = \mathbf{\sigma_{si} K G_1} + \mathbf{\tau_{si} K G_2} \tag{III.82}$$

$$\mathbf{\sigma_{si}} = \frac{2\pi}{b_{oa}} \mathbf{\eta_{si}} \tag{III.83}$$

$$\mathbf{\tau_{si}} = \frac{2\pi}{b_{oa}} \mathbf{\xi_{si}} \tag{III.84}$$

$$\mathbf{K} = diag\left(1, 2, \cdots, K\right) \tag{III.85}$$

$$\mathbf{G}_1 = \left[G_1(1), G_1(2), \cdots, G_1(N)\right]^T \tag{III.86}$$

$$\mathbf{G}_2 = \left[G_2(1), G_2(2), \cdots, G_2(N)\right]^T \tag{III.87}$$

$$\mathbf{P_{si}} = \mathbf{\sigma_{si} K \lambda} \tag{III.88}$$

$$\mathbf{Q_{si}} = \mathbf{\tau_{si} K \lambda} \tag{III.89}$$

$$\mathbf{\lambda} = diag\left(\lambda(1), \lambda(2), \cdots, \lambda(N)\right) \tag{III.90}$$

$$\mathbf{\chi} = diag\left(\chi_1, \chi_2, \cdots, \chi_M\right) \tag{III.91}$$

Again, (III.77) shows that the scalar potential distributions of all slots are coupled together. They need to be solved simultaneously to completely account for the influence between slots. However, it will be shown later that if the influence between slots is simplified, (III.77) will also be simplified to account for the slot individually and the model becomes essentially the same as the model in the previous sub-domain model based on one slot/pole.

Equation (III.77) can be rewritten as:

$$\mathbf{\delta_t C_{3t}} = \mathbf{Y_{st}} - \mathbf{P_{st}} \mathbf{\eta_{st}}^{\mathrm{T}} \mathbf{\chi_t C_{3t}} - \mathbf{Q_{st}} \mathbf{\xi_{st}}^{\mathrm{T}} \mathbf{\chi_t C_{3t}} \tag{III.92}$$

where

$$\mathbf{\delta_t} = diag\left(\mathbf{\delta}, \mathbf{\delta}, \cdots, \mathbf{\delta}\right)_{N_s\times N_s} \tag{III.93}$$

$$\mathbf{C}_{3t} = \begin{bmatrix} \mathbf{C}_{31}^{\mathrm{T}} & \mathbf{C}_{32}^{\mathrm{T}} & \cdots & \mathbf{C}_{3N_s}^{\mathrm{T}} \end{bmatrix}^{\mathrm{T}} \tag{III.94}$$

$$\mathbf{Y}_{st} = \begin{bmatrix} \mathbf{Y}_{s1}^{\mathrm{T}} & \mathbf{Y}_{s2}^{\mathrm{T}} & \cdots & \mathbf{Y}_{sN_s}^{\mathrm{T}} \end{bmatrix}^{\mathrm{T}} \tag{III.95}$$

$$\boldsymbol{\sigma}_{st} = \begin{bmatrix} \boldsymbol{\sigma}_{s1}^{\mathrm{T}} & \boldsymbol{\sigma}_{s2}^{\mathrm{T}} & \cdots & \boldsymbol{\sigma}_{sN_s}^{\mathrm{T}} \end{bmatrix}^{\mathrm{T}} \tag{III.96}$$

$$\boldsymbol{\tau}_{st} = \begin{bmatrix} \boldsymbol{\tau}_{s1}^{\mathrm{T}} & \boldsymbol{\tau}_{s2}^{\mathrm{T}} & \cdots & \boldsymbol{\tau}_{sN_s}^{\mathrm{T}} \end{bmatrix}^{\mathrm{T}} \tag{III.97}$$

$$\boldsymbol{\eta}_{st} = \frac{b_{oa}}{2\pi}\boldsymbol{\sigma}_{st} \tag{III.98}$$

$$\boldsymbol{\xi}_{st} = \frac{b_{oa}}{2\pi}\boldsymbol{\tau}_{st} \tag{III.99}$$

$$\mathbf{P}_{st} = \boldsymbol{\sigma}_{st}\mathbf{K}\boldsymbol{\lambda} = \begin{bmatrix} \mathbf{P}_{s1}^{\mathrm{T}} & \mathbf{P}_{s2}^{\mathrm{T}} & \cdots & \mathbf{P}_{sN_s}^{\mathrm{T}} \end{bmatrix}^{\mathrm{T}} \tag{III.100}$$

$$\mathbf{Q}_{st} = \boldsymbol{\tau}_{st}\mathbf{K}\boldsymbol{\lambda} = \begin{bmatrix} \mathbf{Q}_{s1}^{\mathrm{T}} & \mathbf{Q}_{s2}^{\mathrm{T}} & \cdots & \mathbf{Q}_{sN_s}^{\mathrm{T}} \end{bmatrix}^{\mathrm{T}} \tag{III.101}$$

$$\boldsymbol{\chi}_t = diag\left(\chi, \chi, \cdots, \chi\right)_{N_s \times N_s} \tag{III.102}$$

Thus, the coefficient $C_{3t}(m)$ can be obtained as

$$\mathbf{C}_{3t} = \left(\boldsymbol{\delta}_t + \mathbf{P}_{st}\boldsymbol{\eta}_{st}^{\mathrm{T}}\boldsymbol{\chi}_t + \mathbf{Q}_{st}\boldsymbol{\xi}_{st}^{\mathrm{T}}\boldsymbol{\chi}_t\right)^{-1}\mathbf{Y}_{st} \tag{III.103}$$

However, $\mathbf{C}_{3t}$ is difficult to calculate numerically because it can cause overflow. In order to ease numerical computation, the following variable is introduced:

$$\mathbf{C}_{et} = \boldsymbol{\chi}_t\mathbf{C}_{3t} \tag{III.104}$$

viz.

$$\mathbf{C}_{et} = \begin{bmatrix} \mathbf{C}_{e1}^{\mathrm{T}} & \mathbf{C}_{e2}^{\mathrm{T}} & \cdots & \mathbf{C}_{eN_s}^{\mathrm{T}} \end{bmatrix}^{\mathrm{T}} \tag{III.105}$$

where

$$C_{ei}(m) = C_{3i}(m)\chi_m \tag{III.106}$$

Thus, the left term of (III.77) can be expressed as:

$$\boldsymbol{\delta}_t\mathbf{C}_{3t} = \boldsymbol{\delta}_t\boldsymbol{\chi}_t^{-1}\mathbf{C}_{et} = \mathbf{W}_{et}\mathbf{C}_{et} \tag{III.107}$$

where

$$\mathbf{W}_{et} = \boldsymbol{\delta}_t\boldsymbol{\chi}_t^{-1} \tag{III.108}$$

where

$$\mathbf{W}_{et} = diag\begin{pmatrix} \mathbf{W}_e & \mathbf{W}_e & \cdots & \mathbf{W}_e \end{pmatrix}_{N_s \times N_s} \tag{III.109}$$

$$\mathbf{W}_e = diag\begin{pmatrix} W_e(1) & W_e(2) & \cdots & W_e(M) \end{pmatrix}_{M \times M} \tag{III.110}$$

$$W_e(m)=\frac{\delta_m}{\chi_m}=\begin{cases}\dfrac{F_m}{R_s}\dfrac{\left(\dfrac{R_s}{R_{sb}}\right)^{2F_m}+1}{\left(\dfrac{R_s}{R_{sb}}\right)^{2F_m}-1} & \text{Internal rotor}\\ \dfrac{F_m}{R_s}\dfrac{1+\left(\dfrac{R_{sb}}{R_s}\right)^{2F_m}}{1-\left(\dfrac{R_{sb}}{R_s}\right)^{2F_m}} & \text{External rotor}\end{cases} \tag{III.111}$$

Thus, (III.77), (III.92), and (III.103) can be rewritten as:

$$\mathbf{W_e C_{ei}} = \mathbf{Y_{si}} - \mathbf{P_{si}}\sum_{l=1}^{N_s}\boldsymbol{\eta}_{\mathbf{sl}}{}^{\mathbf{T}}\mathbf{C_{el}} - \mathbf{Q_{si}}\sum_{l=1}^{N_s}\boldsymbol{\xi}_{\mathbf{sl}}{}^{\mathbf{T}}\mathbf{C_{el}} \tag{III.112}$$

$$\mathbf{W_{et} C_{et}} = \mathbf{Y_{st}} - \mathbf{P_{st}}\boldsymbol{\eta}_{\mathbf{st}}{}^{\mathbf{T}}\mathbf{C_{et}} - \mathbf{Q_{st}}\boldsymbol{\xi}_{\mathbf{st}}{}^{\mathbf{T}}\mathbf{C_{et}} \tag{III.113}$$

$$\mathbf{C_{et}} = \left(\mathbf{W_{et}} + \mathbf{P_{st}}\boldsymbol{\eta}_{\mathbf{st}}{}^{T} + \mathbf{Q_{st}}\boldsymbol{\xi}_{\mathbf{st}}{}^{T}\right)^{-1}\mathbf{Y_{st}} \tag{III.114}$$

According to (III.114), it can be seen that in the exact sub-domain model, the inverse of a matrix with $N_s{}^2M^2$ elements needs to be solved, while a matrix with K^2 elements needs to be inversed in the model in [III4].

The harmonics of scalar potential distribution along the slot openings, (III.29) and (III.30), can be rewritten as:

$$A_{stator}(k)=\sum_i\sum_m C_{ei}(m)\eta_{si}(m,k) \tag{III.115}$$

$$B_{stator}(k)=\sum_i\sum_m C_{ei}(m)\xi_{si}(m,k) \tag{III.116}$$

Thus, the airgap flux density can be expressed by:

$$B_{rg}=\sum_k B_{rck}\cos k\alpha+\sum_k B_{rsk}\sin k\alpha \tag{III.117}$$

$$B_{\alpha g}=\sum_k B_{\alpha ck}\cos k\alpha+\sum_k B_{\alpha sk}\sin k\alpha \tag{III.118}$$

where

$$B_{rck}=\left(K_{Brc}+K_{B\alpha s}\right)f_{Br}-g_{Br}A_{stator} \tag{III.119}$$

$$B_{rsk}=\left(K_{Brs}-K_{B\alpha c}\right)f_{Br}-g_{Br}B_{stator} \tag{III.120}$$

$$B_{\alpha ck}=\left(-K_{Brs}+K_{B\alpha c}\right)f_{B\alpha}-g_{B\alpha}B_{stator} \tag{III.121}$$

$$B_{\alpha sk}=\left(K_{Brc}+K_{B\alpha s}\right)f_{B\alpha}+g_{B\alpha}A_{stator} \tag{III.122}$$

where for the internal rotor machine:

$$f_{Br}=\left(\frac{r}{R_s}\right)^{k-1}\left(\frac{R_m}{R_s}\right)^{k+1}+\left(\frac{R_m}{r}\right)^{k+1} \tag{III.123}$$

$$f_{B\alpha} = -\left(\frac{r}{R_s}\right)^{k-1}\left(\frac{R_m}{R_s}\right)^{k+1} + \left(\frac{R_m}{r}\right)^{k+1} \tag{III.124}$$

$$g_{Br} = \frac{\mu_0 k}{R_s}\left[A_{5k}\left(\frac{r}{R_s}\right)^{k-1} + A_{6k}\left(\frac{R_m}{r}\right)^{2k}\left(\frac{r}{R_s}\right)^{k-1}\right] \tag{III.125}$$

$$g_{B\alpha} = \frac{\mu_0 k}{R_s}\left[A_{5k}\left(\frac{r}{R_s}\right)^{k-1} - A_{6k}\left(\frac{R_m}{r}\right)^{2k}\left(\frac{r}{R_s}\right)^{k-1}\right] \tag{III.126}$$

and for the external rotor machine:

$$f_{Br} = \left(\frac{r}{R_m}\right)^{k-1} + \left(\frac{R_s}{r}\right)^{k+1}\left(\frac{R_s}{R_m}\right)^{k-1} \tag{III.127}$$

$$f_{B\alpha} = -\left(\frac{r}{R_m}\right)^{k-1} + \left(\frac{R_s}{r}\right)^{k+1}\left(\frac{R_s}{R_m}\right)^{k-1} \tag{III.128}$$

$$g_{Br} = \frac{\mu_0 k}{R_s}\left[A_{5k}\left(\frac{R_s}{r}\right)^{k+1}\left(\frac{r}{R_m}\right)^{2k} + A_{6k}\left(\frac{R_s}{r}\right)^{k+1}\right] \tag{III.129}$$

$$g_{B\alpha} = \frac{\mu_0 k}{R_s}\left[A_{5k}\left(\frac{R_s}{r}\right)^{k+1}\left(\frac{r}{R_m}\right)^{2k} - A_{6k}\left(\frac{R_s}{r}\right)^{k+1}\right] \tag{III.130}$$

Similarly, the flux density in the magnets can be obtained:

$$B_{1r} = B_{1r-slotless} - \sum_k g_{Br} A_{stator} \cos k\alpha - \sum_k g_{Br} B_{stator} \sin k\alpha \tag{III.131}$$

$$B_{1\alpha} = B_{1\alpha-slotless} - \sum_k g_{B\alpha} B_{stator} \cos k\alpha + \sum_k g_{B\alpha} A_{stator} \sin k\alpha \tag{III.132}$$

where $B_{1r\text{-}slotless}$ and $B_{1\alpha\text{-}slotless}$ are the flux densities identical to those in the corresponding slotless machines and can be found in [III2], and for the internal rotor machine:

$$g_{Br} = \frac{2\mu_0\mu_r k}{R_s\rho}\left[\left(\frac{r}{R_s}\right)^{k-1} + \left(\frac{R_r}{R_s}\right)^{k-1}\left(\frac{R_r}{r}\right)^{k+1}\right] \tag{III.133}$$

$$g_{B\alpha} = \frac{2\mu_0\mu_r k}{R_s\rho}\left[\left(\frac{r}{R_s}\right)^{k-1} - \left(\frac{R_r}{R_s}\right)^{k-1}\left(\frac{R_r}{r}\right)^{k+1}\right] \tag{III.134}$$

and for the external rotor machine:

$$g_{Br} = \frac{2\mu_0\mu_r k}{R_s\rho}\left[\left(\frac{r}{R_r}\right)^{k-1}\left(\frac{R_S}{R_R}\right)^{k+1} + \left(\frac{R_S}{r}\right)^{k+1}\right] \tag{III.135}$$

$$g_{B\alpha} = \frac{2\mu_0\mu_r k}{R_s\rho}\left[\left(\frac{r}{R_r}\right)^{k-1}\left(\frac{R_S}{R_R}\right)^{k+1} - \left(\frac{R_S}{r}\right)^{k+1}\right] \tag{III.136}$$

The flux density in the each slot can be given by:

$$B_{3ir} = \sum_m B_{3irm} \sin\left[F_m\left(\alpha + b_{o\alpha}/2 - \alpha_i\right)\right] \tag{III.137}$$

$$B_{3i\alpha} = \sum_m B_{3i\alpha m} \cos\left[F_m\left(\alpha + b_{o\alpha}/2 - \alpha_i\right)\right] \tag{III.138}$$

where for the internal rotor machine:

$$B_{3irm} = -\frac{\mu_0}{R_s} C_{ei} F_m \left[\left(\frac{r}{R_{sb}}\right)^{2F_m} + 1\right]\left[\left(\frac{R_s}{R_{sb}}\right)^{2F_m} - 1\right]^{-1}\left(\frac{R_s}{r}\right)^{F_m+1} \tag{III.139}$$

$$B_{3i\alpha m} = -\frac{\mu_0}{R_s} C_{ei} F_m \left[\left(\frac{r}{R_{sb}}\right)^{2F_m} - 1\right]\left[\left(\frac{R_s}{R_{sb}}\right)^{2F_m} - 1\right]^{-1}\left(\frac{R_s}{r}\right)^{F_m+1} \tag{III.140}$$

and for external rotor machine:

$$B_{3irm} = -\frac{\mu_0}{R_s} C_{ei} F_m \left[1 + \left(\frac{r}{R_{sb}}\right)^{-2F_m}\right]\left[1 - \left(\frac{R_s}{R_{sb}}\right)^{-2F_m}\right]^{-1}\left(\frac{R_s}{r}\right)^{-F_m+1} \tag{III.141}$$

$$B_{3i\alpha m} = -\frac{\mu_0}{R_s} C_{ei} F_m \left[1 - \left(\frac{r}{R_{sb}}\right)^{-2F_m}\right]\left[1 - \left(\frac{R_s}{R_{sb}}\right)^{-2F_m}\right]^{-1}\left(\frac{R_s}{r}\right)^{-F_m+1} \tag{III.142}$$

Reference

[III1] Z. Q. Zhu, L. J. Wu, and Z. P. Xia, "An accurate subdomain model for magnetic field computation in slotted surface-mounted permanent-magnet machines," *IEEE Trans. Magn*., vol. 46, no. 4, pp. 1100-1115, April 2010.

[III2] Z. Q. Zhu, D. Howe, and C. C. Chan, "Improved analytical model for predicting the magnetic field distribution in brushless permanent magnet machines," *IEEE Trans. Magn*., vol. 38, no. 1, pp. 229-238, Januray 2002.

[III3] F. Dubas, and C. Espanet, "Analytical solution of the magnetic field in permanent-magnet motors taking into account slotting effect: No-load vector potential and flux density calculation," *IEEE Trans. Magn*., vol. 45, no. 5, pp. 2097-2109, May 2009.

[III4] B. Ackermann, and R. Sottek, "Analytical modelling of the cpgging torque in permanent magnet motors," *Elect. Eng*., vol. 78, no. 2, pp. 117-125, 1995.

APENDIX IV PUBLICATIONS

Journal papers published or in press:

[J1] Y. Shen, Z. Q. Zhu, J. T. Chen, R. P. Deodhar, and A. Pride, "Analytical modeling of claw-pole stator SPM brushless machine having SMC stator core," *IEEE Trans. Magn*., 2013, in pess.

[J2] Y. Shen, and Z. Q. Zhu, "Analysis of electromagnetic performance of Halbach PM brushless machines having mixed grade and unequal height of magnets," *IEEE Trans. Magn*., 2013, in press.

[J3] Y. Shen, and Z. Q. Zhu, "Investigation of permanent magnet brushless machines having Unequal magnet height pole," *IEEE Trans. Magn*., vol. 48, no. 12, December 2012, in press.

[J4] Y. Shen, and Z. Q. Zhu, "Analytical prediction of optimal split ratio for fractional-slot external rotor PM brushless machines," *IEEE Trans. Magn*., vol. 47, no. 10, pp. 4187-4190, October 2011.

Journal papers submitted:

[J5] Y. Shen, G. Y. Liu, Z. P. Xia, and Z. Q. Zhu, "Determination of maximum electromagnetic torque in PM brushless machines having 2-segment Halbach array," submitted to *IEEE Trans.Ind. Electron.*

[J6] Y. Shen, and Z. Q. Zhu, "General analytical model for calculating electromagnetic performance of PM brushless machines having segmented Halbach array," submitted to *Proc. IET*.

[J7] W. Q. Chu, Z. Q. Zhu, and Y. Shen, "Analytical optimisation of external rotor permanent magnet machines," submitted to *IET*.

Conference papers:

[C1]Y. Shen, Z. Q. Zhu, J. T. Chen, R. P. Deodhar, and A. Pride, "Analytical modeling of claw-pole stator SPM brushless machine having SMC stator core," *2013 Intermag*, USA

[C2]Y. Shen, Z. Q. Zhu, J. T. Chen, and R. P. Deodhar, "Analysis of claw-pole rotor brushless machine with DC excitation by lumped-parameter magnetic circuit model," *2012 IEEE Power Electronics and Drives and Energy Systems*, India.

[C3]Y. Shen, and Z. Q. Zhu, "Analytical prediction of optimal split ratio for fractional-slot external rotor PM brushless machines," *2011 Intermag*,Taiwan, China.

[C4]Y. Shen, Z. Q. Zhu, and L. J. Wu, "Analytical determination of optimal split ratio for overlapping and non-overlapping winding external rotor PM brushless machines," *2011IEEE International Electric Machines and Drives Conference*, Canada.